NUREG/CR-0330
PNL-2696
R3

DIST

Ex-Reactor Determination of Thermal Gap and Contact Conductance Between Uranium Dioxide: Zircaloy-4 Interfaces

Stage I: Low Gas Pressure

John E. Garnier
Stefan Begej

April 1979

Prepared for
the U.S. Nuclear Regulatory Commission

Pacific Northwest Laboratory
Operated for the U.S. Department of Energy
by Battelle Memorial Institute

Battelle

PNL-2696

NOTICE

PACIFIC NORTHWEST LABORATORY
operated by
BATTELLE
for the
UNITED STATES DEPARTMENT OF ENERGY
Under Contract EY-76-C-06-1830

Printed in the United States of America
Available from
National Technical Information Service
United States Department of Commerce
5285 Port Royal Road
Springfield, Virginia 22151
Price: Printed Copy $____*; Microfiche $3.00

*Pages	NTIS Selling Price
001-025	$4.00
026-050	$4.50
051-075	$5.25
076-100	$6.00
101-125	$6.50
126-150	$7.25
151-175	$8.00
176-200	$9.00
201-225	$9.25
226-250	$9.50
251-275	$10.75
276-300	$11.00

NUREG/CR-0330
PNL-2696
R3

EX-REACTOR DETERMINATION OF THERMAL GAP AND CONTACT CONDUCTANCE BETWEEN URANIUM DIOXIDE: ZIRCALOY-4 INTERFACES

STAGE I: LOW GAS PRESSURE

John E. Garnier and Stefan Begej
Ceramics and Graphite Section
Materials Department

April 1979

Prepared for
the U.S. Nuclear Regulatory Commission
under a Related Services Agreement
with the U.S. Department of Energy
Contract EY-76-C-06-1830
FIN No. B2043

Pacific Northwest Laboratory
Richland, Washington 99352

ACKNOWLEDGMENTS

The authors would like to gratefully acknowledge the support of the United States Nuclear Regulatory Commission, Reactor Safety Research Fuels Behavior Research Branch. The assistance of T. George and D. McCahn in the development of the Modified Pulse Design experimental analytical model and computer code is appreciated. W. W. Wise and K. M. Pierce were involved in the research program at various stages as part of NORCUS undergraduate training program and their efforts are also appreciated.

The authors would also like to acknowledge the work of A. O. Desjarlais and D. R. Lundell of Dynatech, Inc., Cambridge, Massachusetts, who were involved in the development of the Modified Longitudinal Design apparatus and subsequent experimentation.

SUMMARY

A study of thermal gap and contact conductance between depleted uranium dioxide (UO_2) and Zircaloy-4 (Zr4) has been made utilizing two measurement apparatuses developed as part of this program. The Modified Pulse Design (MPD) apparatus is a transient technique employing a heat pulse (laser) and a signal detector to monitor the thermal energy transmitted through a UO_2/Zr4 sample pair which are either physically separated or in contact. The Modified Longitudinal Design (MLD) apparatus is a steady-state technique based on a modified cylindrical column design with a self-guarding sample geometry. Description of the MPD and MLD apparatus, data acquisition, reduction and error analysis is presented along with information on specimen preparation, thermal property and surface characterization. A technique using an optical height gauge to determine the average mean-plane of separation between the simple pairs is also presented.

Both gap and contact conductance experiments were performed using the MPD and MLD techniques as a function of temperature (293 K to 873 K), gas composition (Helium, Argon and He:Ar and He:Xe gas mixtures), average mean-plane separation distances (56 μm to 2.7 μm (contact)), contact pressure (0 to 14.7 MN/m^2; MLD only) and surface morphology (varying surface roughness and error of form) at atmospheric pressure: it was seen that H_g is dependent on all these variables. In addition, the gap separation distance is found to depend on both the roughness and error-of-form of the UO_2 and Zr4 specimen surfaces. Comparison of MPD and MLD gap conductance results shows agreement between the two measurement techniques to be within the experimental uncertainties.

A review of heat transfer formulations appropriate to estimation of gaseous conduction in the continuum and free molecular regime of gas dynamics is made with emphasis on the imperfect exchange of energy between gas molecules and surfaces and the difficulty in describing the "separation distance" between "real" surfaces in close proximity. Various theoretical and empirical models for describing gap conductance are inspected and inconsistencies in their convergence to free molecular expressions discussed. These inconsistencies are

later examined in relation to the results of this study and are considered to be of a second order importance insofar as any variation in the accommodation coefficient is masked by surface roughness effects at narrow gaps.

Comparison of the "ideal" gap conductance expression

$$H_g = K_{gas}/d + g_1 + g_2$$

to the experimental results of this study for various temperature jump distance (g) models is performed and an examination made of the various definitions of the gap separation and models for the temperature jump distance. Computation of the aforementioned expression is made using algorithms for the gas conductivity (K_{gas}) and the temperature jump distance as applied in GAPCON-THERMAL II (a computer code) under conditions where the "ideal" gap is assumed to be the average mean-plane of separation determined in this study and $g_1 \approx g_2$. This comparison shows that the "ideal" gap conductance expression, when used to predict gap conductance for "nonideal" gap geometries, yields a conservative estimate for H_g. The dependence of the "ideal" gap conductance expression on gas composition, temperature and accommodation coefficient is also examined in relation to experimental results.

Comparison of MLD contact conductance (H_c) results with those reported by the investigators Ross and Stoute, Dean, and Rapier is made. The H_c results are seen to converge at higher contact pressures (14.7 MN/m^2) to the results reported by Ross and Stoute. At lower contact pressures the H_c results are below that reported by Rapier by a factor of 2 to 5. This effect is attributed to variations in the initial number of contact points at the UO_2:Zr4 interface. However, the presence of a fill gas was found to cause a substantial improvement in the total conductance. The total conductance (H_T) was found to increase by an order of magnitude with an argon fill gas at 0.172 MPa up to a contact pressure of 1 MN/m^2. The H_T results are also observed to be in agreement and the total conductance results reported by Dean in 1 atm argon.

A review of models for predicting solid:solid thermal contact conductance based on surface roughness and elastic/plastic deformation of asperities and on

surface waviness and elastic deformation is made. These models are compared to the results and a discussion is given on the observed discrepancies in the predicted $(PA/H)^N$ dependence among the various theoretical and empirical models. The Mikic-Todreas model is seen to be in best agreement with the results of this study. However, the exponent N in the relationship $H_c \alpha (PA/H)^N$ is found not to be constant but rather increases with increasing pressure. Similarities between the results and a model proposed by Dundurs and Panek suggest that the surface waviness (rather than surface roughness) exerts a first order effect on H_c.

Based on the experimental results of this study and examination of various heat transfer expressions and models for predicting gap and contact conductance, a discussion is made of areas where additional information is required.

CONTENTS

592 009

FIGURES

TABLES

1.0 INTRODUCTION

The design and operation of nuclear reactors requires a detailed understanding of the normal operating conditions which exist in nuclear fuel assemblies, as well as ascertaining the effects of off-normal conditions (i.e., loss-of-coolant accident, power-cooling mismatch, etc.). The nuclear fuel assemblies are comprised of clusters of fuel rod subassemblies. The fuel rods in these subassemblies serve as containment vessels for the nuclear fuel pellets and are the primary barriers to the release of radioactivity. This primary barrier contains not only the fuel pellets but also the fission products which are generated along with useful heat from the fission process itself. This heat must cross the gap between the fuel and the cladding before entering the coolant. In order to ensure that the normal and off-normal conditions affecting the heat transfer through the cladding are properly considered in reactor design and safety analysis, a thorough understanding of the heat transfer process between the fuel pellet and surrounding cladding is of necessity.[1]

Although the principles which govern heat transfer across the fuel:clad interface are considered to be well understood,[2-10] the heat transfer process within an actual fuel rod is complex and difficult to predict. The primary heat transfer mechanisms across the fuel:clad interface are considered to be conduction through the fill gas, radiation, convection, and solid:solid contact conduction. Other supplementary mechanisms of energy transport have been proposed[11] such as improved gas conductivity from radiation-induced ionization and chemical enthalpy transport by thermal diffusion. When the fuel:clad gap becomes very narrow, additional mechanisms may become operative. For instance, the heat transfer between the fuel:clad becomes quite sensitive to the exchange of energy between the gas molecule and the surface.[12] Under these conditions, a reduction in the number of molecular encounters within the fill gas occurs when the mean free path of the gas molecule approaches the dimensions of the gap (i.e., Knudsen Regime). It has been suggested[13] that enhanced conduction under these conditions may occur if the gas molecules possess a non-maxwellian velocity distribution.

All these mechanisms are interdependent and their effects are difficult to evaluate precisely because of their dependence upon a number of variables which are not easily defined in a fuel rod. For example, when the fuel:clad interfaces are in contact, heat may be transferred through solid:solid contacts and the gas phase which occupies the voids between contact spots. The actual area of contact is, in turn, dependent on the surface morphology characteristics, the applied load, and the mechanical properties of the mating materials. If the fuel:clad interfaces are not in contact, heat transfer can occur only through the gas phase. In a fuel rod these types of interfaces may occur separately or simultaneously (e.g., if a nonconcentric fuel pellet is in partial contact with the surrounding cladding). Thus, the total heat transfer or interface conductance, H_T, can be considered to consist primarily of contributions arising from contact conductance, H_c (fuel and cladding in contact), and gap conductance, H_g (fuel and cladding separated). The heat transfer contribution arising from radiation is not considered in this study.

The heat transfer across the interface is known to be dependent on the gap size, gas composition in the gap, temperature in the gap and on its boundaries, the extent and pressure of fuel:cladding interaction, fabrication parameters, and operating history of the fuel rod.[14] These parameters may be separated into seven variables whose range of interest are shown in Table 1.

TABLE 1. Range of Factors Which Influence the Heat Transfer Between UO_2 and Zr4

Interface Temperature:	Room temperature to 900 K or higher.
Gas Pressure:	Up to 13.8 MPa (2000 psia).
Gas Composition:	Pure He, He-Xe-Kr and other gas mixtures representative of the gas atmosphere in fuel rods.
Gap Width:	0.127 mm (0.005 in) to contact.
Interfacial Contact Pressure:	0 to 34.5 x $10^6 N/m^2$ (5000 psi).
Surface Morphology:	Typical of contemporary fuel element designs.
Time (at constant pressure):	Up to several hours.

Current available ex-reactor and in-reactor values for H_T have been considered to have a degree of uncertainty such that heat transfer correlations are difficult to make.[14,15] In-reactor experiments designed to measure the dependence of interfacial heat transfer on the factors listed in Table 1 are complicated because of the difficulties and uncertainties in measuring and controlling the variables which affect the heat transfer across the interface (e.g., the eccentricity or non-uniformity of surface contact between the fuel and the clad). On the other hand, ex-reactor experiments have mainly studied the dependence of H_T and H_c on contact pressure and temperature.

The objective of this research program is to provide well-characterized H_g and H_c data to test existing theories for predicting gap and contact heat transfer. The determination of the sensitivity of the interface conductance to changes in the variables listed in Table 1 would allow a further refinement of computer programs such as COMETHE,[16] GAPCON-THERMAL,[17,18] FRAP-S,[19] and IAMBUS[20] which predict the effects of gap and contact conductance in oxide fuel elements. The goal of this research is to extend measurements of H_g and H_c to higher temperatures and gas pressures than obtained in previous ex-reactor investigations and to extend measurements to actual gap conditions.

The purpose of this report is to describe the two ex-reactor measurement techniques developed to measure H_g and H_c, and to report on the results of current experiments using these techniques. A review of previous in-reactor and ex-reactor experimentation is made in Section 2, "Previous Experiments." A discussion of heat transfer formulations, gap geometry, and selected calculational models for H_g and H_c are discussed and summarized in Section 3, "Heat Transfer Across Interfaces."

Section 4, "Experimental," discusses the details of specimen preparation and the experimental aspects of the measurement techniques. Section 5, "Results and Discussion," is divided into a series of subsections based on comparison of MPD/MLD technique, results, presentation of gap and contact conductance results, and comparison to H_g and H_c model predictions. Section 6, "Conclusions

and Recommendations," contains the conclusions reached thus far in this investigation, outline of Stage II and III objectives, and recommendations for additional studies. This section is then followed in the usual manner by the References and various Appendices.

2.0 PREVIOUS EXPERIMENTS

2.1 IN-REACTOR

Lanning et al.[14] have made an extensive review of in-reactor data for UO_2 pellet fuel where internal temperatures were measured by thermocouples and/or estimated by microstructural features. From this large body of data, estimates of the fuel surface and cladding inner temperatures were made and interface conductances were calculated under a consistent set of conditions. The experimental errors in the parameters used to infer H_T were estimated from the reported variances and reasonable uncertainties based on a number of irradiation experiments. The parameters that appear to dominate the estimation of H_T are: linear power, internal fuel temperature, UO_2 thermal conductivity, fuel thermocouple location, and gap width. However, the reasonable uncertainties chosen for the input parameters led to quite high uncertainties in the calculated interface conductance values. This was confirmed by the authors' attempt to fit the data to simple models.

In a recent investigation by Cunningnam, Lanning et al.[21] into the state-of-the-art of fuel temperature, gap conductance, and stored energy calculations, emphasis was placed on propagation of input and model uncertainties. The uncertainty analysis was performed by identifying major thermal models and collecting them in an abstract of a thermal performance code. A method of linear propagation of uncertainties was applied to the models in the code and comparison made to observed variability of selected experimental data for fuel centerline temperatures and gap conductance values. The report concluded that the relative uncertainty in stored energy (applicable to standard BWR's at a linear power of 500 W/cm) is approximately ±20% (3σ) at BOL (beginning of life) increasing to ±25% to 40% at EOL. In addition, the gap conductance was found to be of minor importance in determining the stored energy.

A recent Canadian study by Campbell et al.[22] of fuel-to-sheath heat transfer coefficients between UO_2 and stainless steel concluded that an existing calculational expression used for the fluid phase (i.e., gap) component heat transfer is adequate to describe the in-reactor results provided the

temperature jump distance is adequately described; whereas, an existing equation based on the Ross and Stoute model cited for the solid phase (contact) component underpredicts the in-reactor coefficients and overestimates the dependence on interfacial pressure. The total conductance summed from the expressions for H_g and H_c were found to correlate well with the in-reactor results. No estimation was made of the uncertainty in the measured in-reactor results.

2.2 EX-REACTOR

Although thermal contact conductance measurements on a variety of metal:metal pairs have been investigated,[23-27] few laboratory measurements have been performed on ceramic:metal pairs,[28-33] in particular, UO_2:Zr.[27-29] No ex-reactor experimental gap conductance work has been found in the literature on either metal:metal pairs or ceramic:metal pairs other than a report presented previously by the authors.[13]

Of the ex-reactor studies performed on ceramic:metal pairs, the earliest was by Wheeler,[27] who measured values of H_c between UO_2: graphite, UO_2:Zr2, and UO_2:Al. The values obtained on UO_2:Zr2 were at low pressure (0.44 and 0.8 MN/m^2 at 564 and 733 K respectively.) The reliability of these results is considered poor, as the sample surfaces were not well characterized. Dean[28] measured the variation of H_T on UO_2:Zr2 surfaces at contact pressures ranging from 1.84 to 4.65 MN/m^2 in argon at 1 atm. The mean interface temperatures were varied from 477 to 560 K. Typical values obtained ranged from 0.49 to 0.66 x 10^4 W/m^2-K between 1.84 and 4.65 MN/m^2 for a UO_2:Zr2 pair having a RMS (root-mean-square) surface roughness of 3.7 μm and 1.5 μm, respectively. Ross and Stoute[29] have determined experimental values of the heat transfer coefficient between UO_2:Zr2 surfaces in contact under the following conditions: contact pressure 4.9 to 53.9 MN/m^2; maximum interface temperature of 633 K; in vacuum (H_c) and in atmospheres of He, Ar, Kr, and Xe at atmospheric pressure (H_T). The H_c values ranged from 0.12 x 10^4 to 1.4 W/m^2-K depending on surface roughness and contact pressure. The H_T results were found to depend on the interstitial fill gas, contact pressure, and surface roughness. Typical results

for H_T at 1 atm argon ranged from 0.5 to 0.9 x 10^4 W/m^2-K between 9.8 and 49 MN/m^2 for a UO_2:Zr2 pair having RMS surface roughnesses of 3.4 μm and 1.7 μm, respectively. Differences in the range of contact pressures as compared to those employed by Dean[28] makes direct comparison of the results difficult.

Rapier et al.[30] determined the effect of different gases, roughness, contact pressures, and interfacial pressures on H_c between UO_2 and stainless steel interfaces. They concluded that for hard materials the solid:solid conductance contributes only a small portion to the total conductance. A study by Williams et al.[31] on UN-metal interfaces showed the importance of stress, hardness, thermal conductivity, and surface topography on H_c. The experiments were designed to hold the surface roughness characteristics approximately constant. The data suggested that the surface characteristics of UN controlled the ultimate contact area, but the initial area of contact may be dependent on the mating characteristics of the respective surfaces (i.e., error of form). Madhusudana[32] investigated the effect of the interfacial fluid (gas) on the thermal contact conductance between specially machined surfaces of UO_2:Zr2, Nilo:UO_2, and Nilo:stainless steel. He concluded that H_c improves with the presence of a gas filling the voids between mating surfaces. The improvement is most significant at low contact pressures but decreases with increasing contact pressure. The contribution by the gas at any contact pressure decreases with decreasing gas pressure, with a significant decrease in fluid conductance occurring at pressures below 0.013 MPa. Recently, Khan[33] conducted an experimental investigation between surfaces of silicon-oxy-nitride and stainless steel. The various specimen pairs had CLA (centerline average) surface roughnesses ranging from 0.02 to 2.5 μm. The experiments were performed in vacuum (H_c) and at one atmosphere (H_T) in helium and argon at various interfacial pressures from 0 to 0.7 MN/m^2 and temperatures to 530 K. Several of the conclusions reported in this investigation were: a distinctive two regime behavior was observed for variation of H_c with interfacial pressure; H_c shows only a slight dependence on interfacial temperature; that higher H_c results were usually obtained for relatively smooth surface combinations, and that the Ross and Stoute model is in agreement with the results of the study.

In several of the reports and investigations examined, the authors have proposed models to describe their measured dependence of H_c on interfacial pressure (i.e., Dean,[28] Ross and Stoute,[29] Rapier[30]). These models will be reviewed and summarized in the section following.

3.0 HEAT TRANSFER ACROSS INTERFACES

3.1 INTRODUCTION

Extensive theoretical and experimental investigations have been directed towards the development of models for predicting thermal gap and contact conductance with sufficient accuracy for design and safety purposes. The emphasis for these efforts arises from the substantial influence of the thermal resistance of the fuel:clad interface on fuel temperature (design). Alternately, the thermal resistance of the interface has been shown to be of secondary importance in influencing the stored energy residing in the fuel rod (safety)[21].

This section discusses the difficulty in describing the regime of gas dynamics (i.e., continuum, transition, and free molecular) with respect to the complexity of the physical separation between noncontacting surfaces in close proximity. Review of heat transfer formulations appropriate to the estimation of gaseous conduction in the continuum and free molecular regime of gas dynamics is made with emphasis on the imperfect exchange of energy between gas molecules and surfaces. Various theoretical and empirical models developed to account for the imperfect exchange of energy between gas molecules and surfaces are summarized. Inspection of models, appropriate for use in the continuum regime, reveal inconsistencies in their convergence to the free molecular expressions. These inconsistencies are examined in relation to the energy exchange between gas molecules and surfaces under three general cases. The form of a generalized expression for the total conductance across a gas "gap" which spans the free molecular, transition, and continuum regimes is discussed. Examination of the behavior of the expression is made for the three general cases cited.

The development of various models for predicting solid:solid thermal conductance is discussed based on the assumption that the thermal contact resistance is closely coupled to surface roughness and the elastic/plastic deformation of asperities. A review of a recent theoretical model development which considers only the effect of surface waviness and elastic deformation on the thermal contact resistance is also presented.

No endorsement is made in this report as to a recommended model to describe the imperfect energy exchange between gas molecules and surfaces. A program at the University of Missouri-Columbia has been established to undertake such an analysis.(a)

3.2 HEAT TRANSFER BY GAS MOLECULES BETWEEN NONCONTACTING SURFACES

3.2.1 Definition of Knudsen Number

The kinetics of heat transfer by gas molecules within a gas "gap" is dependent on the particular gas regimes present. Proper use of heat transfer formulations within the continuum and free molecular regimes will depend on the value of the Knudsen number which is commonly referred to as the ratio of the mean free path of the gas molecule, λ, to "gap distance" as given by

$$KN = \frac{\lambda}{\text{Gap Distance}} \qquad (1)$$

Heat transfer formulations appropriate to the continuum and free molecular regimes may be applied with confidence with KN <0.01 (continuum) and KN >100 (free molecular). Determination of KN, however, requires the use of a realistic value for the "gap distance".

3.2.2 Definition of "Gap Distance"

The most general case of a "gap" between solid materials across which heat will flow if a temperature differential is present is shown schematically in Figure 1. The "gap" between UO_2 and the Zr4 is an artist's rendering of measured Talysurf profiles for a sample pair (ISM-I) used in this study. The use of "gap distance" in Equation 1 implies that the spacial separation between surfaces can be reduced to a one-dimensional parameter whose value can be expressed in units of length. If this procedure is followed, the one-dimensional separation between UO_2 and Zr4 shown in Figure 1 can be defined in a number of ways, which, in reference to this report, are:

(a) Prof. S. K. Loyalka, Nuclear Engineering Department, University of Missouri-Columbia, Columbia, Missouri 65201. NRC-RSR Contract No. NRC-04-78-201.

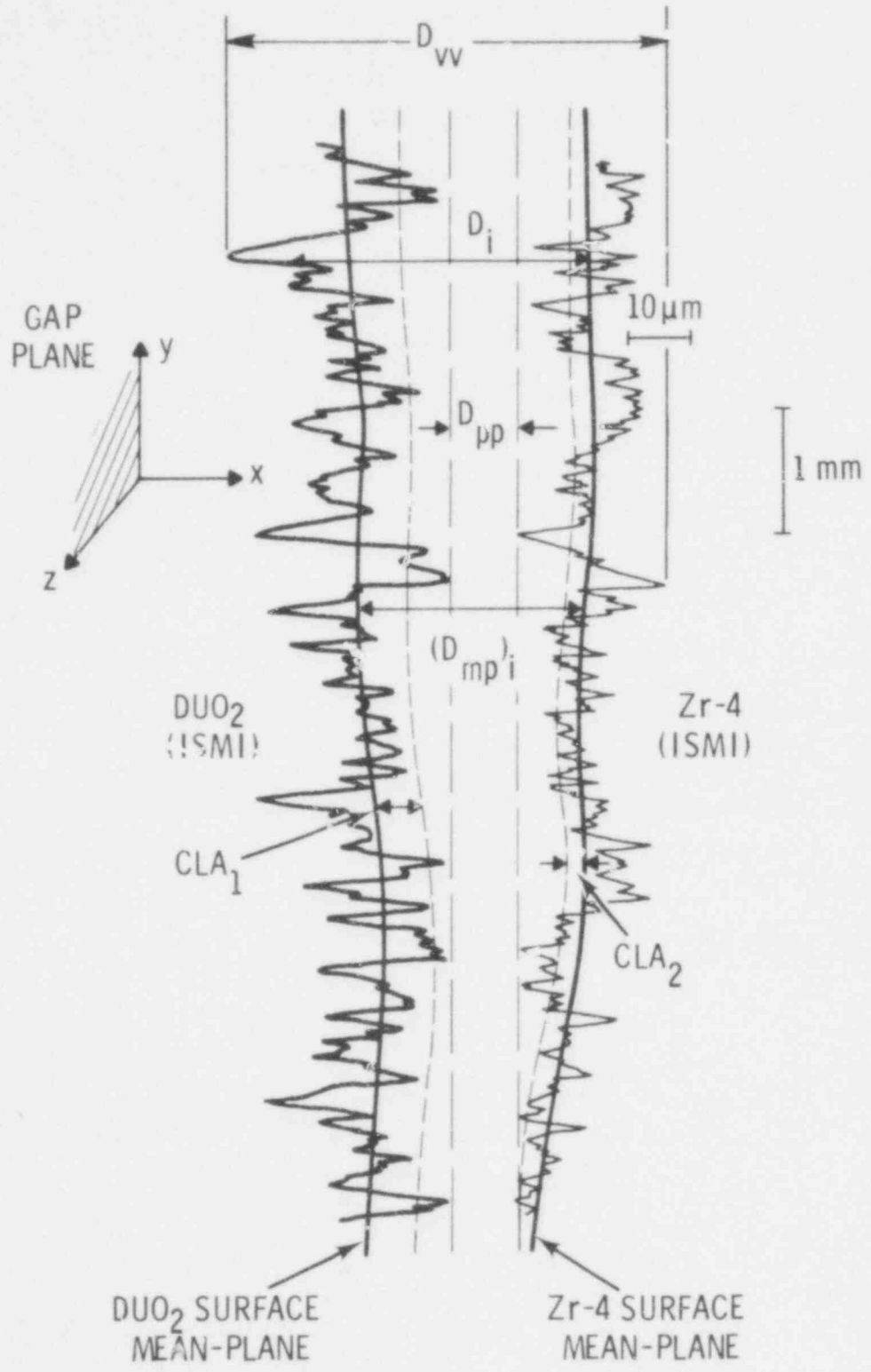

FIGURE 1. Schematic Representation of the "Real Gap" Between UO_2 and Zr4

D_{vv} = the separation distance between parallel surface planes defined by the three deepest valleys on each surface.

D_{pp} = the separation distance between parallel surface planes defined by the three highest peaks on each surface. Its value is equivalent to the separation distance that would be achieved if the UO_2 and Zr4 were rigidly abutted against an ideally parallel spacer which was subsequently removed.

$(D)_i$ = the local surface separation distance. The index "i" refers to some specific (y, z) coordinate.

D = the arithmetic average of all $(D)_i$.

$(D_{mp})_i$ = the local separation distance between the surface mean-planes, where the mean-plane on each surface is computed over some specified averaging interval.

D_{mp} = is the arithmetic average of all $(D_{mp})_i$.

It is noted that if a large number of $(D)_i$ values are averaged over the entire surface, the resulting value of D would be equivalent to D_{mp}.

Assuming that no surface error of form exists on either surface, the fractional uncertainty in D_{mp} due to surface roughness can be defined to be

$$\psi_R = \frac{\theta(CLA_1) + \theta(CLA_2)}{D_{mp}} \qquad (2)$$

where θ is a constant which has a value of 5 for a "uniformity random" surface.[34] The value of $\psi = 0.1$ corresponds to a ±5% (3σ) uncertainty in $(D_{mp})_i$ or D_{mp}. For ψ values much less than 0.1, the approximation can be made that $D_{mp} = D_{pp}$. The surfaces can be treated as ideally flat, smooth planes with the gap separating the surfaces considered as being "well defined." In this case the averaged value of the Knudsen number would be

$$KN = \frac{\lambda}{\text{Gap Distance}} = \frac{\lambda}{D_{mp}} \qquad (3)$$

For ψ_R values much larger than 0.1, the surface roughness can no longer be neglected and the value of the Knudsen number as given by Equation 3 becomes questionable. Development of a similar argument can be made on the basis of mating error of form (macrowaviness) (e.g., ψ_{EOF}) if the surface roughness is assumed to be zero.

Under circumstances where the total fractional uncertainty in η_{mp} (ψ) is greater than 0.1, the determined "gap" conductance is no longer uniquely defined by the single distance parameter, the "gap distance". By virtue of differences in surface roughness and/or error of form, many "gap distances," different in value, could result in the same value of "gap" conductance. To specify a special separation unique to a measured value of "gap" conductance, consideration of all the independent variables relating the surface separation to the "gap" conductance (e.g., surface roughness, mean-plane separations, surface error of form and amplitude) is required. The "gap" conductance cannot be uniquely determined in reference to a distance parameter called the "gap distance" except under ideal conditions (i.e., $\psi<0.1$). Theoretical treatment of this problem, although not considered in this report, is considered necessary.

3.2.3 Regions of Gas Dynamics

The problem of specifying an existing regime of gas dynamics may be discussed by considering the two extreme ranges of gas dynamics, the continuum and free molecular regimes, along with the transition regime. These regimes and ranges of KN and ψ are illustrated in Figure 2.

The continuum regime is said to exist when the value of KN $\lesssim$0.01 as shown in regions 1 and 2. Conditions are in the free molecular regime when KN $\gtrsim$100 (i.e., regions 7 and 8). The transition regime is present when 0.01 $\lesssim$ KN $\lesssim$100. The conditions within the transition regime are closest to the continuum regime when 0.01 $\lesssim$ KN $\lesssim$ 1 (regions 3 and 4); and, correspondingly closest to the free molecular regime when 1 $\lesssim$ KN $\lesssim$ 100 (regions 5 and 6). The three regions are further segmented depending on the value of ψ being greater or less than 0.1.

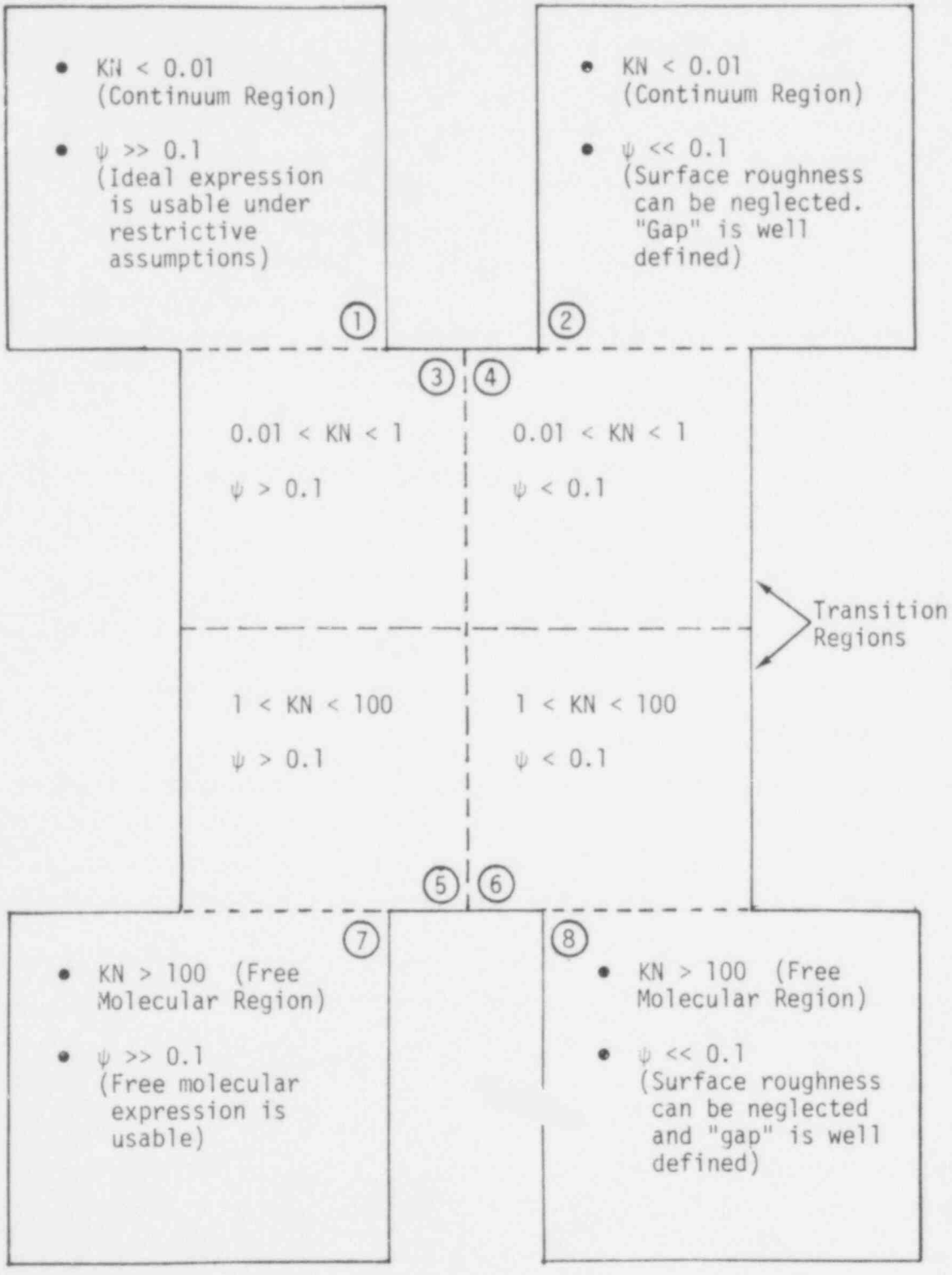

FIGURE 2. The Relationship Between the Extreme Ranges of KN and ψ and the Transition Regime

592 031

The range of values for KN and ψ for conditions within an actual fuel:clad gap will depend on many factors. Gas composition, pressure, and temperature will determine the value of the mean free path. Fuel and clad surface roughness and error of form, nonconcentric fuel pellet location and extent of gap closure will certainly influence the local fuel:clad separation distance $(D)_i$. Limits on the local value of the Knudsen number (KN_L) and ψ_R, for instance, can be established if the maximum value of $(D)_i$ is assumed to be 250 μm, and the lower limit is zero (local fuel:clad contact). If typical fuel surface roughnesses are considered[28] to span the ranges from 0.3 μm $\leq CLA_{Fuel} \leq$ 4 μm and 0.2 μm $\leq CLA_{Clad} \leq$ 1.5 μm, the local value of ψ_R will range from 0.01 to infinity. Furthermore, if the local gap temperature is 473 K for a helium fill gas at one atmosphere, the value of KN_L would span the range from 0.004 to infinity (e.g., $(D)_i = 0$). Changing the fill gas to another mixture (i.e., He:Xe) and raising the pressure will only reduce the lower limit on KN_L (to 0.002 for a He:Xe (50:50) mixture at 20 atmospheres) if no "gap" closure occurred.

In reference to Figure 2, it can be seen that typical fuel:clad "gap conditions" therefore tend to be skewed towards the regions 1, 3, 5, and 7 favoring the transition regime and large ψ values. Heat conduction models for use in describing the heat transfer within the transition regime of 3 to 6 remain to be developed. Theoretical heat conduction models have been developed where appropriate to values of KN and ψ as outlined in regions 2 and 7 and 8. Semiempirical models have been formulated on the basis of conditions appropriate to region 1.

The following section will review and discuss these heat conduction models.

3.2.4 Heat Conduction Models

3.2.4.1 Continuum Regime (Region 2: "gap" is well-defined).

When KN < 0.01 and $\psi \ll 0.1$, the heat conduction problem will reduce to the idealized case of heat conduction between flat parallel plates.[3,36] The geometry of the problem and the assumed temperature profile across the interface are shown in Figure 3 where $d = D_i = (D_{mp})_i = D_{mp} = D_{pp}$. The

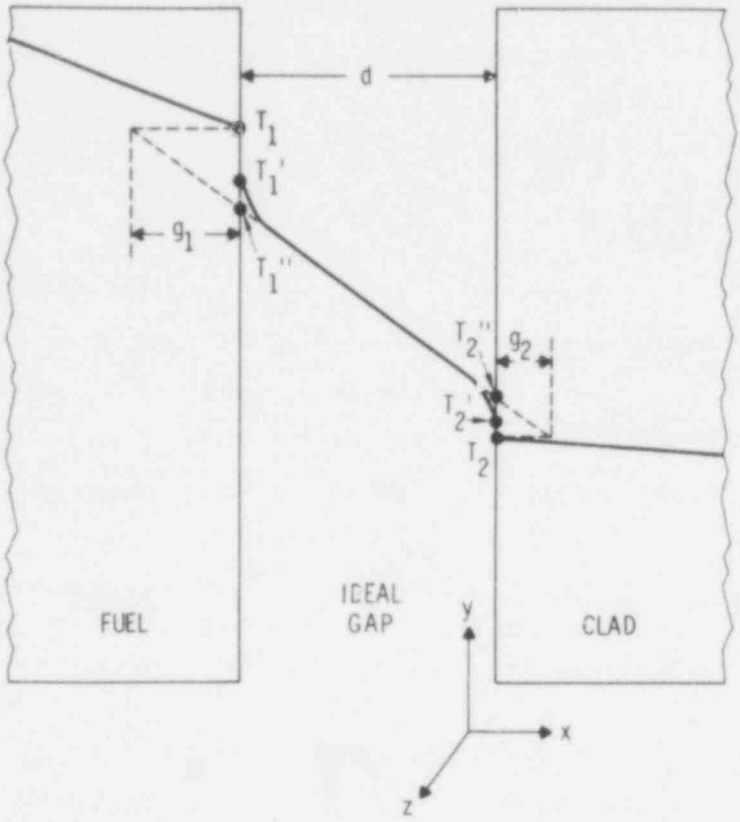

FIGURE 3. Idealized Temperature Profile Across Gap in the Continuum Regime ($KN < 0.001$ and $\psi << 0.1$).

temperature discontinuity at the surfaces is caused by incomplete thermal accommodation of the gas molecules to the surface temperature; whereas, the nonlinearity of the temperature gradients near the walls are caused by the inability of gas molecules leaving the surfaces to completely exchange their energy with neighboring gas molecules. Since the bulk of the gas is in the continuum regime, one can use Fourier's law of heat conduction to write the following expression for the heat transfer per unit area per second:

$$Q = K_{gas} \frac{\Delta T}{\Delta x} = K_{gas} \frac{T_1'' - T_2''}{d} \qquad (4)$$

where K_{gas} is the thermal conductivity of the gas; d the separation distance between fuel and clad; and, T_1'' and T_2'' are the respective fuel and clad wall temperatures resulting from extrapolation of the temperature gradient in the gas. As T_1'' and T_2'' are generally not known, the concept of the temperature jump distance (TJD), g_1 and g_2, is introduced to take into account the temperature discontinuities and nonlinearity of the temperature gradient at and near the walls. The heat flux can be written as

$$Q = K_{gas}\left(\frac{T_1 - T_2}{d + g_1 + g_2}\right) \tag{5}$$

where T_1 and T_2 are the surface temperature of the fuel and clad, respectively. The gap conductance is defined as

$$H_g \equiv \frac{Q}{\Delta T} = \frac{Q}{T_1 - T_2} \tag{6}$$

hence

$$H_g = \frac{K_{gas}}{d + g_1 + g_2} \tag{7}$$

The theory of the temperature jump was first treated by Maxwell[35] and subsequently refined by Lloyd,[36] Kennard,[3] and more recently Loyalka.[37] Their results can be summarized by expressing the TJD in a generalized format:

$$g_i = \frac{C\, K_{gas}\sqrt{T_{gas}}}{GP} F(a_i, f_i, M_i) \text{ meters} \tag{8}$$

where i = 1, 2 standing for the fuel and clad, respectively

C = constant

F = function of the thermal accommodation coefficient a_i; mole fraction, f_i; and molecular weight, M_i of gas species i (kg/mole)

GP = gas pressure (P_a)

T_{gas} = mean gap temperature $(T_1 + T_2)/2$ (K)

K_{gas} = thermal conductivity of the gas mixture (W/m-K).

Table 2 lists the constant C and the function F for the three theoretical models. In addition, the expression used in the GAPCON-THERMAL II fuel performance code is also listed. The latter uses the Lloyd model which has been modified by an empirical correction factor.

TABLE 2. Equations for Temperature Jump Distance

Model	Constant C	Function F For Mixed Gases	The Function F For Pure Gases
Lloyd	0.2171	$\frac{1}{\Sigma a_i f_i / \sqrt{M_i}}$	$\sqrt{M}/a$
Kennard	0.2174	$\left(\frac{2-a_{mix}}{a_{mix}}\right)\sqrt{\frac{1}{\Sigma f_i/M_i}}$	$\left(\frac{2-a}{a}\right)\sqrt{M}$
Loyalka	0.2174	Kennard·$(1+0.162a_{mix})$	Kennard $(1+0.162a)$
GAPCON-THERMAL II	1.8·Lloyd	Lloyd	Lloyd

The models differ from each other in two aspects: first, in the manner in which they handle mixed gases and, secondly, in the way the accommodation coefficient enters the expression.

The coefficient of accommodation describes the extent to which molecules achieve thermal equilibrium with the surface upon collision. It was defined by Knudsen[38] as

$$a \equiv \frac{\theta_I - \theta_R}{\theta_I - \theta_W} \qquad (9)$$

where θ_I = mean energy of the incident molecules

θ_R = mean energy of the reflected molecules

θ_W = mean energy of the reflected molecules if they were to reach thermal equilibrium with the wall.

If the incident and reflected molecules possess a Maxwellian velocity distribution, one can replace the mean energies by the concept of a temperature for the molecules, resulting in:

$$a = \frac{T_I - T_R}{T_I - T_W} \tag{10}$$

where T_I and T_R are the temperature of the incident and reflected molecules, respectively, and T_W the temperature of the wall. Blodgett and Langmuir[39] pointed out that the concept of a temperature, T_R, for the escaping molecules has no clearly defined meaning unless the molecules depart with a Maxwellian energy distribution which is probably not the case unless a = 1. Thus a definition of the coefficient of accommodation in terms of energy changes, Equation 9, is more satisfactory. For instance, Loyalka[37] has considered the effect of diffuse specular reflectance on the velocity distribution of θ_R which results in a correction to the (2-a)/a relationship as shown in Table 2. It should also be noted that values of "a" for translational, rotational, and vibrational energy are not necessarily the same. This assumption is usually made for the sake of simplicity in arriving at the expressions for "a" in Table 2. The reader is referred to the work by Knudsen[38] and Sasaki et al.[40] for further discussion.

According to Equation 10, the accommodation coefficient ranges in value from 0 to 1, corresponding to the case of negligible and complete thermal equilibration of the incident molecules with the surface, respectively. The particular value for "a" has been found to depend very strongly on the atomic species at the surface and also on the surface geometry (i.e., roughness). It has been shown[38] that if the surface atom is considered to act as an independent particle (i.e., by ignoring neighboring bonds between the surface atom and surrounding lattice) and if the collision between the gas atom and surface

atom is assumed elastic, then the thermal accommodation will be most complete when the gas and surface atoms are of equal mass. This may explain why the accommodation coefficient will be higher on a contaminated surface (e.g., H_2O, He, or Xe monolayer absorption) than on a surface which is atomically clean. The accommodation coefficient will also be found to vary with temperature insofar as the temperature influences the presence of any absorbed species or by the way surface atoms are coupled to the lattice.

Most measured values of "a" take no account of the possibility of multiple collisions of the gas molecule with the surface due to its microscopic roughness. Roberts[41] has derived an expression relating the measured accommodation coefficient "a" to the value "a*" that would be obtained with an atomically smooth surface. The relationship found was

$$a = 1 - (1 - a^*)^n \qquad (11)$$

where "n" is the average number of collisions a gas molecule would make with a surface before escaping. It can be seen from Equation 11 that a rougher surface would have a higher value of "a" than for a smoother surface due to the greater number of wall collisions within the deeper crevasses of the rougher surface.

In reference to the expression for H_g as given by Equation 7 and the TJD models listed in Table 1, the influence of the accommodation coefficient on H_g will be the strongest when $(g_1 + g_2) \geq d$. When $d >> (g_1 + g_2)$, the influence of the accommodation coefficient on H_g is masked by the thermal resistance of the bulk gas in the gap.

3.2.4.2 Free Molecular Regime (Regions 7 and 8).

In the free molecular regime ($KN > 100$) H_g is found to be independent of the surface separation, thereby making H_g independent of ψ. An expression for H_g in the free molecular regime is given by[42]

$$H_{FM} = H_g = \frac{GP}{4} \left(\frac{2R}{\pi}\right)^{1/2} \left(\frac{\gamma + 1}{\gamma - 1}\right) \frac{1}{\sqrt{T}} \left(\frac{a}{2 - a}\right) \qquad (12)$$

where GP = pressure (P_a)

R = gas constant (8.31 J/mole - K)

γ = ratio of specific heats, C_p/C_v

T = temperature (K)

a = accommodation coefficient.

The accommodation coefficient is seen to enter into this expression more strongly than in the TJD expressions used in the continuum regime as given by Equation 7. This implies that a stronger dependence of H_g on surface roughness occurs in the free molecular regime than in the continuum regime. It is also noted that in the limit when d = o, Equation 7 converges to Equation 12, exactly, when the Kennard expression for the TJD is used. Use of other TJD models in Equation 7 will result in a limiting case expression related to Equation 12 through the manner in which the accommodation coefficient is expressed in the TJD model.

3.2.4.3 Continuum and Transition Regimes (Regions 1, 3, and 5: gap is ill-defined).

Region 1 (KN < 0.01), Region 3 (0.01 < KN < 1) and Region 5 (1 < KN < 100) where $\psi >> 0.1$, as shown in Figure 2, can be visualized as existing under the surface conditions illustrated by Figure 1. An expression for the gap conductance under such conditions can be developed in the following manner.

Consider first the ideal situation when 0.01 < KN < 100, but $\psi << 0.1$ (i.e., ideal gap). The gap conduction expression at the two extremes of KN are known (Equations 7 and 12), so it remains only to combine them in some "appropriate" manner so as to describe the gap conductance in the transition region.

The assumption is made that the fractional contribution of H_{FM} (Equation 12) to the total conductance is directly proportional to the probability that a molecule could reach the opposite wall without intervening collisions, i.e., probability = $\exp(-D_i/\lambda)$. It is also assumed that the contribution from Equation 7 will be directly related to the probability that an atom will have at least one collision before reaching the opposite wall, i.e., as $[1 - \exp(-D_i/\lambda)]$. Then, the total conductance in the transition region can be written as

$$H_{TR} = H_{FM}[\exp(-D_i/\lambda)] + H_g(1 - \exp[-D_i/\lambda)]; \qquad (13)$$

utilizing Equation 1, one can write this as

$$H_{TR} = H_{FM}[\exp(-1/KN)] + H_g[1 - \exp(-1/KN)] \qquad (14)$$

An expression for H_{TR} in the more general case of $\psi>0.1$ can be developed in a similar fasnion given the following additional assumptions:

- One dimensional heat flow exists in both the solid and gas phases.
- D_i can be specified for the entire gap region of concern, either by actual measurement or by a suitable mathematical approximation.
- The correct model for TJD is known for the case $\psi<<0.1$.

On the basis of these assumptions, the projected gap area can be divided into a large number, N_c, of thin rectangular columns wherein each column of height D_i has the property that $\psi<<0.1$. The contribution to the total conductance from each column is given by Equation 14. The total conductance in the transition regime is the sum of the contribution from each column:

$$H_{TR} = \frac{1}{N_c}\sum_{i=1}^{N_c} H_{FM}\exp(-1/KN_i) + \frac{K_{gas}[1 - \exp(-1/KN_i)]}{D_i + g_1 + g_2} \qquad (15)$$

On the basis of the assumptions used in its development, this equation is valid not only for the transition region ($0.01 < KN < 100$) and $\psi>0.1$, but for <u>all</u> values of KN and ψ. Equation 15 emphasizes two important points:

1. The gap conductance is not merely a simple function of "the gap" (however that single parameter is defined) but instead depends on the geometry of the gap which necessarily must be expressed in terms of the gap geometry function, $D_i(y, z)$.
2. The free molecular contribution to the gap conductance is significant even for values of KN $\tilde{>}$ 1.

3.2.5 Model Convergence to the Free Molecular Gap Conductance

Gas molecules within a continuum regime have a Maxwellian velocity distribution[38] and therefore molecules leaving the gas continuum and striking a surface will do so with an incident velocity distribution which is Maxwellian. On the other hand, if free molecular conditions are present the molecules reflected from one surface will not have a Maxwellian velocity distribution[39] unless the reflected molecules were first absorbed and re-emitted at exactly the temperature of the surface, an event which is considered unlikely. These molecules will strike the second surface with a non-Maxwellian velocity distribution. The free molecular accommodation coefficient, a_{FM}, under these conditions may be different than the accommodation coefficient when a continuum (i.e., a_c) is present by virtue of a difference in the mean energy of the incident molecules alone (refer to Equation 9). Three general cases can be considered where a_{FM} is less than, equal to, or greater than the value of a_c. With respect to these three general cases, information on the behavior of the gap conductance can be obtained by inspection of Equations 7, 14, and 15 as the absolute value of the gap distance decreases and the local value of KN increases.

In reference to Figure 4, the reciprocal of Equations 7 and 14 and 15 are plotted versus d or D_{mp}, D_{pp}, etc., respectively, and the following observations can be made:

- Equation 7: the "gap distance" is given by d with the continuum regime present (e.g., region 2; $\psi<0.1$; Figure 2).

  The gap conductance will be specified by a straight line of slope $1/K_{gas}$ which converges to a value of $(g_1 + g_2)/K_{gas}$ when d = o. Although Equation 7 converges in the limit as d = o to the free molecular expression, it predicts that gas molecules in the transition regime behave in the same manner as if a continuum were present.

- Equation 14: the "gap distance" is given by d with the gap conductance containing contributions from the free molecular and continuum (i.e., regions 1, 4, 6, and 8; $\psi<0.1$; Figure 2).

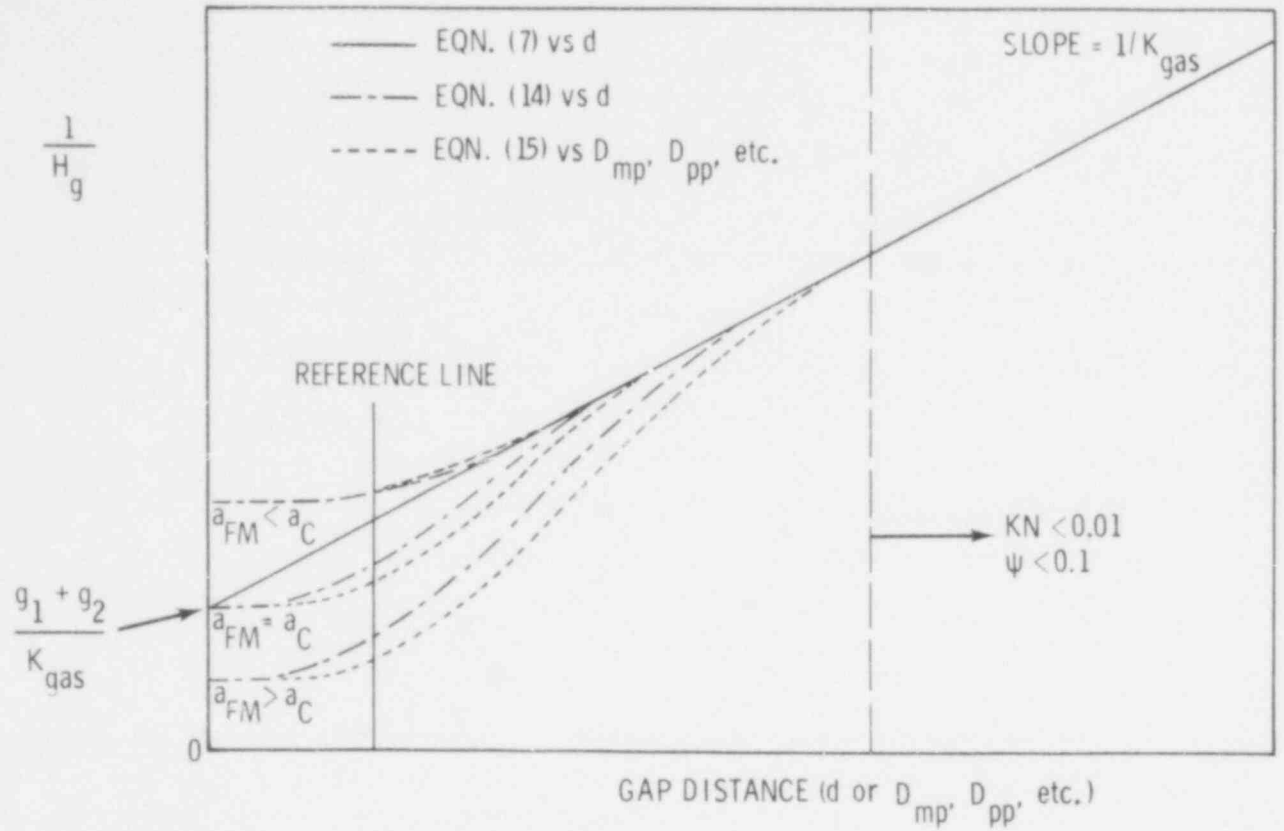

FIGURE 4. Comparison of Equation 15 to Equation 7 for Three General Cases Where $a_{FM} < a_c$; $a_{FM} = a_c$; and $a_{FM} > a_c$

At large values of d, Equation 14 converges to Equation 7. If a_{FM} is equal to a_c, the presence of a free molecular contribution to the gap conductance requires departure from Equation 7 to higher conductance values at smaller values of d. For example, if conditions within the gap were such that the gas molecules have a mean free path of 1 μm, Equation 14 would show that the influence of H_{FM} would still be significant at values of d of several μm. This value of d is considerably greater than the value of 0.01 μm that the common use of the restriction KN > 100 imposes on the range of validity of H_{FM}. When d = 0 convergence of Equation 14 to a value of $(g_1 + g_2)/K_{gas}$ is obtained. If a_{FM} is less than a_c, the presence of a free molecular contribution requires departure to lower values of H_g than predicted by Equation 7. When d = 0, Equation 14

592 041

will converge to a value of $(g_1 + g_2)/K_{gas}$ which will be less than predicted in the case where $a_{FM} = a_c$. If a_{FM} is greater than a_c, the presence of a free molecular contribution requires a departure to higher values of H_g upon decreasing d than predicted by Equation 7. If the gas molecules have a mean free path of 1 μm, examination of Equation 14 would show that the influence of H_{FM} would extend to values of d greater than under conditions of $a_{FM} = a_c$ described previously. All three cases predict curvature at small values of the gap distance when Hg is plotted in the manner shown in Figure 4.

- Equation 15: the "gap distance" is given by D_{mp}, D_{pp}, etc., with the gap conductance containing contributions from the free molecular and continuum (i.e., regimes 1, 3, 5, and 7; $\psi > 0.1$; and, regions 2, 4, 6, and 8; $\psi < 0.1$; Figure 2.)

At large values of D_{mp}, D_{pp}, etc., convergence to Equation 7 is predicted. When D_{mp}, D_{pp}, etc. is allowed to go to zero, convergence to Equations 14 and 7 is obtained when $a_{FM} = a_c$ and to Equation 14 alone when a_{FM} is greater or less than a_c. The presence of a surface roughness, error of form (ψ_R and/or $\psi_{EOF} > 0.1$), however, will cause an extension of the influence of the free molecular contribution to even greater values of the gap distance. Thus, at the same absolute value of d and D_{mp} (shown by the vertical reference line in Figure 4), the value of H_{TR} (D_{mp}, D_{pp}, etc.) will be greater than H_{TR} (d) under conditions where $a_{FM} = a_c$ and $a_{FM} > a_c$. If a_{FM} is $< a_c$ then $H_{TR}(D_{mp}, D_{pp}$, etc.) will be less than H_{TR} (d).

3.2.6 Application of Heat Conduction Models to Reactor Conditions

Various heat conduction expressions have been discussed and Equations 7, 14, and 15 appropriate to describing the gap conductance under various "gap" conditions presented in a generalized manner. In addition various TJD models for describing the imperfect energy exchange between gas molecules and surfaces are presented. It is appropriate to ask the following questions in regards to the use of the aforementioned heat conduction expressions and TJD models in predicting fuel: clad gap conductance in the various regions diagrammed in Figure 2:

- Is the value of H_g as currently computed in reactor safety codes such as GAPCON-THERMAL II using the "ideal" gap conductance expression (Equation 7) conservative or nonconservative when compared to experimental H_g values obtained under realistic, nonideal gap geometries (i.e., regions 1 and 3 to 6 in Figure 2)?

- Which TJD model when used in conjunction with the "ideal" gap conductance expression (Equation 7) is most accurate in predicting the gap conductance under nonideal conditions?

Currently, Equation 7 is used for determining the "gap" conductance contribution to the total heat transfer in various fuel performance codes. For example, the Lloyd[36] expression for the TJD is modified by an empirical correction factor and is used in the GAPCON-THERMAL II code.[10] Attempts have been made to modify Equation 7 for use under $\psi >> 0.1$ conditions by such means as adding the quantity $C(CLA_1 + CLA_2)$ to "d" (the ideal gap) where CLA_1 and CLA_2 are the fuel:clad centerline average surface roughnesses and C is an empirically determined constant.[22,29]

Rapier et al.[30] attempted to calculate an "effective gap width" by various methods but was forced to interject an empirically determined factor in order to obtain agreement with experimental results.

The experiments performed in this study have been designed to determine the extent which Equation 7 can predict realistic estimates of H_g in regions 1, 3, and 4 (Figure 2). As measurements of H_g have been made on values of D_{mp} representative of regions 1, 3, and 4, a test of Equation 7 can be made by letting the "ideal" gap distance, d, be equal to D_{mp} and expressing this equation as

$$H_g = \frac{K_{gas}}{D_{mp} + g_1 + g_2} \qquad (16)$$

The predictive capability of a particular fuel performance code (e.g., GAPCON-THERMAL II) may be evaluated by use of Equation 16. The reader is referred to the Results and Discussion section for further details.

3.3 CONTACT CONDUCTANCE MODELS

As a result of an increase in fuel temperature, swelling and thermal expansion of the fuel will occur. The fuel:clad gap will close under these conditions and may appear as depicted schematically in Figure 5. Heat is then transported by solid conduction through the fuel:clad contact points as well as the gas contained in the gap between the abutting surfaces. The extent of solid:solid conductance will depend upon the pressure or local compressive stress which, if high enough, will increase the localized area of contact through plastic deformation of the softer material (cladding) by the harder material (fuel). The surface roughness (R_1 and R_2), peak to peak asperity separation (L_1 and L_2), error of form (surface macrowaviness), and mechanical properties of the fuel and clad are important parameters in determining the extent of fuel:cladding contact. The amount of literature on the topic of thermal contact resistance is extensive and may be considered to consist of two areas. In the first area theoretical treatments[43,44] and model development[28-30,45-48] of the subject has been based on the assumption that the thermal contact resistance is closely coupled to surface roughness and the elastic/plastic deformation of asperities. The second area considers that the contact resistance is dependent on the effect of surface waviness and elastic deformation. This area has received little attention with the exception of a recent theoretical treatment[49] on the subject.

In the former area, models have been developed which are based on the early work of Cetinkale and Fishenden.[45] This model proposes that abutting surfaces form a series of cylindrical contact spots of equal area which are uniformly distributed. The flow of heat converges to the points of contact which are considered to be cylindrical heat channels. Later work by Holm[46] suggested the importance of elastic and plastic deformation of the surface asperities. The model developed by Rapier, Jones, McIntosh[30] (based on the Cetinkale and Fishenden model) required reference to the experimental work of Bowden and Tabor[47] to show that the ratio of the actual area and the apparent area of contact was related directly to the ratio of applied pressure and

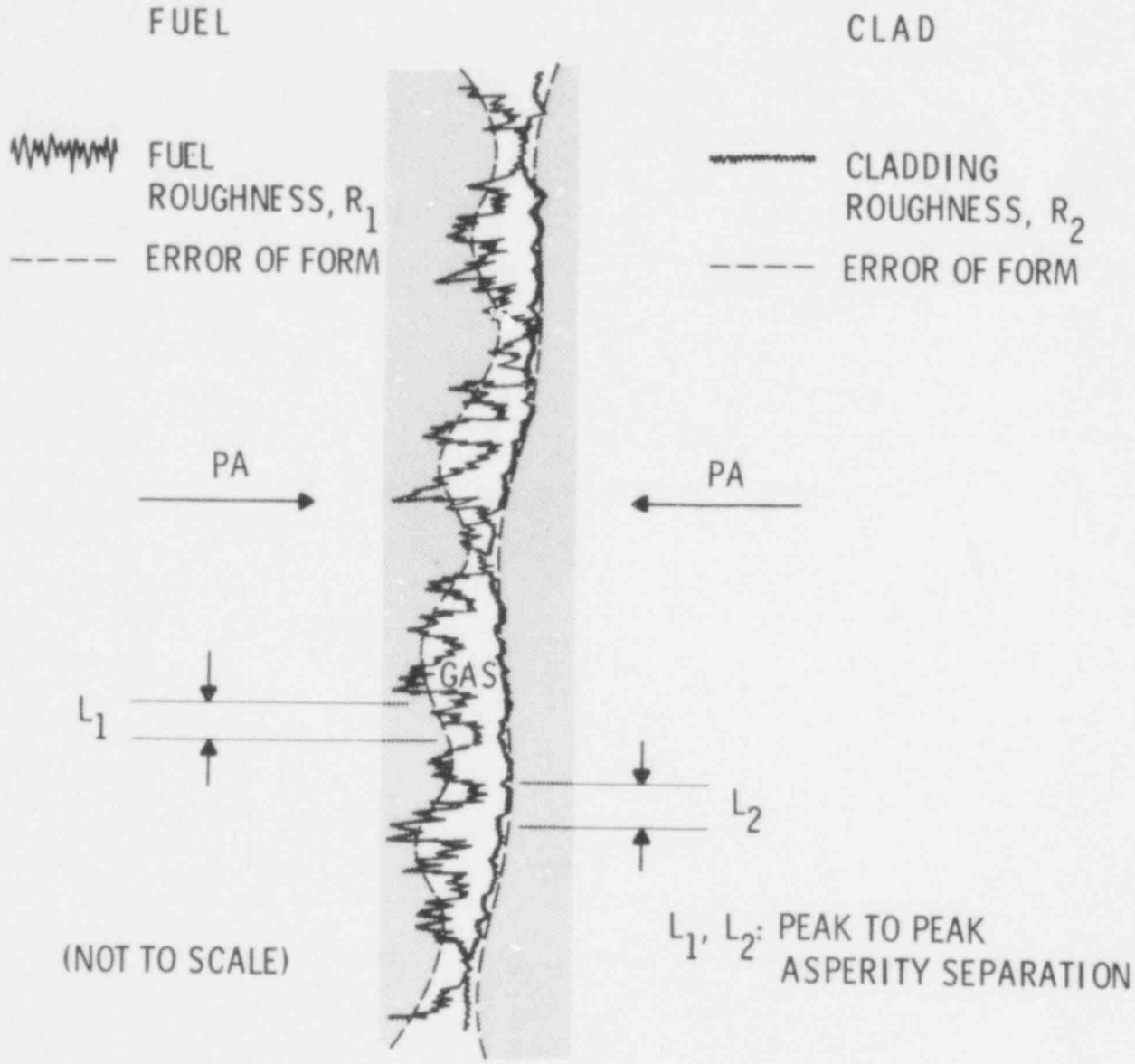

FIGURE 5. Schematic of a Closed Fuel:Clad Gap

592 045

the hardness of the softer abutting surface. Ross and Stoute[29] also referenced the work of Bowden and Tabor but used a somewhat different relationship than reported by Holm for relating the applied pressure to the hardness of the softer material. By the manner in which the number of contact spots per unit area was handled, the Rapier model obtains a square root dependence of H_c on applied pressure whereas the Ross-Stoute model predicts a linear dependence. The difference in the exponent dependency of H_c depends on whether the contact points are assumed to remain constant in number but increase in area, or remain constant in area but increase in number as the contact pressure increases. Others such as Dean,[28] Fenech and Rohsenow,[7] Todreas,[8] Mikic,[43] and Shlykov[48] have put forth models in an attempt to fit specific experimental measurements or correlate the work of others.

The basic form of the models cited is:

$$H_c = CK_m F(L_i \text{ and/or } R_i)(PA/H)^N \frac{W}{m^2 - K}, \quad \begin{matrix} i = 1 \text{ (fuel)} \\ = 2 \text{ (cladding)} \end{matrix} \qquad (17)$$

where C is a constant and

K_m = mean conductivity, $2K_1K_2/(K_1 + K_2)$, W/m - K

F = a function of surface roughness R and/or L the peak to peak asperity separation; units of R and L are in meters

PA = apparent interfacial pressure, N/m^2

H = Meyer's hardness of softer material, N/m^2

N = an exponent (between 0.5 and 1.0) whose value depends on how the number of contact points/unit area is considered to vary with contact pressure (e.g., remain constant in number but increase in area N = 0.5; remain constant in area but increase in number N = 1.0).

A summary of the aforementioned models in compatible format is shown in Table 3.

TABLE 3. Equations for Thermal Contact Conductance (After Lanning[10])

Authors	Values for C	The Function "F"	Values of N
Cetinkale and Fishenden	132.6	$1/(L_1 + L_2)$	1.33
Rapier and Jones	1.0	$1/L_1$	0.5
Ross and Stoute	11.88	$1/(R_1^2 + R_2^2)^{1/4}$	1.0
Dean	11.67	$1/(L_1 L_2)^{1/2}$	1.0
Fenech and Rohsenow (Approximated)	1.89	$\left[1.89(R_1 + R_2) + \sqrt{\frac{PA}{H}}\, L_1\right]^{-1}$	1.0
Mikic and Todreas	2.314	$R_1/(R_1^2 + R_2^2)^{1/2} L_1$	0.5 PA<6.89MPa 1.0 PA>6.89MPa
Shlykov	1.189E4	$Q^{0.86}$	0.86

Q = 1 for $(R_1 + R_2) > 30$ μm; $\left(\frac{30 \times 10^{-6}}{R_1 + R_2}\right)^{1/3}$ for 10 μm $< (R_1 + R_2) < 30$ μm;

and, $\left(\frac{15 \times 10^{-6}}{R_1 + R_2}\right)$ for $(R_1 + R_2) < 10$ μm.

From inspection it can be seen that for a given set of conditions none of the aforementioned models will yield the same results. Lanning and Hann[10] in their review concluded that the variety in the models probably occurs because each model is only a correlation to the data which the various authors developed or chose to examine. The models by Dean, Ross and Stoute, and Rapier et al. are based on individual UO_2:metal results that are scattered not only in magnitude, but also in experimental conditions. For instance, the Dean model was verified on the basis of experimental results performed by the author between UO_2 and Zr2 in an argon atmosphere at atmospheric pressure. No attempt was

made in this reported work to determine the appropriateness of the contact conductance model under vacuum conditions when the contribution by H_g to the total conductance would be negligible. The variations in the models may occur as a result of the assumption that the inclusion of the physically important characteristics of the contact surfaces (i.e., roughness, peak to peak asperity separation and/or elastic/plastic deformation of asperities) is sufficient or even necessary to describe the problem. The extent of surface mating between ceramic:metal surfaces may be dominated by the error of form or macrowaviness of the harder surface. None of the models in Table 3 considers the error of form to be a first order effect.

Dundurs and Panek[49] have recently developed a theoretical treatment covering the conductive heat transfer between two solids with wavy surfaces. The description of the abutting surfaces is set in two dimensions, and it is assumed that the surface profiles are purely sinusoidal and deformations elastic. It is further assumed that heat is transmitted only where there is solid to solid contact, and there is no resistance due to contamination of the surfaces. In this treatment, the temperature problem is solved exactly. Deformations are treated by relying on the well-known theory of Hertz for contact between two bodies with cylindrical surfaces. The constriction resistance of the interface is defined by

$$CR = \Delta T/q^{\infty} \tag{18}$$

where q^{∞} is the far field heat flux and ΔT the temperature difference that must be supplied to drive through the wavy surface the same amount of heat as flows in two bodies with perfect contact. The resistance can be related to the applied pressure PA and q^{∞} by applying the theory of Hertz. The resulting expression for the resistance is:

$$CR = -\frac{2\ell}{\pi}\left(\frac{1}{K_1} + \frac{1}{K_2}\right) \log (\sin 1/2\ C) \tag{19}$$

where K_1 and K_2 are the respective bulk material thermal conductivities, ℓ the half wave length of surface profile and C a term representing the extent of contact. The term C is given by

$$C = Aq^{\infty} (f_1 - f_2) + \sqrt{\{[Aq^{\infty}(f_1 - f_2)^2] + B\}} \qquad (20)$$

where $A = \frac{8\ell^2}{\pi 3b} \geq 0$ b = amplitude of the sinusoidal gap

$B = \frac{16PA\ell(S_1 + S_2)}{\pi b} \geq 0$ S_1, S_2 = uniaxial compliance in plane strain

and, $f_{1,2} = \frac{\alpha(1 + \nu)}{k}$ α = coefficient of thermal expansion

ν = Poisson's ratio

The term f in Equation 20 is called the distortivity of the material and relates the distortion of a straight boundary to the local value of the heat flux. The expression for the constriction resistance given by Equation 19 is seen to decrease with increasing applied pressure and indicates that a directional effect will occur upon reversal of heat flow or exchange of materials [(e.g., term $q^{\infty} (f_1 - f_2)$] in Equation 20.

A comparison of the contact conductance models as given by Equation 17 and Table 3 and Equation 19 to current results is made in the Results and Discussion Section. The reader is referred to this section for details concerning the calculation of the various terms.

4.0 EXPERIMENTAL

4.1 TECHNIQUE SELECTION

A variety of methods exist for the determination of the thermal conductivity of solid materials[2] and the thermal contact conductance between materials at low and intermediate temperatures and pressures ≤1 atm.[27-31] However, there is no generally acceptable technique available for measuring both the thermal gap and contact conductance between materials at the elevated temperatures and gas pressures considered in this study. It was concluded that--with modification--the thermal diffusivity (pulse) and classical axial (longitudinal) techniques could be applied to obtain reliable measurements over the range of variables of interest to this study (Table 1). A valuable advantage of using both techniques is that the results of the modified pulse design (MPD) could be verified by comparison to data obtained from the modified longitudinal design (MLD). The following sections discuss the experimental details of the Modified Pulse Design and Modified Longitudinal Design apparatus.

4.2 MODIFIED PULSE DESIGN (MPD) TECHNIQUES

4.2.1 General Features

The MPD technique is a modification of the classical heat pulse (flash) method commonly used to determine the thermal diffusivity and conductivity of materials.[50] In the MPD technique, a laser is used to supply a heat pulse to the front face of a UO_2-Zr sample pair (under light contact or separated by a gap). The subsequent temperature rise on the back face of the Zircaloy is then monitored by an intrinsic fast response thermocouple. From this transient temperature and knowledge of the thermal properties of the respective specimens, the thermal gap conductance can be determined as a function of changing variables (i.e., temperature, mean-plane gap width, gas composition, etc.). A photograph of the MPD apparatus is shown in Figure 6. A detailed description of the MPD apparatus and measurement technique is discussed in the following sections.

4.2.2 Mathematical Description

The following basic assumptions enter into the mathematical description of the MPD experiment:

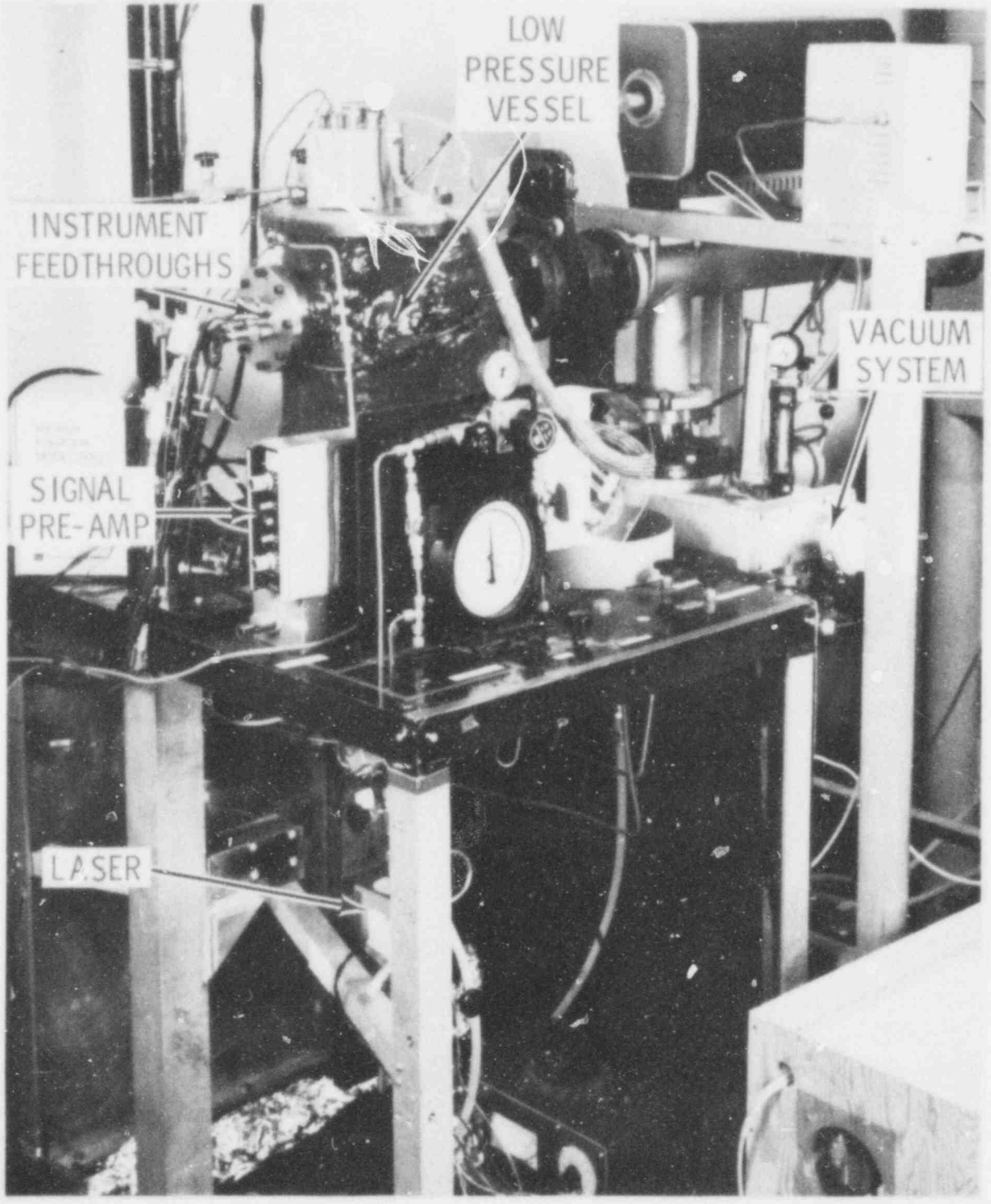

FIGURE 6. Photograph of MPD Experimental Apparatus

- Only one-dimensional heat conduction needs to be considered. (From an experimental viewpoint this assumption is considered quite good since the specimen holder assembly and specimens were designed to minimize lateral heat losses. Furthermore, Parker et al.[50] and Cape and Lehman[51] have shown that the lateral heat losses for the parallel plate geometries used in the flash method can generally be neglected).
- The thermal properties of the specimens do not vary over the range of the temperature transient. (Experimentally, it was found that the temperature transients were no greater than 4 K).
- Heat losses exist at the front and back surfaces of the samples.

Figure 7 describes the problem geometry and boundary conditions. The known parameters are the thermal diffusivities, α_i, the thermal conductivities, k_i, the sample thicknesses, ℓ_i, and the radiant pulse shape, w(t). The unknown quantities are the front and back face heat losses, q_f and q_b, and the heat transfer across the gap, q_1 and q_2.

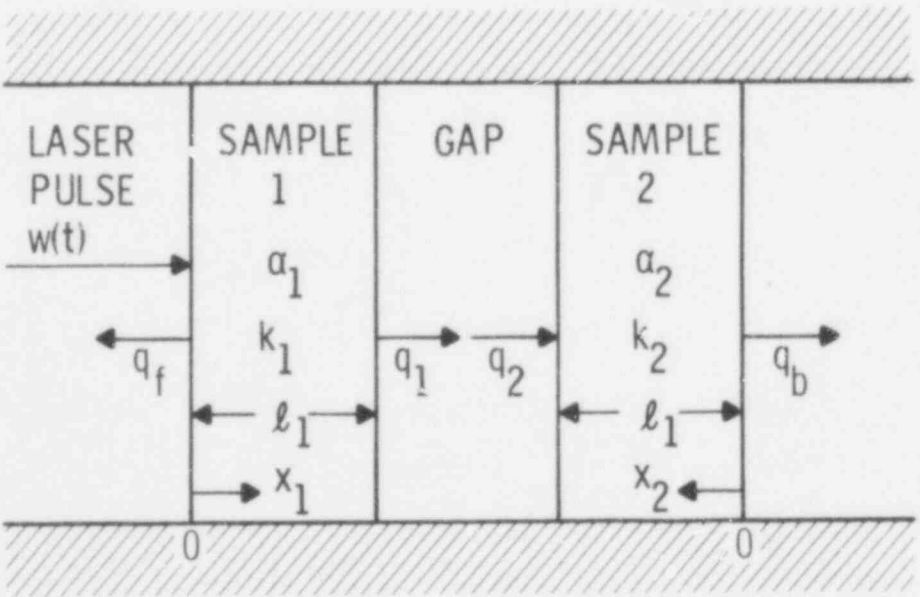

FIGURE 7. Problem Geometry and Boundary Conditions for MPD Analysis

The governing equations for the temperatures of the two samples are:

$$\left(\frac{1}{\alpha}\right)\frac{\partial T_i}{\partial t} = \frac{\partial^2 T_i}{\partial x_i^2} \qquad i = 1, 2 \tag{21}$$

where T_1 and T_2 are the temperature deviations from the ambient. The associated boundary conditions are:

$$-k_1 \frac{\partial T_1(t,x_1)}{\partial x_1} = w(t) - q_f = w(t) - h_1 T_1(t,o), \qquad x_1 = o \tag{22}$$

where h_1 is the unknown film coefficient for the front face. Also,

$$-k_1 \frac{\partial T_1(t,x_1)}{\partial x_1} = h_2 \left[T_1(t,\ell_1) - T_2(t,\ell_2)\right], \qquad x_1 = \ell_1 \tag{23}$$

where h_2 is the unknown gap conductance. In addition,

$$-k_1 \frac{\partial T_1(t,x_1)}{\partial x_1} = k_2 \frac{\partial T_2(t,x_2)}{\partial x_2}, \qquad x_1 = \ell_1, x_2 = \ell_2 \tag{24}$$

$$k_2 \frac{\partial T_2(t,x_2)}{\partial x_2} = q_b = h_3 T_2(t,o), \qquad x_2 = o \tag{25}$$

where h_3 is the unknown film coefficient for the back face.

Implicit in the boundary conditions is the assumption that the heat capacity of the gap is negligible, i.e., $q_1(t) = q_2(t)$.

Applying the Laplace Transform to the governing equations results in:

$$\left(\frac{1}{\alpha}\right) p\, \bar{T}_i\,(p,x_i) = \frac{\partial^2 \bar{T}_i}{\partial x_i^2}(p,x_i), \quad i = 1,2 \tag{26}$$

592 053

These partial differential equations have the general solutions:

$$\bar{T}_i = A_i \cosh\lambda_i x_i + B_i \sinh\lambda_i x_i, \quad i = 1,2 \tag{27}$$

where

$$\lambda_i = \sqrt{p / \alpha_i} \quad i = 1,2 \tag{28}$$

The coefficients, A_i, B_i, are determined from the transformed boundary conditions:

$$-k_1 \frac{\partial \bar{T}_1}{\partial x_1} (p,o) = \bar{w}(p) - h_1 \bar{T}_1 (p,o) \tag{29}$$

$$-k_1 \frac{\partial \bar{T}_1}{\partial x_1} (p,\ell_1) = h_2 [\bar{T}_1 (p,\ell_1) - \bar{T}_2 (p,\ell_2)] \tag{30}$$

$$-k_1 \frac{\partial \bar{T}_1}{\partial x_1} (p,\ell_1) = k_2 \frac{\partial \bar{T}_2}{\partial x_2} (p,\ell_2) \tag{31}$$

$$k_2 \frac{\partial \bar{T}_2}{\partial x_2} (p,o) = h_3 \bar{T}_2 (p,o) \tag{32}$$

The laser pulse time is very short compared to the time required for the back face temperature to reach a maximum. Therefore, w(t) is assumed to have a Dirac Delta form

$$\bar{w}(p) = C, \text{ a constant.} \tag{33}$$

It is sufficient to obtain an analytic expression for the back face transient temperature to compare with the experimental data. Substitution of Equation 27 into Equations 29 to 32 and some algebra yields:

$$\bar{T}_2(o,p) = \frac{\bar{w}(p)\beta_1\beta_2 h_2}{Dh_3} \tag{34}$$

where

$$\beta_i = k_i\lambda_i, \quad i = 1,2 \tag{35}$$

and

$$\begin{aligned} D = h_1 \Bigg[& \beta_1 \cosh z_1 + h_2 \sinh z_1 \left(\frac{\beta_2^2}{h_3} \sinh z_2 + \beta_2 \cosh z_2 \right) \\ & + \beta_1 \cosh z_1 \left(\frac{\beta_2}{h_3} h_2 \cosh z_2 + h_2 \sinh z_2 \right) \Bigg] \\ & + \beta_1 \Bigg[\left(\beta_1 \sinh z_1 + h_2 \cosh z_1 \right) \left(\frac{\beta_2^2}{h_3} \sinh z_2 + \beta_2 \cosh z_2 \right) \\ & + \beta_1 \sinh z_1 \left(\frac{\beta_2}{h_3} h_2 \cosh z_2 + h_2 \sinh z_2 \right) \Bigg] \end{aligned} \tag{36}$$

where

$$z_i = \lambda_i \ell_i, \quad i = 1,2 \tag{37}$$

Determining the coefficients A_i and B_i from the transformed boundary conditions, one can then determine the analytic expression for the temperature as a function of time using the inversion theorem:

$$T_2(t,o) = \frac{1}{2\pi i} \lim_{L \to \infty} \int_{\sigma - iL}^{\sigma + iL} e^{tp} \bar{T}_2(p,o)\,dp \tag{38}$$

592 055

Contour integration methods can be applied if σ is chosen so that all the poles of the integrand are to the left of the line $x = \sigma$ in the complex plane. The contour integral can be easily evaluated using the Cauchy residue theorem provided all the poles can be located and their orders determined. For the purpose of fitting the temperature function to experimental data, it is generally sufficient to locate and determine the order of only the first few poles. The form of the integrand is rather complex and the possibility that there are no poles of order greater than one for any choice of h_1, h_2 and h_3 is not precluded. If some choice of h_1, h_2 and h_3 results in a higher order pole, a slight adjustment of the h's should eliminate the multiple pole without significantly changing the shape of the back-face temperature function. Hence, the search for a best fitting back-face temperature function should not be hampered by limiting the choice to those functions whose first few poles are all of order one.

By the Cauchy residue theorem the back-face temperature can then be written as:

$$T_2(t,o) = \sum_{i=o}^{\infty} C_i e^{V_i t} \tag{39}$$

where the V_i are the poles of the integrand of Equation 38 and

$$C_i = \left(\frac{d\bar{T}_2}{dp}\right)^{-1}, \quad p = V_i \tag{40}$$

It can be shown that all poles of the integrand lie along the negative real axis. Hence it is convenient to make the substitution $p = -s$ in Equation 38 and convert to circular form to solve for the poles.

Since $\bar{w}(p)$ appears as a constant in Equation 3 it is convenient to normalize the back-face temperatures by dividing by the maximum temperature. This normalization is also easily performed on the data. In this way, it is not necessary to know the magnitude of the laser pulse.

The problem is now reduced to choosing values of h_1, h_2 and h_3, deriving the corresponding expression for the back-face transient temperature, and

checking the analytic result against the experimental data. The h's can then be adjusted in a suitable manner so that the analytic temperature function may more closely fit the experimental data. This procedure is carried on iteratively until the agreement between the analytic temperature function and the experimental data is satisfactory.

4.2.2.1 Determining the Unknown Parameters

There are a variety of techniques available for determining unknown parameters in a functional expression such that the resulting function best fits a given set of data. Since the expressions dealt with here are highly non-linear, a method developed by Peckham[52] was chosen. This particular method has been shown to be fairly effective in problems involving non-linear functions.[61]

Peckham's method attempts to minimize the sum of the squared errors, as do many parameter fitting schemes, but it does not require the explicit calculation of gradients. The equation to be minimized is

$$S = \sum_{k=1}^{m} \left[f_k \left(h_1, h_2, h_3 \right) \right]^2 \tag{41}$$

where h_1, h_2 and h_3 are the unknown parameters, and

$$f_k = T_2 \left(t_k, o \right) - T_E \left(t_k \right) \tag{42}$$

where t_k is the time of the kth data point, $T_E \left(t_k \right)$ is the experimentally determined back-face temperature at time t_k, and m is the number of data points (equal to 6 in this study) at various times along the temporal history curve.

The difference function, f_k, may be linearly approximated by

$$\tilde{f}_k = E_k + \sum_{i=1}^{3} g_{ki} h_i \tag{43}$$

If values for E_k and g_{ki}, k = 1,2,...m are known then it is straight-forward to find h_i, i = 1, 2, 3 to minimize Equation 40. Since the functions, $\tilde{f}_k$, are

nonlinear, $\bar{h}$ will not be the true minimum but can be used as a starting point for the next iteration. Details on the derivation and application of this method can be found in the reference by Peckham.

In Peckham's method a set of guesses for the minimizing h-set is used to get a new estimate. Rather than calculating the coefficients in the linear approximation by numerical differentiation, they are chosen to minimize the m expressions

$$\sum_{\ell=1}^{n'} w_\ell^2 \left(h_k + \sum_{i=1}^{3} g_{ki} x_{i\ell} - f_{k\ell} \right)^2 \qquad (44)$$

where n' is the number of guesses being used and w_ℓ is a suitable weighting factor. Once the values for E_k and g_{ki} are determined they can be substituted into Equation 43 to determine the new estimated h-set to minimize Equation 41.

The iterative procedure used to find the h-set which best fits the data is described in Appendix G.

This technique has been shown to be quite effective for a variety of parameter fitting problems. For this particular problem the data must be very accurate (to three decimal places if possible). To obtain data of this accuracy a curve fit of the digitized temporal history curve can be made to enhance the signal-to-noise ratio. From this curve the selected $T_2(t,o)$ datum points are obtained. Also initial estimates for the unknown parameters, h_1, h_2 and h_3 within ± one order of magnitude are required.

4.2.3 Samp e Preparation and Thermal Property Characterization

Depleted UO_2 specimens used in this study were prepared by pressing highly sinterable powder into discs and sintering at 1923 K for 4 hr in a hydrogen atmosphere. The resultant 2 mm thick by 14.5 mm diameter discs were mounted (in groups of nine) on a polishing block and ground to the desired thickness (between 0.5 and 1.0 mm) in a manner producing a nondirectional finish, using 400 grit SiC (silicon carbide) powder on a flat, cast iron surface. These specimens were designated as Interfacial Surface Morphology-II (ISM-II) specimens. ISM-III specimens were produced by polishing with 1 μm size aluminum oxide powder, while ISM-I specimens were produced by light abrasion of

the ISM-II surfaces with 80 grit abrasive paper. Talysurf-4 profilometer measurements of surface roughness yielded centerline average (CLA) values of 14.4 ± 2.8 μm, 1.6 ± 0.7 μm, and 0.25 ± 0.05 μm for the ISM-I, ISM-II and ISM-III specimens, respectively, at a wavelength cutoff of 760 μm. The UO_2 stoichiometry was determined gravimetrically to be 2.000 ± 0.002, and the density found to be 94.1% TD.

The Zr4 specimens were cut from an ingot of Zr4 reactor grade material and lathe machined into 1.02 mm thick by 14.5 mm diameter discs. A small notched groove was machined near the outer circumference of the disc for the purpose of providing a barrier to lateral heat flow and to minimize any heat-shunting effects through the spacers and specimen support contact points. The Zr4 specimens were individually hand-ground on flat glass plates with 400 grit SiC powder in a manner producing a nondirectional finish (ISM-II). ISM-III Zircaloy specimen surfaces were prepared in the same manner as the ISM-III UO_2 specimens. ISM-I surfaces were produced by grit blasting the ISM-II specimens with 80 grit SiC particles. Talysurf-4 profilometer measurements of surface roughness yielded centerline average (CLA) values of 4.5 ± 0.4 μm, 0.4 ± 0.2 μm, and 0.17 ± 0.05 μm for the ISM-I, ISM-II, and ISM-III specimens, respectively, at a wavelength cutoff of 760 μm.

To remove the effects of stresses induced by machining and polishing, the UO_2 and Zr4 samples were heat treated in a gettered Helium atmosphere at 1273 K and 1 hr prior to surface macrowaviness measurements. The Zr4 specimens were given an additional heat treatment at 973 K for several hours to ensure that only the alpha phase was present.

Essential to the accurate determination of thermal gap conductance from the measured temporal history curves is the need for accurate values of specimen thermal diffusivity, conductivity, and thermal expansion. The thermal diffusivity of the Zr4 specimens used in this study were determined in this laboratory from measurements on representative samples. Thermal conductivity and expansion values for Zr4 were obtained from a study[53] conducted earlier in this laboratory on specimens fabricated from the same bar stock from which both the MPD and MLD samples were obtained.

The thermal diffusivity of the UO_2 specimens were determined in this laboratory from measurements on a series of representative samples. The thermal expansion value of UO_2 was computed from an expression cited by Bates.[54] The thermal conductivity of UO_2 was calculated from heat capacity,[54] thermal diffusivity, and temperature-corrected density values.

The reader is referred to Appendix A for particulars on the thermal property equations used in this study.

4.2.4 Average Mean-Plane Gap Determination

The mating surface macrotopology of the UO_2 and Zircaloy-4 specimens were determined from a point-wise topographical surface map obtained using an optical height gauge measurement technique. Height elevations were taken at 25 coordinate positions on the specimen surfaces relative to an optically flat base plane on which the specimen was mounted, as shown in Figure 8. The individual specimens were rigidly mounted during measurement by employing either a vacuum hold-down or a low shrinkage dental plaster. A computer program re-referenced the measured height elevations to a plane defined by the three gap spacer contact points common to each specimen. The local gap between asperity tips, $(D_a)_i$, at each of the 25 coordinate positions could then be determined for any three gap spacer thicknesses, as illustrated in Figure 9.

For the MPD sample pairs the average gap between asperities is

$$D_a = \sum_{i}^{N_c} (D_a)_i / N_c, \quad N_c = 19 \tag{45}$$

Due to the geometry of the Zircaloy specimen, only the coordinates within the annular ring are of significance in determining the D_a. The uncertainty in D_a is a function only of the surface roughness since the same probe stylus was used for all surface morphologies. The 3σ uncertainty in D_a was determined to be ± 3.4 μm, ± 2.2 μm, and ± 1.7 μm for the ISM-I, ISM-II and ISM-III surfaces, respectively.

592 060

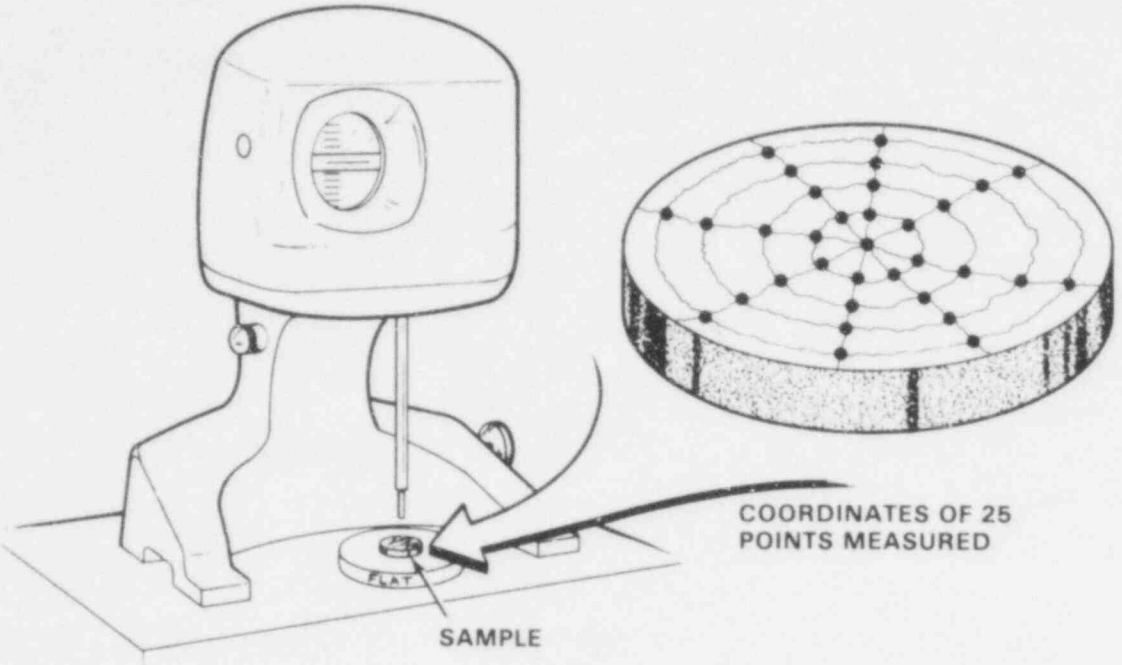

FIGURE 8. Characterization of the Specimen Topology Using an Optical Height Gauge

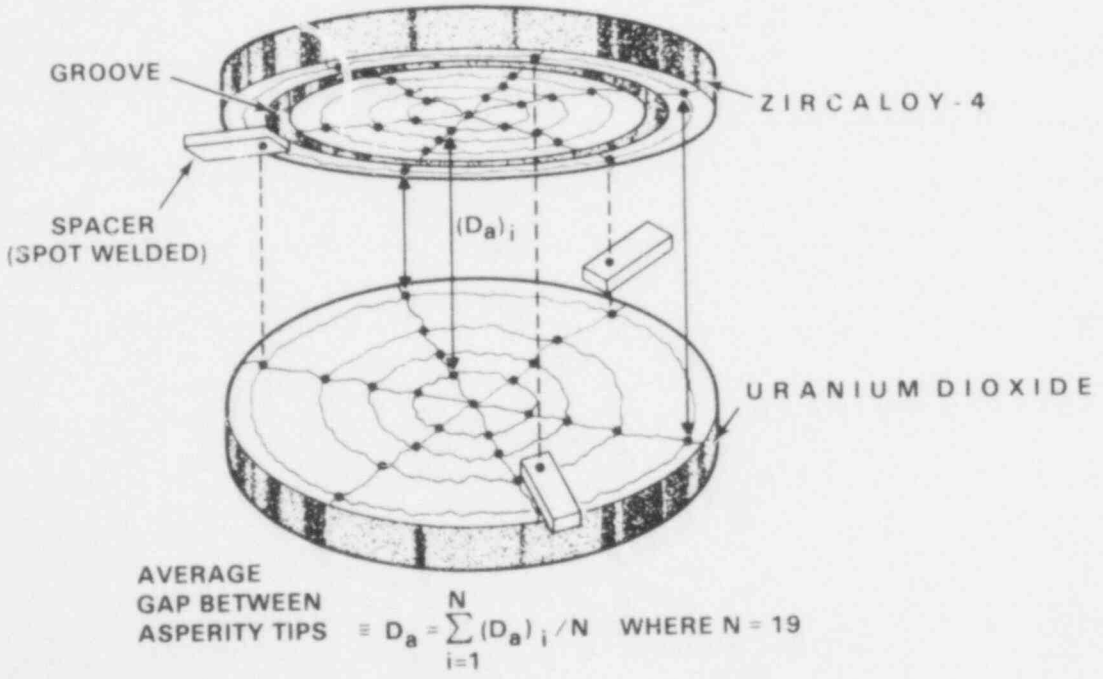

FIGURE 9. Determination of Average Gap Between Asperity Tips from Measured Height Elevations

592 001

The local mean-plane gap $(D_{mp})_i$ is the distance between respective surface mean-planes (as shown earlier in Figure 1) and related to $(D_a)_i$ by

$$(D_{mp})_i = (D_a)_i + (\gamma_1)_i + (\gamma_2)_i \tag{46}$$

where $(\gamma_1)_i$ and $(\gamma_2)_i$ represent the local distance from the tip of the probe stylus to the surface mean-plane on the UO_2 and Zr4 surfaces, respectively. As $(\gamma_1)_i$ and $(\gamma_2)_i$ cannot be determined at the time of measurement of $(D_a)_i$, average values of γ_1 and γ_2 were determined graphically from the Talysurf traces and a scale model of the stylus tip as shown in Figure 10. The average mean-plane gap can then be expressed as

$$D_{mp} = \left[\sum_{i=1}^{19} (D_a)_i\right] \times \frac{1}{19} + \gamma_1 + \gamma_2 \tag{47}$$

Substituting Equation 45 into Equation 47 results in

$$D_{mp} = D_a + \gamma_1 + \gamma_2 \tag{48}$$

Values of $(D_a)_i$, D_a, γ_1 and γ_2, and D_{mp} for the various gap separations and surface morphologies used in this study can be found in Appendix F.

An evaluation of the reproducibility of the mean gap width values using the optical height gauge technique was obtained by a repetitive mounting and recharacterization [$(D_a)_i$ measurement] procedure for sample pair DUO2-25: ZR4-25 (ISM-II). The uncertainty associated with the average gap between asperities was found to be $3\sigma = \pm 2.1$ μm. Repetitive mounting and redetermination of the gap width yielded a 3σ uncertainty of ±4 μm about the mean D_{mp} value. The change in D_{mp} before and after each experimental run was found to be no more than 0.5 μm. The standard deviation $\sigma_{D_{mp}}$ about each determined gap width in this study was found to be equal to or greater than $\sigma_{(Da)i}$, depending on the respective specimen surface error of form (or macrowaviness). The $3\sigma_{D_{mp}}$ uncertainties for each specimen pair can be found on the appropriate figures in the Results section and in the MPD data appendix, Appendix D.

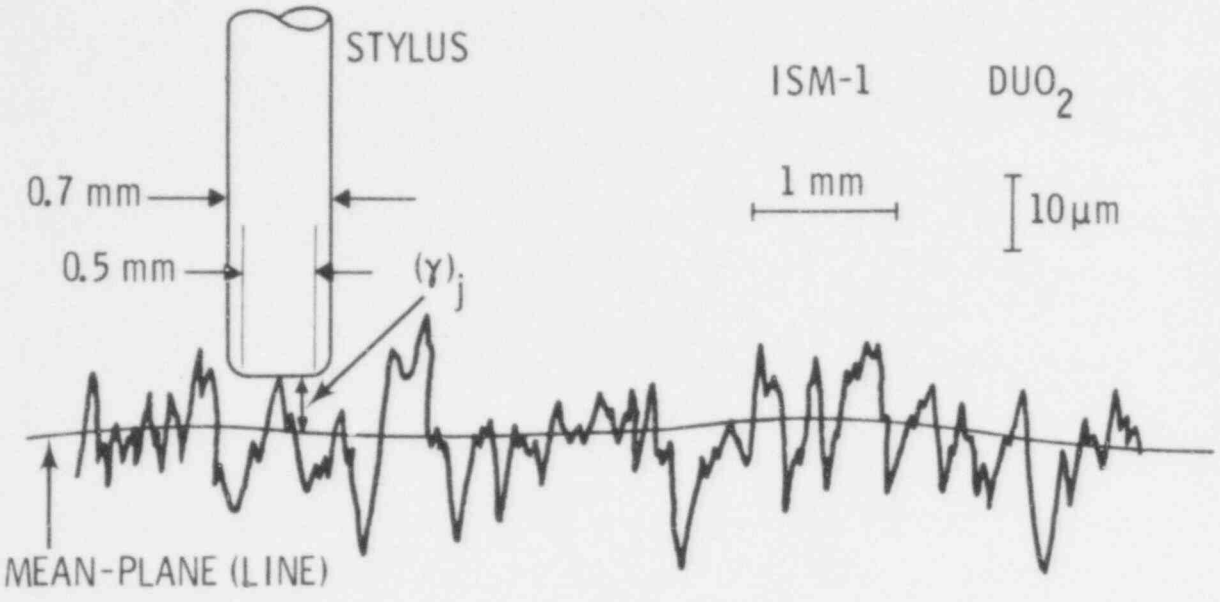

$$\gamma_{UO_2} \text{ OR } \gamma_{Zr_4} = \sum_{j=1}^{M} (\gamma)_j / M \quad \begin{pmatrix} \text{WHERE } 25 < M < 80 \text{ OVER} \\ \text{a 1 cm INTERVAL} \end{pmatrix}$$

FIGURE 10. Graphical Determination of γ_1 (UO_2) and γ_2 (Zr4) Using Talysurf Traces and a Scale Model of the Stylus

The specimen thicknesses (ℓ_1 and ℓ_2) were also determined from the optical height gauge measurements. The specimen thickness was defined as being the average of the specimen thicknesses at the same nineteen coordinate positions at which the gap width was determined. The variation in sample thickness over the diameter of the disc was found to be no greater than ±2%.

4.2.5 MPD Experimental System

4.2.5.1 Test Apparatus

The MPD experimental test apparatus and sample pair holder assembly are shown schematically in Figures 11 and 12. The sample pair is illuminated on the front face of the UO_2 sample with a laser pulse (30 joule maximum output; 800 μsec pulse duration) and the resultant temperature transient on the back surface of the Zr4 specimen is monitored by a 25.4 μm diameter Chromel-Constantan (type E) intrinsic thermocouple spot welded near the center of the disc.

The resulting emf output of the thermocouple was amplified by a differential dc pre-amplifier (gain ~3050) and recorded on a transient waveform recorder in digitized form. The transient temperature curve could then be displayed in analog form on an oscilloscope for visual inspection prior to transmission of the signal in RS-232C format to a graphic computing system for storage and subsequent analysis.

The ambient temperature of the samples was determined by use of a 127 μm diameter, chromel-alumel (type K) thermocouple spot welded on the perimeter of the Zr4 sample.

Heat losses to the specimen holder during the passage of the transient heat pulse were minimized by supporting the UO_2 and Zr4 samples on the front and back faces by three equally spaced Al_2O_3 pins, as illustrated in Figure 12.

A fixed gap width was maintained between the UO_2 and Zr4 specimens by three stainless steel spacers spot welded to the outer Zr4 support ring. A notched groove machined in the periphery of the Zr4 specimen was employed to minimize thermal shunting through the spacers during the measurement period following the absorption of the laser pulse on the front surface of the UO_2.

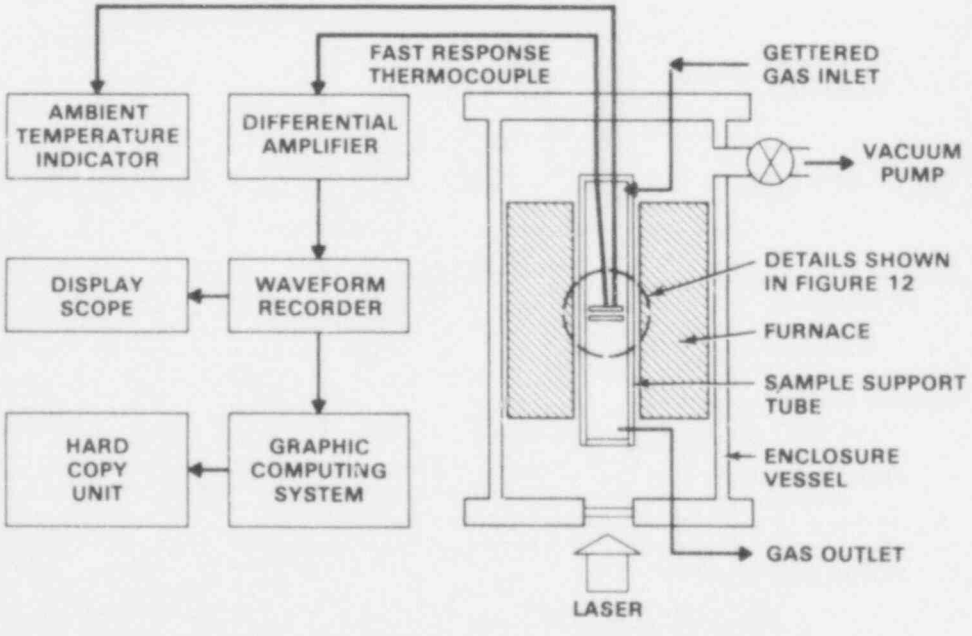

FIGURE 11. Schematic Diagram of Modified Pulse Design (MPD) Test Apparatus

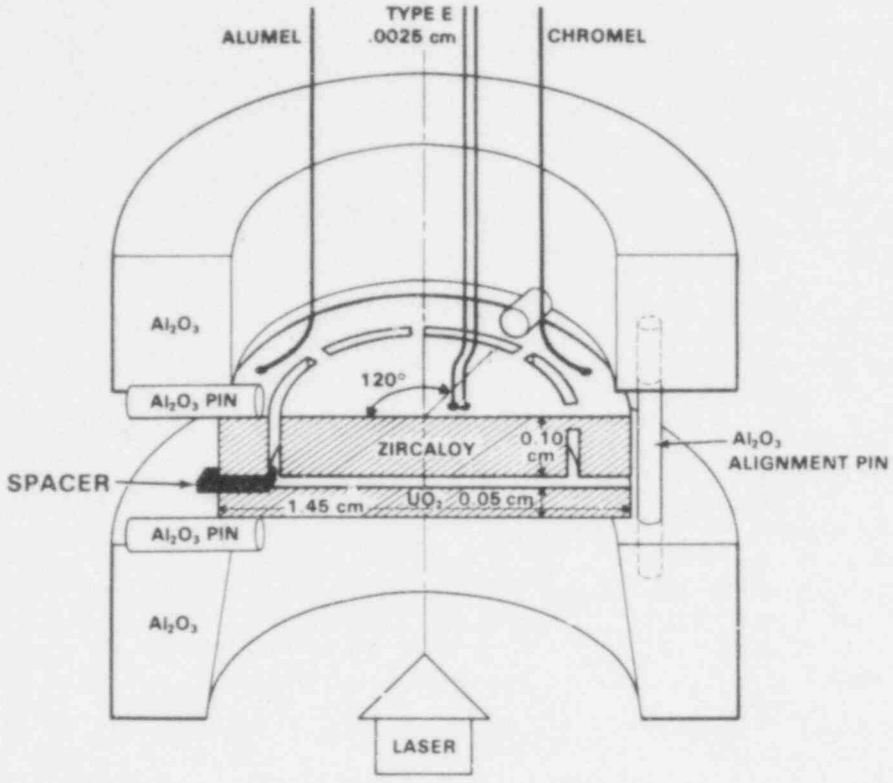

FIGURE 12. MLD Sample Holder Assembly

4.2.5.2 Sample Environmental Control

The construction of the MPD apparatus for Stage I measurements allows the use of assorted gases at various pressures from atmospheric to 0.26 MPa. In addition, the system also provides for evacuation of the test chamber for gaseous backfilling operations and for the removal of residual oxygen from the gas supply. The gases used in this experimentation consisted of Helium (100), He:Ar (51.8:48.2), Argon (100), He:Xe (89:11), and He:Xe (51:49). The gases were obtained from a vendor premixed and analyzed as to composition and purity. A list of the gas compositions and purity analyses used in the MPD measurements can be found in Table 4. Due to the affinity for oxygen by Zr4 at elevated temperatures, care was taken to assure removal of any residual oxygen from the gas. An oxygen-free atmosphere was continually maintained by passing the gas through two zirconium oxygen gettering systems before admission into the specimen chamber. Further gettering was obtained within the specimen chamber by the

placement of sacrificial zirconium sheets in proximity to the specimens and specimen holders. The moisture content of the inlet gas was monitored with an electrolytic hygrometer and determined to be <5 ppm.

Backfilling of the system was achieved by means of a control valve and mechanical vacuum pump. The gas pressure within the enclosure vessel was measured using a master test gauge accurate to 0.5%.

TABLE 4. Compositions and Impurity Analysis for Gases Used in MPD Experiments

Gas Composition	Analysis	Grade	Purity (min)	Impurity Content
Helium (100)	99.999 min	Ultrapure	99.999	--
Argon (100)	99.999	Ultrapure	99.999	<1 ppm O_2
	99.999	O_2-free grade	99.999	<0.5 ppm O_2
He:Ar 51.86: 48.14	51.86% He	Ultrapure	99.999	--
	Balance Ar	Ultrapure	99.999	--
	51.79% He	Ultrapure	99.999	--
	Balance Ar	Ultrapure	99.999	--
He:Xe 89.8: 10.2	10.2% Xe	Research Grade	99.995	--
	Balance He	Ultrapure	99.999	--
	11.0% Xe	Research Grade	99.995	--
	Balance He	Ultrapure	99.999	--
He:Xe 51:49	49% Xe	Research Grade	99.995	--
	51% He	Ultrapure	99.999	--

4.2.5.3 Data Acquisition and Reduction

The magnitude of the resulting emf signal produced by the type E thermocouple during a temperature transient ranged from approximately 150 μV to 320 μV (2 to 4 K). This signal was amplified and stored in digitized form in a minicomputer. A program for reduction of the time-temperature history curve was then executed in which the curve was signal averaged over 60-cycle time intervals to enhance the signal to noise ratio, normalized, and segmented into two overlapping ranges. Each range was fitted with a 4 to 6th order polynominal and a set of six temperature-time points were calculated from the

polynominal curve fits at normalized temperature values of 0.5, 0.7, 0.85, 0.98, 0.99, and 0.988. (These six values were selected somewhat arbitrarily, primarily for computational convenience. The final result was found to be independent of which particular set of six points was chosen). This set of experimental $T_2(t,o)$ data was used along with the appropriate thermal and physical property values for UO_2 and Zr4 as the basis for determining th experimental gap conductance using the procedure discussed in the Mathematical Description section.

4.2.5.4 Determinate/Indeterminate Errors

The errors involved in the measurement of thermal gap conductance, H_g, via the MPD technique can be divided into two areas--determinate and indeterminate. Determinate errors are associated with the measurement of quantities used in calculating a particular property. These errors can be determined by the inaccuracies associated with instruments used to measure and reproduce the quantities. Indeterminate errors arise from system variation, from assumed boundary conditions, and from other sources that are often difficult to recognize and eliminate. The purpose of this section is to assess the uncertainty in the calculation of H_g and to discuss probable sources and effects of indeterminate errors in its measurement.

The various determinate errors associated in the determination of H_g are listed in Table 5.

TABLE 5. Determinate Errors in MPD Experiment

Determinate Error	% Uncertainty, $\pm 3\sigma$	Comments
ℓ_1 and ℓ_2	2	Dependent on error of form. Corrected for thermal expansion effects.
k_1 and k_2	4	Measured quantities or generated from C_p and thermal diffusivity data.
α_1	12	Measured results on four samples.
α_2	5	Measured.
T	0.5	Calibrated type K thermocouples.
Temperature-Time Waveform	0.6	Transient waveform recorder used in recording and computer analysis of waveform.
D_{mp}	7-144	Dependent on $3\sigma_{D_{mp}}$, uncertainties in γ values, and magnitude of Dmp.

The uncertainty in T and the temperature-time waveform was small compared to the other variables and considered negligible. The MPD system apparatus (used in the measurement of α) was calibrated using ARMCO iron and PYRO CERAM 9606. The thermal diffusivity results are shown in Figures 13 and 14. The results are in satisfactory agreement, ±5%, with reported literature values. The measured results on four samples of UO_2, however, were found to lie within a 3σ band of ±12% between 293 and 1023 K (refer to Appendix A). The $3\sigma_H$ uncertainty in the MPD technique was calculated to be $\tilde{\sim}$±12%. The reader is referred to Appendix B for the details of this calculation.

The 3σ uncertainty in the average mean plane gap is dependent on $3\sigma_{Da}$ and the error of form of a particular specimen surface. The specific values for $3\sigma_{Dmp}$ are presented in Appendix F for the various UO_2-Zr4 pairs used in this study.

The indeterminate errors postulated to occur during the MPD experiment are summarized in Table 6.

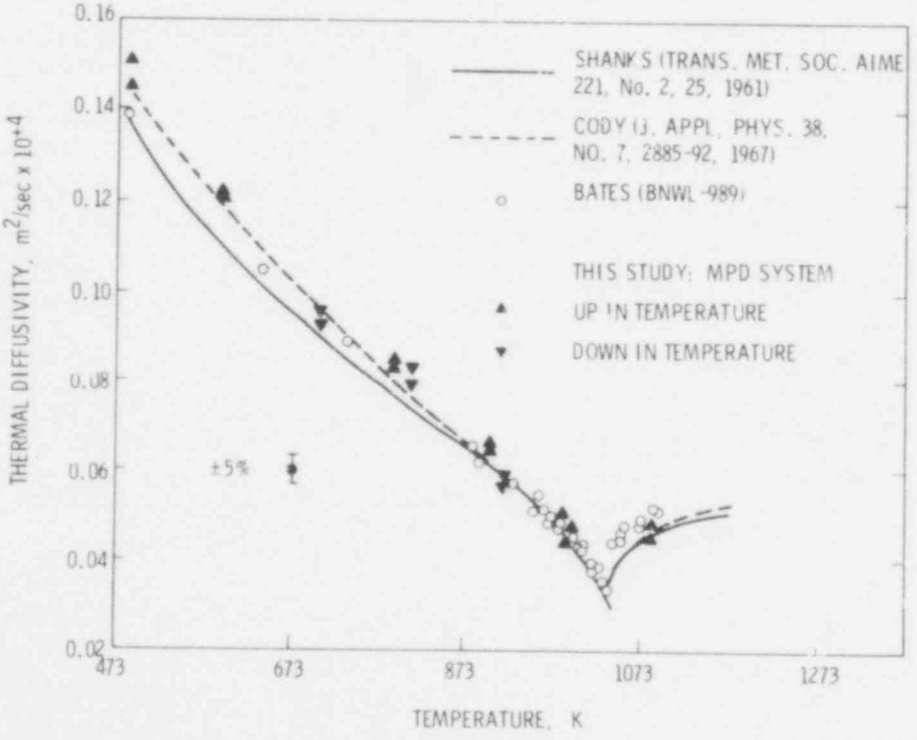

FIGURE 13. Comparison of the Thermal Diffusivity of ARMCO Iron as Determined in the MPD System to Results Obtained by Others

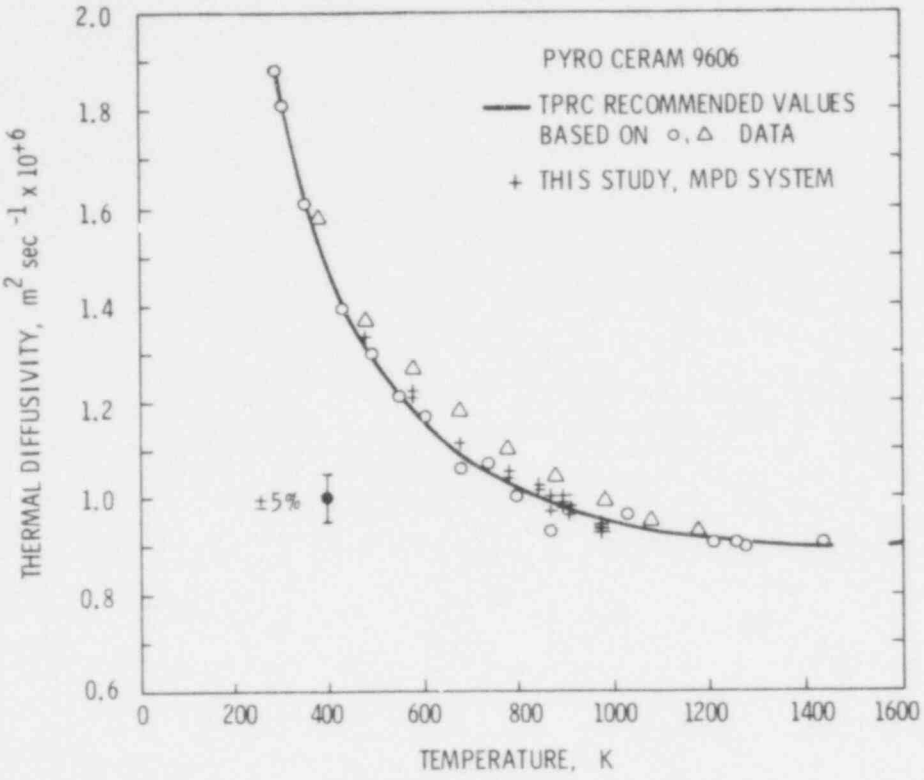

FIGURE 14. Comparison of the Thermal Diffusivity of PYRO CERAM 9606 as Measured in the MPD System to Results Reported by Others

TABLE 6. Indeterminate Errors in MPD Experiment

Indeterminate Error	Comments
Radial heat losses occurring during measuring period.	Dependent on sample thickness and gap separation; minimized by reducing specimen thickness and maximizing specimen diameters.
Thermal shunting by spacers and heat losses to specimen holder.	Minimized by groove and notching of Zircaloy sample. Also, each sample is supported on Al_2O_3 pins.
Sample deflection occurring as result of absorbed laser heat pulse on front sample.	The effect on H_g was found to be negligible.
Extraneous radiation.	Reduced by radiation shielding.
True interface boundary.	Dependent on sample surface deviation from averaged interfacial planes of separation.

Thermal shunting through the spacers, heat losses to the sample holder, and laser induced thermal buckling of the UO_2 specimer were considered to potentially be the largest source of indeterminance in the experiment. Thermal shunting through the spacers was minimized by using spacers of small dimensions ($\sim$1/2 mm square) and by grooving and notching the Zr4 specimen to provide a barrier to radial heat flow. In addition, the spacers were placed in positions relative to the grooves that would maximize the thermal path length from the spacer to the fast response thermocouple. Heat losses to the sample holder were minimized by utilizing point contact supports on Al_2O_3 pins. The effectiveness of these measures is demonstrated by the observation that no significant thermocouple output over a 10 second interval was detected when a sample pair separated by a gap was pulsed under vacuum (2.67Pa) conditions.

Laser induced thermal buckling of the UO_2 was considered a potentially serious problem because of the variation in the gap width it caused during the course of the (transient) experiment.

It was expected that H_g would tend to decrease with increasing laser intensity due to larger deflections--and thus larger gap widths--at the higher intensity levels. This effect, however, was not experimentally observed, but rather H_g was found to be independent of the laser intensity, as shown in Figure 15 where H_g is plotted versus maximum Zr4 specimen temperature rise.

To guard against any other possible effects of laser buckling the following precautions were taken:

1) Keeping the laser intensity at levels as low as possible but still producing an adequate signal/noise ratio associated with the fast response thermocouple signal.

2) Maximizing the sample thickness within the constraints set by S/N ratio and the need to maintain one dimensional heat flow.

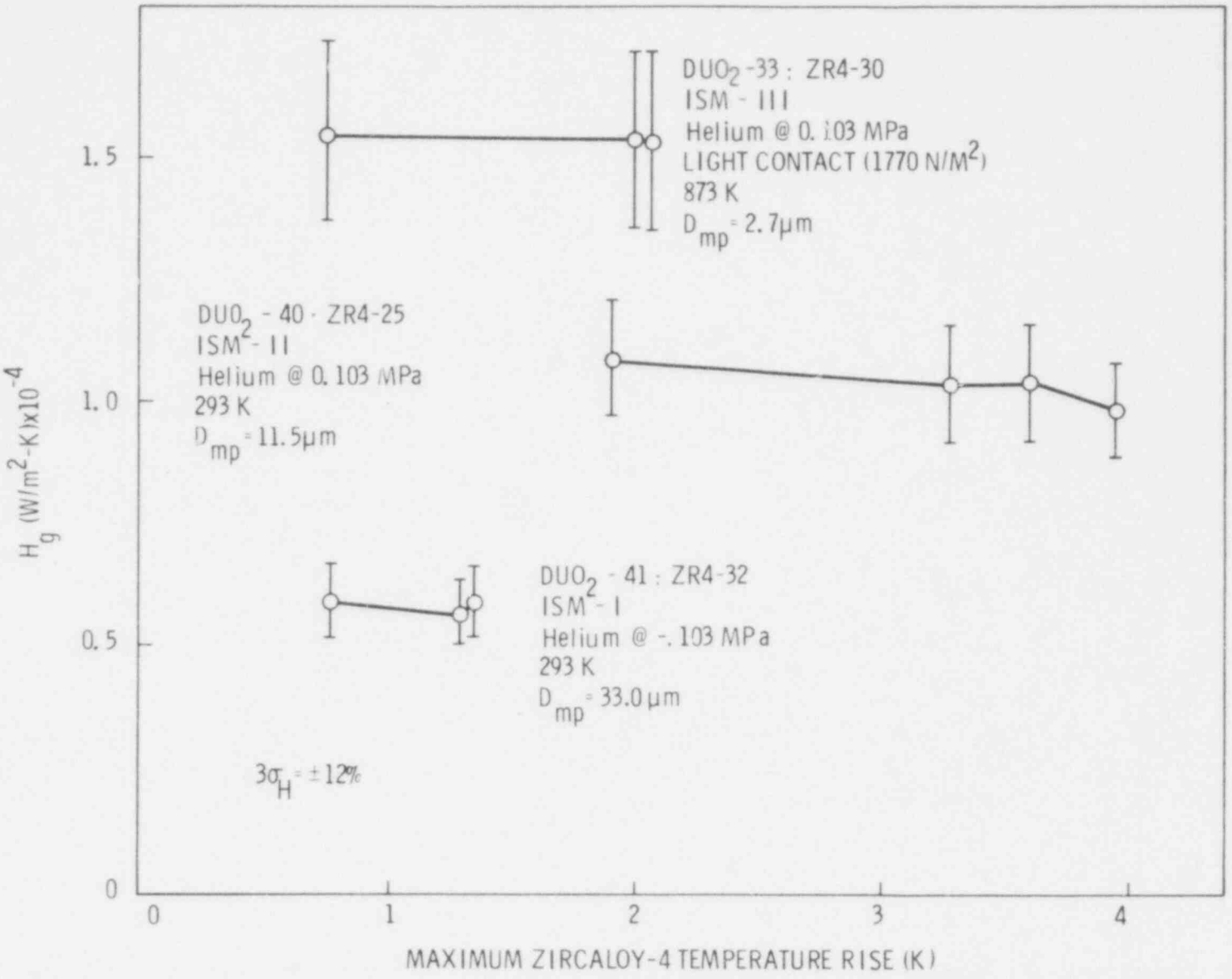

FIGURE 15. H_g Versus Maximum Zr4 Specimen Temperature Rise (i.e. laser intensity)

4.3 MODIFIED LONGITUDINAL DESIGN (MLD) TECHNIQUE

4.3.1 General Features

A schematic diagram of the Modified Longitudinal Design (MLD) test apparatus is shown in Figure 16. The principle of operation is that once a steady-state heat flux is established across two meter bars of known thermal conductivity, the interfacial thermal conductance between the meter bars can be determined. The primary difference between the MLD system and classical axial (longitudinal) design systems (employed previously by other investigators) is the use of a double guarding technique consisting of a guard ring integral to the meter bar and an enveloping electrically heated guard tube. Both of these guards were used to minimize the temperature guarding problem inherent in longitudinal heat flow designs.

The system has been operated from 0.13 Pa up to 2 MPa at a maximum mean interface temperature of 900 K. A hydraulic ram integral to the vessel is used to vary the contact force at the interface during contact conductance measurements. A series of photographs depicting the MLD apparatus in various stages

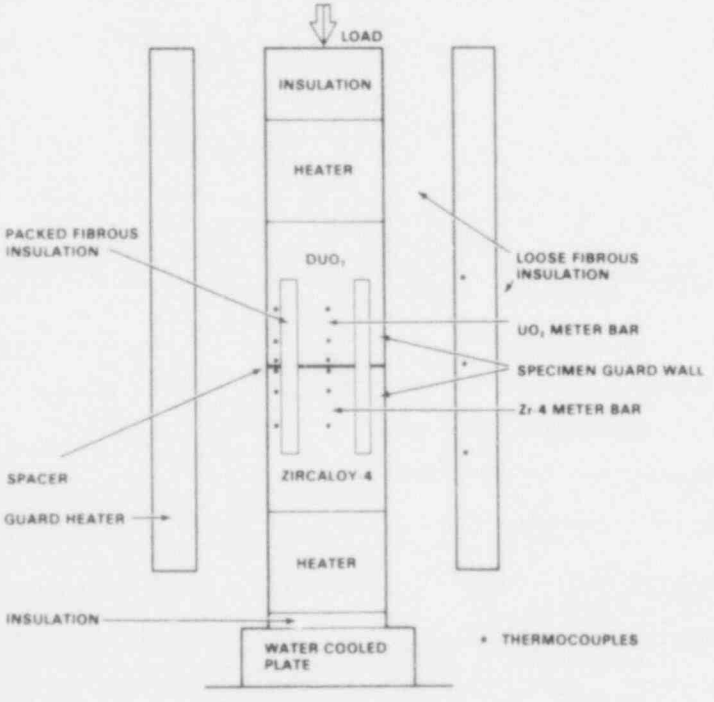

FIGURE 16. Schematic of the Modified Longitudinal Design (MLD) Apparatus

of assembly is shown in Figure 17. A detailed description of the MLD apparatus and measurement technique is contained in the following sections.

4.3.2 Mathematical Description

The determination of thermal conductances H_T, H_g, and H_c is based on the steady-state measurement of geometry, heat flux, and temperature, and is derived from the relationship:

$$H_T \text{ or } H_g \text{ or } H_c = \frac{1}{2}\left[\left(k_1 A \frac{dT}{dx}\right)_{r_1}\left(\frac{1}{A\Delta T}\right)_s + \left(k_2 A \frac{dT}{dx}\right)_{r_2}\left(\frac{1}{A\Delta T}\right)_s\right] \qquad (49)$$

where $k_{1,2}$ = thermal conductivity of meter bar one and two

A = cross sectional area

$\frac{dT}{dx}$ = temperature gradient in meter bar

ΔT = temperature difference across interface

r_1 = parameters of one meter bar (i.e., UO_2)

r_2 = parameters of other meter bar (i.e., Zr4)

s = parameters of interface.

The apparent heat flux in each meter bar was calculated from the relationship:

$$q_{A_{1,2}} = k_{1,2} A\Delta T_m/\Delta x \qquad (50)$$

where $q_{A_{1,2}}$ = uncorrected heat flux in meter bar 1 or 2

$k_{1,2}$ = thermal conductivity of meter bar 1 or 2

ΔT_m = temperature difference across the distance Δx in the meter bar

Δx = distance between temperature sensors.

A model of radial heat flow between concentric cylinders of finite length as described by Jakob[55] was used to correct for energy interchange between the meter bars and the guard wall. The energy exchange with the guard wall was calculated from:

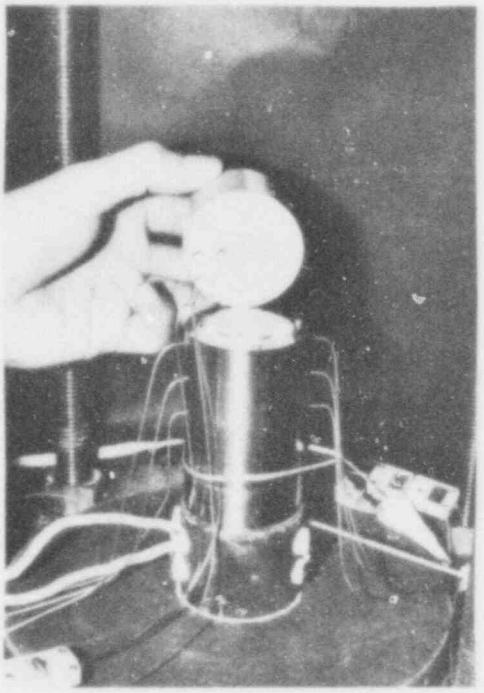

A

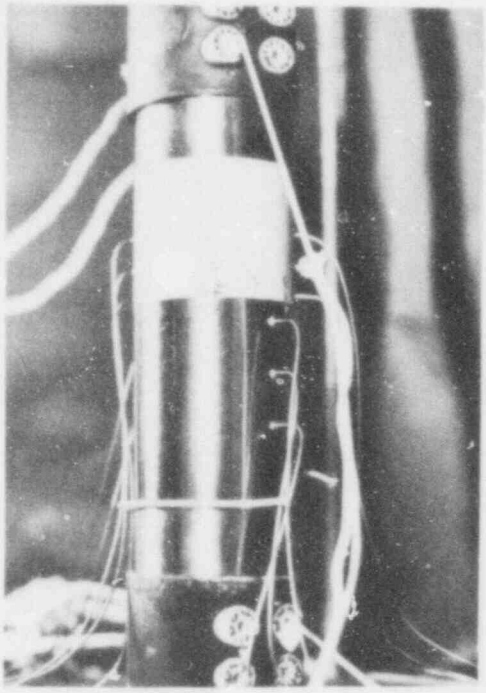

B

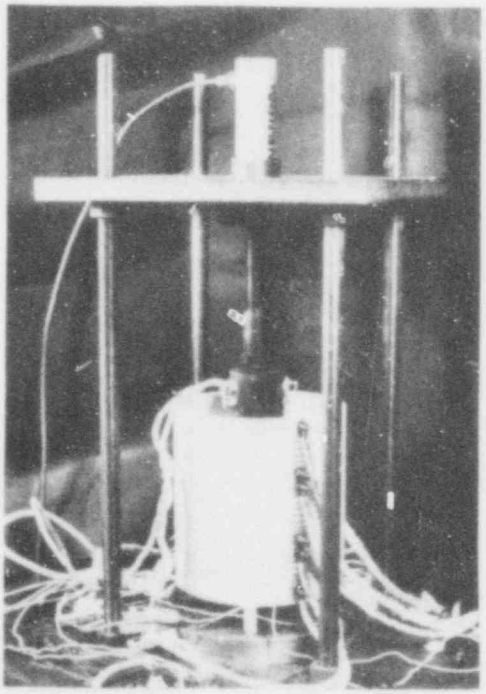

C

D

FIGURE 17. Photographs of MLD System
a) Partially Assembled Meter Bars
b) Fully Assembled Meter Bars
c) Outer Guard
d) View of Open System

$$q_{L_{1,2}} = \frac{K_I L \pi (r_2 + r_1) T_G}{\phi (r_2 - r_1)} \tag{51}$$

where $q_{L_{1,2}}$ = energy exchange between meter bar one or two and surrounding annular guard

K_I = thermal conductivity of insulation (packed quartz) between meter bar and guard

L = Length of meter bar over which correction is applied

r_1 = outer radius of inner cylinder (meter bar)

r_2 = inner radius of outer cylinder (ID of guard)

ΔT_G = temperature difference between meter bar and guard

ϕ = a tabulated shape factor depending on r_1/r_2.

The corrected average heat flux Q was determined from the average of the heat fluxes in the respective meter bars. This correction can be expressed as:

$$Q = \frac{1}{2}\left[\left(q_{A_1} \pm q_{L_1}\right) + \left(q_{A_2} \pm q_{L_2}\right)\right] \tag{52}$$

and is based on the assumption of a constant Q down the column stack. This assumption is justified by the observation that the corrected heat fluxes in the respective meter bars were experimentally found to be within 2%.

The temperature difference across the interface ΔT was determined from calculation (by linear regression) of the respective interfacial surface temperatures. Under the assumption of a constant Q down the column stack, equation 49 can be expressed as:

$$H_T \text{ or } H_g \text{ or } H_c = \frac{Q}{A \cdot \Delta T} \tag{53}$$

where H_T = total conductance when specimens are in contact, $H_T = H_g + H_c$

H_g = gap conductance

H_c = contact conductance (under vacuum conditions only)

Q = corrected average heat flux

A = cross sectional area

ΔT = temperature difference across the interface.

4.3.3 MLD Sample Preparation and Thermal Property Characterization

The depleted UO_2 MLD meter bars used in this study were prepared from the same lot of sinterable powder as were the MPD specimens. The specimens were manufactured from approximately 1 kg of UO_2 as-pressed in solid cylinders 68 mm in diameter and 51 mm in length, with a green density of $5.15 \pm 0.05 \times 10^3$ kg/m^3. To obtain a uniform pressed density of 3[illegible]%, the powder was ball-milled for 12 hr and blended with the as-received powder prior to slugging in the powder preparation process. The slug density was 4.3×10^3 kg/m^3, granulation to -20 mesh and 0.3 wt.% Sterotex used as a lubricant. The pressing pressure was 117.2×10^6 N/m^2. The samples were pre-sintered in a hydrogen atmosphere at 1500 K (~50°/hr) prior to machining to improve the green strength. The pre-sintered specimens were mounted in a lathe and a special tungsten carbide cutting tool used to machine the annular groove. The thermocouple holes were drilled with solid carbide drills. The machined specimens were sintered at 1930 K for four hours in a hydrogen atmosphere at a heating and cooling rate of 50°/hr. The final density of the specimens ranged from 93-94% TD. The single alumina specimen (Coors AD-85, nominally 85% Al_2O_3) was used initially in this study due to difficulties in producing a suitable specimen of UO_2. The Zr4 MLD specimens were machined from the same ingot material as were the MPD specimens. Dimensional detail of the UO_2, alumina, and Zr4 specimen geometries are shown in Figure 18.

The desired surface finish was imparted to the specimen surface by hand grinding the specimens on flat cast iron plates in a manner producing a non-directional finish. The specimens were maintained in an upright position inside a 100 mm OD x 54.7 mm ID x 51 mm high steel cylinder during the polishing operation. The same polishing procedure as described earlier for the MPD specimens was used. To remove effects of machining and polishing induced stresses, the UO_2 and Zr4 specimens were heat treated in the same manner as described previously for the MPD specimens. Similarly, the alumina specimen was heated in air to 1273 K for one hour.

The values for the thermal conductivity for Zr4 and UO_2 were the same as those used for the MPD specimens. The thermal conductivity values for the alumina specimens were obtained using a Dynatech Model TCFCM-N20 cut-bar

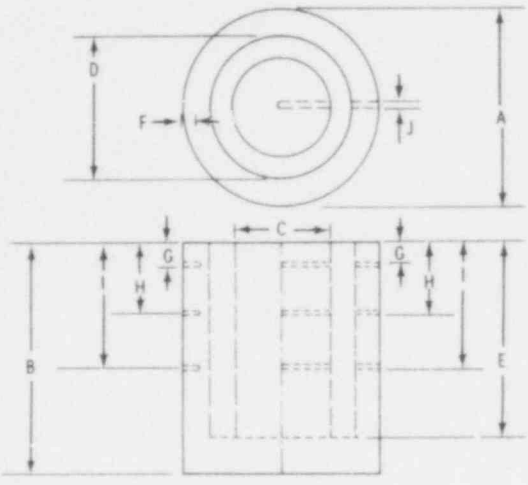

DIMENSION	Al_2O_3	Zr-4	UO_2	Zr-4
A	5.08 cm	5.08 cm	5.39 cm	5.39 cm
B	4.30	6.35	4.28	6.37
C	2.54	2.54	2.54	2.54
D	3.84	3.84	3.96	3.96
E	2.83	5.09	2.53	5.08
F	0.31	0.31	0.36	0.36
G	0.35	0.64	0.22	0.64
H	1.31	2.23	1.12	2.22
I	2.32	3.82	1.94	3.81
J	0.082	0.082	0.082	0.082

FIGURE 18. Geometry and Nominal Dimensions of Alumina/Zr4 and UO_2/Zr4 MLD Meter Bars

and Comparative Instrument over the range 473 to 863 K. The reader is referred to Appendix A for particulars on the thermal property values used in this study.

4.3.4 Interfacial Surface Morphology and Average Mean-Plane Gap Determination

Talysurf-4 profilometer measurements were performed which yielded CLA results within the uncertainty determined for the MPD specimens. The results for the alumina specimens were the same as obtained on UO_2 for the same surface (i.e., ISM-III).

The optical height gauge technique described earlier was used to characterize the MLD specimen surfaces. The procedure was the same as used for the MPD specimens: all 19 points in the center annulus were used to determine the gap width. The uncertainties in the individual gap widths are notes on appropriate figures in the "Results" section.

4.3.5 MLD Experimental System

4.3.5.1 Basic Facility

A schematic of the MLD system is shown in Figure 19. The meter bar apparatus is contained within a high-pressure bell jar. The bell jar system consists of a 190 mm thick by 810 mm diameter steel base flange with an accompanying steel bell having a matching flange. These two sections were bolted together during testing with twelve 75 mm diameter bolts through the flanges. A vacuum and pressure tight fit between the flange was achieved by means of a steel composite gasket designed to accept a loading of 1100 kg. When working on the test stack the bell is lifted by a winch mounted to the ceiling. The entire structure is mounted on a concrete pedestal with access space below.

The interior of the bell measures 250 mm diameter by 610 mm in height. Four 19 mm diameter rods support an elevated base plate which consists of a water-cooled heat sink, electrical connections, and thermocouple terminals. The 19 mm rods extend to the top of the bell, where a top plate is mounted to accommodate the hydraulic ram. All wires and plumbing extend through the

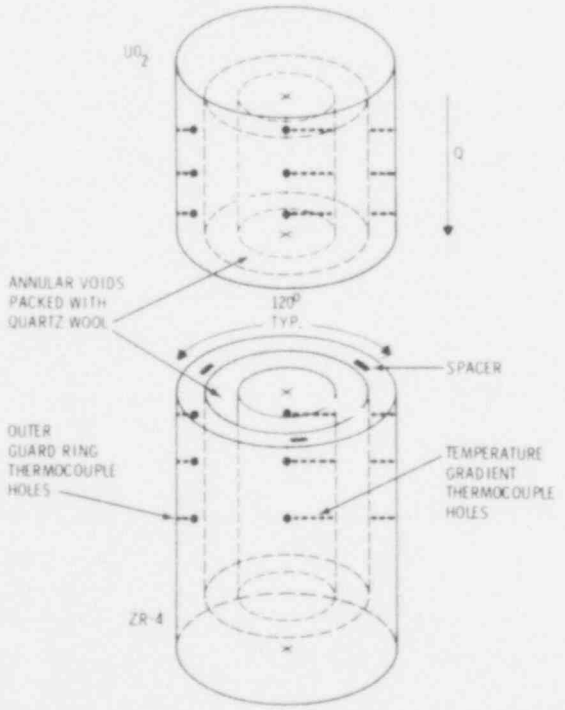

FIGURE 19. Diagram of Meter Bar Assembly

316 stainless steel wherever possible. The temperature probes consisted of calibrated Type K thermocouples which were insulated with MgO and sheathed in Inconel. These probes were then connected to appropriate terminals on the base plate. From the terminals, Type K extension wire is passed through gas-tight feedthroughs and extended to a remote control area.

The extension wire is terminated in an isothermal block, where the thermocouple wire is joined to copper wire. The individual unreferenced thermocouple outputs are connected to a selector switch. The output of the switch is referenced to an electronic ice reference unit. The temperature was read in millivolts using a digital voltmeter having a resolution of one microvolt (approximately equal to 0.025 K).

4.3.5.2 Meter Bar Instrumentation and Insulation

A diagram showing the meter bar assembly is shown in Figure 19. The temperature sensors chosen for the measurement of temperature were chromel/alumel (Type K) thermocouples. The ungrounded thermocouple probes were packed in MgO and sheathed in Inconel 600. The overall diameter of the probes was 0.81 mm. Prior to installation all the temperature sensors were pre-bent to the final installation configuration corresponding to the particular locations in the assembly and radiographed to accurately locate the thermocouple bead. Additionally all the temperature sensors were pre-tested over the range from 290 K to 1000 K by placement in a common test block. Those probes that indicated a reading of more than ±1 K outside the average reading were discarded. The distance between thermocouple holes was determined from measurement of the midpoints of the thermocouple holes on the exterior of the specimens with appropriate corrections applied for the location of the thermocouple bead for the particular sensor inserted. Radiographs of the MLD specimens prior to insertion of the sensors revealed that the thermocouple holes were drilled perpendicular to the axis of the meter bars.

The thermocouples were coated with a silicone heat sink compound prior to insertion into the meter bars. The emf output of the thermocouples were referenced to an electronic ice reference unit. The respective thermocouple temperatures were read directly in millivolts on a digital microvoltmeter having a resolution of 1 μV (approximately 0.025 K).

Insulation was required to minimize effects of gas convection within the annular cavity and to minimize radial heat flow between the meter bars and annular guard. Low density quartz wool was selected as the insulation material on the basis of compatibility with the sensors and meter bars, ease of use, stability over the temperature range of use, and accuracy of known values of apparent thermal conductivity over the temperature range of use. The quartz wool was packed in the annular cavity at approximately 130 kg/m^3. Measurements of the apparent thermal conductivity from 373 to 873 K were carried out in accordance with ASTM C177-76, "Steady-State Thermal Transmission Properties by Means of the Guarded Hot Plate." The results of this evaluation are given in Appendix A.

4.3.5.3 System Atmosphere

The MLD facility allows for the use of assorted gases at various pressures. In conjunction with this it also provides for the efficient removal of residual oxygen from the gas supply.

Gases used in the current experimentation consist of Helium (100), Argon (100), and a 50:50 mixture of the two.

Gas pressure requirements currently range from vacuum to 1.7 MPa. Vacuum capability is 3 Pa without a diffusion pump and is measured with a 0-338 Pa McLeod gauge.

A zirconium gettering system with allowable flow rates of 0.01 to 5.0 liters (atm)/min and a maximum pressure of 2 MPa was used to getter the inlet gases to below 0.1 ppm O_2. A high-pressure rotameter was connected to the getter to ensure the proper flow rate. Since the bell jar pressure was constantly changing during vacuum and backfill procedures, the getter and rotameter were kept at a constant 1.9 MPa to ensure a uniform flow rate. Computer calibrations of different floats (glass, carbolloy, stainless steel) were used depending on gas composition to produce a full-scale indication at 5 ℓ/min. Backfilling was achieved by the manipulation of the control and metering valves. Pressure was measured with various ranges of pressure gauges and excess pressure bled through a 6.9 kPa check valve.

4.3.5.4 Hydraulic Loading System

During some modes of MLD experimentation variation in the contact pressure between the UO_2 and Zr4 was required. A heavy plate was mounted 380 mm above the elevated base plate by four 19 mm stainless steel rods. Threaded into the center of this plate is a water-cooled hydraulic cylinder having a 4500 Newton capacity. The cylinder connected through the base flange to a hand pump with a safety check valve and a 0 to 4500 Newton gauge at the control area. The gauge and ram were regularly checked with a Dillon force gauge standard.

Because of the high temperature levels in adjacent areas, the top plate and ram were water cooled with copper tubing and the temperature of the ram was monitored. The heavy gauge stainless steel tubing carrying the hydraulic fluid was also cooled.

After completion of various gap conductance measurements on the meter bars, approximately 0.2 mm of material was machined from the surface of the outer annular guard ring on the Zr4 meter bar. This procedure ensured that only the center meter bar sections would be in contact for subsequent contact conductance measurements.

4.3.5.5 Temperature Control System

During the MLD testing, five separate heater assemblies were used. Two of these, the main and auxiliary, were used to set the temperature gradient along the test specimen. The other three heaters were used to thermally guard the stack by matching the sample gradient. A group of three controllers and two variacs were used to set the temperatures in the MLD experiments. A precision two-mode controller was used for the main guard. Two single-mode controllers were used for the auxiliary and middle guard, and the top and bottom guards were powered by variacs. The three-control thermocouples were Type K. Heaters at either end of the column were energized and adjusted until the desired mean temperature and column temperature gradient were achieved. The power to the outer guard tube sections was adjusted until the temperature gradients of the inner wall guard and test column were matched as closely as possible. The criterion for achievement of steady-state conditions was that the measured thermal interface conductance at successive readings of 20 minutes apart change by no more than 1%.

4.3.5.6 Determinate/Indeterminate Errors

The purpose of this section is to assess the uncertainty (3σ) in the measurement of H_T and H_c and to discuss the probable sources and effects of indeterminate errors in its measurement.

The various determinate errors associated in the measurement of the thermal gap or contact conductance are listed in Table 7. Of the various determinate errors considered, the uncertainty in dT/dx was considered to be the largest when the extrapolated temperature drop at the interface was small. Based on an analysis presented in Appendix C, the 3σ uncertainty, W_H, can be determined for each datum on the basis of the relationship between the W_H and the corrected heat flux Q and the extrapolated temperature drop ΔT:

TABLE 7. Determinate Errors in MLD Experiment

Factors Contributing to the Uncertainty in the Value of H_g or H_c	Uncertainty $\pm 3\sigma$	Comments
Knowledge of dT/dx in the meter bars	$3\sigma_{\Delta T} = 1.5°K$	Refer to Appendix C for detail
Thermocouple location	$3\sigma_a = 0.5$ mm	
Thermocouple reading	$3\sigma_{T_c} = 0.5°K$	
Knowledge of heat flux (Q) in meter bars	$3\sigma_Q = 3\%$	Neglecting possible TC lead shunting and spacer shunting effects
Radial heat loss	--	Determined in each measurement and corrected for (see Appendix E)
Thermal conductivity of meter bars	$3\sigma_k = 2\%$	Measured
D_{mp}	2-88%	Dependent on $3\sigma_D$, uncertainty in γ values and magnitude of D_{mp}

$$W_H = \frac{Q}{\Delta T}\left(5063 + \left(\frac{2960}{\Delta T}\right)^2\right)^{1/2} \qquad (54)$$

This relationship is the basis for the determined 3σ uncertainties which appear in the appropriate figures in the "Results" section.

The indeterminate errors postulated to occur in the MLD experiment are summarized in Table 8.

TABLE 8. Indeterminate Errors in MLD Experiment

Indeterminate Error	Comments
Axial and radial distortion around the thermocouples and holes.	Minimized by use of as small a thermocouple as practical.
Gas convection effects.	Minimized by packing the annular region in the meter bar with quartz wool.
Nonuniform interface contact between meter bars during contact experiments.	Minimized by having as large a distance as practical between the thermocouples and the interface.
Heat flow down thermocouple leads.	Minimized by using small diameter thermocouples and radial guarding.
Heat shunting through spacers.	Minimized by use of small spacer and placement on outer annular guard (∿1 mm x 7 mm).
Change in meter bar properties during experimentation.	Conduct before/after experiments prior to meter bar removal showed similar results.

5.0 RESULTS AND DISCUSSION

5.1 INTRODUCTION

The "traditional" method of design of experiment is to observe the effect of one factor on one other dependent variable while holding all other factors constant. In this approach, control of conditions becomes important to achieving data reliability. In this study, the factors varied in the determination of H_g and H_c and are summarized in Table 9.

TABLE 9. Factors Varied in H_g and H_c Experiments

Factor	Symbol
Temperature (MPD: ambient; MLD: mean)	T
Interfacial contact pressure	PA
Average mean-plane separation distance	D_{mp}
Gas composition	GC
Interfacial surface morphology	ISM
Gas pressure	GP
Time	TM

In reference to Table 9 the reader will recall that the use of a one-dimensional parameter, D_{mp}, to describe the separation distance between surfaces under nonideal conditions (i.e., when the fractional uncertainty in D_{mp} due to roughness and/or error of form is greater than 0.1) is not sufficient to uniquely define the determined value of H_g. Inspection of Tables F.8 and F.9 shows that $\psi > 0.1$ for most all D_{mp} values measured in this study. The quantity D_{mp} represents only the average of the 19 local separation distances $(D_a)_i$ between asperity tips to which was added a term (γ) determined for each ISM (refer to Appendix F and Section 4.2.4 for details). The reader will recognize that the one-dimensional factor D_{mp} is only an approximation to the multi-dimensional gap geometry of experiment. However, the assumption is made that the measured value of H_g is unique to the determined value of D_{mp} at least within the 3σ uncertainty in D_{mp}. A test of this assumption is made in

Section 5.2 where the results of the MPD and MLD experiments are compared. Additional discussion is made in Section 5.4 where the consequences of using D_{mp} (rather than some other average one-dimensional distance parameter) are examined.

If the "traditional" approach is followed, the question as to whether all other conditions can be held constant must be determined. In the H_g experiments, TM need only be considered if changes in ISM conditions would occur (assuming all other factors are held constant). The factor of TM was tested repeatedly in the MPD measurements after each temperature and gas composition run from 293 to 873 K to 293 K by reintroduction of a helium fill gas at 293 K. Comparison of the H_g value thus obtained was compared to the initial H_g helium fill gas value determined at the start of a given set (e.g., a set being defined as a collection of H_g values obtained under various gas compositions at a fixed value of D_{mp} and ISM). No change in the value of H_g with TM was observed. The factors of T and GC were varied in a controlled fashion; whereas, the factors of D_{mp} and ISM were held constant for a given set of measurements for experimental convenience. The factor of GP was fixed at a constant value of 0.103 MPa. For the H_c measurements, TM is a factor to be considered as results obtained on increasing and decreasing PA were found to vary. This factor can be accounted for insofar as the H_c results are considered in the order in which they were determined.

In the MPD and MLD experiments, the levels (values) of all the factors were arranged in an organized manner to maximize the breadth of conclusion for a minimum amount of experimental work. This organization also allows the systematic investigation of interaction among the factors given in Table 9. Interaction may be defined as the change in measured response due to one factor caused by a change in another factor. For example, does H_g for a given surface morphology (i.e., ISM-I) respond to temperature in the same fashion as H_g for a different surface morphology (i.e., ISM-II or III) with all other factors kept constant? Analysis of varying levels of interactions among factors [e.g., two-factor (D_{mp} versus T), three-factor (D_{mp} versus T versus ISM)] can also yield information related to: validity of the assumption that the thermodynamic state of the system was at equilibrium; possible sources and magnitude of experimental error associated with variables; and, corrections to the data on the basis of time effects.

The MPD experiments have been conducted as a function of temperature (293 to 873 K), gas composition (Helium; He:Ar (51.8:48.2), Argon; He:Xe (89:11) and He:Xe (51:49), mean-plane gap width (33.0 μm to 2.7 μm) and surface morphology (ISM-I, II, and III). The MPD H_g data is listed in tabulated form in Appendix D. These data represent the average of two or more measurements taken at the same conditions of experiment. The $3\sigma_H$ uncertainty in these results was determined to be ±12% (Appendix B). A number of independent MLD experiments were performed[(a)] to provide data for correlation to the MPD H_g results. The remainder of the MLD experiments were designed as a scoping study to investigate the effect of contact pressure (0 to 14.68 MN/m^2), surface roughness (ISM-I and II), and surface error of form on H_c. The conditions of the MLD experiment and tabulated results are listed in the order of determination in Appendix E. Each datum represents the measured H_T or H_c value at steady-state conditions as defined previously in Section 4.3.5. The $3\sigma_H$ uncertainty has been determined according to an analysis presented in Appendix C. For convenience, the determined uncertainties appear adjacent to each datum in Appendix E. The average mean-plane separation distance (D_{mp}) along with their associated uncertainties can be found in the appropriate tables in Appendix F and adjacent to each set of tabulated results in Appendix D and E.

5.2 COMPARISON OF MPD/MLD GAP CONDUCTANCE DATA

An assessment of the MPD and MLD techniques can be performed through comparison of H_g data generated by both techniques under similar conditions of temperature and fill gas. Plots of H_g versus D_{mp} for all MPD and MLD results in Helium (100) and Argon (100) fill gases at 473, 673, 873 K are shown in Figures 20, 21, and 22, respectively. In these figures, graphic delineation among the various MPD surface morphologies (e.g., ISM-I, II, and III) has not been made. The MPD and MLD (Alumina:Zr4) block 00 results were obtained at a gas pressure of 0.103 MPa. The remainder of the MLD (DUO_2:Zr4) results in Figures 20 and 21 were obtained at a gas pressure of 0.172 MPa. The vertical error bar about each datum represents the absolute uncertainty (3σ) in the experimentally

(a) Dynatech, Inc., Cambridge, MA 02939.

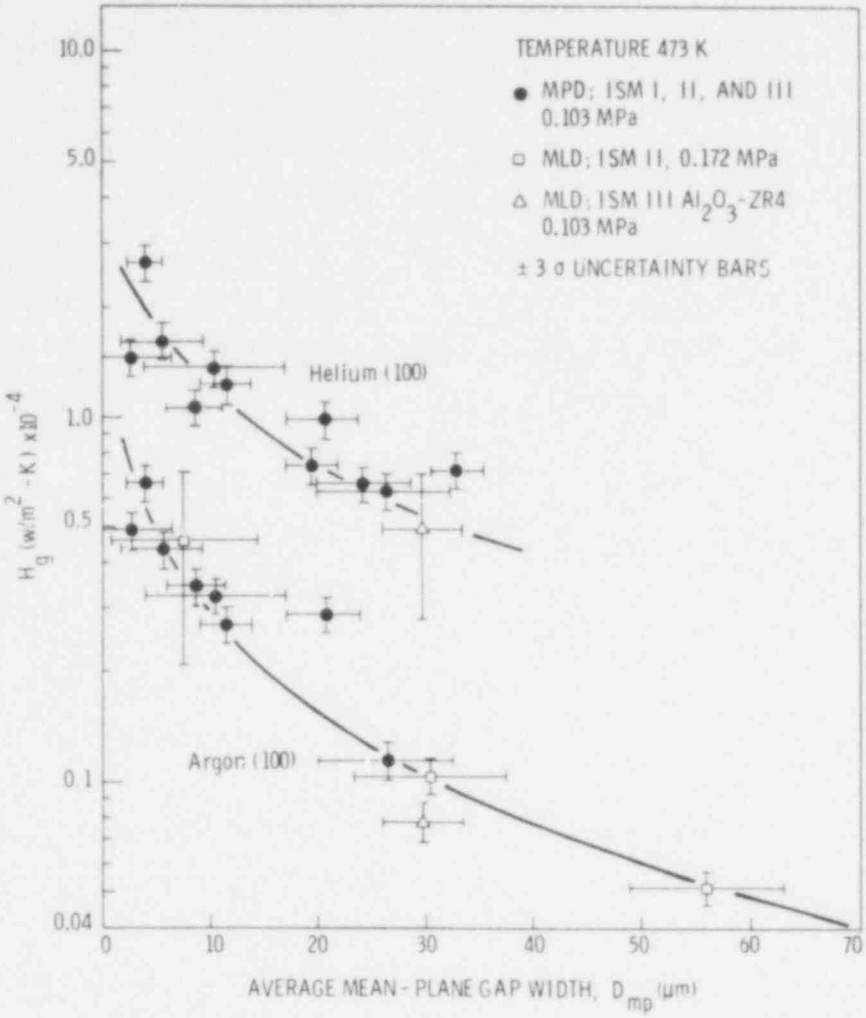

FIGURE 20. H_g Versus D_{mp}. Comparison of all MPD and MLD results at 473 K for Helium (100) and Argon (100) fill gases.

determined value of H_g. In the MPD data this uncertainty is due mainly to the uncertainties in the thermal property values of UO_2 and Zr4. The uncertainties in the MLD data are dependent not only the knowledge of the respective meter bar thermal conductivities but also in the accuracy with which ΔT_{gap} can be determined. The horizontal error bars about each datum represent the 3σ deviation about the average mean-plane gap width (as defined in Section 3.2.1 and determined by Equation 48).

The good agreement between the MPD and MLD data (within experimental uncertainty) shown in Figures 20 through 22 for a wide variety of temperatures, gap

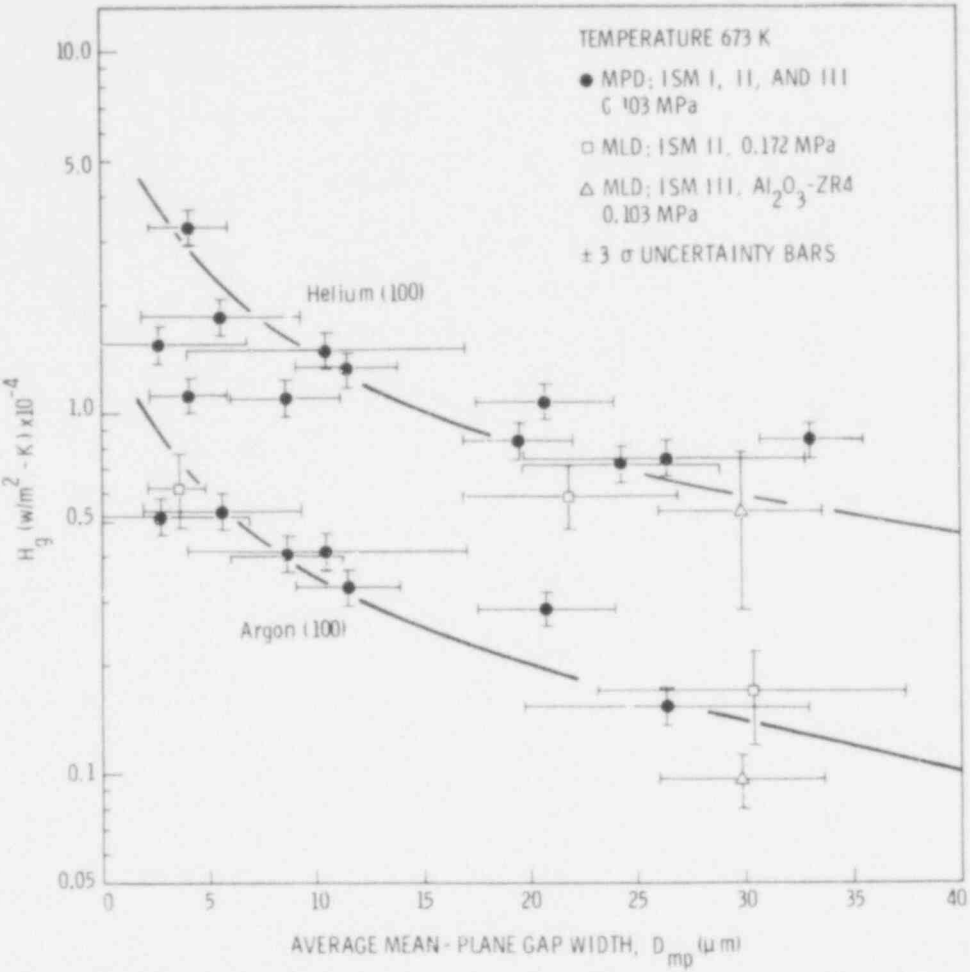

FIGURE 21. H_g Versus D_{mp}. Comparison of all MPD and MLD results at 673 K for Helium (100) and Argon (100) fill gases.

separations, and gas compositions strongly indicates an absolute accuracy in H_g for either technique to be no larger than the experimental uncertainties shown in the figures since the two techniques are independent of one another. Thus, the MPD and MLD techniques can be used to generate a data base to which various computer modeling codes for predicting gap conductance can be compared for code verification.

5.3 "GAP" CONDUCTANCE RESULTS

The dependence of H_g on D_{mp}, T, GC can be shown in the "traditional" manner by plotting the dependent versus independent variable and observing the particular

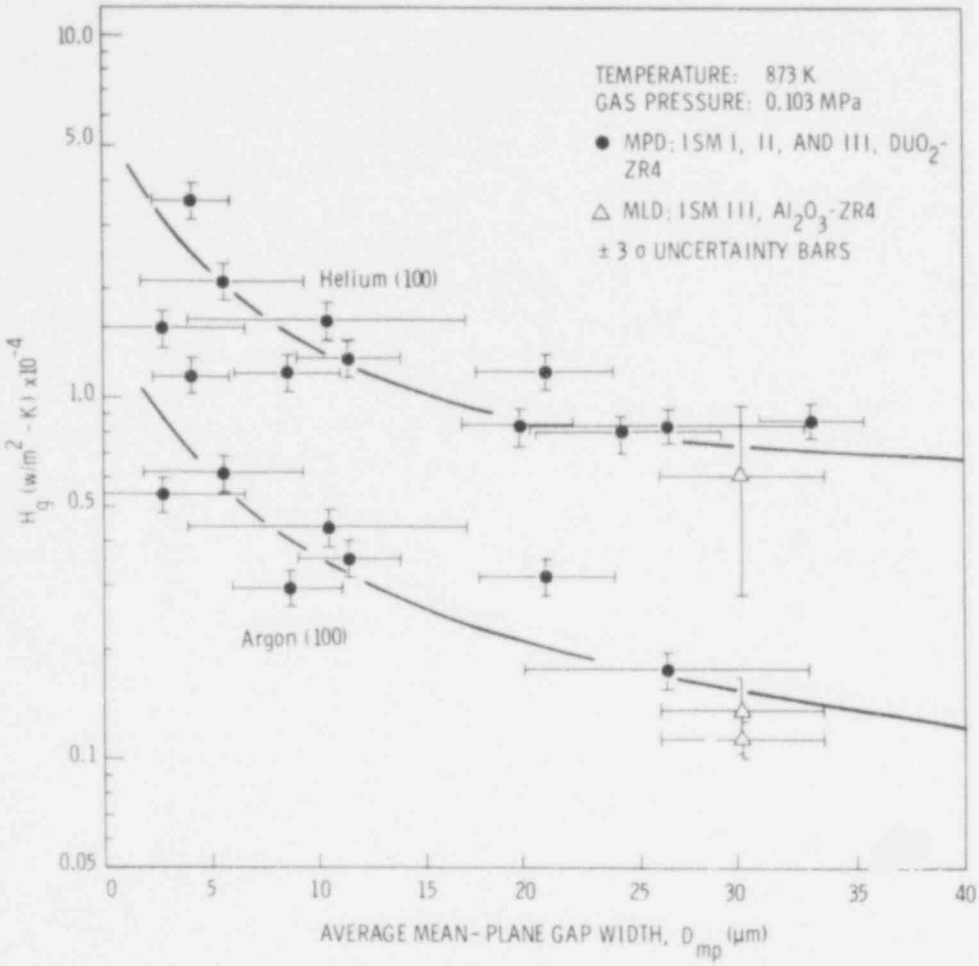

FIGURE 22. H_g Versus D_{mp}. Comparison of all MPD and MLD results at 873 K for Helium (100) and Argon (100) fill gases.

trend that exists. Various two-factor interactions can be observed by selection of the proper third variable in accordance to Table 9 and determining if any deviation from a family of curves defined by the selected variable exists. The two-factor interaction of T-ISM and GC-ISM requires a fixed value of D_{mp} at various levels of ISM. As a fixed value of D_{mp} is difficult to achieve experimentally at various ISM, observations of this interaction may be obtained by extrapolation of results to some particular value of D_{mp}.

5.3.1 H_g Versus D_{mp} at Various ISM

The dependence of H_g on D_{mp} for various ISM at a fixed value of T, GC, and GP are shown in Figures 23 through 26. In Figures 23 and 24, H_g results are

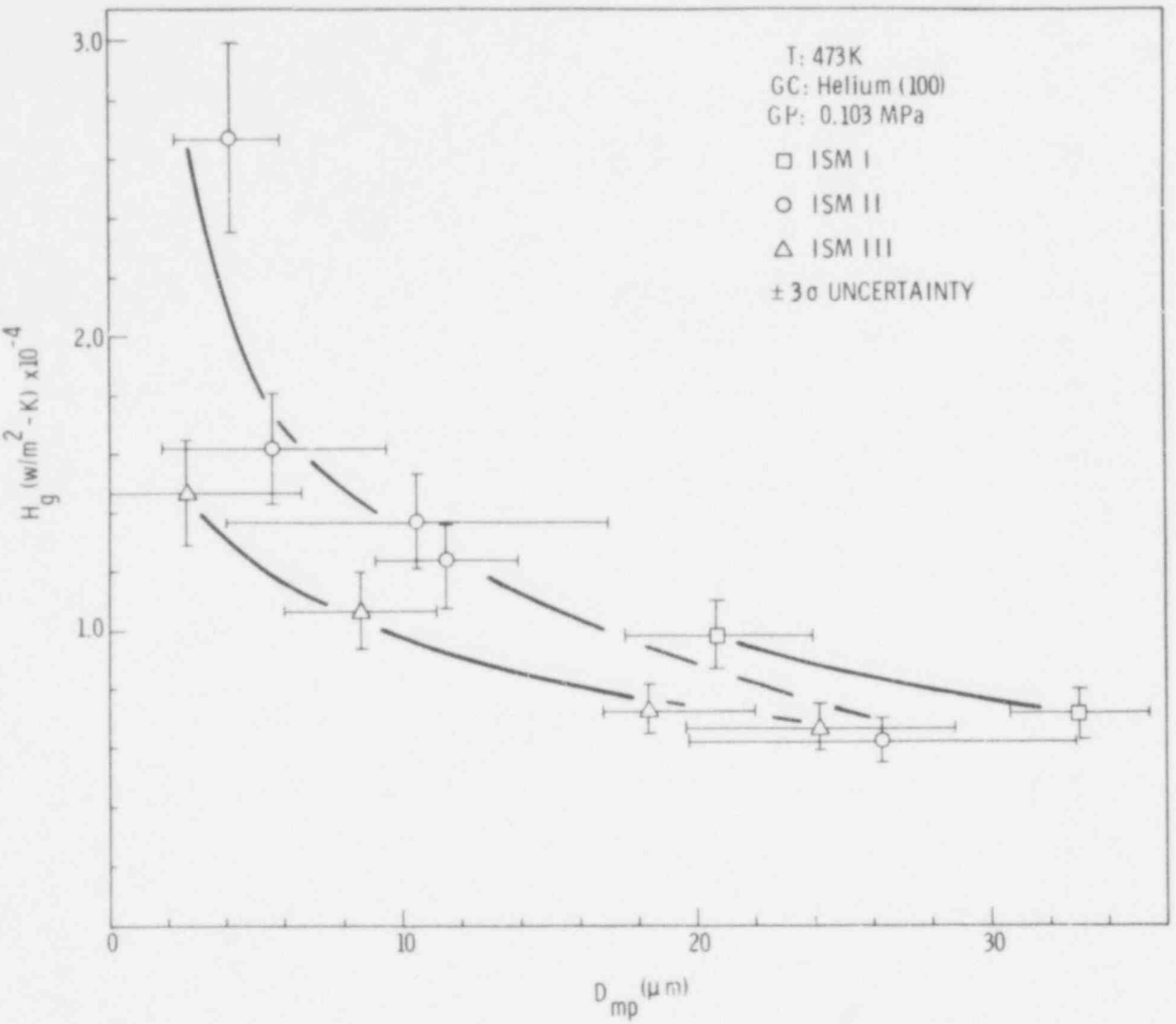

FIGURE 23. H_g Versus D_{mp} for ISM-I, II, and III. T = 473 K; GC = Helium (100); GP = 0.103 MPa.

shown for a Helium (100) fill gas at a pressure of 0.103 MPa at 473 K and 873 K, respectively. In Figures 25 and 26, results are shown for an Argon (100) fill gas at the same pressure at 473 K and 873 K, respectively. The error bars indicate the corresponding 3σ uncertainty in H_g and D_{mp}. In reference to these Figures, H_g is seen to decrease with increasing D_{mp}. When D_{mp} is less than approximately 20 μm it can be seen that H_g (ISM-II) > H_g (ISM-III); whereas, at larger values of D_{mp}, H_g (ISM-I) > H_g (ISM-II) $\gtrsim$ H_g (ISM-III). A two-factor interaction between D_{mp} and ISM is observed which is more pronounced in a

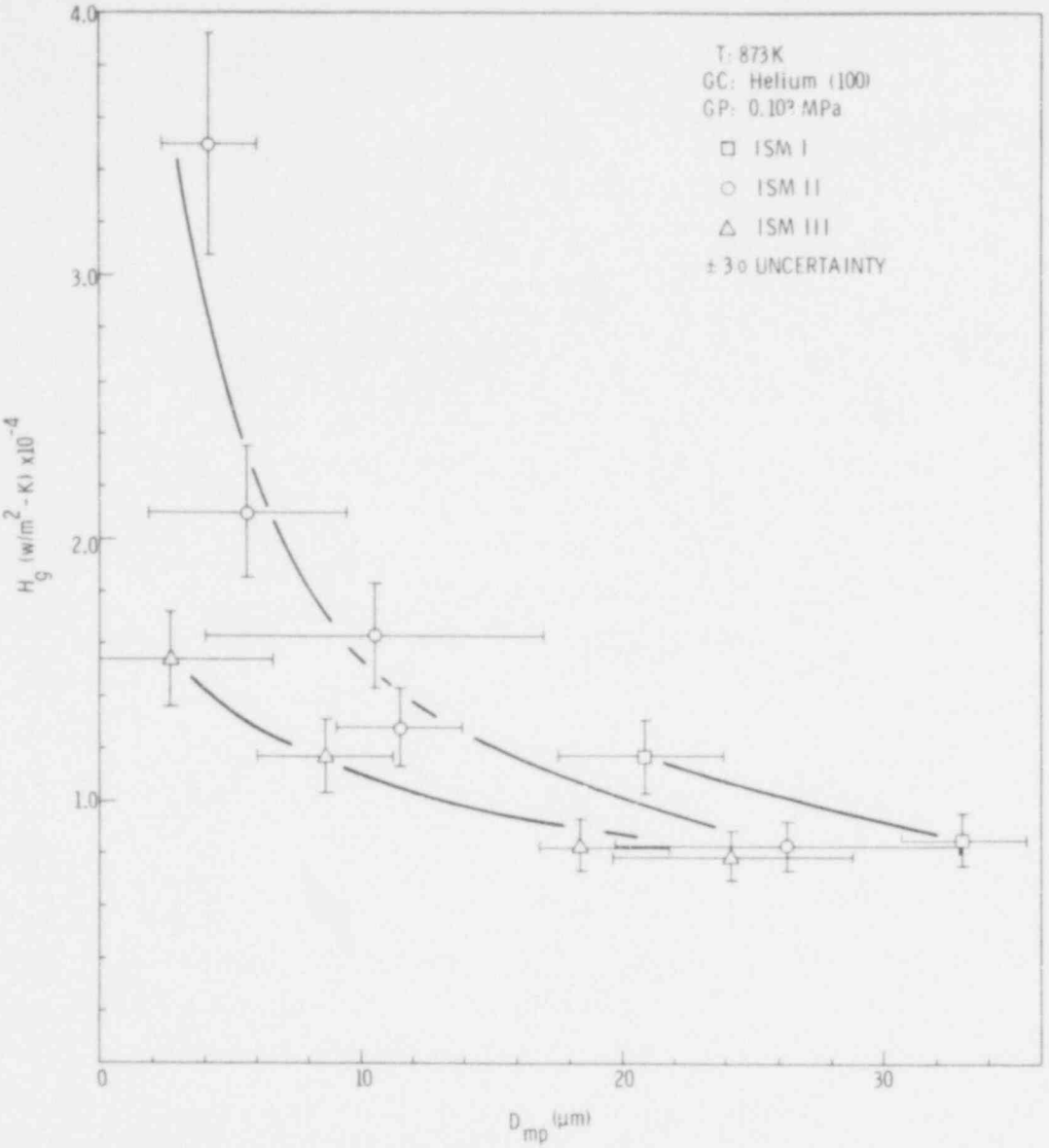

FIGURE 24. H_g Versus D_{mp} for ISM-I, II, and III. T = 873 K, GC = Helium (100), GP = 0.103 MPa.

Helium atmosphere at 873 K and small values of D_{mp} (Figure 24) than for an Argon atmosphere at larger values of D_{mp} at 473 K (Figure 25). A similar observation can be made at other temperatures (293 and 673 K) and fill gases. In general, the interaction between D_{mp} and ISM becomes more pronounced with decreasing separation distance below 20 μm and increasing gas conductivity (i.e., Argon to Helium).

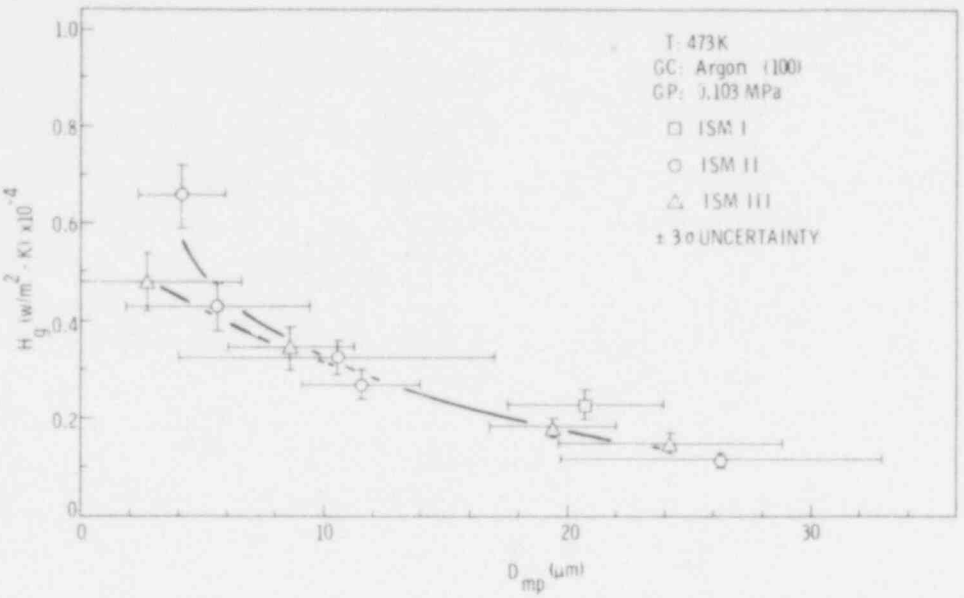

FIGURE 25. H_g Versus Dmp for ISM-I, II, and III. T = 473 K, GC = Argon (100), GP = 0.103 MPa.

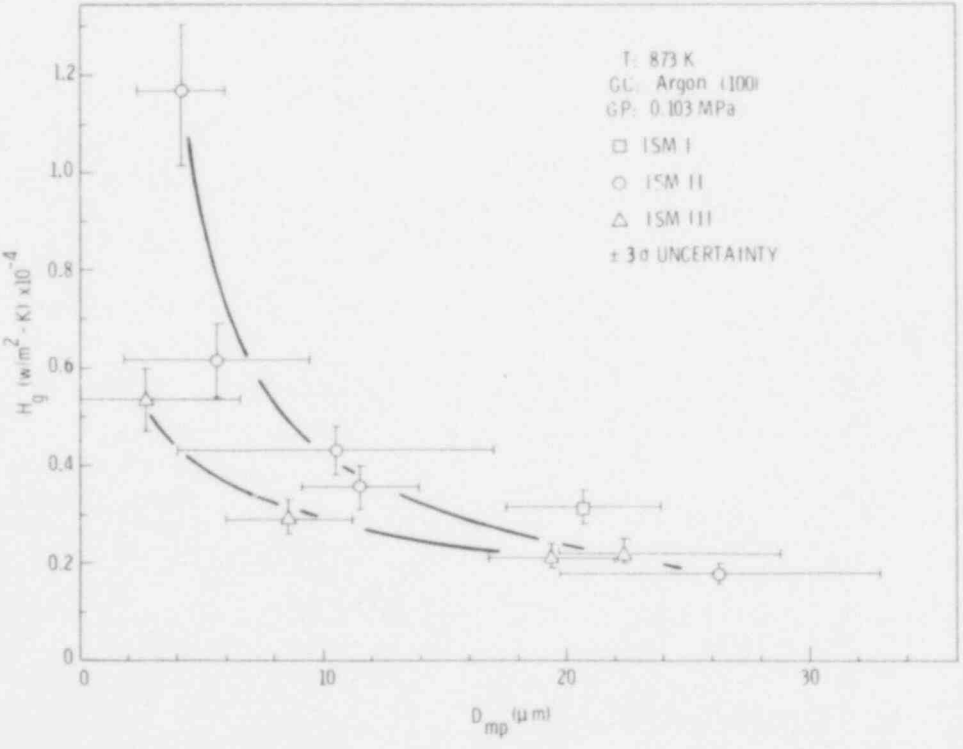

FIGURE 26. H_g Versus Dmp for ISM-I, II, and III. T = 873 K, GC = Argon (100), GP = 0.103 MPa.

5.3.2 H_g Versus D_{mp} at Various GC

The presence of a two-factor interaction between D_{mp} and GC can be determined from a plot of H_g versus D_{mp} for various GC at a fixed ISM and T as shown in Figure 27. The effect of increasing thermal resistance of the gas is seen to cause a decrease in H_g in a manner consistent with the known decrease in the thermal conductivity of the gas. For instance at D_{mp} = 11.5 μm, H_g decreases in the same manner as $K_{He} > K_{He:Xe\ (89:11)} > K_{He:Ar\ (51.8:48.2)} > K_{He:Xe\ (51:49)} >$

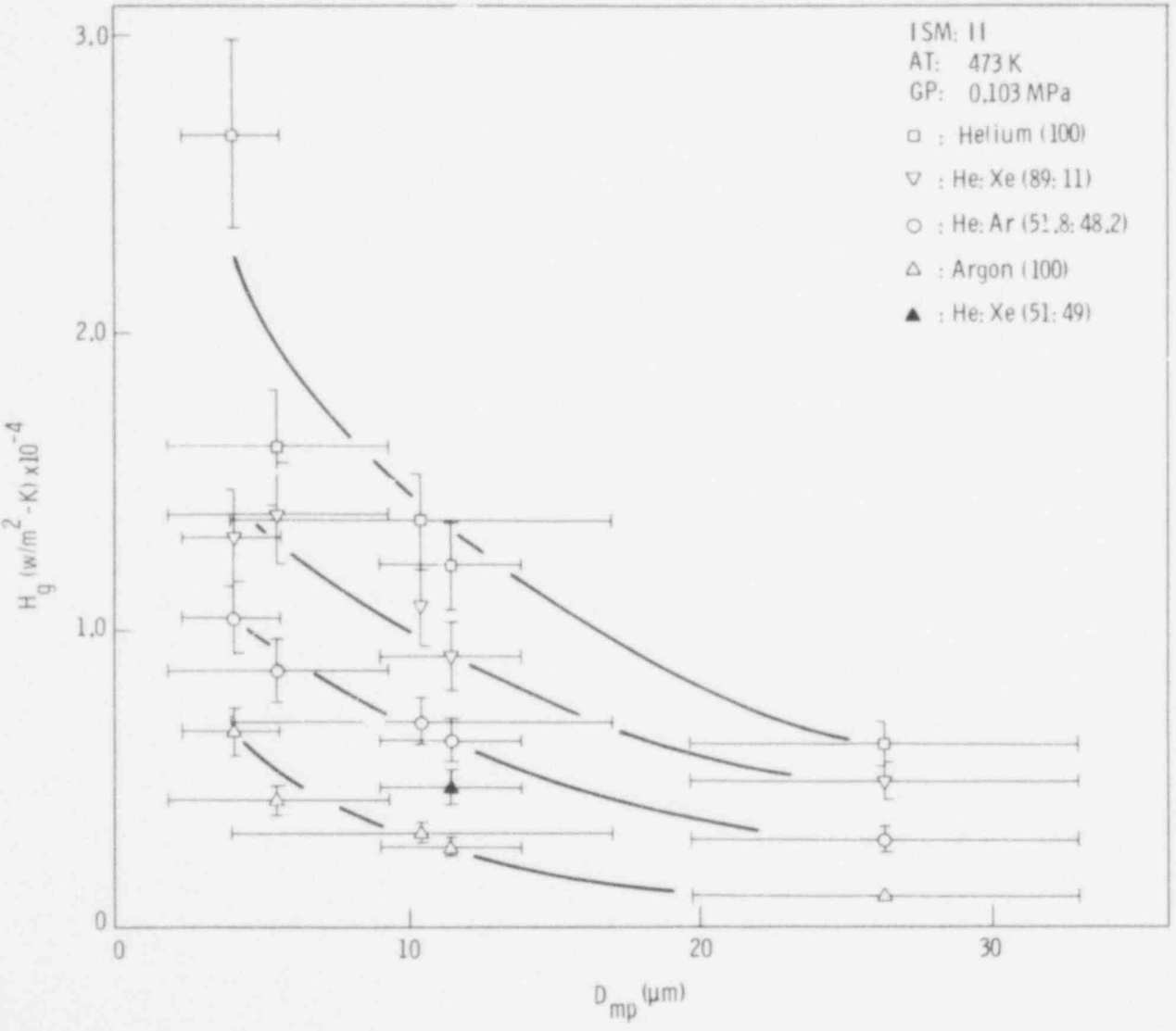

FIGURE 27. H_g Versus D_{mp} for Various Gas Compositions; T = 473 K; P = 0.103 MPa; ISM-II.

K_{Ar}. A two-factor interaction between D_{mp} and GC as shown by the family of curves, is not apparent for the Argon, He:Ar, and He:Xe fill gases. Only for the Helium (100) fill gas when $D_{mp} < 10$ μm is a two-factor interaction seen. The interaction between D_{mp} and GC is not as pronounced as seen in the previous section between D_{mp} and ISM.

5.3.3 H_g Versus D_{mp} at Various T

The dependence of H_g on D_{mp} at temperatures of 473 and 873 K for an ISM-II sample pair at a pressure of 0.103 MPa for a Helium (100) and Argon (100) atm is shown in Figures 28 and 29, respectively. The effect of increasing temperature at a given value of D_{mp} is seen to cause only a 20 to 30% increase in H_g. The increase in H_g with T is an accordance with the increase in gas conductivity with T.

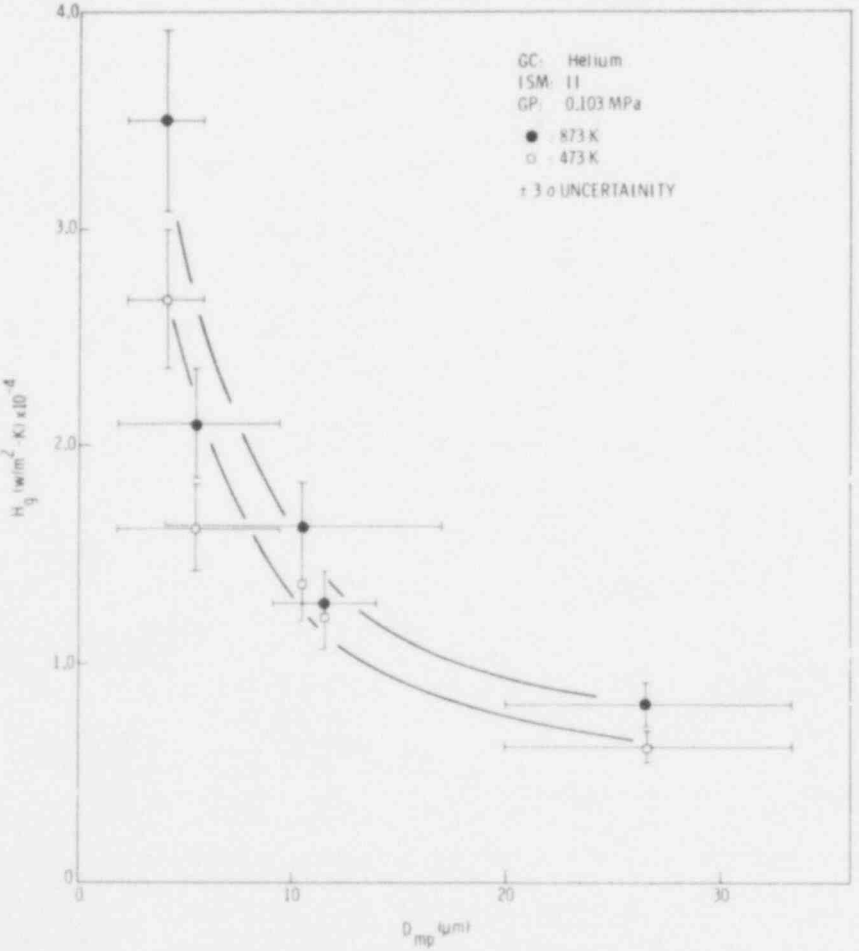

FIGURE 28. H_g Versus D_{mp}; GC = Helium (100); ISM-II; GP = 0.103 MPa

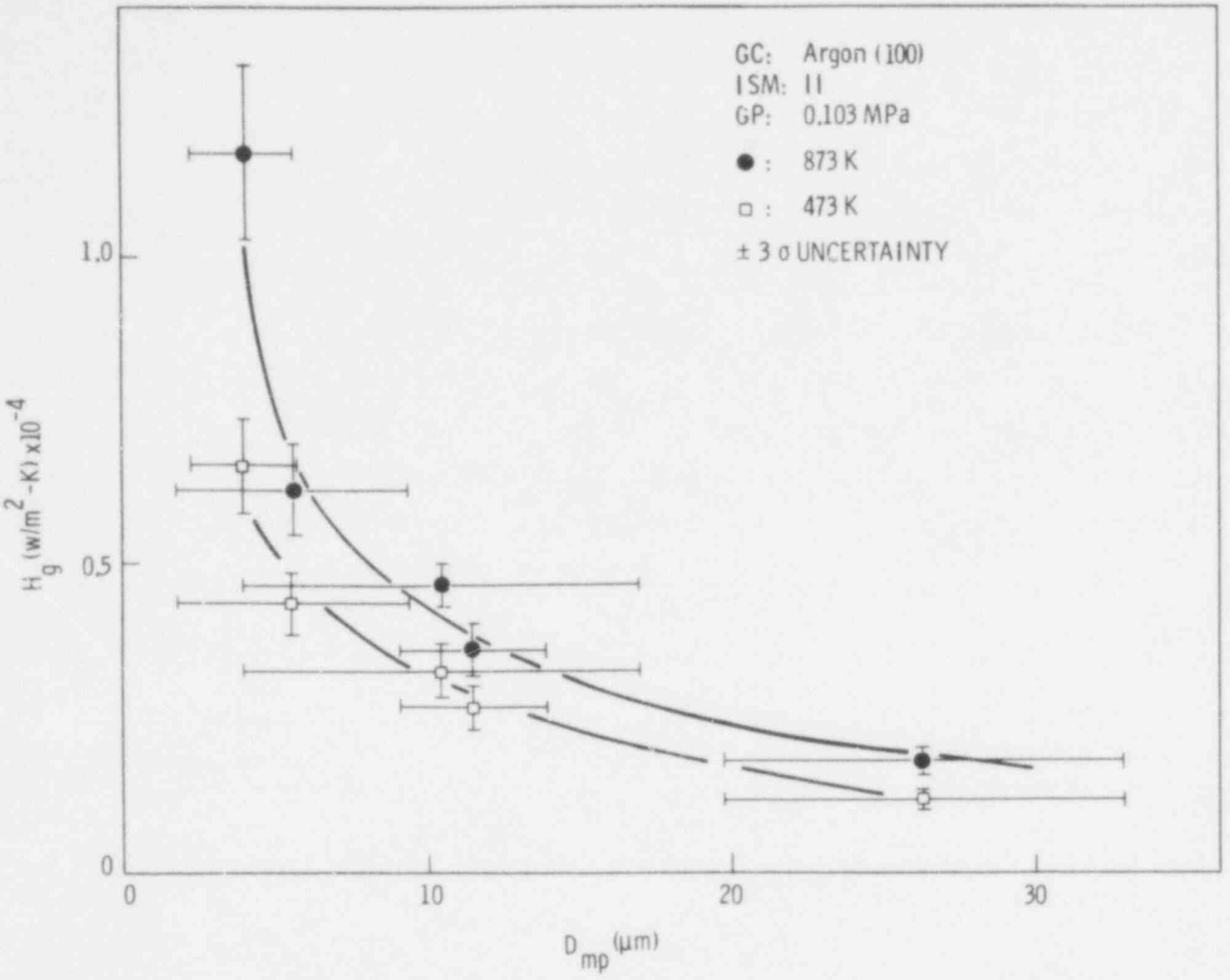

FIGURE 29. H_g Versus D_{mp}; ISM-II; GC = Argon (100); GP = 0.103 MPa

However, at values of D_{mp} < 6 μm, a more pronounced dependence of H_g with temperature is seen for an Argon fill gas than for Helium. A two-factor interaction between D_{mp} and T is apparent at values of D_{mp} < 6 μm in an Argon atmosphere (Figure 29); whereas, in a Helium atmosphere (Figure 28) such an interaction is not apparent.

5.3.4 H_g Versus T at Various GC

The dependence of H_g on temperature between 293 and 873 K for the various gases, D_{mp} values, and surface morphologies at a pressure of 0.103 MPa are shown in Figures 30 to 39 inclusive. The $3\sigma_{H_g}$ uncertainties at selected values of H_g are represented by the error bars. In Figures 30 through 33 (ISM-III), a

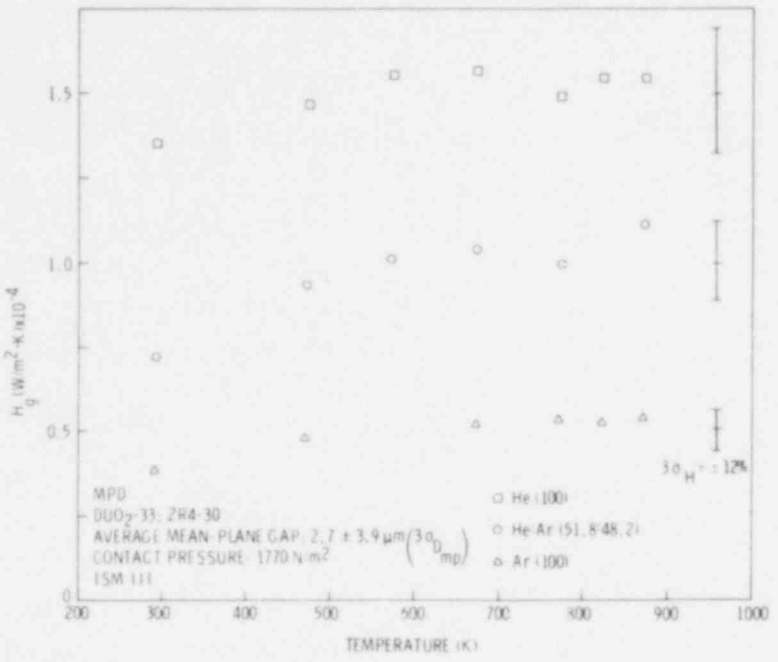

FIGURE 30. H_g Versus Temperature for ISM-III Surfaces in Light Contact (D_{mp} = 2.7 μm)

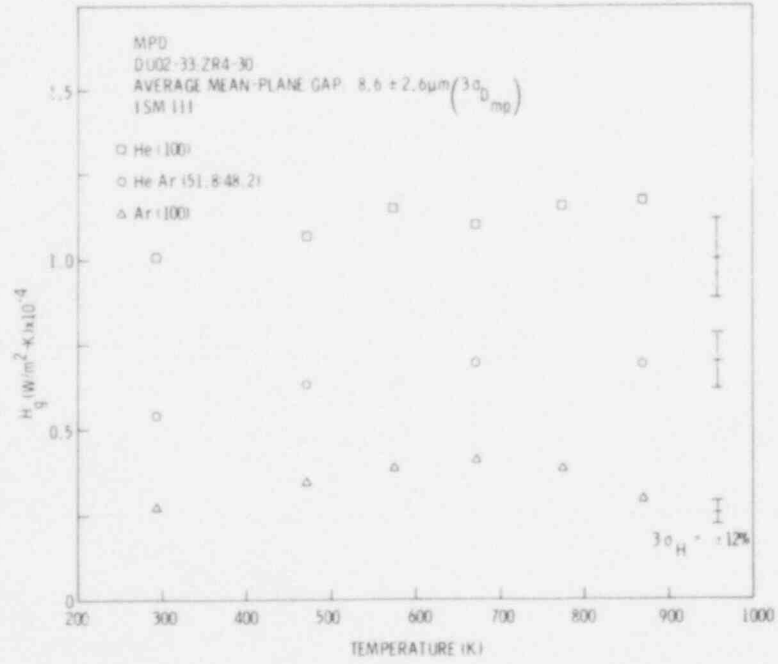

FIGURE 31. H_g Versus Temperature for ISM-III Surfaces (D_{mp} = 8.6 μm)

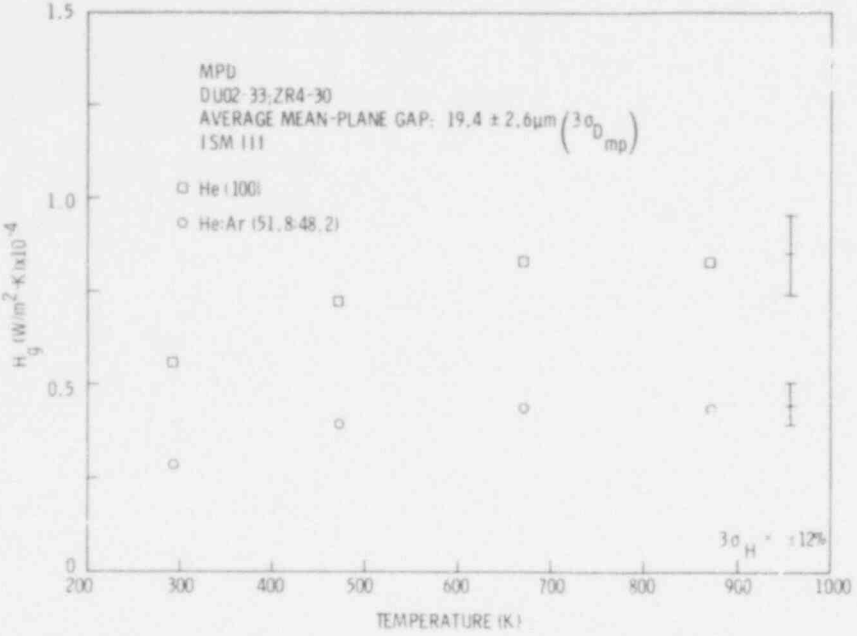

FIGURE 32. H_g Versus Temperature for ISM-II Surfaces (D_{mp} = 19.4 μm)

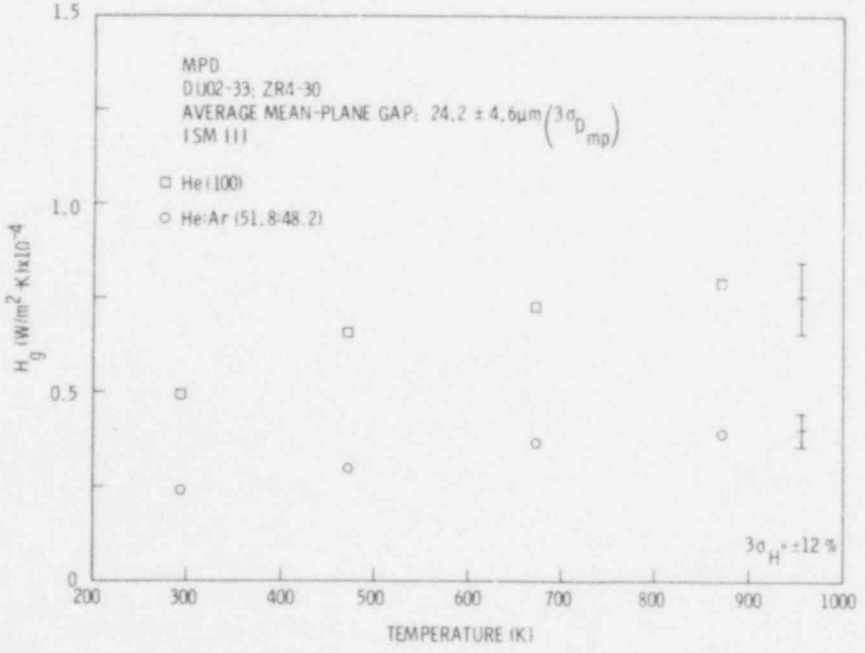

FIGURE 33. H_g Versus Temperature for ISM-II Surfaces (D_{mp} = 24.2 μm)

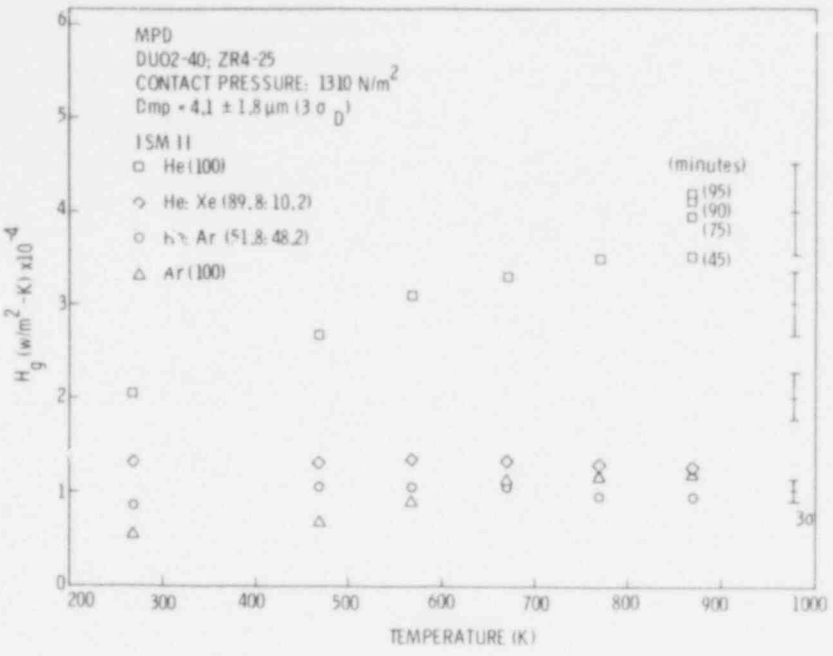

FIGURE 34. H_g Versus Temperature. ISM-II in Light Contact (D_{mp} = 4.1 µm)

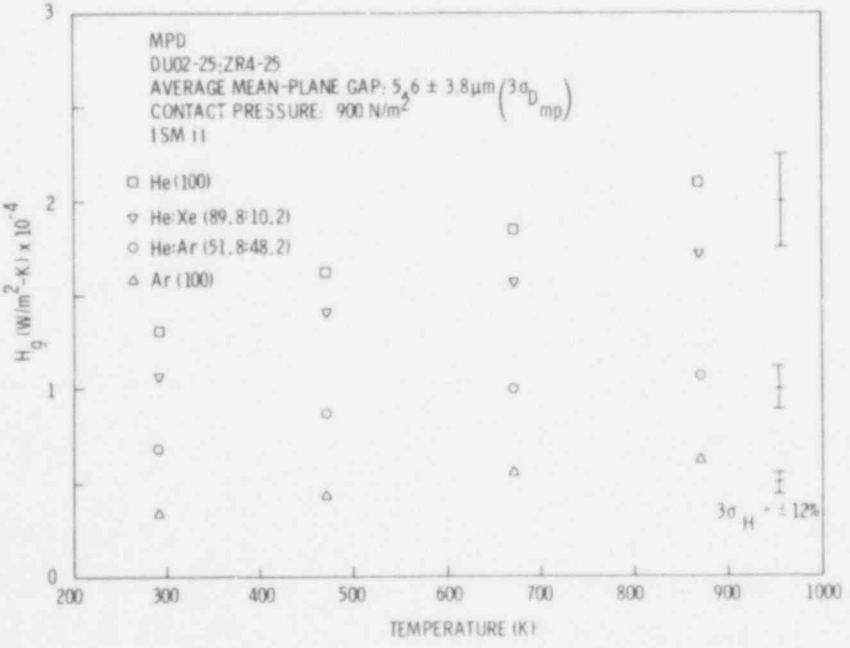

FIGURE 35. H_g Versus Temperature for ISM-II Surfaces in Light Contact (D_{mp} = 5.6 µm)

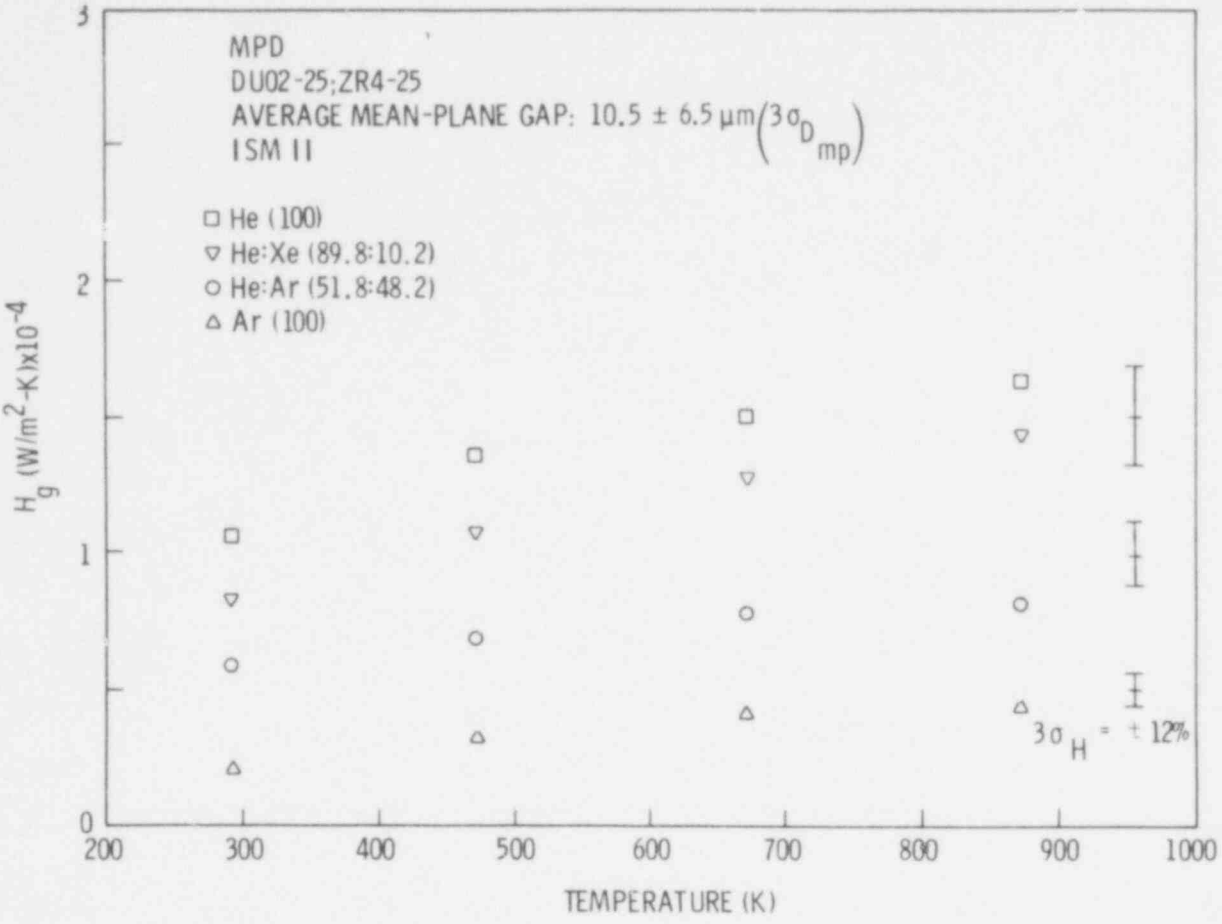

FIGURE 36. H_g Versus Temperature for ISM-II Surfaces (D_{mp} = 10.5 μm)

moderate dependence on T for the Helium (100 fill) gas is observed at D_{mp} values of 2.7 and 8.6 μm. However, at D_{mp} values of 19.4 and 24.2 μm a more pronounced dependence on T is observed. For fill gases of He:Ar (51.8:48.2) and Argon (100), a dependence on T is observed at all values of D_{mp}. In Figures 34 through 38 (ISM-II), H_g is seen to increase with increasing temperature for all values of D_{mp} ranging from 4.1 to 26.3 μm and for all gas compositions with the exception of the He:Xe (89.8:10.2) and He:Ar (51.8:48.2) gases at D_{mp} = 4.1 μm (sample pair:DUO_2-40; Zr4-25) as seen in Figure 34. When D_{mp} = 5.6 μm (sample pair: DUO_2-25; Zr4-25), Figure 35, this effect is not observed, nor is it observed in Figures 36 and 37 where D_{mp} = 10.5 μm (sample pair:DUO_2-25; Zr4-25) and D_{mp} = 11.5 μm (sample pair:DUO_2-40; Zr4-25), respectively. The behavior of H_g at

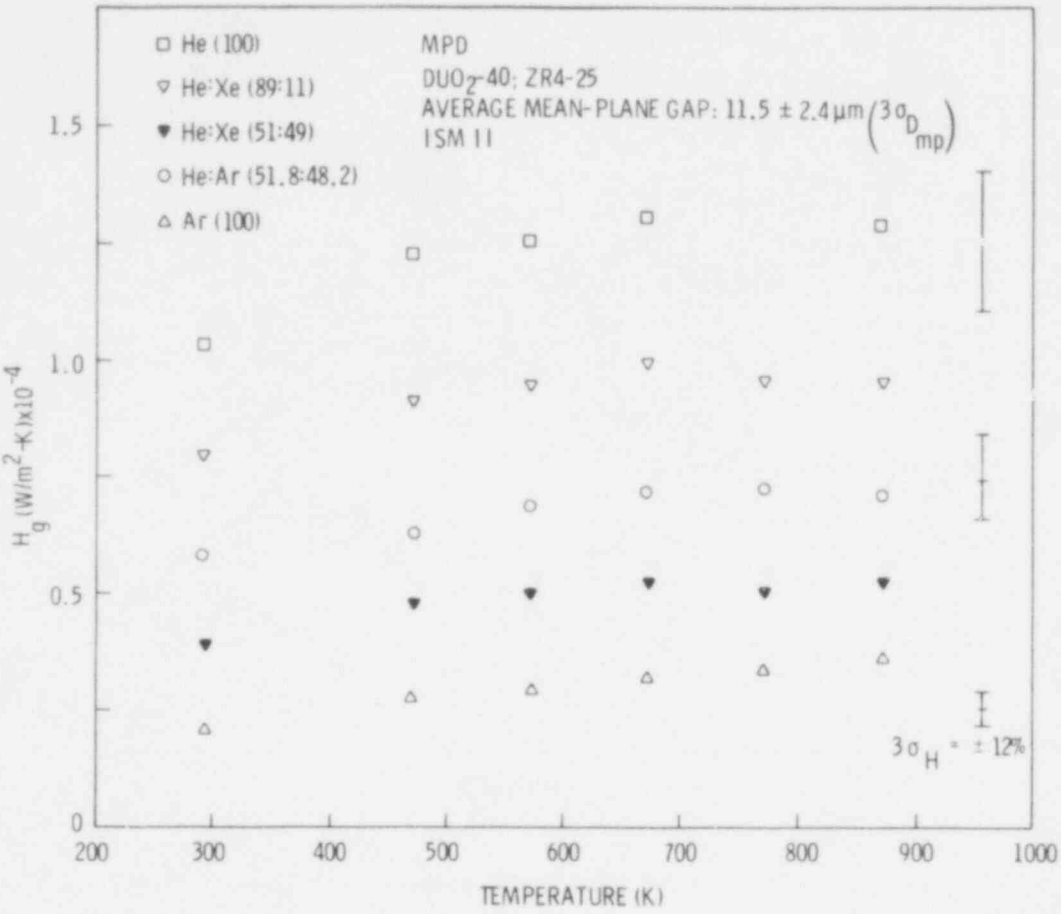

FIGURE 37. H_g Versus Temperature for ISM-II Surfaces (D_{mp} = 11.5 μm)

D_{mp} = 4.1 μm (Figure 34) is attributed to possible interactions among the factors of GC, D_{mp}, ISM, and I. A discussion of interactions is made in a later section. In Figure 39 (ISM-I), H_g is again seen to increase with increasing T.

In all cases, with its exceptions as noted earlier, H_g is found to increase with increasing temperature. The two-factor interaction between T and GC can be seen in Figures 30 to 39 by noting that the dependence of H_g with increasing T is defferent for the different gas compositions.

5.3.5 H_g Versus T for Various ISM

The dependence of H_g on T for various ISM sample pairs is shown in Figure 40 for a Helium (100) fill gas at 0.103 MPa. At D_{mp} values of 20.7 μm (ISM-I),

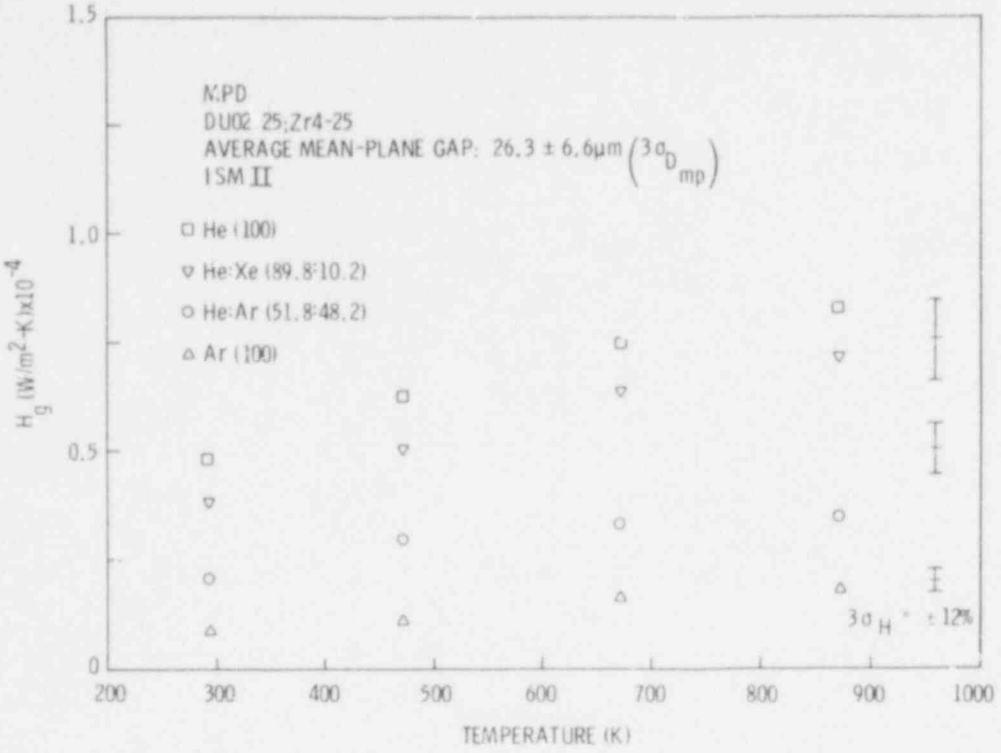

FIGURE 38. H_g Versus Temperature for ISM-II Surfaces Separated by a 26.3 μm Average Mean-Plane Gap

24.6 μm (ISM-III), and 26.3 μm (ISM-II), H_g is seen to exhibit the same dependence on T for all three surface morphologies. At smaller values of D_{mp}, 5.6 μm (ISM-II) and 2.7 μm (ISM-III), a change in the dependence of H_g on T is observed where the ISM-II sample pair exhibits a greater dependence on T than the ISM-III sample pair. A two-factor interaction between T and ISM is apparent at D_{mp} values less than approximately 10 μm; whereas, at larger values of D_{mp} no such interaction is apparent. A discussion of this observation is given in the next section.

5.3.6 Summary of H_g Results

In Sections 5.3.1 to 5.3.5, H_g is seen to depend on the variables of D_{mp}, T, ISM, and GC. In addition, two-factor interactions are observed among the variables and are summarized in Table 10.

The interaction between D_{mp} and T, ISM, and GC is an indication that the thermodynamic state of the system is not at equilibrium with respect to the

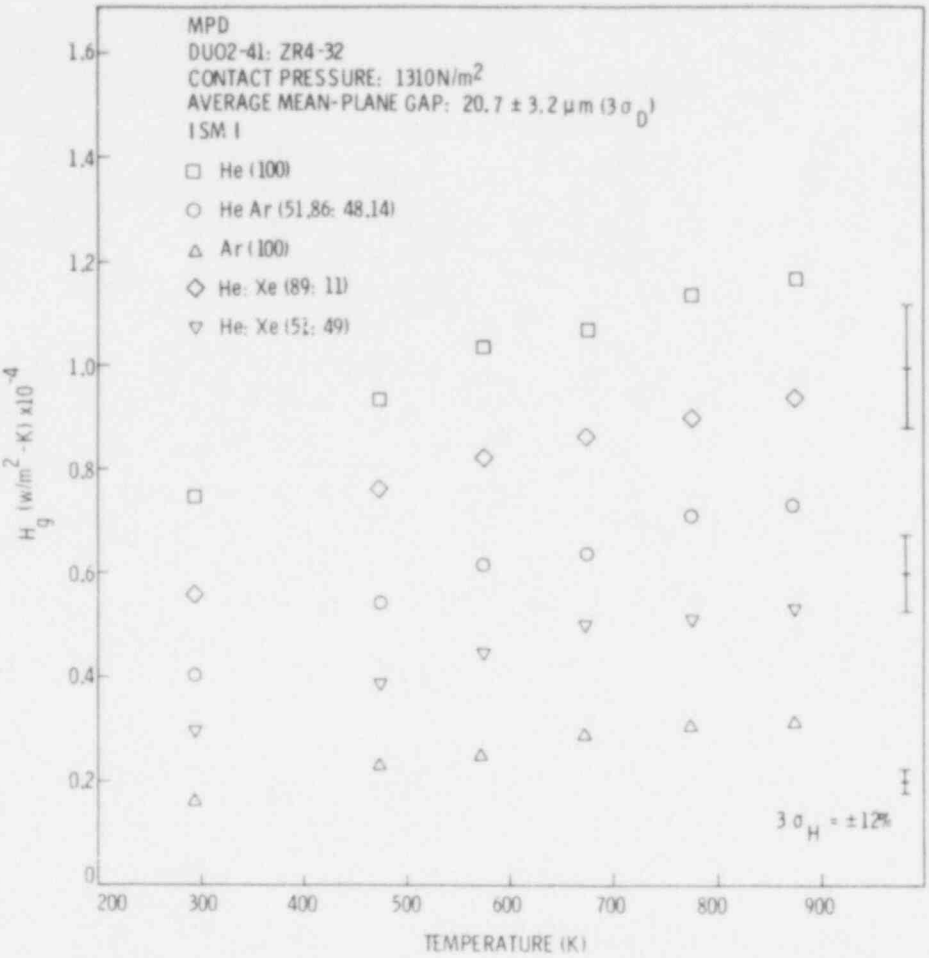

FIGURE 39. Hg Versus T for an ISM-I Sample Pair at D_{mp} = 20.7 μm

TABLE 10. Observed Two-Factor Interactions

Observed Two-Factor Interaction	Section	Comments
D_{mp} - ISM	5.3.1	Most pronounced below 20 μm and at higher temperatures
D_{mp} - GC	5.3.2	Only for Helium (100); D_{mp} <10 μm
D_{mp} - T	5.3.3	Only for Argon (100):D_{mp} <10 μm
T - GC	5.3.4	Only at D_{mp} >10 μm
T - ISM	5.3.5	Only at D_{mp} <10 μm

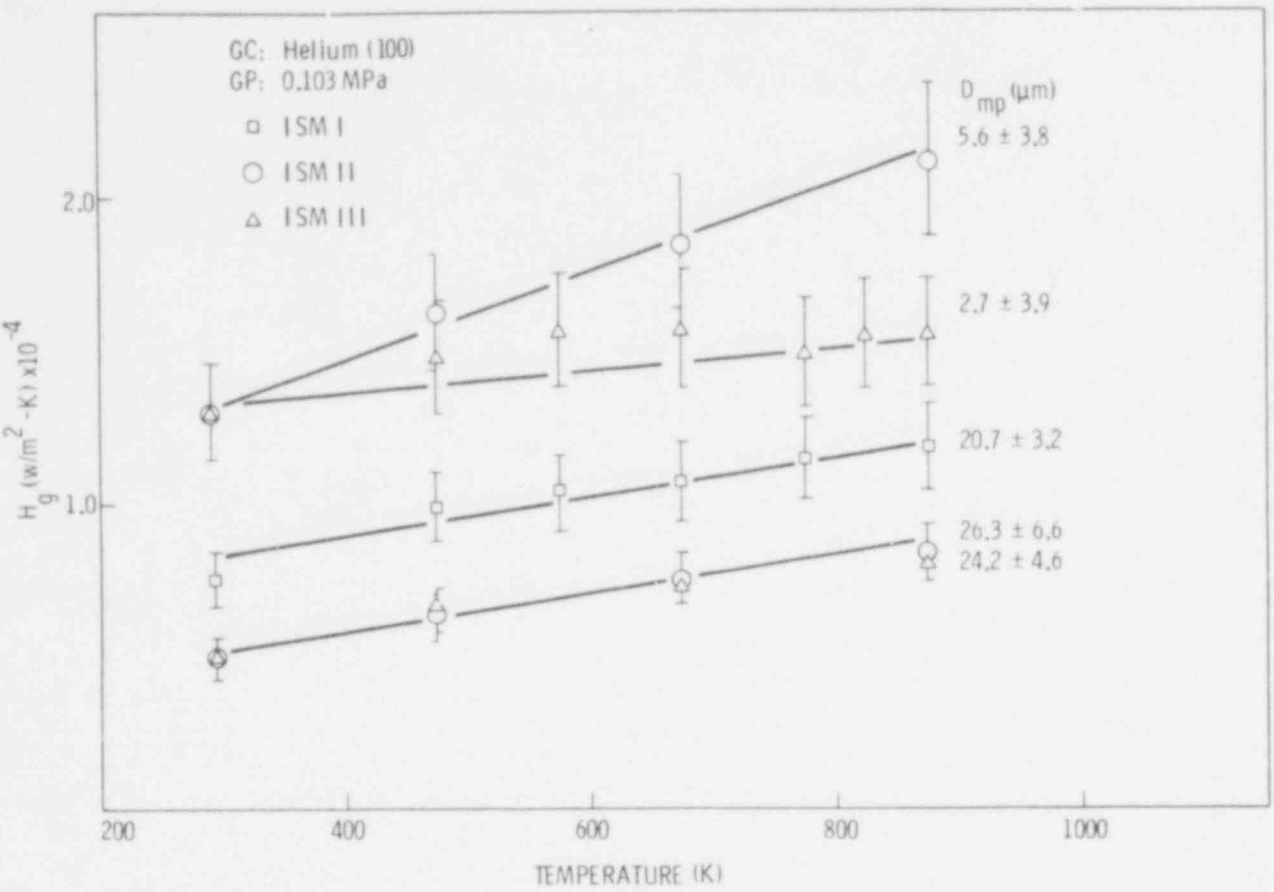

FIGURE 40. H_g Versus T for ISM-I, II, and III; GC = He (100); GP = 0.103 MPa; D_{mp} = 2.7, 5.6, 20.7, 24.2, and 26.3 μm

physical quantity D_{mp} at various conditions summarized in Table 10. This finding is to be expected in that the gap conductance is not directly related to the physical separation between surfaces in close proximity. When the temperature jump distance is approximately equal to or greater than the separation distance, the imperfect exchange of energy between the molecules and surface needs to be considered. The two-factor interaction between D_{mp} and ISM, GC, and T indicates that the surface roughness, gas composition, and temperature are factors that must be accounted for when relating the gap conductance to the physical separation distance. The manner in which the factors of ISM, GC, and T interact with D_{mp} are examined in the next section.

5.4 GAP CONDUCTANCE MODELS

5.4.1 Computation of Gap Conductance

The dependence of H_g on temperature, gas composition, and gap width at a fixed gas pressure can be calculated from the relationship

$$H_g = \frac{K_{gas}}{D_{mp} + g_1 + g_2} \qquad (16)$$

where D_{mp} is substituted for the "ideal" separation distance and g_1 and g_2 the respective TJD at the UO_2 and Zr4 surfaces. The temperature used in calculating Equation 16 can be taken as the mean temperature of the experiment since the MPD technique involves transient temperature measurement where the ΔT is no more than a few degrees Kelvin (Section 4.2); and, that in the MLD measurements H_g was found to be independent of ΔT gap over the range of 2 to 50 K (Appendix F). Furthermore, if the accomodation coefficients at the UO_2 and Zr4 surfaces are considered to be equivalent, Equation 16 may be approximated as

$$H_g \approx K_{gas}/(D_{mp} + 2g) \qquad (55)$$

where

$$g = g_1 = g_2$$

The quantity g can be determined from various TJD models (Table 2). The thermal conductivity of the gases and mixtures can be determined from the MATPRO relationships[56] for calculating the thermal conductivity of a monatomic gas and gas mixture. Accordingly, the thermal conductivity of the individual rare gases based on the correlated work of Gandi and Saxena[57] are:

$$K_{Helium} = 3.366 \times 10^{-3} \cdot T^{0.668}$$
$$K_{Argon} = 3.421 \times 10^{-4} \cdot T^{0.701} \qquad (56)$$
$$K_{Xenon} = 4.0288 \times 10^{-5} \cdot T^{0.872}$$

where T is in degrees Kelvin and K has units of W/m - K. The conductivity of a gas mixture is based on the work of Brokaw[58] and can be determined from:

$$K_{mix} = \sum_{i=1}^{n} \left(\frac{K_i}{1 + \sum_{\substack{j=1 \\ j \neq i}}^{n} \psi_{ij} \frac{x_j}{x_i}} \right)$$

where

$$\psi_{ij} = \phi_{ij} \left[1 + 2.41 \frac{(M_i - M_j)(M_i - 0.142M_j)}{(M_i + M_j)^2} \right] \qquad (57)$$

and

$$\phi_{ij} = \frac{\left[1 + \left(\frac{K_i}{K_j} \right)^{1/2} \left(\frac{M_i}{M_j} \right)^{1/4} \right]^2}{2^{3/2} \left(1 + \frac{M_i}{M_j} \right)^{1/2}}$$

and

n = number of components in mixture

m = molecules weight

x = mole fraction

K = thermal conductivity as given by Equation 56

The accommodation coefficient (a) used in the model calculation is based on results by Ullman et al.[59] who measured the accomodation coefficients of

Helium and Xenon on UO_2 and stainless steel. The data span the temperature range from 500 to 1000 K. The dependence of the accommodation coefficient with temperature can be expressed[10] as:

$$a_{He} = 0.425 - 2.3 \times 10^{-4} T \tag{58}$$

$$a_{Xe} = 0.749 - 2.5 \times 10^{-4} T \tag{59}$$

where T is the average interface temperature (Kelvin). Calculation of a_{mix} and a_i for other gases (i.e., Argon) are computed using a linear extrapolation between a_{He} and a_{Xe} based on molecular weight. The effective molecular weight of the gas mixture is:

$$\sum_i f_i M_i \tag{60}$$

where f_i is the mole fraction of species i. Justification for this procedure is given in Reference 10.

The free molecular heat conduction as given by Equation 12 can be conveniently expressed as

$$H_g = \epsilon \cdot GP \cdot \left(\frac{273}{T}\right)^{1/2} \left(\frac{a}{2-a}\right) \tag{61}$$

where

$$\epsilon = 18.746 \left(\frac{2R}{\pi M\ 273}\right)^{1/2} \left(\frac{\gamma + 1}{\gamma - 1}\right)$$

is expressed in units of $W \cdot m^{-2}\ deg^{-1}\ Pa^{-1}$. Values of ϵ for Helium and Argon have been reported[42] as 2.19 and 0.693, respectively.

The value of the accommodation coefficient for Helium and Argon are determined according to Equations 58 through 60.

5.4.2 Comparison of Predicted to Experimental H_g Results

Based on the mathematical relationships and assumptions described in the previous section, the gap conductance using various TJD models can be calculated at conditions of temperature, gas composition, gas pressure, and gas separation consistent with the measurement of H_g under the experimental conditions in this study (Appendix D and E). In the following sections graphical comparison of predicted H_g to experimental results is made along with appropriate discussion on the following: effect of the definition used for the physical gap separation; comparison of the TJD models, changing fill gas composition, influence of temperature, effect of the absolute value of the accommodation coefficient.

5.4.2.1 Effect of the Definition Used for the Physical Gap Separation

In Section 3.2.2 the definition of D_{pp} (peak to peak asperity separation); D_{mp} (average mean plane separation) and D_{vv} (average valley to valley separation) were introduced. As D_{pp} is the minimum physical separation distance between two surfaces, the maximum physical separation between two surfaces can be represented by D_{vv}. The quantities D_{pp} and D_{vv} are defined to be

$$D_{vv} = D_{mp} + 2.5\ (CLA_1 + CLA_2) \qquad (62)$$

$$D_{pp} = D_{mp} - 2.5\ (CLA_1 + CLA_2) \qquad (63)$$

where CLA_1 and CLA_2 are the center line average of the UO_2 and Zr4 surfaces and D_{mp} as defined by Equation 47. From inspection of Equations 62, 63, and 47, it is apparent that $D_{vv} > D_{mp} > D_{pp}$ when nonideal surface geometric conditions are present. The extent to which the definition used for the separation distance affects the predicted value of H_g can be shown by plotting the predicted H_g (i.e., Equation 55, GAPCON-THERMAL II TJD MODEL) deviation from experimental results $[(H_g\ (model) - H_g)/H_g]$ versus H_g. These calculations are shown in Figures 41, 42, and 43 for the gap separation as defined by D_{vv}, D_{pp}, and D_{mp}, respectively. In these plots, no delination is made among the various interfacial surface morphologies. In Figure 41, the use of D_{vv} in Equation 55 is found to result in a conservative estimate for the gap conductance as seen by

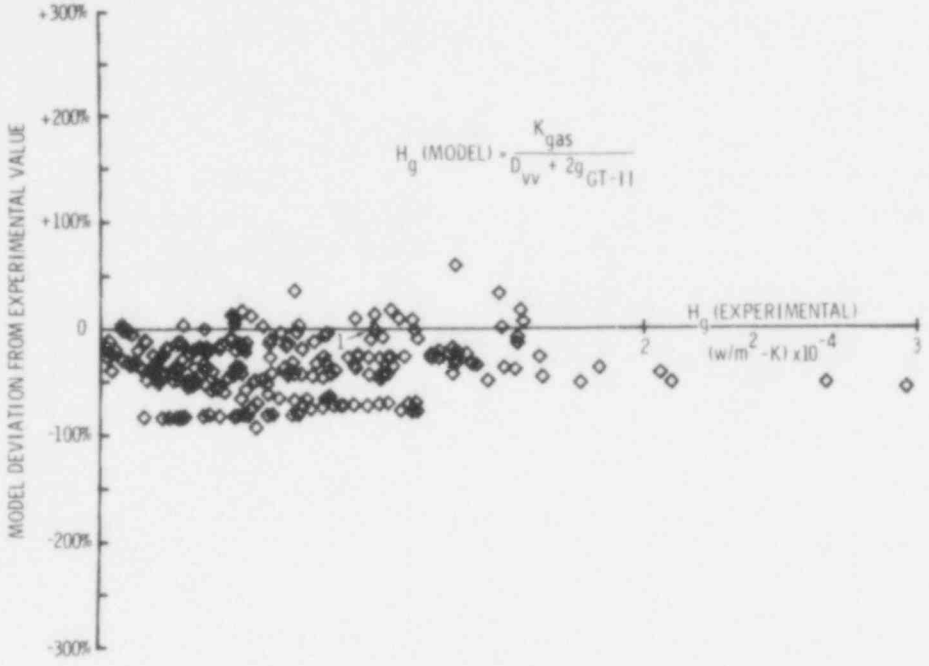

FIGURE 41. H_g Model Deviation from Experimental Value Versus H_g (expt) Using D_{vv} and g (GAPCON-THERMAL II). All MPD AND MLD data are plotted.

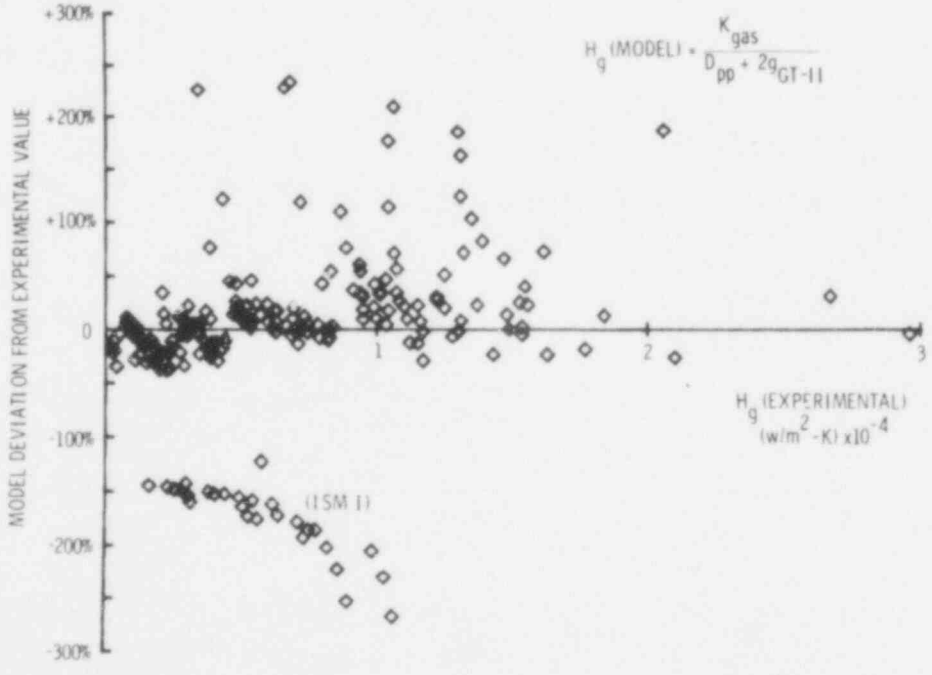

FIGURE 42. H_g Model Deviation from Experimental Value Versus H_g (expt) Using D_{pp} and g (GAPCON-THERMAL II). All MPD and MLD data are plotted.

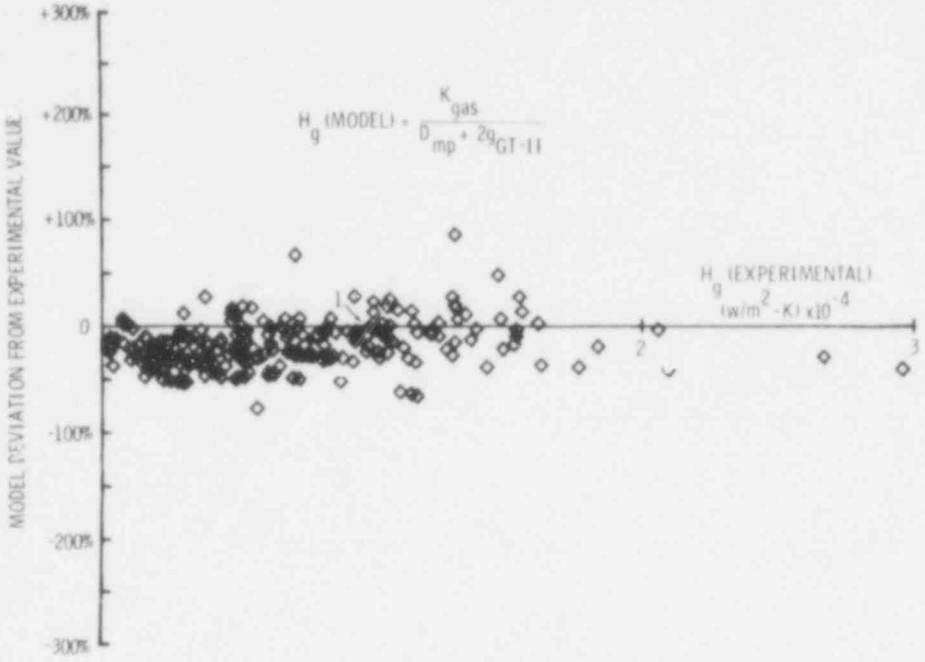

FIGURE 43. H_g Model Deviation from Experimental Value Versus H_g (expt) Using D_{mp} and g (GAPCON-THERMAL II). All MPD and MLD data are plotted.

the clustering of calculated results below the line of zero deviation. The definition of D_{vv} implies that the solid surface asperities have the same thermal properties as the fill gas; whereas, the definition D_{pp} implies that the gas molecules contained within the valley regions below the plane defined by the three highest peaks on each surface possess the same thermal property characteristics as the solid. In Figure 42, the use of D_{pp} in Equation 55 results in a positive (nonconservative) departure from the line of zero deviation. The results for the ISM-I (coarse) surface are seen to cluster at negative values. This occurs as a result of the predicted H_g acquiring a negative value since D_{pp} will be negative when $2.5\ (CLA_1 + CLA_2) > D_{mp}$ and $|D_{pp}| > 2_g$. The ISM-I results demonstrate the inappropriateness of using D_{pp} as a definition of the gap separation distance.

The definition of D_{mp} implies that the gas contained in the region below the mean plane of separation has the same thermal properties of the solid; whereas, the solid contained in the region above the mean plane of separation has the same thermal properties of the gas. The results of these

calculations are shown in Figure 43 and are seen to cluster below the line of zero deviation. Insertion of D_{mp} into Equation 55 results in a conservative estimate for H_g. For example, of the 230 datum points shown in Figure 43, only ≈40 of the model calculated points are seen to lie above the line of zero deviation. The assumptions of D_{mp} = d(ideal), $g_1 = g_2$, and that the calculated accommodation coefficient is the same as the experimental value are considered responsible for the conservative results shown in Figure 43.

5.4.2.2 Comparison of TJD Models

The general influence of the TJD model in predicting the gap conductance according to Equation 55 is shown in Figures 44, 45, and 46 for the Kennard, Lloyd, and GAPCON-THERMAL II TJD models, respectively. The quantity D_{mp} is used in these calculations. The general features revealed in Figures 44 through 46 show that the manner in which the accommodation coefficient is expressed in the TJD model will exert an influence on the predicted H_g. In Figure 44, the accommodation coefficient in the Kennard TJD model is expressed as (2-a)/a; whereas, in Figure 45, the accommodation coefficient in the Lloyd TJD model is

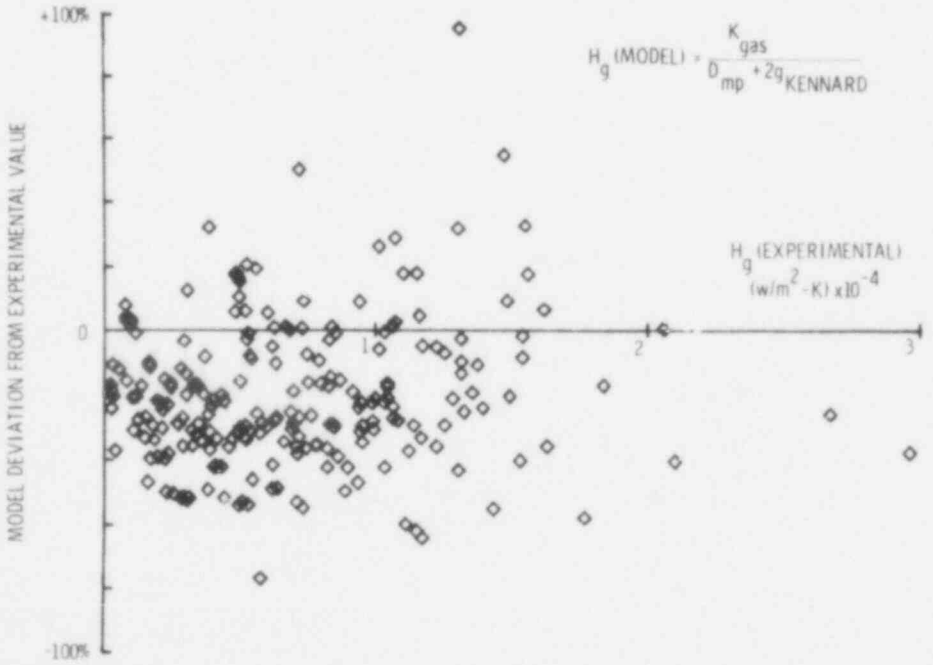

FIGURE 44. H_g Model Deviation from Experimental Value Versus H_g (expt) Using D_{mp} and g (Kennard). All MPD and MLD data are plotted.

592 110

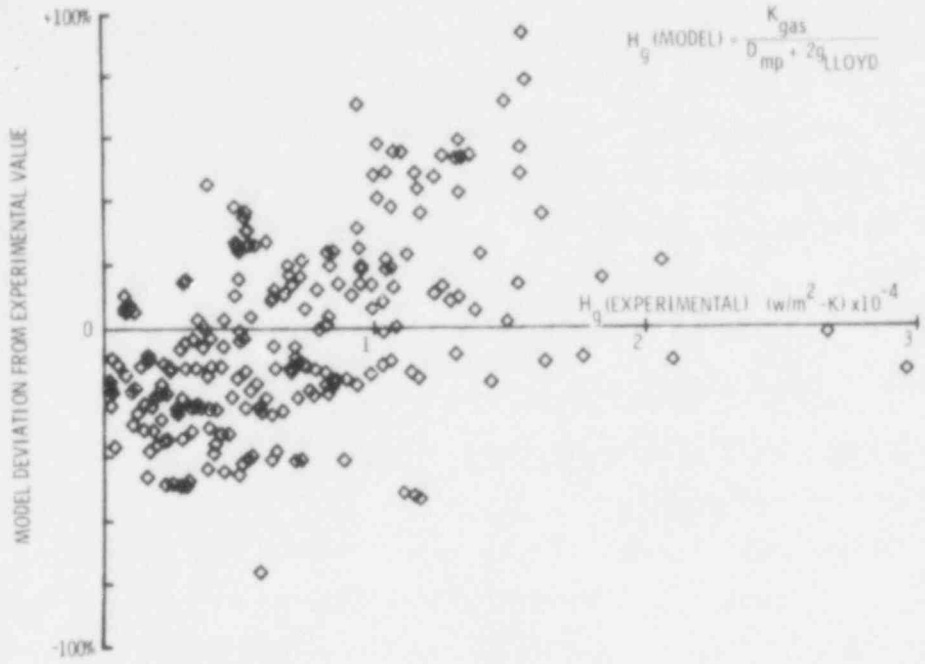

FIGURE 45. Hg Model Deviation from Experimental Value Versus Hg (expt) Using D_{mp} and g (LLOYD). All MPD and MLD data are plotted.

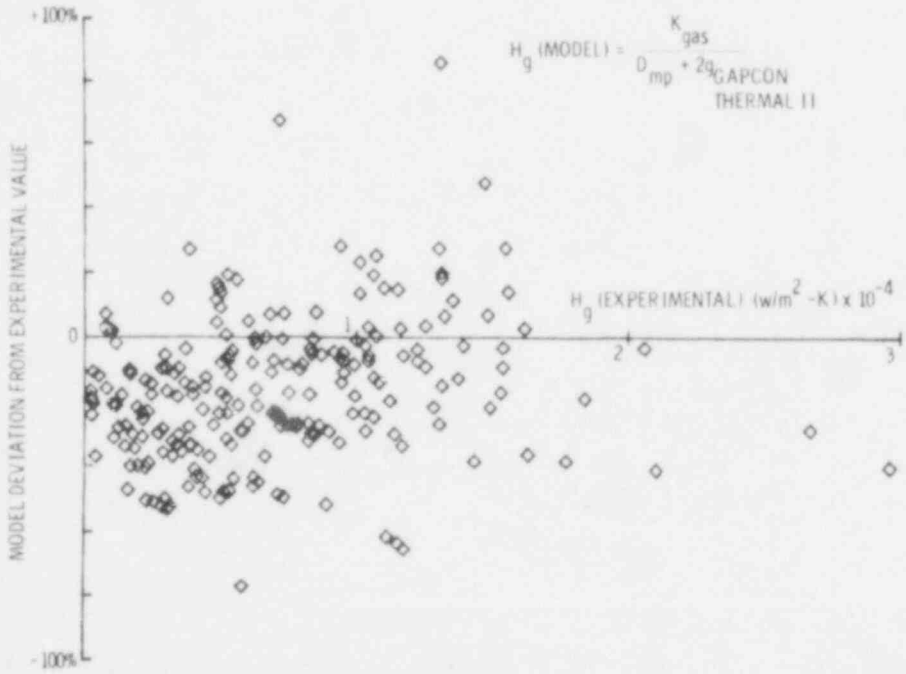

FIGURE 46. Hg Model Deviation from Experimental Value Versus Hg (expt) Using D_{mp} and g (GAPCON-THERMAL II). All MPD and MLD data are plotted.

expressed as (1/a). The predicted gap conductance using the Lloyd TJD model shows a skew to more positive (i.e., nonconservative) values at higher H_g values. However, as shown in Figure 46, this effect is corrected in the GAPCON-THERMAL II TJD Model by inclusion of an empirical correction factor of 1.8 [i.e., g(GAPCON-THERMAL II) = 1.8 g(Lloyd)]. In addition, the factor 1.8 in the GAPCON THERMAL II Model results in a more conservative estimate of H_g than the Kennard model as comparison of Figures 44 and 46 will reveal.

5.4.2.3 Changing Fill Gas Composition

The influence of the fill gas composition enters the expression for gap conductance, Equation 55, in two ways: first, as the thermal conductivity of the gas and second, through the expression for the accommodation coefficient. The dependence of the predicted H_g on K_{gas} will be the same for all TJD models but will differ according to the manner in which the accommodation coefficient is expressed. Comparison of H_g to Equation 55 using the GAPCON-THERMAL II, Lloyd, and Kennard TJD models is shown in Figure 47 where H_g is plotted versus

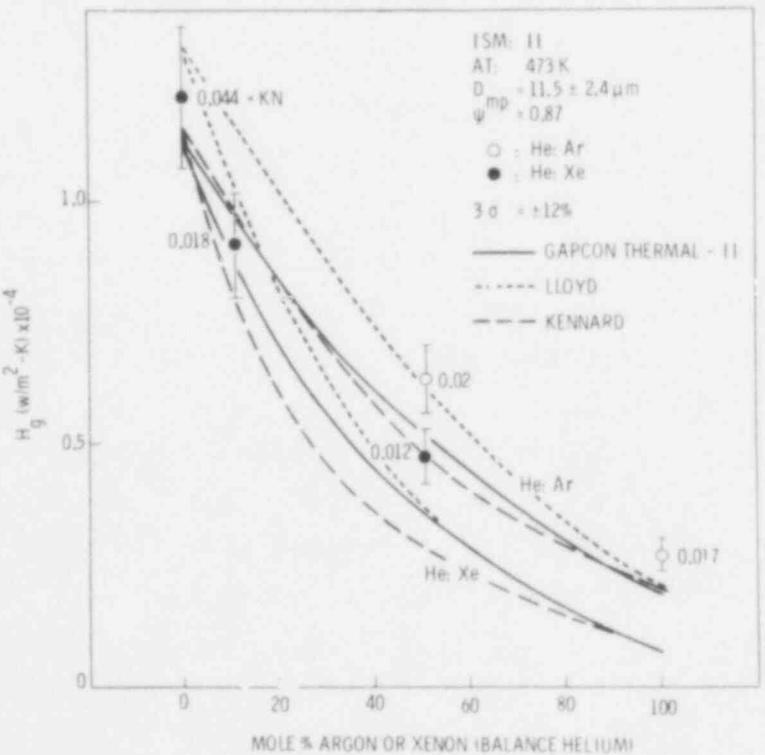

FIGURE 47. H_g Versus Gas Composition (Knudsen numbers appear adjacent to the data points).

mole % Argon (or Xenon). The MPD ISM-II H_g data shown was obtained at a value of D_{mp} = 11.5 μm at 473 K. For all TJD models Equation 55 predicts a nonlinear decrease in the gap conductance with either increasing mole % of Argon or Xenon. Agreement of Equation 55 to the H_g results is seen for only the Helium 100% and He:Xe (89:11) gas mixtures. At concentrations greater than 50 mole % Argon (and Xenon), Equation 55 is found to underpredict H_g by ≈30% at Argon 100%. These differences may be accounted for if the computed value of the accommodation coefficient were less than the actual accommodation coefficient.

5.4.2.4 Influence of Temperature

The influence of temperature on the predicted H_g is accounted for in Equation 55 in three ways: first, as a square root dependence in the expression for the TJD (Equation 8); second, in terms of the expression for the thermal conductivity of the gas (Equation 56); and third, in the calculation of the accommodation coefficient (Equations 58 through 60).

In Figures 48 and 49, H_g versus temperature is plotted for the MPD ISM-II sample pair at D_{mp} = 11.5 and 26.5 μm, respectively, along with the Lloyd, Kennard, Loyalka, and GAPCON-THERMAL II TJD models. Symbols for various fill gas compositions are also given in the legends.

At T = 673 K, the value of 2g will range from 6.56 to 11.82 μm [Helium (100)]; 2.36 to 6.46 μm [He:Xe (51:49)]; and 1.97 to 3.56 μm [Argon (100)] for Lloyd, Kennard, Loyalka, and GAPCON-THERMAL II TJD models. Since $D_{mp} \approx 2g$, the differences among the TJD models are apparent as inspection of Figures 48 and 49 shows. In general, the TJD models predict an increase in the gap conductance with increasing temperature with a broad maximum at elevated temperatures, shifting to higher temperatures with a decrease in the thermal conductivity of the fill gas. However, the temperature dependence predicted by Equation 55 for the various TJD models is not substantiated by the H_g results. For instance, the H_g dependence on temperature for Helium (100) in Figure 48 is different than predicted by Equation 55 using any of the TJD models. For gases of lower thermal conductivity [i.e., He:Xe (51:49)], the H_g dependence is similar to that predicted by Equation 55.

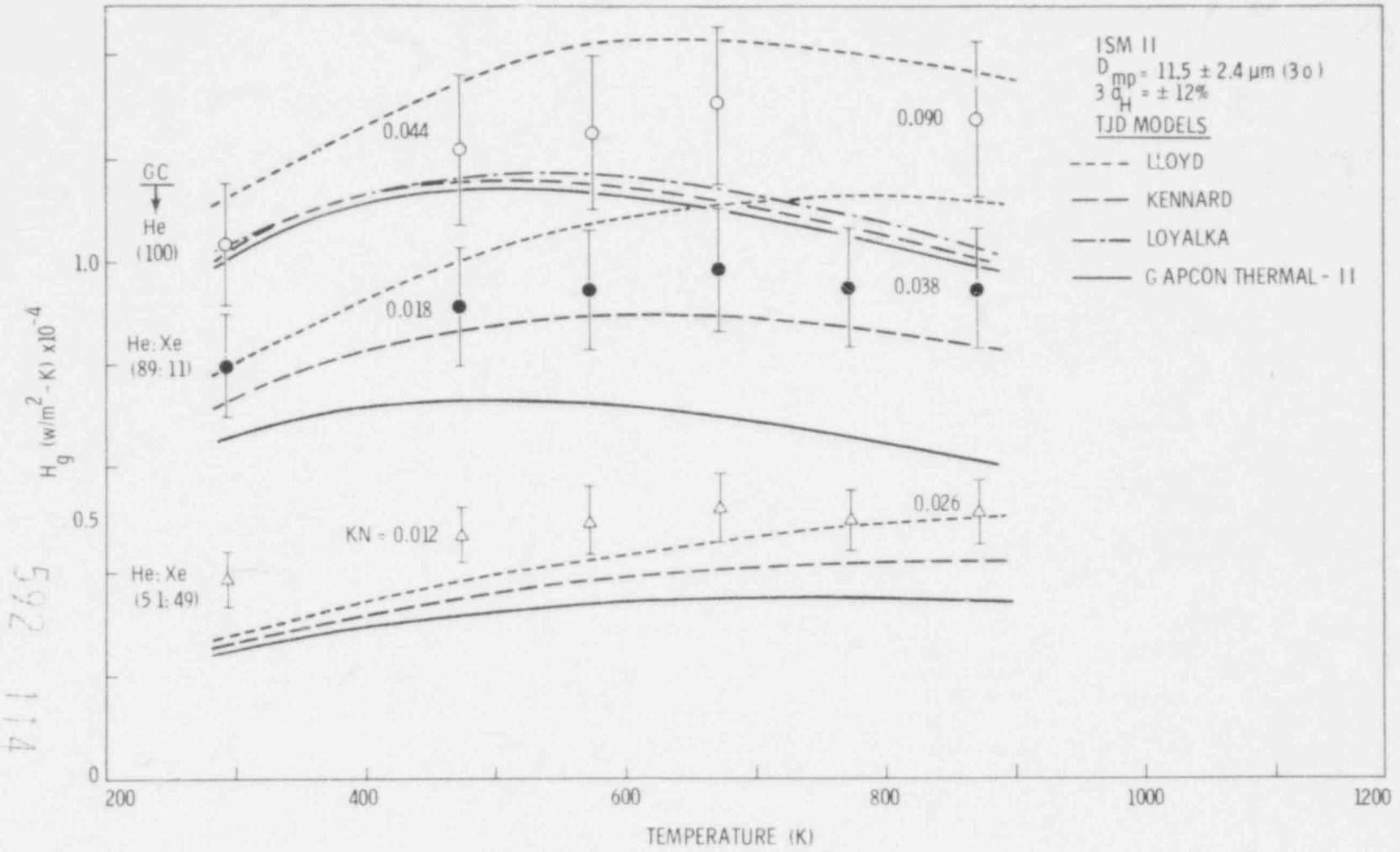

FIGURE 48. H_g Versus Temperature for ISM-II Specimens With D_{mp} = 11.5 μm

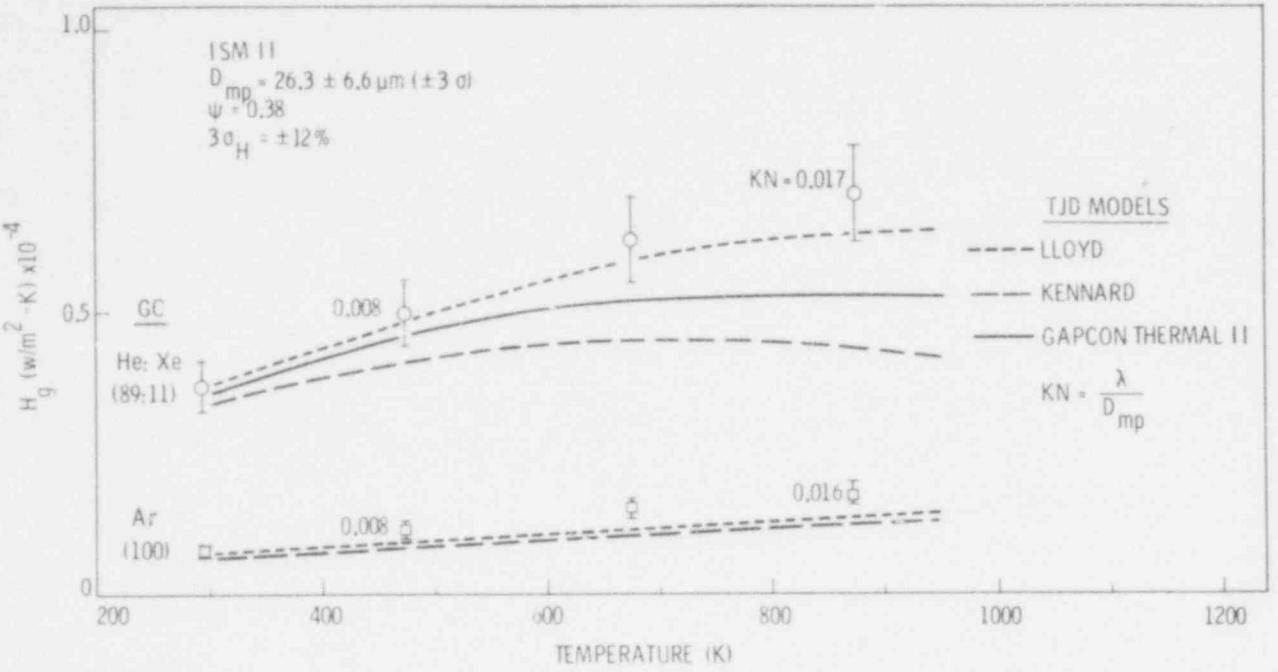

FIGURE 49. H_g Versus Temperature for ISM-II Specimens with D_{mp} = 26.3 μm Under He:Xe and Argon Fill Gas

5.4.2.5 Absolute Value of the Accommodation Coefficient

Equation 55 will be sensitive to the value of 2g whenever $D_{mp} \lesssim 2g$ and the value of $g_1 + g_2$ will increase directly as the square root of T. However, the increase in g with temperature is initially compensated for by the absolute value of the accommodation coefficient at lower temperatures. As temperature is increased the compensating effect of the accommodation coefficient will depend on its temperature dependence (e.g., Equations 59 and 60). In an analogous manner the experimental results are expected to vary depending on the conditions of experiment and the temperature dependence of the accommodation coefficient.

The effect of the accommodation coefficient on the absolute value of the gap conductance can be illustrated if it is assumed that for a given value of H_g the corresponding value of D_{mp} is unique. Using Equation 55 and the Kennard or Lloyd TJD model, a model dependent accommodation coefficient can be determined using the H_g results at D_{mp} = 19.4 and 26.3 μm for the respective ISM-II and III sample pairs.

The accommodation coefficient determined in this manner for a Helium fill gas is plotted versus temperature in Figure 50. A similar calculation can also be made on the basis of a free molecular model (Equation 61) using values of H_g at D_{mp} = 5.7 and 2.7 μm. Also shown is the accommodation coefficient reported by Ullman et al.[59] and approximated[10] by Equation 59.

The experimental trend in the model calculated a_{He} is found to increase with increasing surface roughness (i.e., ISM-III to ISM-II) and to increase with increasing temperature for all models. The absolute values of a_{He} at 293 K were also found to be in reasonable agreement with a value of 0.3 obtained by

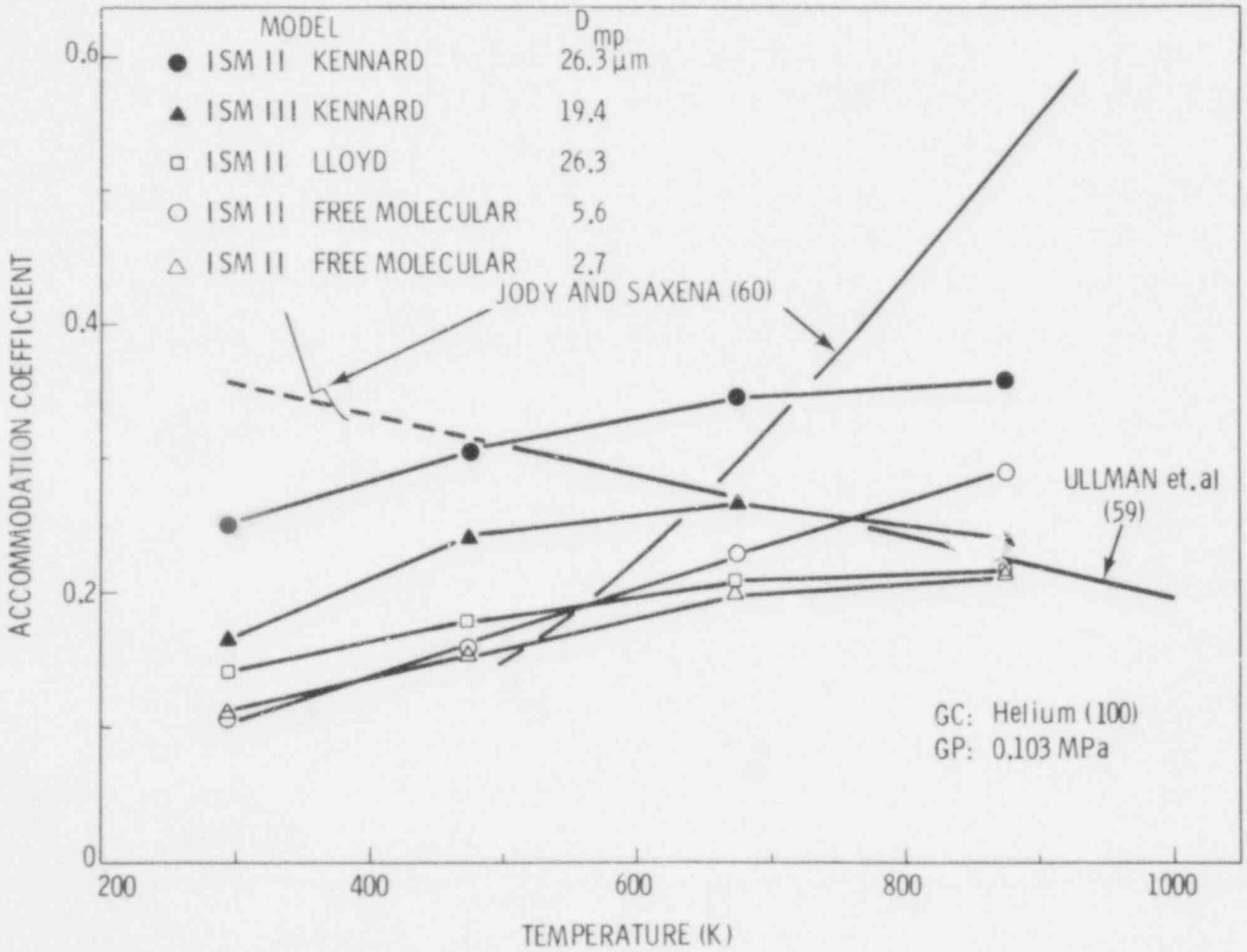

FIGURE 50. Accommodation Coefficient Versus Temperature for Helium Gas

Loyalka for a_{He} on a Zr4 sphere. The results by Ullman et al., however, indicate a decrease in a_{He} with increasing temperature. This difference in the temperature dependence of a_{He} is attributable to the fact that the Ullman et al. measurements were performed under vacuum conditions, while in this study measurements were performed near atmospheric pressure.

Also shown in Figure 50 are the reported results by Jody and Saxena[60] for a_{He} on partially gas-covered platinum in the temperature range 300 to 1400 K as calculated from results obtained using a constant power method. In these measurements the variation in a_{He} was attributed to changing surface conditions as the accommodation coefficient on pure metals is a very weak function of temperature. Desorpsion of weakly held adsorbate particles and rearrangement or migration of adsorbate particles within the surface layer can cause a pronounced temperature dependence. The rapid increase in a_{He}, seen in the range 500 to 775 K, was attributed to diffusion of gas adsorbates from the bulk to the surface and/or oxidation of the platinum surface in the temperature range 700 to 1400 K. Thus, if an appreciation for the differences in specimen surface condition, atmospheric conditions and assumptions made in the use of Equation 55, an account for the differences between H_g and the predicted gas conductance can be made through this absolute value of the accommodation coefficient above, i.e., adjustment of the calculated value of the accommodation coefficient in Equation 55 can bring the calculated H_g values into agreement with experiment.

5.4.2.6 Convergence to the Free Molecular Limit

In Section 3.2.5 a discussion is given on the manner in which the gap conductance may be expected to behave when the separation distance between two surfaces is reduced to zero (e.g., Figure 4). Three expressions for the gap conductance are examined (i.e., Equation 7, 14, and 15) to which consideration of the behavior of the gap conductance is made in respect to the value of the "free molecular" accommodation coefficient being equal to, less than or greater than the value of the accommodation coefficient when a continuum regime is present. The purpose of this section is to examine the H_g results to determine if the accommodation coefficient and/or free molecular gap conductance, H_{FM}, will exert a first order effect on H_g.

592 117

Examination of H_g in relation to convergence to the free molecular limit can be made by plotting the reciprocal of H_g versus D_{mp} as shown in Figures 51 and 52 for Helium and Argon fill gases respectively at 473 K. The gap conductance expression as given by Equation 55 is represented in these figures as a straight line of slope $1/K_{gas}$. The intercept at $D_{mp} = 0$ will depend on the TJD model, i.e., Kennard, Lloyd, GAPCON-THERMAL II. Equation 55 reduces to the free molecular expression (Equation 61) exactly for the Kennard TJD model and is shown by the horizontal line in Figures 51 and 52.

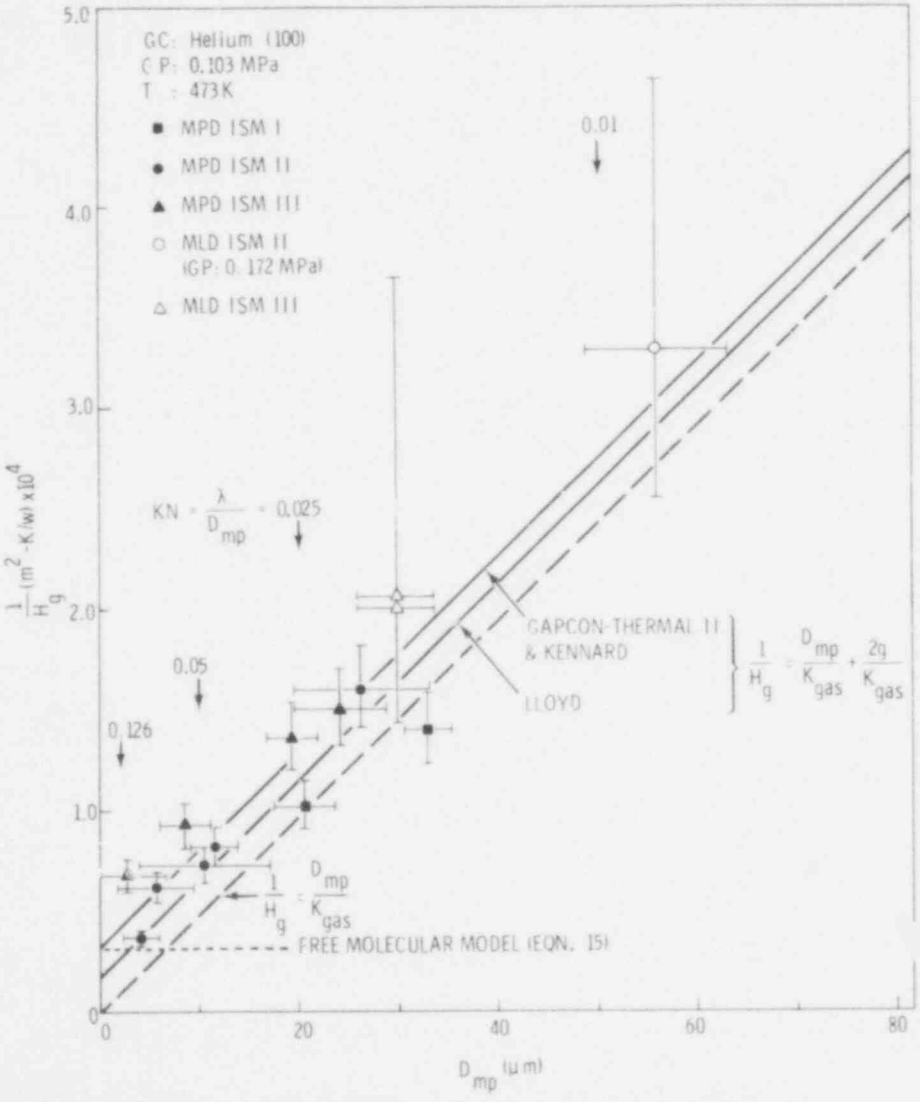

FIGURE 51. $1/H_g$ Versus D_{mp} for a Helium Fill Gas at 473 K. Lines represent calculations based on various models for the TJD.

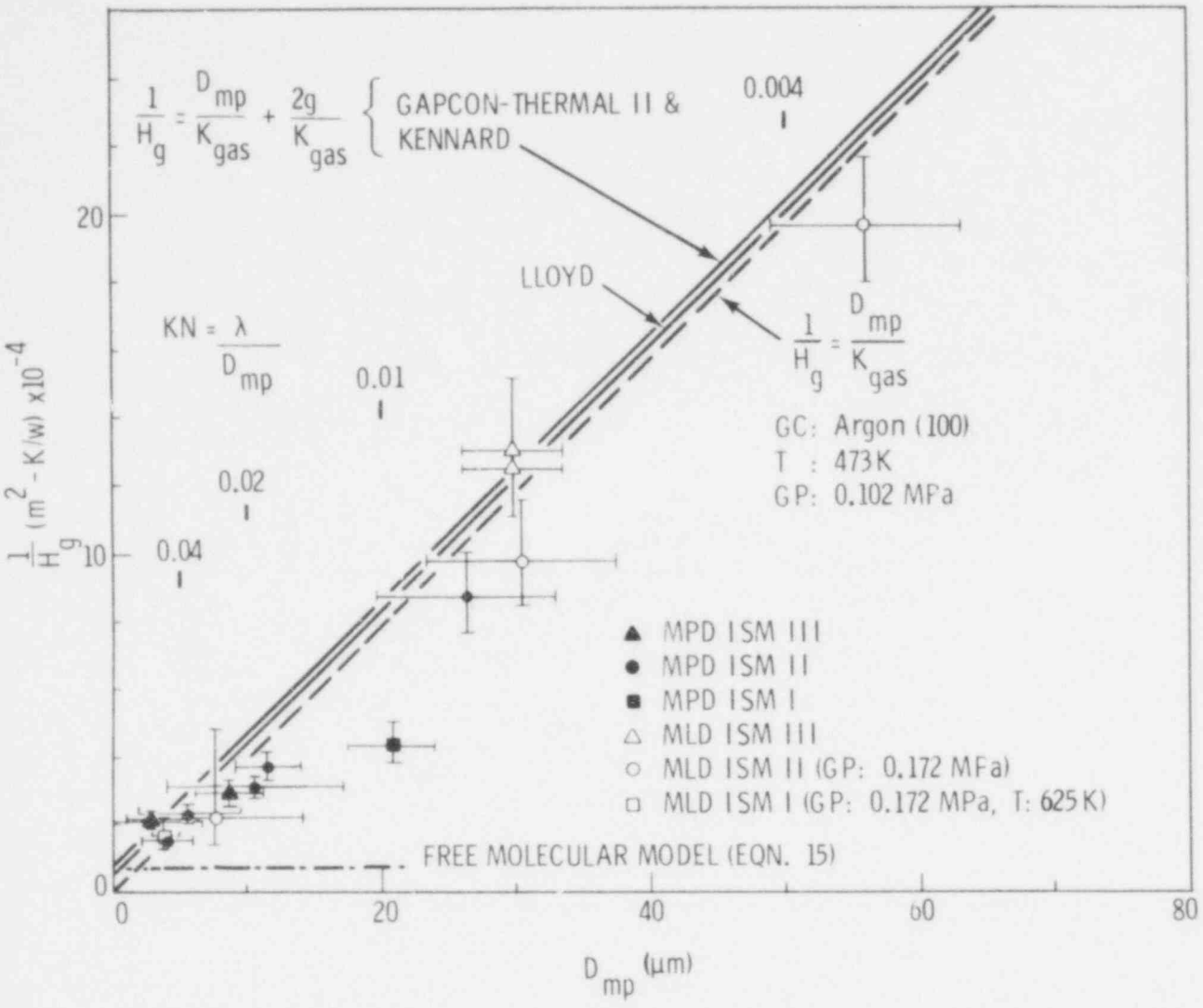

FIGURE 52. $1/H_g$ Versus D_{mp} for Argon Fill Gas at 473 K. Lines represent calculations based on various models for TJD.

The ISM-II H_g results shown in Figures 51 and 52 do not indicate the presence of a significant departure from the slope of $1/K_{gas}$ within the 3σ experimental H_g and D_{mp} uncertainties. The ISM-III H_g results for Helium (Figure 51) indicate that departure to lower H_g values with increasing Knudsen number (i.e., KN > 0.05) may be real. However, the effect appears to be overpowered by the increasing surface roughness (ISM-II) or increasing Knudsen number (Figure 52 Argon fill gas). It appears, therefore, that the manner in which convergence to the free molecular limit is achieved is a second order effect at least when the Knudsen number is less than 0.1.

The ISM-I results shown in Figures 51 and 52 are seen to approach or exceed the limiting case where $H_g = K_{gas}/D_{mp}$. The fact that the ISM-I H_g result at $D_{mp} = 33.0$ μm falls below the limiting case is a strong indication that the use of the one-dimensional distance parameter D_{mp} is not sufficient to uniquely describe the multi-dimensional gap geometry of two nonideal surfaces in close proximity. The reader will recall that both H_g and D_{mp} are independently determined experimental quantities. It is clear from inspection of Figure 2 and the accompanying discussion that the problem of defining a "nonideal gap" is complex. The experimentally determined value of D_{mp} (Section 4.2.4) is based on the definition of the averaged mean plane of separation (Section 3.2.1). If the definition of D_{mp} were relaxed and the experimental value of the physical separation distance taken as D_a, for example (e.g., Equation 35 where γ_1 and γ_2 are set equal to zero), this would result in a lowering of the ISM-I, II, and III D_{mp} values by 19.3, 3.2, and 0.29 μm, respectively (Table F-7). For example, in Figures 51 and 52, the ISM-I H_g results plotted at $D_{mp} = 20.7$ μm would now be shifted to the left to a value of $D_a = 1.4$ μm.

5.5 CONTACT CONDUCTANCE RESULTS

A scoping study was performed using the MLD apparatus to investigate the effect of contact pressure (0 to 14.68 MN/m^2), surface roughness (ISM-I and II) and surface error of form on H_c. Information was also acquired under Argon atmospheric conditions (0.172 MPa) to measure the total gap conductance H_T. This information was obtained for the purpose of comparison to the reported results of Ross and Stoute,[29] Dean,[28] and Rapier;[30] and was acquired in a manner which would bridge the differences in previously reported contact pressures.

The results of this scoping study are shown in Figure 53 where H_c (or H_T) is plotted versus applied contact pressure at an approximate interface temperature of 680 K. The results for Block 0 (ISM-II), Block 1 (ISM-II), and Block 2 (ISM-I) are shown with conditions of experiment appropriate to the datum symbols given in the legend. Additional information or conditions of experiment (e.g., ΔT_{gap}) or corrections to the data (radial heat loss) are located in Appendix E. The error bars about each datum represent the 3σ uncertainties associated with

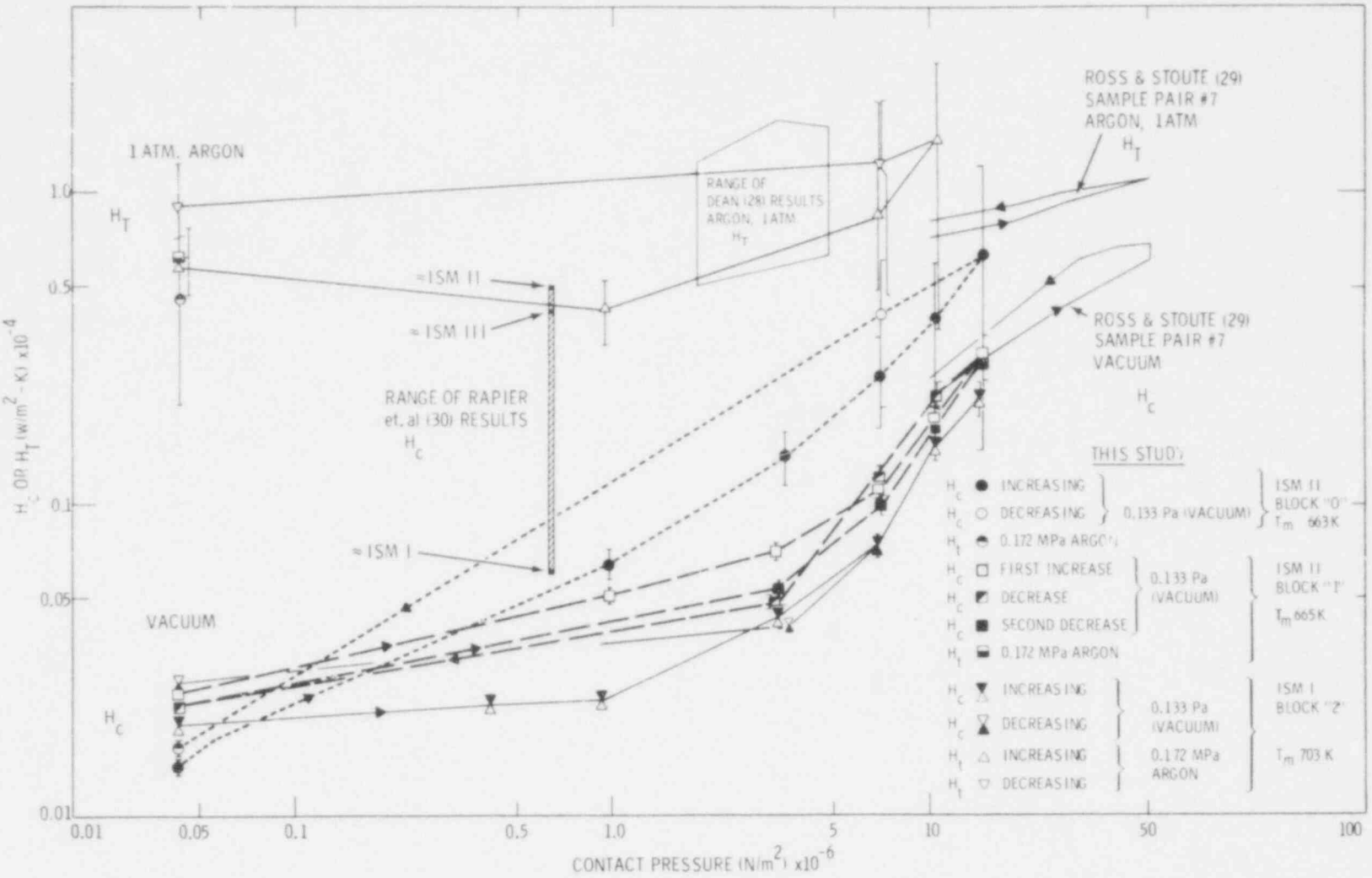

FIGURE 53. H_C or H_T Versus Applied Contact Pressure and Showing Results Reported by Dean,[28] Ross and Stoute,[29] and Rapier[30]

each determination (Apperdix C). The H_c results for all blocks show an increase in H_c with increasing pressure from 0.043 to 14.68 MN/m^2. The value of H_c at 0.043 MN/m^2 ranges between 0.01 x 10^4 to 0.025 x 10^4 W/m^2-K; whereas, at 14.68 MN/m^2 the results range from 0.21 x 10^4 to 0.63 W/m^2-K. The introduction of Argon gas improves the interfacial conductance most significantly at lower contact pressures but this contribution decreases with increasing contact pressure.

The effect of surface roughness on H_c can be seen by comparison of the Block 1 (ISM-II) and Block 2 (ISM-I) test results. The ISM-I and ISM-II sample pairs exhibit a similar dependence on applied pressure. The Block 0 (ISM-II) and Block 1 (ISM-II) results on the other hand show a different dependence on applied pressure. The Block 0 results are in general higher than the Block 1 results and exhibit a greater dependence on applied pressure. This is attributed to the difference in "error of form" between these sample pairs as inspection of Figures F-9 and F-10 (Appendix F) shows, rather than the surface roughness.

Comparison with the reported results by Ross and Stoute, Dean, and Rapier is made in Figure 53. The H_T results are in agreement with the H_T results reported by Dean at 1 atmosphere of Argon. On the other hand, the H_c ISM-I results at lower contact pressures are below that reported by Rapier (whose value of H_c approximately corresponding to the surface roughness of the ISM-I sample pair is indicated) by about a factor of 2 and by about a factor of 5 for the ISM-II sample pair. The reason for these differences is attributed to differences in mating error of form which will determine the number of initial interfacial contact points and hence the initial value of H_c. At high contact pressures the Block 1, 2, and 3 results are in apparent agreement with the reported results by Ross and Stoute (sample pair No. 7).

5.6 CONTACT CONDUCTANCE MODELS

As outlined in Section 3.3, two main approaches have been taken in developing models to predict H_c as a function of applied contact pressure. The first

approach emphasizes the surface roughness and elastic/plastic deformation of micro-asperities and results in a general expression of the form

$$H_c = C \cdot K_m \cdot F(L_i \text{ and/or } R_i) \cdot (PA/H)^2 \frac{w}{m^2 - K} \qquad (17)$$

where the various terms have been defined previously in Section 3.3 and listed in convenient form for various models in Table 3.

Values of K_m are computed using the thermophysical property relationships listed in Appendix A. The temperature at which Equation 17 is evaluated is taken to be the approximate mean temperature at the interface region of the experiment (e.g., 660 K). The values of L_i and R_i (i.e., CLA_i) for the various MLD specimens are derived from the Talysurf-4 profilometer traces and are listed in Table 11.

The Meyer's hardness is taken to be the value reported by Peggs[62] for UO_2 and Zr2.

The second theoretical approach developed by Dundars and Panek[49] emphasizes the viewpoint that the contact resistance is dependent primarily on the surface waviness and surface deformation. The contact conductance is given by the reciprocal of Equation 19

$$\frac{1}{H_c} = CR = \frac{-2\ell}{\pi} \left(\frac{1}{K_1} + \frac{1}{K_2}\right) \log \left[\sin \left(\frac{1}{2} c\right)\right] \qquad (19)$$

TABLE 11. Relevant MLD Specimen Surface Parameters

Block	ISM	CLA		Peak to Peak		Initial	Half Wave-length	Amplitude
		DUO_2	ZR-4	L_1	L_2	D_{mp}	UO_2	UO_2
0	II	1.6	0.4	70	30	7.6	3000	20
1	II	1.6	0.4	70	30	3.6	3000	12
2	I	14.4	4.5	160	110	21.8	--	--

This expression was evaluated for the MLD Block 0 (ISM-II) Block 1 (ISM-II) sample pairs assuming that the mean interface temperature of the experiment was 660 K. The amplitude of the sinusoidal gap (b) and the half wavelength (ℓ) are given in Table 11 and are approximated from the surface error of forms given in Appendix F. Poisson's ratio for UO_2 and Zr4 are taken to be 0.35[63] and 0.25,[64] respectively. The uniaxial compliances in plane strain (S_1 and S_2) are taken to be 4.903E-12 and 1.219E-7 m^2/N for UO[63] and Zr4,[64] respectively.

Comparison of the Centinkale and Fishenden, Dean, Fenech and Rohsenow, Mikic/Todreas, Rapier, Ross and Stoute, and Shlykov contact conductance models to the Block 2 (ISM-I) results is shown in Figure 54. The Mikic/Todreas model is seen to be in the best agreement with the Block 2 (ISM-I) results, especially in the range from 1 to 7 MN/m^2. This model, however, underestimates H_c at lower contact pressures 0.04 to 1 MN/m^2 and higher contact pressures 7 to 14.68 MN/m^2. The Ross and Stoute model underpredicts H_c; whereas, the other models are seen to overestimate H_c, at contact pressures above $\sim$1 $MN|m^2$.

In Figure 55 comparison of the models shown in Figure 54 (which the addition of the Dundurs and Panek model) is made to the Block 0 (ISM-II) and Block 1 (ISM-II) results. Within the 3σ H_g experimental uncertainties the Mikic/Todreas model is in excellent agreement with the Block 0 results. However, the same model overestimates the Block 1 results. The Dundurs and Panek model is in agreement with the Block 0 results over the range of contact pressures from 2 to 14.68 MN/m^2, but overestimates the results at lower contact pressures (0.043 to 2 MN/m^2). The Dundurs and Panek model is not seen to be in agreement with the Block 1 results. However, it does predict correctly a decrease in contact conductance with decreasing surface error of form amplitude. In addition, the model predicts a crossover in the Block 0 and 1 results at 3.8 MN/m^2 whereas the data shows a crossover between 0.1 and 0.25 MN/m^2. The Ross and Stoute model overpredicts the Block 0 and 1 results; whereas, the remaining models are seen to overestimate H_c at contact pressures above $\sim$0.4 MN/m^2.

Assuming that the contact pressure is proportional to the applied pressure raised to exponent (i.e., $H_c \propto PA^N$), determination of this exponent from the H_c

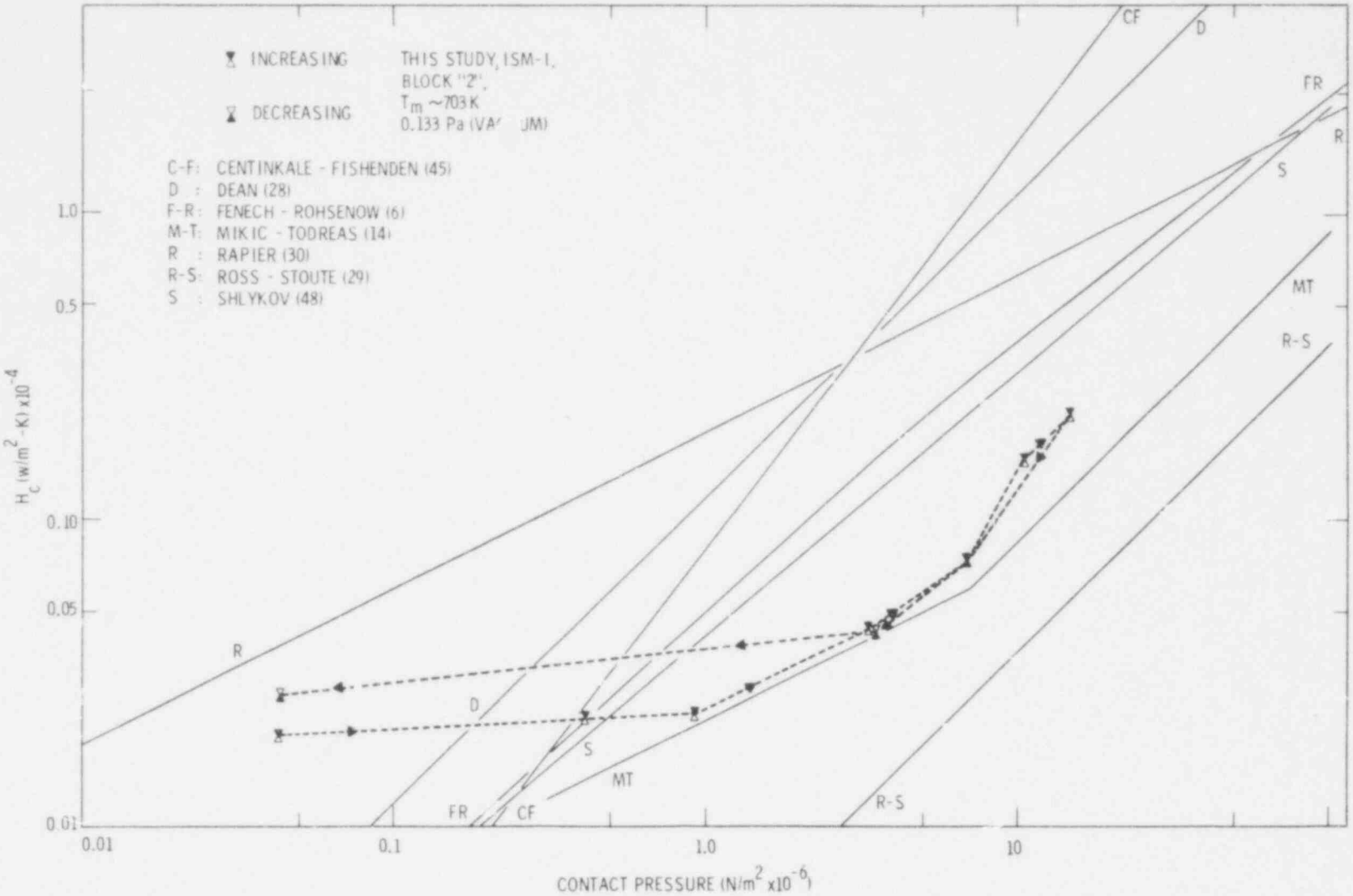

FIGURE 54. H_C Block 2 (ISM I) Results Versus Applied Contact Pressure. The various models are also shown.

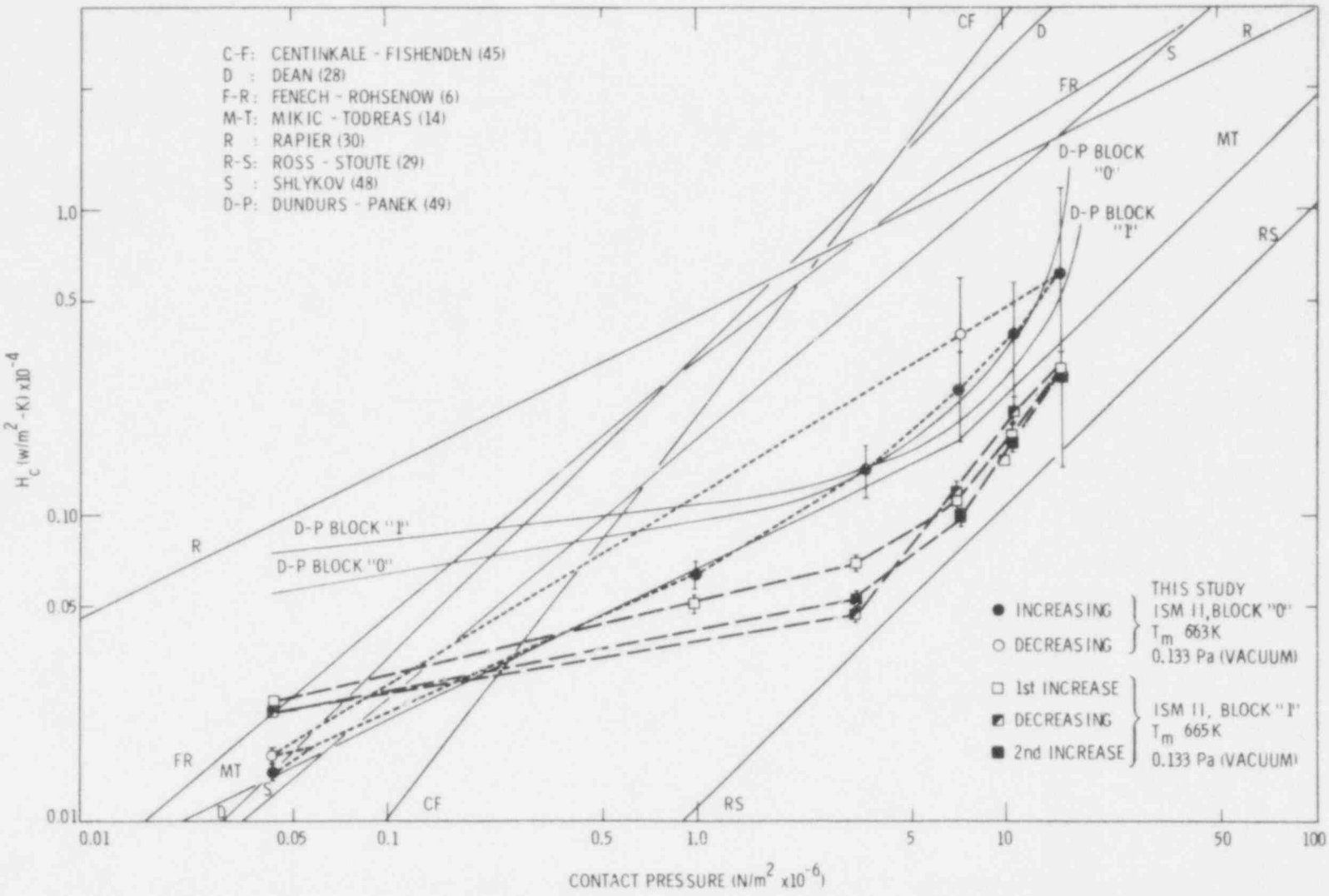

FIGURE 55. Hc Block 0 and 1 (ISM-II) Versus Applied Contact Pressure. The various models are also shown.

results can be performed and comparison to the exponent used in various models made. This comparison is shown in Figure 56 where N is plotted versus applied contact pressure. The experimental value of N for the different Blocks is determined from the change in slope between various H_c determinations on the first increase in pressure. The value of N use in the models listed in Figure 56 is shown as lines appropriate to the models listed in the legend. The value of N is seen to increase as a function of increasing pressure for all the sample pairs measured. For Block 0 (ISM-II), N exhibits a straight line dependence increasing with increasing pressure from ∿0.5 at lower pressures to ∿1.35 at 12.7 MN/m^2. However, the value of N calculated from the Block 1 and 2 results does not show a similar dependence of N with increasing pressure. The

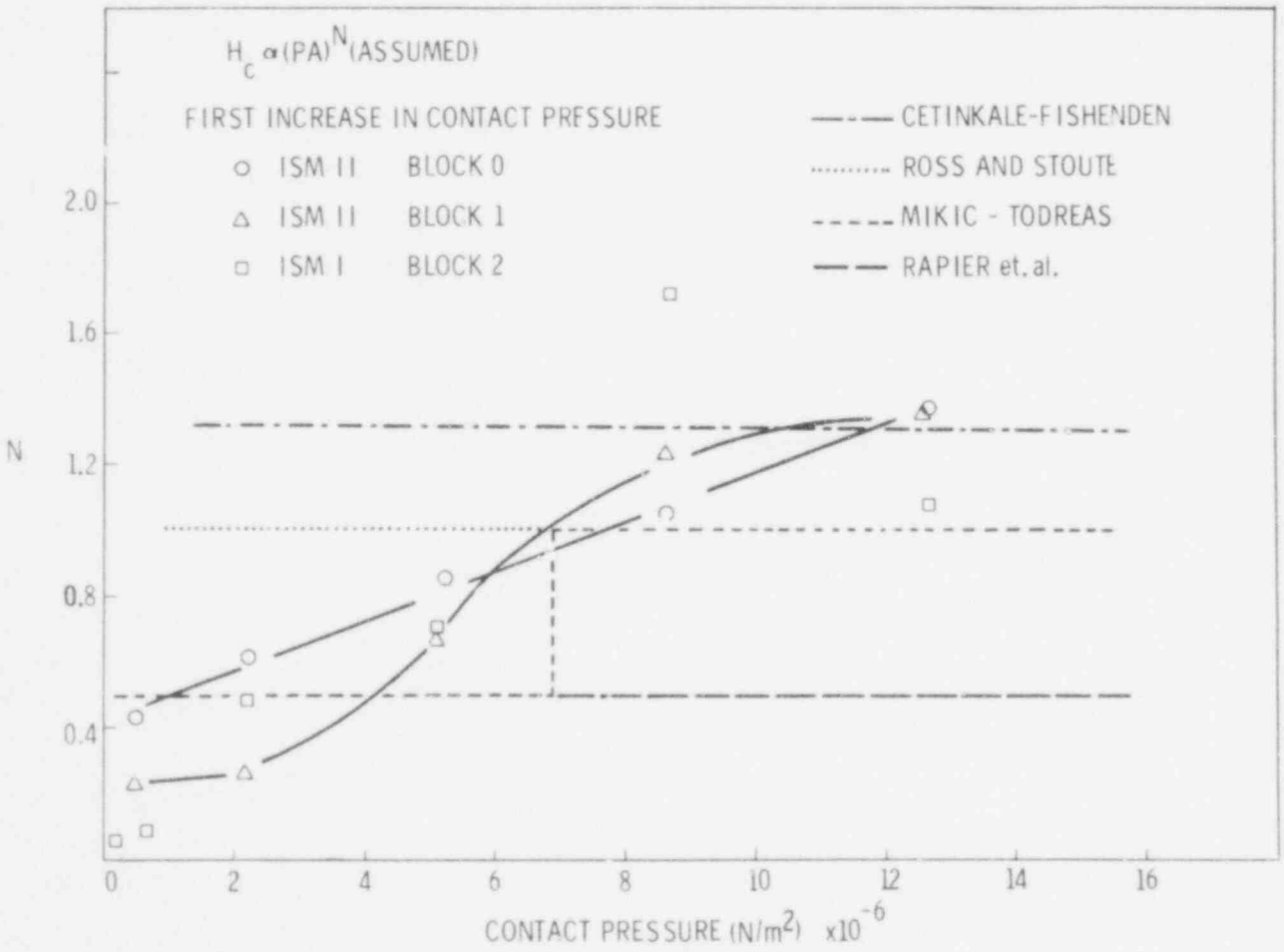

FIGURE 56. N Versus the Applied Contact Pressure. The experimental results are compared to the models.

592 127

results indicate that N does not have a unique value; but rather will vary with pressure and surface conditions. Thus, the assumption that N has a fixed value is incorrect. However, this point has been considered in the Mikic/Todreas model and the approximation of the value of N = 0.5 between 0 and 6.9 MN/m^2 and N = 1.0 at pressures above 6.9 MN/m^2 is seen to be a good first approximation to the experimental results of this study. The agreement between the Mikic/Todreas model and H_c as noted earlier in Figures 54 and 55 is attributed to the aforementioned approximation.

The results of this study suggest that the surface waviness may exert a first order effect[21] on determining the magnitude and pressure dependence of the thermal contact conductance. The controversy over the covert exponent N in the relationship between the applied pressure and the hardness of the cladding [i.e., $(PA/H)^N$] would cease to exist if the hypothesis put forth in the Dundurs and Panek model is found to be correct since the $(PA/H)^N$ relationship does not enter into their model. Additional experiments are needed however to substantiate or refute the necessity for inclusion of the surface wavelength in any model describing the contact conductance between UO_2 and Zr4.

6.0 CONCLUSIONS AND RECOMMENDATIONS

6.1 EXPERIMENTAL TECHNIQUES

6.1.1 MPD Measurement Technique

The MPD measurement technique and apparatus described is capable of measuring the thermal gap conductance between two surfaces in close proximity under a variety of experimental conditions. Data has been acquired at temperatures ranging from 293 to 873 K for various fill gases, surface morphologies, and separation distances. The mathematical description of experiment satisfaction of the mathematical model boundary conditions was achieved by minimizing potential sources of indeterminate experimental error, i.e, radial heat losses, thermal shunting through the spacers, and laser induced buckling of samples. Sources of determinate error were minimized through the use of well-characterized specimen thermal and physical property data and the use of experimental and computer techniques to enhance the temperature transient signal to noise ratio. The MPD technique cannot be used to measure H_c primarily due to the difficulty in applying suitable contact pressures to the specimens.

The MPD technique can be used to measure H_g at gas pressures above atmospheric by the use of an autoclave. However, attention must be given to the elimination of heat losses at the outer specimen surfaces that would occur from gaseous convection within the autoclave. Enclosure of the specimens within a quartz or sapphire container maintained in an isothermal temperature zone would reduce the potential of this effect.

6.1.2 MLD Measurement Technique

The MLD measurement technique and apparatus is capable of measuring H_g, H_c, and H_T. The double guarding system is effective in maintaining an outer radial temperature gradient which minimizes the corrections to the data arising from radial heat losses. In addition to the requirement of accurate thermal and physical property data on the specimens used, care is needed in thermocouple selection and accurate positioning. The major source of error in this technique, is the determination of ΔT_{gap}. This can be reduced by maximizing ΔT_{gap} by increasing the heat flux.

6.1.3 Gap Measurement Technique

The description of the "gap" between two non-ideal surfaces in close proximity is a difficult problem both in its definition as well as its determination. Knowledge of the separation distances between two surfaces in close proximity, whether ideal or non-ideal surfaces are involved, is essential to a meaningful measurement of H_g or H_T. The optical height gage technique used in this study can provide precise and accurate data on a surface geometry relative to an optical flat. The use of welded spacers allows a fixed plane to be maintained above the Zr4 surface. Referencing the optical height gage surface measurements of the UO_2 to the plane defined by the welded spacers can provide information on the interface gap geometry. However, it should be noted that the gap geometry determined by the 19 points $(Da)_i$ in the study is not necessarily sufficient to uniquely define the gap geometry under non-ideal surface conditions.

Additional information is considered necessary if an adequate description of the interface geometry is to be obtained. The use of a Talysurf profilometer coupled to a data acquisition system can be used to acquire more data on the respective surfaces. The use of various stylus heads and cutoff wavelengths will also allow the determination of interfacial separation distance over various wavelengths of the surface. Information of this type would be useful in arriving at a gap geometry function relating a non-ideal separation geometry to one that is ideal (i.e., one dimensional). The use of a device that would allow the separation of two surfaces in-situ may be a better method than using welded spacers. Such a device, however, may not be practical considering the necessity of maintaining a uniformly parallel surface separation geometry, the gap distances involved (e.g., microns), and the precision required (e.g, ±0.1 μm) at narrow gaps.

6.1.4 Specimen Preparation

The surfaces of specimens used in this study all were created by grinding and polishing on optically flat surfaces with SiC or Al_2O_3 particles. This method was found to be incapable of consistently reproducing surface flatnesses (error of form) of less than approximately 1 μm. Considerable improvement in the sample surface flatness and in the ability to impart specific surface

waveforms on the specimen surfaces could be achieved with the use of high precision diamond tool machining techniques. Surface flatness on the order of 5E-10 meters have been claimed for soft materials such as copper and aluminum, however, the feasability of utilizing such techniques to machine hard ceramic materials such as UO_2 and metals such as Zr4 needs to be established.

6.2 INTERFACIAL HEAT TRANSFER

6.2.1 Gap Conductance

The gap conductance between UO_2 and Zr4 was measured using a transient (MPD) and steady state (MLD) technique. Comparison of the MPD and MLD results shows agreement between the techniques within the 3σ H_g and D_{mp} experimental uncertainties. The measured gap conductance exhibits a dependence on temperature (T), gas composition (GC), interfacial surface morphology (ISM), and gap separation (D_{mp}). Two factor interactions of D_{mp}-T, D_{mp}-GC, D_{mp}-ISM, T-GC, and T-ISM are observed amongst the variables. The interactions of D_{mp} with T, GC, and ISM serve to demonstrate that the gap conductance is not uniquely related to a fixed physical separation distance and that allowance for the temperature jump distance at the respective interfaces must be made.

Comparison of results to various expressions for the gap conductance was made. The "ideal" gap conductance expression, Equation 55, was examined for various definitions of the separation distance, D_{mp}, D_{vv}, and D_{pp} and temperature jump distance models. Computation of Equation 55 using algorithms for the gas conductivity and the temperature jump distance as applied in the GAPCON-THERMAL II fuel performance code was made under conditions consistent with experimental results, i.e., temperature, gas composition, and average mean plane separation distance. Comparison of the predicted and experimental H_g results shows that the GAPCON-THERMAL II TJD model yields a conservative estimate for H_g. Comparison of results to the free-molecular model reveals convergence to this limit and also reveals no first order effects due to accommodation coefficient changes or surface roughness within the 3σ uncertainties in H_g or D_{mp}. The results for the ISM-III sample pair shows an apparent departure from the slope of the reciprocal of the gas conductivity for Helium (100). However, this effect is overpowered by both increasing surface roughness and increasing Knudsen number.

6.2.2 Contact Conductance

The thermal contact conductance between UO_2 and Zr4 was measured for three sample pairs of differing roughness and error of form. The results show an increase in H_c with increasing pressure with the presence of a fill gas (e.g., Argon) causing a substantial improvement in the interfacial heat transfer at lower contact pressures. The H_c results on Block 1 (ISM-II) and Block 2 (ISM-I) do not appear to substantiate the hypothesis that H_c has a first order dependence on the surface roughness. The Block 0 (ISM-II) and Block 1 (ISM-II) results show that the error of form can effect the dependence of H_c on the applied load. The MLD results support the reported results by Ross and Stoute[29] in that convergence of H_c at higher contact pressures (e.g., 14.68 MN/m^2) to the lower pressure results of Ross and Stoute is observed. At contact pressures similar to that reported by Rapier,[30] the H_c results are found to be below the Rapier results by a factor of 2 to 5 (depending on sample pair). This difference is attributed to differences in mating error of form. This effect can alter the number of initial solid:solid contact spots and hence the absolute value of H_c measured. The measurements of H_T are seen to be in agreement with the results reported by Dean[28] at 1 atm of Argon.

Comparison has been made with various contact conductance models which are based on the assumption that surface roughness and elastic/plastic deformation are the dominant factors in predicting the thermal contact conductance.

Of the models examined the Mikic/Todreas[10] model is in best agreement with the results of the study. Computation of the experimental factor N in the relationship $H_c \propto (PA/H)^N$ is made and the results show that N will vary as a function of pressure. The recommended values of N suggested by the Mikic/Todreas model ($N = 0.5$, $PA < 6.8$ MN/m^2; $N = 1$, $PA > 6.8$ MN/m^2) appears to be a good first approximation. The observation that N is not a constant but varies with pressure also suggests the H_c may not be related to $(PA/H)^N$ alone.

A new model developed by Dundurs and Panek[49] which considers that the contact resistance is dependent on the surface waviness and elastic deformation, is compared to the experimental results. The similarity in features between

this model and the results (crossover of H_c with increasing wavelength and continuously increasing value of H_c with pressure) suggest that the surface waviness exerts a first order effect in determining the magnitude and pressure dependence of the thermal contact resistance. The controversy over the covert exponent, N, in the relationship between the applied pressure and the hardness of the cladding would cease to exist if the hypothesis put forth in the Dundurs and Panek model is found to be correct since the $(PA/H)^N$ relationship does not enter into their model.

6.3 FUTURE STUDIES

The measurement of H_g will be extended to higher gas pressures. These results would provide information to test the ability of fuel performance codes such as GAPCON-THERMAL II to predict the absolute value and dependence of the gap conductance under condiitions of high gas pressure, temperature, gap separation, and interfacial surface morphology. The data will be directly applicable to BWR and LWR operating conditions.

The information will also be valuable in testing the dependence of the temperature jump distance models with increasing pressure and determining the importance of the spacial gap geometry under conditions of high gas pressures.

Experiments of the accommodation coefficient are also in order. If generated as a function of temperature, information of this nature would allow for the determination of the correct temperature jump distance model from the results of this study.

Theoretical treatment of the problem of specifying a "gap" under nonideal conditions is considered necessary. The "gap" conductance cannot be uniquely determined in reference to a one-dimensional distance perameter called the "gap distance" except under ideal conditions. The development of a gap geometry function which considers surface roughness, error of form, wavelength and amplitude would allow for a more refined and meaningful definition of a "gap".

7.0 REFERENCES

1. Light Water Reactor Fuel Behavior Program Project Description--Fuel and Cladding Material Property Requirements. Prepared by the Thermal Reactor Safety Program Division, P. E. MacDonald, ed., Aerojet Nuclear Company, March 31, 1974.

2. Thermal Conductivity, 1 and 2. R. P. Tye, ed., Academic Press, London and New York, 1969.

3. E. H. Kennard, Kinetic Theory of Gases. McGraw-Hill, New York, NY, 1938.

4. R. B. Bird, W. E. Stewart, and E. N. Lightfoot, Transport Phenomena. John Wiley and Sons, New York, NY, 1966.

5. D. R. Flynn, Thermal Conductivity of Ceramics, Mechanical and Thermal Properties of Ceramics. J. B. Wachtman, Jr., ed., NBS Special Publication 303, Washington, DC, p. 63, May 1969.

6. H. Fenech and W. M. Rohsenow, Thermal Conductance of Metallic Surfaces in Contact. NYP-2136, May 1959.

7. H. Fenech and W. M. Rohsenow, "Prediction of Thermal Conductance of Metallic Surfaces in Contact." J. Heat Transfer, 85; p. 15-24, February 1963.

8. N. Todreas and G. Jacobs, "Thermal Contact Conductance in Reactor Fuel Elements." Nuclear Science and Engineering 50:283, 1973.

9. D. G. Bridge, The Fuel-to-Clad Thermal Conductance in Fast Reactor Mixed Oxide Fuel Pins. FRDC/TEWP/P-(73) 743; FRFF/P-(73) 19; TRG-MEMO-6102 (W), February 1973.

10 D. D. Lanning and C. R. Hann, Review of Methods Applicable to the Calculation of Gap Conductance in Zircaloy-Clad UO_2 Fuel Rods. BNWL-1894, April 1975.

11. J. A. Christensen, Supplementary Modes of Energy Transport Across the Fuel-Cladding Gap. Halden Project, HPR-195, March 1976.

12. S. K. Loyalka, "Gap Conductance in Reactor Fuel Elements," LWR Heat Transfer and Fluid Flow Notes. Trans. ANS., p. 466, June 1977.

13. J. E. Garnier and S. Begej, "Ex-reactor Determination of Thermal Gap Conductance Between Uranium Dioxide-Zircaloy 4 Interfaces." Proceedings of the 15th International Thermal Conductivity Conference, , August 24-26, 1977, Ottawa, Ontario, Canada.

14. D. D. Lanning, C. R. Hann, E. S. Gilbert, Statistical Analysis and Modeling of Gap Conductance Data for Reactor Fuel Rods Containing UO_2 Pellets. BNWL-1832, May 1974.

15. Deleted

16. J. T. A. Roberts et al., Planning Support Document for the EPRI LWR Fuel Performance Program EPRI-NP-737-SR, pp. 48-52, 1978.

17. GAPCON-THERMAL-3: Code Description. PNL-2434, January 1978.

18. C. E. Beyer, C. R. Hann, D. D. Lanning, F. E. Panisko, and L. J. Parchen, GAPCON-THERMAL-II: A Computer Program for Calculating the Thermal Behavior of an Oxide Fuel Rod. BNWL-1898, 1975.

19. J. A. Dearien et al., FRAP-S2: A Computer Code for the Steady State Analysis of Oxide Fuel Rods. TREE-NUREG-1107, July 1977.

20. J. Wordsworth, "IAMBUS-1--A Digital Computer Code for the Design, In-Pile Performance Prediction and Postirradiation Analysis of Arbitrary Fuel Rods." Nuclear Science and Engineering 31:309, 1974.

21. M. E. Cunningham, D. D. Lanning, A. R. Olsen, R. E. Williford and C. R. Hann, Stored Energy Calculation: The State of the Art. PNL-2581, May 1978.

22. F. R. Campbell, L. R. Bourque, R. DesHaies, H. Sills and M. J. F. Notley, In-Reactor Measurement of Fuel to Sheath Heat Transfer Coefficients Between UO_2 and Stainless Steel. AECL-5400, May 1977.

23. W. E. Kaspareck and R. M. Dailey, Measurements of Thermal-Contact Conductance Between Dissimilar Metals in a Vacuum. ASME No. 64-HT-38, presented at AIChE-ASME Heat Transfer Conference and Products Show, Cleveland, OH, August 1964.

24. M. L. Minges, Thermal Contact Resistance: A Review of the Literature. Vol. 1, AFML-TR-65-375, April 1966.

25. C. K. Hsick and F. E. Davis, Bibliography on Thermal Contact Conductance. USAF Report, AFML-TR-69-24, 1969.

26. H. Y. Wong, A Survey of the Thermal Conductance of Metallic Contacts. Aeronautical Research Council Report, C.P. 973, HMSO, London, 1968.

27. R. G. Wheeler, Thermal Conductance of Fuel Element Materials. US AEC Report, HW-60343, April 1959.

28. R. A. Dean, Thermal Contact Conductance Between UO_2 and Zircaloy-2. CVNA-127, Westinghouse Electric Corporation, Atomic Power Division, May 1962.

29. A. M. Ross and R. L. Stoute, Heat Transfer Coefficient Between UO_2 and Zircaloy-2. CRFD-1075: AECL-1552, 1962.

30. A. C. Rapier, T. M. Jones, and J. E. McIntosh, "The Thermal Conductance of Uranium Dioxide/Stainless Steel Interfaces." Int. J. Heat Mass Transfer 6:397-416, 1963.

31. R. K. Williams, T. E. Banks and D. L. McElroy, Measurement and Correlation of Thermal Resistances in UN-metal Interfaces. ORNL 4660, 1971.

32. C. V. Madhusudana, "The Effect of Interface Fluid on Thermal Contact Conductance." Int. J. Heat Mass Transfer 18:939-991, 1975.

33. F. M. Khan, Thermal Contact Resistance at the Fuel-Sheath Interface in Candu Reactors--A Simulation Study. Master thesis, The University of New Brunswick, March 1977.

34. Surface Texture, American Standards, ASA B46.1, 1962.

35. J. C. Maxwell. Phil. Trans. Roy. Soc. 170:332-on, 1879.

36. W. R. Lloyd, D. P. Wilkins, and P. R. Hill, "Heat Transfer in Multi-Component Monatomic Gases in the Low, Intermediate, and High Pressure Regime." Nuclear Thermionics Conference, 1978.

37. S. K. Loyalka, "Temperature Jump in a Gas Mixture." Physics Fluids 17:897, 1974.

38. M. Knudsen, "Kinetic Theory of Gases," Methuen's Monographs on Physical Subjects. Methuen and Co. Ltd., London, 2nd ed., 1933.

39. K. B. Blodgett and I. Langmuir. Phys. Rev. 40:78, 1932.

40. N. Sasaki, K. Taku and K. Mirani. Mem. Coll. Sci. Univ., Kyoto, A25, p. 75, 1949.

41. J. K. Roberts. Proc. Roy. Soc., A142, p. 518, 1933.

42. J. D. Swift, "Kinetic Theory of Gases and Gaseous Flow," Handbook of Vacuum Physics. A. H. Beck, ed., Pergamon Press, Vol. 1, part 5, 1966.

43. B. B. Mikic, "Thermal Contact Conductance: Theoretical Considerations." Int. J. of Heat Mass Transfer 14:205-214, 1974.

44. M. M. Yovanovich and S. S. Burde, "Thermal Resistance at Smooth Sphere/Rough Flat Contacts--Theoretical Analysis." Paper No. 78-871, 2nd AIAA/ASME Thermophysics and Heat Transfer Conference, Palo Alto, CA, May 24-26, 1978.

45. T. N. Cetinkale and M. Fishenden, "Thermal Conductance of Metal Surfaces in Contact." International Heat Transfer Conference, General Discussion on Heat Transfer, Conf. of Inst. of Mech. Eng. and Am. Soc. Mech. Eng., pp. 271-275, September 1951.

592 136

46. R. Holm, Electric Contacts, Theory, and Application. Springer-Verlag, 1967.

47. R. P. Bowden and D. Tabor, The Friction and Lubrication of Solids. Clarendon Press, Oxford, p. 21, 1950.

48. Y. L. Shlykov, "Thermal Contact Resistance." Thermal Engineering 12:102, 1966.

49. J. Dundurs and C. Panek, "Heat Conduction Between Bodies With Wavy Survaces." Int. J. Heat Mass Transfer 19:731-736, 1976.

50. W. J. Parker, R. J. Jenkins, C. P. Butler, and G. L. Abbott, "Flash Method of Determining Thermal Diffusivity, Heat Capacity and Thermal Conductivity." J. Appl. Phys. 32(9):1679-1684, 1961.

51. J. A. Cape and G. W. Lehman. J. Appl. Phys. 34:1909, 1963.

52. G. Pekham. The Computer Journal 13(4), November 1970.

53. L. R. Bunnell, G. B. Mellinger, J. L. Bates and C. R. Hann, "High Temperature Properties of Zircaloy-Oxygen Alloys." EPRI NP-524, March 1977.

54. J. L. Bates, "High-Temperature Conductivity of 'Round Robin' Uranium Dioxide." BNWL-1431, July 1970.

55. M. Jakob, Heat Transfer. John Wiley and Sons, Vol. 1, 1949.

56. G. Reymann et al., MATPRO-10: A Handbook of Materials Properties for Use in the Analysis of LWR Fuel Rod Behavior, Appendix C. TREE-NUREG-1180, February 1978.

57. J. M. Gandhi and S. C. Saxena, "Correlated Thermal Conductivity Data of Rare Gases and Their Binary Mixtures at Ordinary Pressures." J. of Chem. and Engr. Data 13:3, 1968.

58. R. S. Brokaw, Alignment Charts for Transport Properties, Viscosity, Thermal Conductivity, and Diffusion Coefficients for Nonpolar Gases and Gas Mixtures at Low Density. NASA-TR-R-81, Lewis Research Center, 1960.

59. A. Ullman, R. Acharya, and D. R. Olander, "Thermal Accommodation Coefficients of Inert Gases on Stainless Steel and UO_2." J. Nucl. Materials 51:277, 1974.

60. B. J. Jody and S. C. Saxena et al., "Thermal Accommodation Coefficient for Helium on Partially Gas Covered Platinum in the Temperature Range 300-1400K." Proceedings of the Seventh Symposium on Thermophysical Properties, 2760-2765, National Bureau of Standards, May 10-12, 1977.

61. D. M. Curry and S. D. Williams, Non-Linear Least Squares--An Aid to Thermal Property Determination. MSC-07048, NASA TM X-58092, June 1972.

592 137

62. I. Peggs. J. Nucl. Matl. 57:246-248, 1975.

63. D. R. Olander, "Fundamental Aspects of Nuclar Reactor Fuel Elements." TID-26711-P1, National Technical Information Service, April 1976.

64. D. B. Scott, "Physical and Mechanical Properties of Zircaloy 2 and 4." UC-25, WCAP-3269-41, May 1965.

65. S. J. Kline and F. A. McClintock, "Describing Uncertainties in Single Sample Experiments." Mech. Engs. 75:3, January 1953.

592 133

8.0 NOMENCLATURE

a	Accommodation coefficient.
A	Cross-sectional area of a MLD meter bar (m^2).
a^*	Accommodation coefficient for an atomically smooth surface.
a_i	Accommodation coefficient for gas species "i" in a gas mixture.
a_{mix}	Net accommodation coefficient for a gas mixture.
b	Amplitude of the sinusoidal gap used in the Dundurs and Panek[49] contact conductance model.
C_p	Specific heat at constant pressure (J/mole - K).
C_v	Specific heat at constant volume (J/mole - K).
$CLA_{1,2}$	Center-line average roughness for DUO_2 and Zr4, respectively (m).
CR	Constriction resistance of an interface (m^2/W).
d	Ideal surface separation distance for perfectly smooth and flat surfaces (m).
$(D_a)_i$	Local separation distance between asperity tips on adjacent surfaces (m).
D_a	Average gap between asperities on adjacent surfaces (m).
D_i	Local surface separation distance (m). (The index refers to some specific y-z coordinate.)
D	Arithmetic average of all D_i.
$(D_{mp})_i$	Local mean-plane separation distance.
D_{mp}	Average mean-plane separation distance [arithmetic average of all $(D_{mp})_i$].
D_{pp}	Separation distance between parallel surface planes defined by the three highest peaks on each surface (m).
D_{vv}	Separation distance between parallel surface planes defined by the three deepest valleys on each surface (m).
DUO_2	Depleted Uranium Dioxide.
f_i	Mole fraction of gas species "i" in a gas mixture.

$g_{1,2}$	Temperature jump distance at the DUO_2 and Zr4 surfaces, respectively (m).
GC	Gas composition.
GP	Fluid (gas) pressure (Pascals).
h_1	Heat transfer coefficient for the front (DUO_2) surface (W/m^2-K).
h_2	Gap conductance value solved for in MPD analytical technique (W/m^2-K).
h_3	Heat transfer coefficient for the rear (Zr4) surface (W/m^2-K).
H	Meyers hardness of the softer material (N/m^2).
H_c	Solid-solid contact conductance (W/m^2-K).
H_{FM}	Gap conductance in the free-molecular flow regime (W/m^2-K).
H_g	Gap conductance (W/m^2-K).
H_T	Total conductance across an interface (W/m^2-K).
H_{TR}	Total gas conductance in the transition regime.
ISM	Interfacial surface morphology.
$k_{1,2}$	Thermal conductivity of DUO_2 and Zr4, respectively.
K_{gas}	Thermal conductivity of a gas (W/m-K).
K_I	Thermal conductivity of the insulation used between the meter bar and guard in the MLD technique (W/m-K).
K_m	Mean-solid conductivity (W/m-K).
KN	Knudsen number.
KN_L	Local Knudsen number.
$\ell_{1,2}$	Thickness of DUO_2 and Zr4 specimens, respectively (m).
L	Length of meter bar over which energy interchange correction is applied (m).
$L_{1,2}$	Peak-to-peak asperity separation on DUO_2 and Zr4 surfaces, respectively (m).
M	Number of digitized data locations along a temperature history curve (MPD technique).
M_i	Molecular weight of atomic species "i" (K_g/mole).
MLD	Modified Longitudinal Design.
MPD	Modified Pulse Design.
n	Average number of collisions a gas molecule would make with an atomically rough surface before escaping.

N	An exponent determining the pressure (PA) dependence of the contact conductance (H_c).
N_c	Number of rectangular columns used in the calculation of H_{TR}.
PA	Apparent interfacial contact pressure (N/m^2).
$q_{A_{1,2}}$	Uncorrected heat flux in meter bar 1 or 2 (W/m^2).
$q_{L_{1,2}}$	Energy exchange between meter bars and surrounding annular guard.
q_1	Heat flux into the gap gas from the DUO_2 surface (W/m^2).
q_2	Heat flux into the Zr4 surface from the gap gas.
q_b	Heat loss from back of Zr4 specimen (W/m^2).
q_f	Heat loss from front (laser irradiated) side of DUO_2 specimen (W/m^2).
Q	Heat flow per unit area per second across a gap (W/m^2).
q^∞	Far field heat flux (W/m^2).
R	gas constant (8.31 J/mole - K).
r_1	Outer radius of inner cylinder in meter bar (m).
r_2	Inner radius of outer guard around meter bar (m).
$R_{1,2}$	Surface roughnesses (equivalent to $CLA_{1,2}$).
$S_{1,2}$	Uniaxial compliance in plane strain for DUO_2 and Zr4, respectively (m^2/N).
TM	Time (sec).
T	Temperature (K).
T_{gas}	Gas temperature (K).
$T_{1,2}$	DUO_2 and Zr4 surface temperatures (K).
T_I	Temperature of a molecular stream impinging upon a wall (K).
T_R	Temperature of a molecular stream reflected from a wall (K).
T_W	Wall temperature (K).
TJD	Temperature Jump Distance
W_H	3σ uncertainty in H_g or H_c using the MLD technique.
x_2	Coordinate perpendicular to the surface plane.
y	Coordinate lying in the plane of the surface.
Z	Coordinate lying in the plane of the surface.
Zr4	Zircaloy-4
$\alpha_{1,2}$	Thermal diffusivity of DUO_2 and Zr4, respectively (m^2/sec).

ΔT Temperature difference across an interface (K).

ΔT_G Temperature difference between meter bar and guard (K).

ΔX Distance between temperature sensors in MLD meter bars (m).

γ Ratio of specific heats, C_p/C_v.

$(\gamma_{1,2})_i$ Local distance from optical gage probe tip to the surface mean-plane on the DUO_2 and Zr4 respectively (m).

$\gamma_{1,2}$ Arithmetic average of all $(\gamma_{1,2})_i$ values (m).

λ Mean free path of a gas molecule (m).

ϕ Tabulated shape factor depending on r_1/r_2.

ψ Total fractional uncertainty in the average mean-plane separation distance = $\psi_r + \psi_{EOF}$.

ψ_R Fractional uncertainty in the average mean-plane separation distance due to the surface roughness.

ψ_{EOF} Fractional uncertainty in the average mean-plane separation distance due to the surface error-of-form.

θ_I Mean energy of a molecular stream incident on a surface (joule/molecule).

θ_R Mean energy of a molecular stream reflected from a surface (joule/molecule).

θ_W Mean energy of molecules within a reflected stream that had reached thermal equilibrium with the wall (joule/molecule).

APPENDIX A

MPD AND MLD SPECIMEN THERMOPHYSICAL PROPERTY DETERMINATION

MPD AND MLD SPECIMEN THERMOPHYSICAL PROPERTY DETERMINATION

A.1 MPD SPECIMENS

A.1.1 UO_2 Thermophysical Properties

Thermal Diffusivity (range: 290 K to 1023 K). The measured diffusivity data in this study are shown in Figure A.1 and were obtained using the flash technique and optical detector. These data are the combined results of four representative UO_2 samples. The data were corrected for thermal expansion and heat loss effects. Finite pulse time effects were found to be negligible. A fourth order polynomial curve fit of the data shown in Figure A.1 yielded the following coefficients:

$$\begin{aligned}\alpha_1 = {} & 3.59426E\text{-}6 \\ & -9.23546E\text{-}9 \times (T - 273.16) \\ & +1.36176E\text{-}11 \times (T - 273.16)^2 \\ & -8.18246E\text{-}15 \times (T - 273.16)^3 \\ & +3.51509E\text{-}19 \times (T - 273.16)^4 \ m^2/sec.\end{aligned} \qquad \text{(A-1)}$$

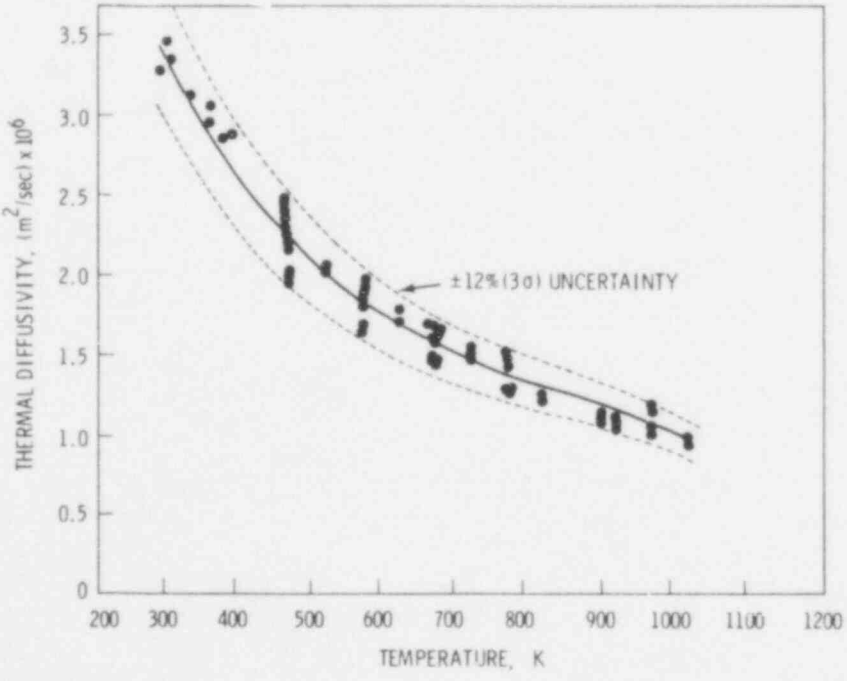

FIGURE A.1. Thermal Diffusivity of Depleted UO_2; O/M = 2.000 ±0.002, 94.1% T.D

The residual error in the curve fit was determined to be 1.16E-6 and the resulting R-square valve was 0.9714. The 3σ uncertainty associated with Equation A-1 is ±12%.

Heat Capacity (range: 300 to 2800 K). Refer to Reference 54 for further details.

$$\begin{aligned} C_{p_1} = {} & 2.288151E+2 \\ & +3.872301E-1 \times (T - 273.16) \\ & -8.325954E-4 \times (T - 273.16)^2 \\ & +1.070569E-6 \times (T - 273.16)^3 \\ & -7.778425E-10 \times (T - 273.16)^4 \\ & +2.891270E-13 \times (T - 273.16)^5 \\ & -4.080387E-17 \times (T - 273.16)^6 \ J/kg - K. \end{aligned} \qquad (A-2)$$

Linear Expansion Coefficient (range: 290 to 2773 K). Refer to Reference 54 for further details.

$$\begin{aligned} L_1 = {} & -2.0701E-4 \\ & +8.4051E-6 \times (T - 273.16) \\ & +1.6502E-9 \times (T - 273.16)^2 \\ & +2.6128E-13 \times (T - 273.16)^3 \ m/m - K. \end{aligned} \qquad (A-3)$$

Density (range: 290 to 2773 K). Refer to Reference 54 for further details. The density of UO_2 specimens used in this study was measured at 297.1 K and was determined to be 1.0317E+4 kg/m^3 (i.e., 94.1% TD). The density at a particular temperature T was calculated from the expansion:

$$\rho_1 = \frac{1.0317E+4}{(1 + L_1)^3} \ kg/m^3. \qquad (A-4)$$

This approximation assumes the thermal expansion to be isotropic.

Thermal Conductivity (range: 290 to 1023 K). The thermal conductivity of UO_2 was determined from the relationship:

$$k_1 = \alpha_1 C_{p_1} \rho_1 \ W/m - K \qquad (A-5)$$

592 145

Impurity Limits for Uranium Dioxide. The milled natural uranium dioxide used in this study was supplied by Exxon Nuclear Company, Richland, Washington. The U-235 content was determined to be 0.25 ±0.005%. The maximum impurity limits in the as-received powder are listed in Table A.1.

TABLE A.1. Impurity Limits for Uranium Dioxide

Element	Limits in ppm by Weight Uranium Dioxide, Max.
Aluminum	500
Beryllium	20
Boron	10
Cadmium	20
Calcium	100
Carbon	150
Chlorine	25
Chromium	200
Cobalt	10
Flourine	50
Iron	400
Lithium	10
Magnesium	25
Nickel	400
Nitride Nitrogen	200
Phosphorus	50
Potassium	200
Sodium	500
Sulfur	300
Vanadium	400
Tantalum	400
Tungsten	100
The sum of copper, zinc, silicon, and titanium	800
The sum of silver, manganese, molybdenum, lead and tin	200
The sum of samarium, europium, gadolinium, and dysprosium	100

A.1.2 Zr4 Thermosphysical Properties

Thermal Diffusivity (range: 290 to 973 K). The data shown in Figure A.2 was obtained using the flash technique with an intrinsic chromel-constantan fast response thermocouple (25.4 μm wire diameter). The results were corrected for heat losses and thermal expansion effects. The finite pulse time correction was negligible. Equation A-6 below is a fourth order polynomial curve fit to the data shown in Figure A.2.

$$\begin{aligned} \alpha_2 = \; & 7.25741E\text{-}6 \\ & -4.99332E\text{-}9 \times (T - 273.16) \\ & +2.52369E\text{-}11 \times (T - 273.16)^2 \\ & -3.56742E\text{-}14 \times (T - 273.16)^3 \\ & +1.86149E\text{-}17 \times (T - 273.16)^4 \; m^2/sec. \end{aligned} \qquad (A\text{-}6)$$

The residual error, R-square, and 3σ uncertainty value for Equation A-6 were determined to be 4.77E-6, 0.845926, and ±5%, respectively.

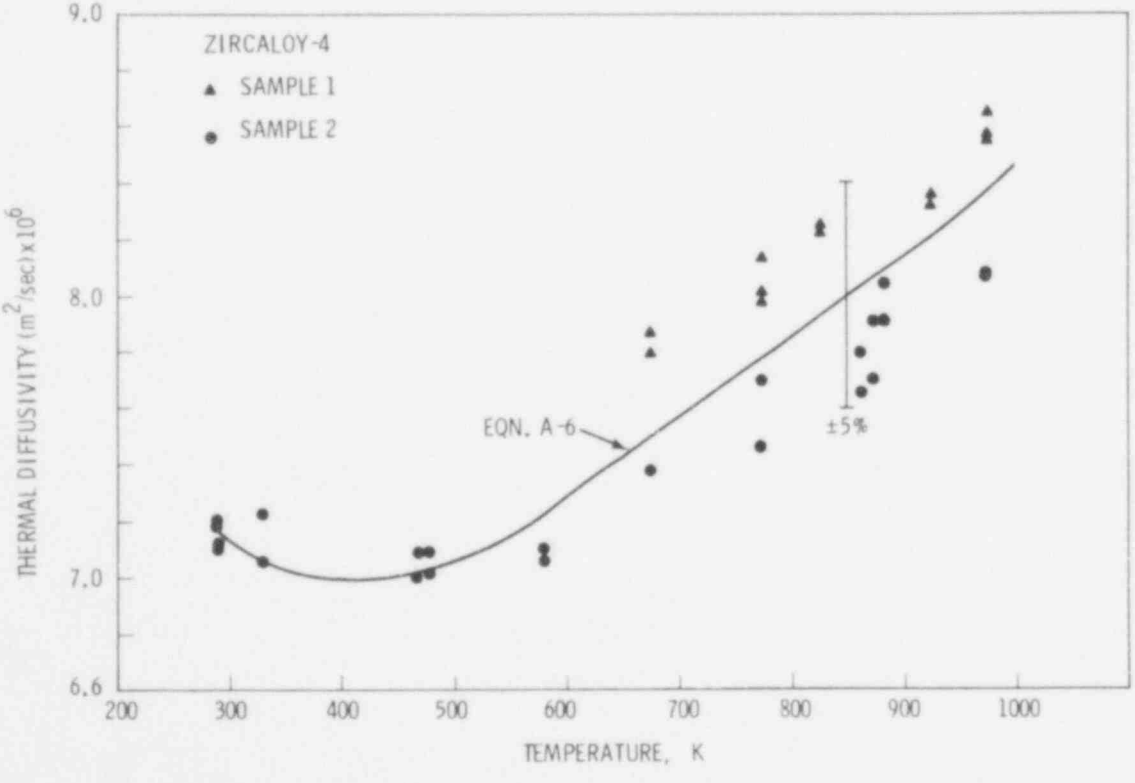

FIGURE A.2. Measured Thermal Diffusivity Values for Zr4

Thermal Conductivity (range: 290°K to 1073 K). Refer to reference (54) for further details.

$$\begin{aligned} k_2 = {} & 1.39543E+2 \\ & +1.86955E-2 \times (T - 273.16) \\ & -7.01687E-5 \times (T - 273.16)^2 \\ & +2.56948E-7 \times (T - 273.16)^3 \\ & -4.34449E-10 \times (T - 273.16)^4 \\ & +2.63369E-13 \times (T - 273.16)^5 \ W/m - K \end{aligned} \qquad (A\text{-}7)$$

Thermal Expansion (range: 293 to 1073 K). Refer to reference (54) for further details. Curve fitted to results for specimen containing 0.7 at % oxygen.

$$\begin{aligned} L_2 = {} & 8.4857E-4 \\ & -8.4687E-6 \times (T - 273.16) \\ & +1.0077E-7 \times (T - 273.16)^2 \\ & -2.9410E-10 \times (T - 273.16)^3 \\ & +3.8536E-13 \times (T - 273.16)^4 \\ & -1.8357E-16 \times (T - 273.16)^5 \ m/m- K \end{aligned} \qquad (A\text{-}8)$$

Density (range: 293 to 1073 K). Refer to reference (54) for further details. ρ_2 at 293 K was taken to be 6.54E+3 kg/m^3, then

$$\rho_2 = \frac{6.54E+3}{(1 + L_2)^3} \ kg/m^3 \qquad (A\text{-}9)$$

Heat Capacity (range. 293 to 1073 K).

$$C_{p_2} = \frac{k_2}{\alpha_2 \rho_2} \ Joules/kg- K \qquad (A\text{-}10)$$

Zr4 Ingot Analysis. The MPD and MLD specimens used in this study were obtained from a single 63.5 mm diameter x 400 mm ingot of Zr4 supplied by

Teledyne Wah Chang Albany, Albany, Oregon. The ingot analysis, impurity content, and product chemistry are listed in Table A.2. The thermal conductivity, thermal expansion, and density results cited from reference (54) were obtained in samples taken from this same ingot.

TABLE A.2. Zircaloy-4 Ingot Analysis, Product Chemistry, and Impurity Content

Ingot Analysis Composition in Percent			
Element	Spec.	Top	Bottom
Sn	1.20-1.70	1.29	1.26R, 1.27R
Fe	0.18-0.24	0.21	0.20
Cr	0.07-0.13	0.12	0.12
Fe+Cr	0.28-0.37	0.33	0.32

Product Chemistry, PPM			
Element	Spec.	1	2
Sn	1.20-1.70%	1.31	1.34
Fe	1800-2400	2090	2100
Cr	700-1300	1180	1180
Al	75	45	46
B	0.5	<0.2	0.2
Cd	0.5	<0.2	<0.2
C	270	80	80
Co	20	<10	<10
Cu	50	10	10
Hf	200	60	57
H	25	7	<5
Mn	50	<25	<25
Ni	70	<35	<35
N	80	23	28
Si	120	66	64
Ti	50	<25	<25
W	100	<25	<25
U	3.5	<0.5	<0.5

Impurities in PPM			
Al	75	46	45
B	0.5	0.2	0.2
Cd	0.5	<0.2	<0.2
C	270	70	80
Co	20	<10	<10
Cu	50	13	14
Hf	200	57	59
H	25	9	6
Mn	50	<25	<25
Ni	70	<35	<35
N	80	37	27
Si	120	73	82
Ti	50	<25	<25
W	100	<25	<25
U	3.5	<0.5	

A.2 MLD SPECIMENS

A.2.1 Al_2O_3

Thermal Conductivity. Coors Ad-85 alumina data was obtained from the manufacturer. The information was generated by ASTM C408-58, "Thermal Conductivity of Whiteware Ceramics." This specification specifically states that materials can only be evaluated up to a maximum of 423 K. The specification is basically a longitudinal heat flow technique using copper as meter bar materials and utilizes no temperature guarding. Therefore, guarded measurements were made using a Dynatech Model TCHCM-N20 Comparative Instrument over the approximate temperature range of 473 to 873 K. Comparing these results to the literature data yielded the following results: At 473 K, the data agreed to 2%; while at 873 K, there was a 16% variation in results, with the literature data being lower than the measured results. This is what would be expected for an unguarded system. The results of these measurements are shown in Figure A.3.

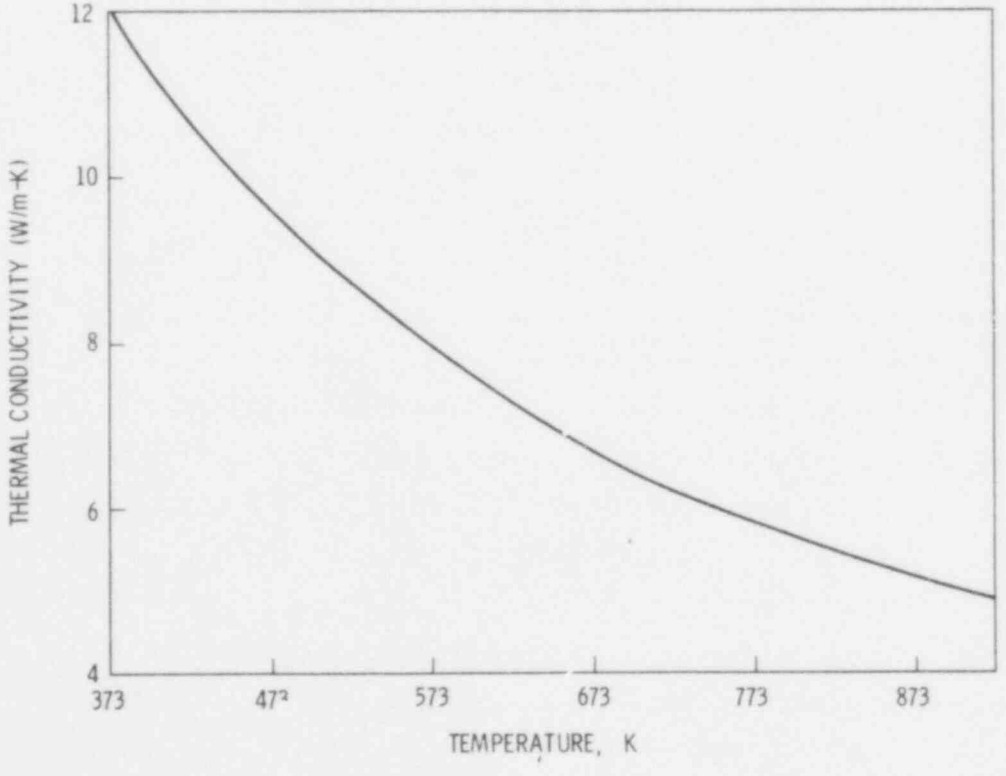

FIGURE A.3. Thermal Conductivity of Coors AD-85 Al_2O_3

Over the temperature range of interest, the comparative method yields results with an accuracy of ±5%. This was determined by evaluating a series of materials of known thermal conductivity.

Thermal Expansion. The coefficient of linear thermal expansion for alumina (from 289 to 973 K) was reported by Coors Porcelain Company to be 6.9×10^{-6} m/m - K.

A.2.2 UO_2

Thermal Conductivity. The thermal conductivity of the UO_2 was taken to be the same as that for the MPD specimens.

A.2.3 Zr4

Thermal Conductivity. The Zr4 thermal conductivity data was obtained from an EPRI report (NP-524, March 1977). This data was obtained on samples taken from the same Zr4 ingot from which the MPD and MLD specimens were obtained.

The measurements were performed utilizing a Dynatech Model TCAGM Axial Rod Instrument. This technique is an absolute method and accuracies of ±2% are obtainable in the temperature range of interest. This accuracy has been determined by evaluating standard materials of known thermal conductivity. A polynominal curve fit expression to this data can be found in Appendix A, "Zr4 Thermophysical Properties."

A.2.4 Quartz Wool

The insulation material selected for insulating the MLD sample column was quartz wool. This material was selected on the basis of minimum contamination possibility with temperature sensors, meter bars and specimens, ease of use, stability over the temperature range of use, and having a low yet well known values of apparent thermal conductivity. The quartz wool was packed in the annular cavity surrounding the specimens at approximately 130 kg/m^3. Measurements of the apparent thermal conductivity from 373 to 873 K were carried out in accordance with ASTM C177-76, "Steady-State Thermal Transmission Properties by Means of the Guarded Hot Plate." The results of this evaluation are given in Figure A.4.

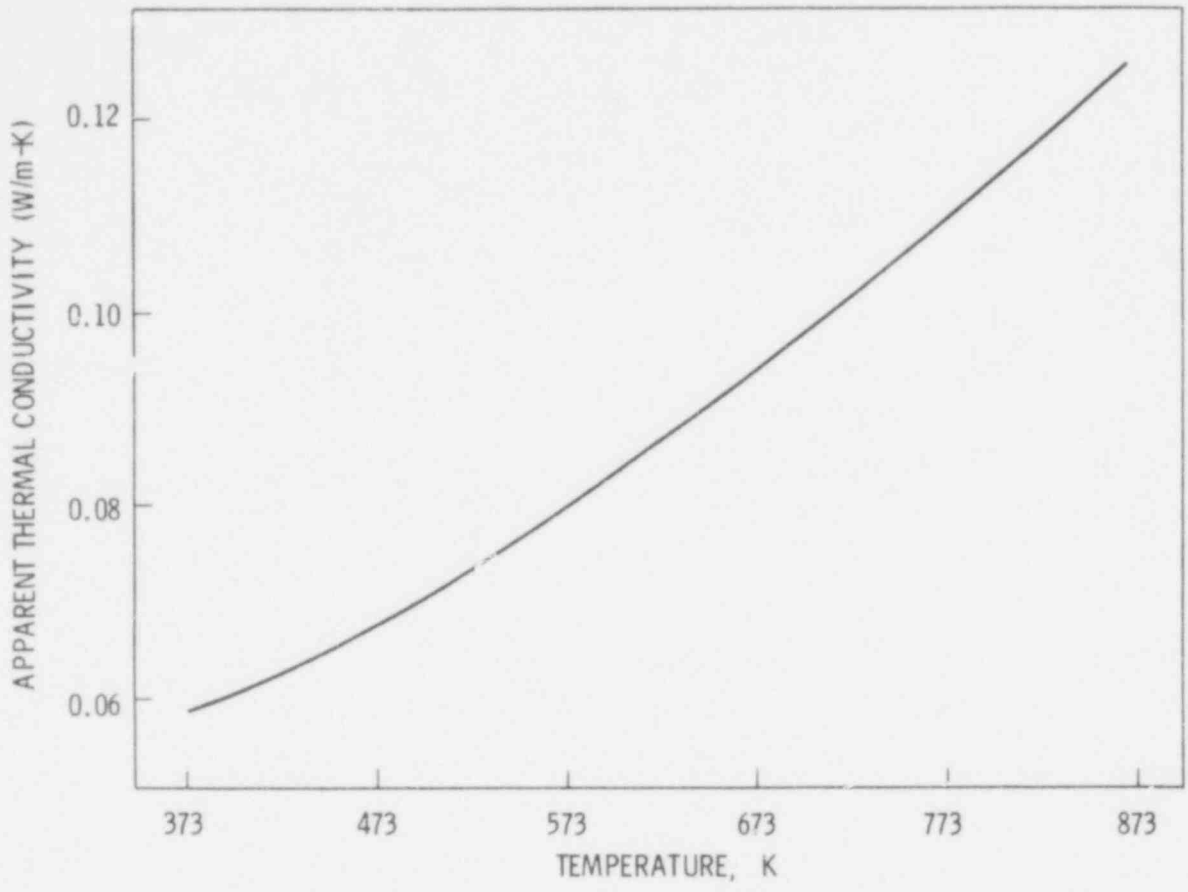

FIGURE A.4. Apparent Thermal Conductivity of Quartz Wool (Density = 130 kg/m³)

APPENDIX B

MPD TECHNIQUE UNCERTAINTY ANALYSIS

MPD TECHNIQUE UNCERTAINTY ANALYSIS

Using a procedure described by Kline and McClintock[65] for estimating the uncertainty of experimental results, the 3σ uncertainty in the interface conductance, W_{H_g}, can be defined as:

$$W_{H_g} = \left[\sum_{i=1}^{n} \left(\frac{\partial H_g}{\partial V_i} W_i\right)^2\right]^{1/2} \qquad \text{(B-1)}$$

where H_g is a function of the independent variables, V_1, V_2, ... V_n.

Since no explicit analytical function is available for H_g, the values of $\partial H_g/\partial V_i$ were numerically determined by calculating the dependence of H_g on V_i for perturbations about each V_i equivalent to the uncertainty in V_i. Using this method, the calculated uncertainty (3σ) inherent in the MPD technique was found to be ≃±12%.

As an example of the calculational procedures, Table B.1 below shows the steps involved in calculating the uncertainty for an arbitrarily selected run in which $H_g = 0.3538 \times 10^4$ W/m^2-K.

TABLE B.1. Example Calculation of Uncertainty in MPD H_g Determination

Variable	W_i (%)	W_i	$\frac{\partial H_g}{\partial V_i}$ (a)	$\frac{\partial H_g}{\partial V_i} \times W_i$	$\left(\frac{\partial H_g}{\partial V_i} \times W_i\right)^2$
X_1 = 1.04E-3	2	2.08 E-5	9.06 E+6	1.88 E+2	3.53 E+4
X_2 = 9.72E-4	2	1.94 E-5	3.28 E+6	6.38 E+1	4.07 E+3
k_1 = 3.91E+0	4	1.56 E-1	3.24 E+2	5.07 E+1	2.57 E+3
k_2 = 1.96E+1	4	7.84 E-1	1.20 E+2	9.44 E+1	8.90 E+3
α_1 = 1.23E-6	12	1.48 E-7	-2.28 E+9	3.37 E+2	1.13 E+5
α_2 = 8.05E-6	5	4.03 E-7	-4.32 E+8	1.74 E+2	3.02 E+4
				$\sum(\ )^2$ =	1.94 E+5

(a) Numerically calculated

Then, from Equation E-1,

$$W_{H_g} = \left[\sum\left(\frac{\partial H_g}{\partial V_i} \times W_i\right)^2\right]^{1/2}$$

$$= \left[1.94\ E{+}5\right]^{1/2}$$

$$W_{H_g} = 4.40\ E{+}2\ W/m^2\text{-}K \qquad (3\sigma)$$

or, expressed fractionally,

$$f_{H_g} = \frac{4.40\ E{+}2}{3.538\ E{+}3} \times 100\% = 12.4\%$$

$$\approx 12\%$$

APPENDIX C

MLD UNCERTAINTY ANALYSIS

C.0 MLD UNCERTAINTY ANALYSIS

The following is a discussion of the analysis made to determine the 3σ uncertainty in the MLD H_g and H_c measurements.

C.1 UNCERTAINTY IN ΔT_{gap}

The standard deviation, $\sigma_{\Delta T}$, associated in determining the temperature drop ΔT at the interface may be expressed as

$$\sigma_{\Delta T} = \sqrt{\left(\sigma_{T_{UO_2}}\right)^2 + \left(\sigma_{T_{Zr4}}\right)^2} \qquad \text{(C-1)}$$

where $\sigma_{T_{UO2}}$ and $\sigma_{T_{Zr4}}$ are the uncertainties in the extrapolated UO_2 and Zr4 interface temperatures, respectively. It is reasonable to assume that the uncertainty in the interface temperature is no greater than twice the uncertainty of the thermocouple reading themselves, thus

$$\sigma_T \approx 2\sigma_{t_c} = 2(0.17\ K) \approx 0.35\ K \qquad \text{(C-2)}$$

Furthermore, if it is assumed that

$$\sigma_{T_{UO_2}} \approx \sigma_{T_{Zr}} = \sigma_T$$

then from Equation C-1

$$\sigma_{\Delta T} = \sqrt{2}\,\sigma_T \approx 0.5\ K$$

or that

$$3\sigma_{\Delta T} \approx 1.5\ K = W_{\Delta T}$$

C.2 UNCERTAINTY IN H_g OR H_c DETERMINATION

According to the procedure described by Kline and McClintock[65] for estimating the uncertainty in experimental results, one can write the uncertainty in $H = H(V_1, V_2, \ldots V_n)$ as

$$3\sigma_H = W_H = \left[\sum_{i=1}^{n} \left(\frac{\partial H}{\partial V_i} W_i\right)^2\right]^{1/2} \qquad \text{(C-3)}$$

The expression for H_c or H_g is given by Equation 25:

$$H_g \text{ or } H_c = \frac{Q}{A\Delta T} \qquad (25)$$

Applying Equation C-3,

$$W_H = \left[\left(\frac{\partial H}{\partial Q} W_Q\right)^2 + \left(\frac{\partial H}{\partial A} W_a\right)^2 + \left(\frac{\partial H}{\partial \Delta T} W_{\Delta T}\right)^2\right]^{1/2} \qquad \text{(C-4)}$$

$$W_H = \left[\left(\frac{W_Q}{A\Delta T}\right)^2 + \left(\frac{-QW_A}{A^2\Delta T}\right)^2 + \left(\frac{-QW_{\Delta T}}{A(\Delta T)^2}\right)^2\right]^{1/2} \qquad \text{(C-5)}$$

The following values of the variables were chosen from the MLD results as a representative example:

Q = variable	$W_Q = (0.03) \times Q$
ΔT = variable	$W_{\Delta T} = 1.5$ K
$A = 5.07\text{E-}4$ m^2	$W_A = 1.014\text{E-}5$ m^2

Insertion into Equation (C-5) yields the following expression:

$$W_H = \frac{Q}{\Delta T}\left[(5063) + \left(\frac{2960}{\Delta T}\right)^2\right]^{1/2} \qquad \text{(C-6)}$$

592 158

Once Q and ΔT are determined experimentally, W_H can be calculated. As an example of the calculational procedures, Table C.1 shows the steps involved in determining the uncertainty in H_g for a Al_2O_3-Zr4 sample pair under the following conditions:

Temperature (mean) = 481 K
Gas atmosphere = Helium
Gas pressure = 0.103 MPa
D_{mp} = 135.0 μm

TABLE C.1. Example Calculation of Uncertainty in MLD H_g or H_c Determination

WT, K	H_g, W/m^2-K x 10^{-4}	$Q = HA\Delta T$, Watts	W_H, W/m^2-K	W_H, %
5	0.166	4.20	501	30.2
6	0.166	5.05	419	25.3
10	0.166	8.42	256	15.4
20	0.166	16.8	138	8.3

The results from Table C.1 are plotted in Figure C.1 and can be compared with Figure C.2 which shows the results for the same sample pair in the Argon atmosphere. Clearly, the 3σ uncertainty in H_g increases with decreasing ΔT. Under conditions of high interfacial stresses, the temperature drop across the interface is often only a degree or two, which suggests that many of the contact conductance values published in the literature contain very large errors. This may, at least in part, explain the discrepancies between much of the reported thermal contact conductance data.

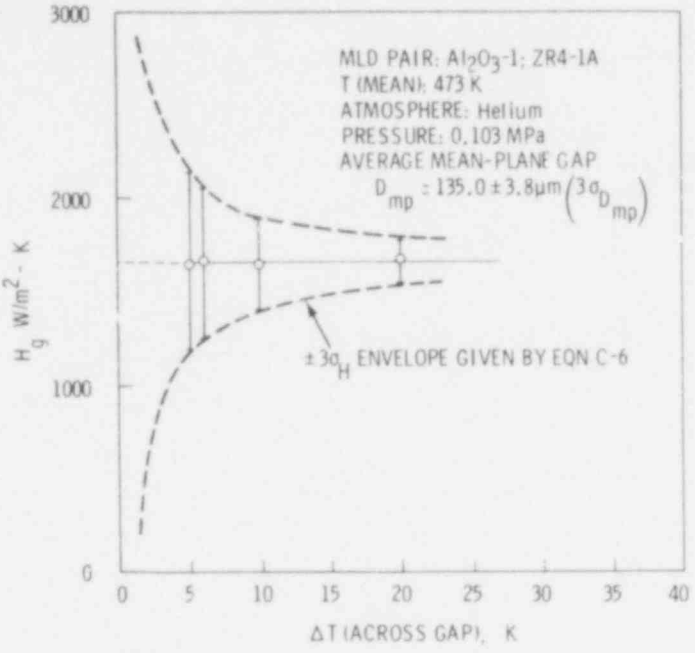

FIGURE C.1. The Uncertainty in H_g as a Function of ΔT Across the Gap for an MLD Al_2O_3:Zr4 Sample Pair in Helium Gas

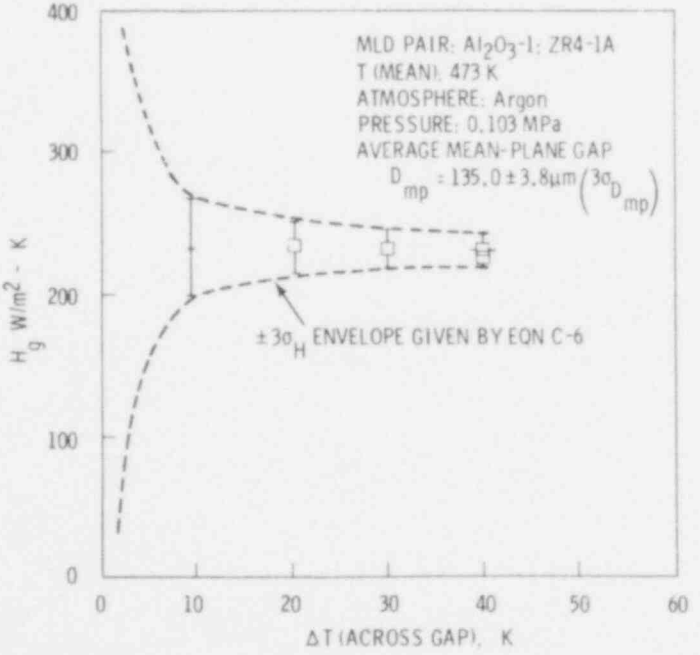

FIGURE C.2. The Uncertainty in H_g as a Function of ΔT Across the Gap for an MLD Al_2O_3:Zr4 Sample Pair in Argon Gas

APPENDIX D

MPD EXPERIMENTAL DATA

MPD EXPERIMENTAL DATA

CONTENTS

592 162

Pair Code: DUO2-41: Zr4-32

ISM-I

Gas Pressure: 0.103

Specimens in light contact:

Contact Pressure: 1310 N/m^2

Average Mean-Plane Gap: D_{mp} = 20.7 ± 3.2 μm ($3\sigma_{D_{mp}}$)

Temp K	H_g (W/m^2 - K) x 10^{-4}				
	He(100)(a)	He:Ar(51.8:48.2)	Ar(100)	He:Xe(89:11)	He:Xe(51:49)
293	0.751	0.405	0.160	0.562	0.297
473	0.984	0.546	0.228	0.778	0.383
573	1.028	0.618	0.255	0.821	0.443
673	1.062	0.638	0.284	0.861	0.498
773	1.138	0.709	0.306	0.895	0.509
873	1.166	0.732	0.314	0.934	0.528

(a) mole%

Specimens separated by spacers:

Gas Pressure: 0.103 MPa

Average Mean-Plane Gap: D_{mp} = 33.0 ± 2.4 μm ($3\sigma_{D_{mp}}$)

Temp K	$\frac{H_g (W/m^2 - K) \times 10^{-4}}{He(100)}$
293	0.581
473	0.717
573	0.764
673	0.829
773	0.844
873	0.847

592 163

Pair Code: DUO2-40: Zr4-25

ISM-II

Gas Pressure: 0.103 MPa

Specimens in Light Contact:

Contact Pressure: 1310 N/m^2

Average Mean-Plane Gap: D_{mp} = 4.1 ± 1.8 μm ($3\sigma_{D_{mp}}$)

(Refer to Results and Discussion Section for comments on this set of results)

Temp K	H_g (W/m^2 - K) x 10^{-4}			
	He(100)	He:Ar(51.8:48.2)(a)	Ar(100)	He:Xe(89:11)
293	2.06	0.850	0.521	1.31
473	2.67	1.04	0.660	1.31
573	2.96	1.04	0.886	1.35
673	3.25	1.06	1.11	1.32
773	3.49	0.935	1.15	1.25
873	3.50(b) - 4.17(c)	0.941	1.17	1.22

(a) mole %
(b) 45 min at 873 K
(c) 95 min at 873 K

Average Mean-Plane Gap: D_{mp} = 11.5 ± 2.4 μm ($3\sigma_{D_{mp}}$)

Temp K	H_g (W/m^2 - K) x 10^{-4}				
	He(100)	He:Ar(51.8:48.2)(a)	Ar(100)	He:Xe(89:11)	He:Xe(51:49)
293	1.03	0.571	0.212	0.798	0.388
473	1.22	0.633	0.270	0.913	0.471
573	1.25	0.688	0.288	0.946	0.492
673	1.31	0.716	0.323	0.986	0.522
773	--	0.743	0.340	0.950	0.500
873	1.28	0.706	0.357	0.950	0.516

(a) mole %

Pair Code: DUO2-25: Zr4-25

ISM-II

Gas Pressure: 0.103 MPa

Specimens in Light Contact:

Contact Pressure: 900 N/m^2

Average Mean-Plane Gap: $D_{mp} = 5.6 \pm 3.8$ μm $(3\sigma_{D_{mp}})$

Temp K	H_g (W/m^2 - K) x 10^{-4}			
	He (100)	He:Ar(51.8:48.2)(a)	Ar (100)	He:Xe(89.8:10.2)
293	1.30	0.680	0.339	1.06
473	1.62	0.866	0.432	1.39
673	1.84	0.990	0.538	1.53
873	2.10	1.031	0.619	1.77

(a) Mole %.

Average Mean-Plane Gap: $D_{mp} = 10.5 \pm 6.5$ μm $(3\sigma_{D_{mp}})$

Temp K	H_g (W/m^2 - K) x 10^{-4}			
	He (100)	He:Ar(51.8:48.2)	Ar (100)	He:Xe(89.8:10.2)
293	1.07	0.598	0.208	0.832
473	1.37	0.693	0.324	1.08
673	1.49	0.783	0.412	1.30
873	1.63	0.820	0.432	1.43

Average Mean-Plane Gap: $D_{mp} = 26.3 \pm 6.6$ μm $(3\sigma_{D_{mp}})$

Temp K	H_g (W/m^2 - K) x 10^{4}			
	He (100)	He:Ar(51.8:48.2)	Ar (100)	He:Xe(89.8:10.2)
293	0.481	0.221	0.080	0.370
473	0.625	0.301	0.115	0.500
673	0.745	0.330	0.152	0.627
873	0.825	0.346	0.177	0.710

592 165

Pair Code: DUO2-33: Zr4-30

ISM-III

Gas Pressure: 0.103 MPa

Specimens in Light Contact:

Contact Pressure: 1770 N/m^2

Average Mean-Plane Gap: D_{mp} = 2.7 ± 3.9 μm ($3\sigma_{D_{mp}}$)

Temp K	H_g (W/m^2 - K) x 10^{-4}		
	He (100)	He:Ar(51.8:48.2)(a)	Ar (100)
293	1.31	0.717	0.384
473	1.47	0.938	0.481
573	1.55	1.01	----
673	1.56	1.04	0.518
773	1.48	0.995	0.529
823	1.54	----	0.524
873	1.54	1.12	0.534

(a) Mole %.

Average Mean-Plane Gap: D_{mp} = 8.6 ± 2.6 μm ($3\sigma_{D_{mp}}$)

Temp K	H_g (W/m^2 - K) x 10^{-4}		
	He (100)	He:Ar(51.8:48.2)	Ar (100)
293	1.01	0.540	0.272
473	1.07	0.629	0.346
573	1.15	----	0.387
673	1.10	0.694	0.416
773	1.16	----	0.383
873	1.17	0.687	0.293

592 166

ISM-III

Average Mean-Plane Gap: $D_{mp} = 19.4 \pm 2.6\ \mu m\ (3\sigma_{D_{mp}})$

Temp K	H_g (W/m^2 - K) x 10^{-4}	
	He (100)	He:Ar(51.8:48.2)
293	0.557	0.281
473	0.733	0.396
673	0.836	0.440
873	0.827	0.442

Average Mean-Plane Gap: $D_{mp} = 24.2 \pm 4.6\ \mu m\ (3\sigma_{D_{mp}})$

Temp K	H_g (W/m^2 - K) x 10^{-4}	
	He (100)	He:Ar(51.8:48.2)
293	0.496	0.242
473	0.666	0.298
673	0.726	0.365
873	0.789	0.393

APPENDIX E

MLD EXPERIMENTAL DATA

MLD EXPERIMENTAL DATA

CONTENTS

TABLE E.1. MLD Experimental Data. Pair Code: AL203-1: Zr4-1A; Block 00; ISM III.

Codes[a] GC	CP	D	Mean T K	ΔT K	% Energy Loss Q1	$H_g \times 10^{-4}$ W/m^2-K	±Error[b] x 10^{-4} W/m^2-K
1	2	2	477	5.97	0.00	0.163†	0.041
1	2	2	481	7.78	0.27	0.166†	0.033
1	2	2	480	9.47	0.10	0.166†	0.027
1	2	2	480	9.54	0.07	0.165†	0.027
1	2	2	676	6.52	-0.39	0.232†	0.054
1	2	2	868	5.67	-0.93	0.244†	0.065
2	2	2	474	39.70	-0.97	0.0226†	0.0012
2	2	2	473	38.82	0.31	0.0231†	0.0012
2	2	2	473	31.78	0.31	0.0232†	0.0014
2	2	2	474	24.42	0.07	0.0234†	0.0017
2	2	2	658	28.12	-0.50	0.0295†	0.0019
2	2	2	843	26.28	-1.43	0.0308†	0.0021
1	2	1	479	3.61	-0.56	0.486	0.203
1	2	1	480	3.37	0.00	0.492	0.220

(a) Code values (this page only).

Gas Composition (Mole %)	Gas Pressure (MPa)	Average Mean-Plane Gap (μm)
GC 1: He (100)	GP 1: 1.33E-7	D 1: 29.8
GC 2: Ar (100)	GP 2: 0.103	D 2: 135.0

(b) 3σ

† Large-gap (133 and 135 μm) data was considered unusable due to the possibility of a 25 μm (0.001 in.) error in the determination of D_{mp}. This error is considered to be the basis of the observation of anomalously high experimental H_g values in comparison to the maximum predicted by theory for both Helium and Argon gas as given by

$$H_g = \frac{K_{gas}}{D_{mp}}$$

where, $g_1 = g_2 = 0$. The experimental values of H_g themselves are not suspect and are considered to be valid within the uncertainty range specified in Tables E.1 through E.6.

TABLE E.2. MLD Experimental Data. Pair Code: AL203-1: Zr4-1A; Block 00; ISM III.

Codes[a] GC	CP	D	Mean T K	ΔT K	% Energy Loss Q1	Hg x 10^{-4} W/m^2-K	±Error[b] x 10^{-4} W/m^2-K
1	2	1	480	2.77	-0.23	0.498	0.270
1	2	1	676	3.17	-0.26	0.524	0.249
1	2	1	870	2.63	-0.55	0.599	0.342
2	2	1	474	12.93	-0.20	0.0781	0.0095
2	2	1	484	14.18	-0.52	0.0800	0.0089
2	2	1	490	8.59	-0.05	0.0768	0.0137
2	2	1	675	12.28	0.00	0.0971	0.0124
2	2	1	668	9.07	0.18	0.0958	0.0162
2	2	1	848	13.19	0.24	0.112	0.013
2	2	1	860	6.50	1.20	0.135	0.032

(a) Code values (this page only).

Gas Composition (Mole %)	Gas Pressure (MPa)	Average Mean-Plane Gap (μm)
GC 1: He (100)	GP 1: 1.33E-7	D 1: 29.8
GC 2: Ar (100)	GP 2: 0.?03	D 2: 135.0

(b) 3σ

TABLE E.3. MLD Experimental Data. Pair Code: DUO2-O: Zr4-O; Block O; ISM II.

Codes[a] GC	CP	D	Mean T K	ΔT K	% Energy Loss Q1	$H_g \times 10^{-4}$ W/m^2-K	±Error[b] x 10^{-4} W/m^2-K
2	2	1	471	9.77	-0.03	0.103	0.016
2	2	1	672	5.60	0.11	0.169	0.046
1	2	2	466	5.25	0.26	0.304	0.088
2	2	2	472	17.09	-0.09	0.0510	0.0048
1	2	3	469	6.64	0.31	0.192†	0.044
1	2	3	666	4.13	0.49	0.289†	0.106
2	2	3	468	32.05	0.55	0.0251†	0.0015
2	2	3	665	22.16	0.44	0.0385†	0.0030

(a) Code values (this page only).

Gas Composition (Mole %)	Gas Pressure (MPa)	Average Mean-Plane Gap (μm)
GC 1: He (100)	GP 1: 1.33E-7	D 1: 30.3
GC 2: Ar (100)	GP 2: 0.172	D 2: 56.0
		D 3: 133.0

(b) 3σ

† Large-gap (133 and 135 μm) data was considered unusable due to the possibility of a 25 μm (0.001 in.) error in the determination of D_{mp}. This error is considered to be the basis of the observation of anomalously high experimental H_g values in comparison to the maximum predicted by theory for both Helium and Argon gas as given by

$$H_g = \frac{K_{gas}}{D_{mp}}$$

where, $g_1 = g_2 = 0$. The experimental values of H_g themselves are not suspect and are considered to be valid within the uncertainty range specified in Tables E.1 through E.6.

TABLE E.4. MLD Experimental Data. Pair Code: DUO2-0: Zr4-0; Block 0; ISM II.

Codes[a] GC	GP	D	CP MN/m^2	Mean T K	ΔT K	% Energy Loss Q1	H_T or H_C x 10^{-4} W/m^2-K	±Error[b] x 10^{-4} W/m^2-K
2	2	4	0.043	466	2.81	-0.71	0.459	0.246
2	1	4	0.043	486	33.57	-1.21	0.00823	0.00047
2	1	4	0.043	671	35.13	0.12	0.0144	0.0008
2	1	4	0.043	661	36.76	1.15	0.0164	0.0009
2	1	-	0.965	663	14.66	0.72	0.0635	0.0069
2	1	-	3.447	660	7.59	0.97	0.140	0.028
2	1	-	6.895	659	4.58	0.95	0.254	0.084
2	1	-	10.342	662	3.10	0.75	0.390	0.189
2	1	-	14.686	659	1.95	0.68	0.633	0.488
2	1	-	6.895	663	2.92	0.55	0.405	0.209
2	1	-	0.043	672	34.03	-1.05	0.0167	0.0010

(a) Code values (this page only).

Gas Composition (Mole %)	Gas Pressure (MPa)	Average Mean-Plane Gap (μm)
GC 1: He (100)	GP 1: 1.33E-7	D 4: 7.6
GC 2: Ar (100)	GP 2: 0.172	

(b) 3σ

TABLE E.5. MLD Experimental Data. Pair Code: DUO2-1: Zr4-1; Block 1; ISM II.

Codes[a] GC	GP	D	CP MN/m^2	Mean T K	ΔT K	% Energy Loss Ql	H_T or H_C x 10^{-4} W/m^2-K	±Error[b] x 10^{-4} W/m^2-K
2	2	4	0.043	628	6.26	1.7	0.616	0.149
2	1	4	0.043	718	53.73	0.72	0.0245	0.0011
2	1	-	0.965	704	35.94	0.29	0.0503	0.0028
2	1	-	3.29	676	32.44	1.62	0.0692	0.0041
2	1	-	6.83	657	23.77	2.19	0.110	0.008
2	1	-	10.41	641	15.83	2.55	0.184	0.019
2	1	-	14.79	630	10.51	2.98	0.299	0.044
2	1	-	10.48	635	13.72	2.68	0.218	0.025
2	1	-	6.94	649	22.56	2.41	0.119	0.009
2	1	-	3.21	670	44.96	1.80	0.0475	0.0023
2	1	-	0.043	735	54.32	-2.07	0.0223	0.0010
2	1	-	3.29	675	40.74	1.67	0.0526	0.0027
2	1	-	7.00	655	26.73	2.28	0.0974	0.0065
2	1	-	10.41	640	17.01	2.56	0.172	0.016
2	1	-	14.65	630	11.38	2.74	0.286	0.039

(a) Code values (this page only).

Gas Composition (Mole %)	Gas Pressure (MPa)	Average Mean-Plane Gap (μm)
GC 1: He (100)	GP 1: 1.33E-7	D 4: 3.6
GC 2: Ar (100)	GP 2: 0.172	

(b) 3σ

TABLE E.6. MLD Experimental Data. Pair Code: DUO2-2: Zr4-2; Block 2; ISM I.

Codes[a] GC	GP	D	CP MN/m^2	Mean T K	ΔT K	% Energy Loss Q1	H_T or H_C x 10^{-4} W/m^2-K	±Error[b] x 10^{-4} W/m^2-K
2	2	4	0.043	625	6.34	2.67	0.578	0.138
2	1	4	0.043	728	57.77	-1.45	0.0196	0.0009
2	1	-	0.414	711	58.28	-0.41	0.0223	0.0010
2	1	-	0.931	710	57.77	0.23	0.0231	0.0010
2	2	-	0.931	696	6.56	1.12	0.417	0.097
2	1	-	3.31	710	36.36	0.06	0.0430	0.0024
2	1	-	6.83	707	27.01	0.08	0.0724	0.0048
2	2	-	6.76	697	3.48	0.83	0.835	0.361
2	2	-	10.41	696	1.98	0.86	1.49	1.13
2	1	-	10.45	697	16.72	1.26	0.151	0.015
2	1	-	14.48	686	13.04	1.67	0.212	0.026
2	2	-	6.90	695	2.40	0.81	1.23	0.77
2	1	-	6.83	706	27.82	0.71	0.0704	0.0046
2	1	-	3.52	706	38.44	0.70	0.0428	0.0023
2	1	-	0.043	736	34.37	-2.93	0.0261	0.0015
2	2	-	0.043	625	4.13	2.21	0.896	0.327

(a) Code values (this page only).

Gas Composition (Mole %)	Gas Pressure (MPa)	Average Mean-Plane Gap (μm)
GC 2: Ar (100)	GP 1: 1.33E-7	D 4: 21.8
	GP 2: 0.172	

(b) 3σ

APPENDIX F

SURFACE CHARACTERIZATION OF MLD AND MPD SPECIMENS

F.0 SURFACE CHARACTERIZATION OF MLD AND MPD SPECIMENS

F.1 OPTICAL HEIGHT GAGE CHARACTERIZATION

Figure F.1 shows the coordinate positions on the sample surface at which the local height elevations were measured. Tables F.1 to F.6 contain the calculated local gap between asperity tips $(D_a)_i$ and the average gap between asperity tips D_a for all MPD and MLD specimen pairs used in this study.

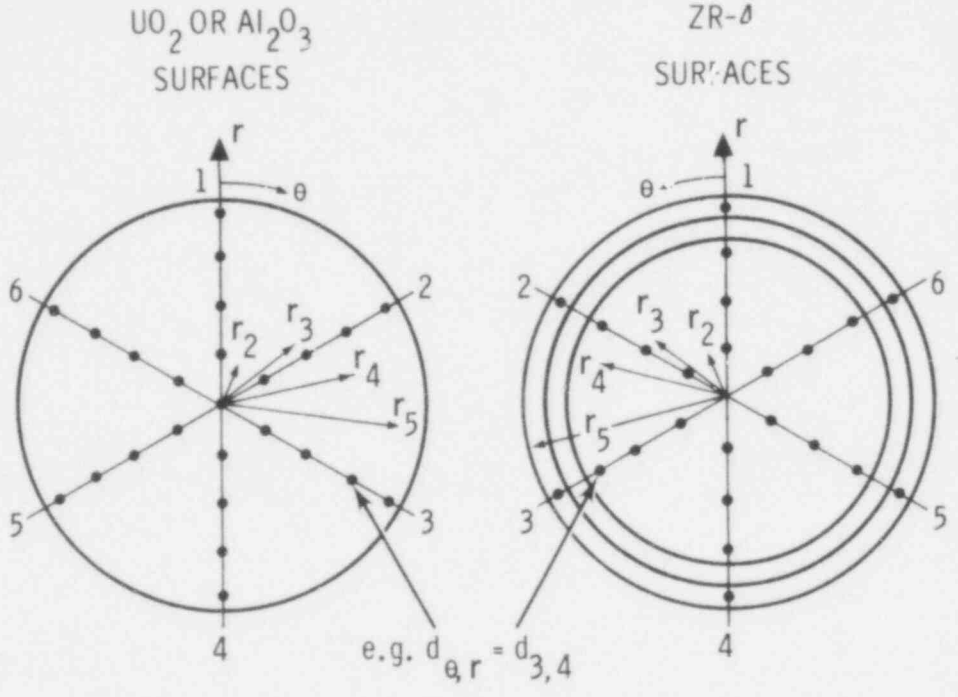

RADIAL COORDINATE	MPD (mm)	MLD (mm) (Al_2O_3-Zr4)	MLD (mm) (UO_2-Zr4)
r_1	0	0	0
r_2	1.73	2.54	2.54
r_3	3.46	5.08	5.08
r_4	5.19	11.43	11.43
r_5	6.92	22.22	23.50

FIGURE F.1. Coordinate Positions Used in the Optical Height Gage Technique for Surface Characterization of MPD and MLD Specimens

TABLE F.1. Local $(D_a)_i$ and Average D_a Gaps Between Asperity Tips for DUO_2-41:Zr4-32 MPD Specimen Pair (ISM-I) as Calculated from Optical Height Gage Measurements

Coordinate Position θ, r	Index i	DUO_2-41:Zr4-32 $(D_a)_i$ [b] (μm)	DUO_2-41:Zr-32 $(D_a)_i$ (μm)
1, 5[a]	20	12.98	0.00
1, 4	14	0.03[c]	12.83
1, 3	8	1.22	13.41
1, 2	2	3.18	13.51
1, 1	1	1.14	13.96
4, 2	5	0.74	13.97
4, 3	11	1.83	13.94
4, 4	17	1.25	15.67
4, 5	23	9.78	24.61
2, 5	21	16.92	26.44
2, 4	15	0.44	12.17
2, 3	9	1.55	14.25
2, 2	3	1.04	12.83
1, 1	1	1.14	13.96
5, 2	6	0.03[c]	13.34
5, 3	12	0.91	14.25
5, 4	18	3.96	14.33
5, 5[a]	24	10.33	0.00
3, 5[a]	22	11.68	10.00
3, 4	16	0.00[c]	12.57
3, 3	10	0.97	13.97
3, 2	4	2.16	14.05
1, 1	1	1.14	13.96
6, 2	7	1.73	14.02
6, 3	13	2.95	14.05
6, 4	19	1.32	12.98
6, 5	25	10.39	22.66
	D_a (μm) =	1.4	13.7
	$3\sigma_{D_a}$ (μm) =	3.2	2.4
	$3\sigma_{D_a}$ (%) =	229%	17%

(a) Spacer location.
(b) Calculated under light contact conditions.
(c) Contact spot (assumed).

592 178

TABLE F.2. Local $(D_a)_i$ and Average D_a Gaps Between Asperity Tips for MPD and ISM-II DUO_2:Zr4 Specimen Pairs as Calculated from Optical Height Gage Measurements

Coordinate Position θ, r	Index i	DUO_2-40 Zr4-25 $(D_a)_i$ (μm)	DUO_2-25 Zr4-25 $(D_a)_i$ (μm)	DUO_2-25 Zr4-25 $(D_a)_i$ (μm)	DUO_2-40 Zr4-25 $(D_a)_i$ (μm)	DUO_2-25 Zr4-25 $(D_a)_i$ (μm)
1, 5[b]	20	1.17	5.13	9.91	0.00	25.65
1, 4	14	1.37	2.36	3.07	9.02	18.82
1, 3	8	1.27	0.08[c]	3.23	7.82	18.97
1, 2	2	1.47	0.69	5.97	7.52	21.72
1, 1	1	0.86	1.50	6.25	7.57	22.00
4, 2	5	1.75	3.78	10.36	8.18	26.11
4, 3	11	0.79	2.44	9.09	8.59	24.84
4, 4	17	1.32	2.64	9.86	9.07	25.60
4, 5	23	0.76	0.00[c]	6.99	9.78	22.73
2, 5	21	0.41	2.79	12.42	11.73	28.17
2, 4	15	0.00[c]	1.15	8.03	9.09	23.77
2, 3	9	0.23	1.09	7.54	7.98	23.29
2, 2	3	0.64	1.73	8.41	7.44	24.16
1, 1	1	0.86	1.50	6.25	7.57	22.00
5, 2	6	1.07	3.68	8.51	7.26	24.26
5, 3	12	0.18	2.92	6.48	7.95	22.23
5, 4	18	0.36	5.08	7.01	8.92	22.76
5, 5[b]	24	0.00[c]	9.07	9.91	0.99	25.65
3, 5[b]	22	1.91	0.00[c]	9.91	0.00	25.65
3, 4	16	0.00[c]	1.52	9.50	9.98	25.25
3, 3	10	0.23	2.41	10.16	9.40	25.91
3, 2	4	1.70	2.16	8.56	8.99	24.31
1, 1	1	0.86	1.50	6.25	7.57	22.00
6, 2	7	0.23	2.57	6.91	7.24	22.66
6, 3	13	1.14	2.97	5.28	8.26	21.03
6, 4	19	1.45	4.57	4.98	8.26	20.73
6, 5	25	2.59	8.38	6.76	10.80	22.50
	D_a (μm) =	0.9[a]	2.4[a]	7.3	8.3	23.1
	$3\sigma_{D_a}$ (μm) =	1.8	3.8	6.5	2.4	6.6
	$3\sigma_{D_a}$ (%) =	200%	158%	89%	29%	29%

(a) Light contact conditions.
(b) Spacer location.
(c) Contact point (assumed).

592 179

TABLE F.3. Local $(D_a)_i$ and Average D_a Gaps Between Asperity Tips for DUO_2-33:Zr4-30 MPD ISM-III Specimen Pairs. Local gaps were calculated from optical height gage measurements.

Coordinate Position θ, r	Index i	$(D_a)_i$ (μm)[a]	$(D_a)_i$ (μm)	$(D_a)_i$ (μm)	$(D_a)_i$ (μm)
1, 5[b]	20	1.35	10.87	21.74	25.20
1, 4	14	0.00[c]	8.59	19.46	23.85
1, 3	8	1.12	8.79	19.66	24.08
1, 2	2	1.19	7.95	18.82	25.56
1, 1	1	3.35	9.19	20.06	24.74
4, 2	5	3.84	8.76	19.63	23.77
4, 3	11	3.30	7.32	18.19	22.15
4, 4	17	3.10	6.20	17.07	20.78
4, 5	23	0.00[c]	2.13	13.00	23.65
2, 5	21	6.12	14.33	25.20	29.18
2, 4	15	0.00[c]	7.80	18.67	24.03
2, 3	9	1.07	8.10	18.97	23.32
2, 2	3	2.26	8.69	19.56	23.55
1, 1	1	3.35	9.19	20.06	24.74
5, 2	6	3.89	9.14	20.01	25.55
5, 3	12	3.89	8.56	19.43	24.00
5, 4	18	3.45	7.54	18.41	24.32
5, 5[b]	24	7.37	10.87	21.74	26.01
3, 5[b]	22	6.35	10.87	21.74	24.56
3, 4	16	2.16	7.01	17.88	20.93
3, 3	10	2.36	7.54	18.41	22.10
3, 2	4	3.84	9.35	20.22	25.25
1, 1	1	3.35	9.19	20.06	24.74
6, 2	7	3.12	9.32	20.19	25.73
6, 3	13	2.41	8.92	19.79	25.50
6, 4	19	1.42	8.26	19.13	25.50
6, 5	25	3.30	10.49	21.36	26.49
	D_a (μm) =	2.4	8.3	19.1	23.9
	$3\sigma_{D_a}$ (μm) =	3.9	2.6	2.6	4.6
	$3\sigma_{D_a}$ (%) =	163%	31%	14%	19%

(a) Light contact conditions.
(b) Spacer location.
(c) Contact point (assumed).

TABLE F.4. Local $(D_a)_i$ and Average D_a Gaps Between Asperity Tips for MLD Block 00 Al_2O_3:Zr4 ISM-III Sample Pair. Local gaps were calculated from optical height gage measurements.

Coordinate Position θ, r	Index i	$(D_a)_i$ (μm)	$(D_a)_i$ (μm)
1, 5[(a)]	20	24.61	129.79
1, 4	14	31.88	137.06
1, 3	8	29.46	134.65
1, 2	2	29.03	134.21
1, 1	1	28.32	133.50
4, 2	5	28.50	133.68
4, 3	11	28.12	133.30
4, 4	17	30.15	135.30
4, 5	23	22.25	127.43
2, 5	21	21.89	127.76
2, 4	15	32.61	137.80
2, 3	9	29.32	135.00
2, 2	3	29.13	134.32
1, 1	1	28.32	133.50
5, 2	6	27.79	132.97
5, 3	12	28.63	133.81
5, 4	18	30.20	135.38
5, 5[(a)]	24	24.61	129.79
3, 5[(a)]	22	24.61	129.79
3, 4	16	30.68	135.86
3, 3	10	29.11	134.29
3, 2	4	28.32	133.50
1, 1	1	28.32	133.50
6, 2	7	29.18	134.37
6, 3	13	29.44	134.62
6, 4	19	30.73	135.92
6, 5	25	29.46	134.65
	D_a (μm) =	29.5	134.7
	$3\sigma_{D_a}$ (μm) =	3.8	3.8
	$3\sigma_{D_a}$ (%) =	13%	2.8%

(a) Spacer locations.

TABLE F.5. Local $(D_a)_i$ and Average D_a Gaps Between Asperity Tips for MLD Block 0 and Block 1 DUO_2:Zr4 ISM-II Sample Pairs. Local gaps were calculated from optical height gage measurements.

Coordinate Position θ, r	Index i	Block 0 $(D_a)_i$ (μm)(b)	Block 0 $(D_a)_i$ (μm)	Block 0 $(D_a)_i$ (μm)	Block 0 $(D_a)_i$ (μm)	Block 1 $(D_a)_i$ (μm)(b)
1, 5[a]	20	--	0.00	25.70	102.77	--
1, 4	14	7.42	29.54	55.25	132.31	0.08
1, 3	8	5.23	27.66	53.37	130.43	0.08
1, 2	2	4.93	27.46	53.16	130.23	0.23
1, 1	1	4.98	27.61	53.31	130.38	0.48
4, 2	5	4.52	27.31	52.98	130.05	0.05
4, 3	11	4.04	26.92	52.63	129.69	0.03[c]
4, 4	17	0.08[c]	23.24	48.95	126.01	1.22
4, 5	23	--	23.95	49.66	126.72	--
2, 5	21	--	17.58	43.28	120.35	--
2, 4	15	0.00[c]	24.82	50.50	127.56	0.00[c]
2, 3	9	4.60	28.27	53.98	131.04	0.15
2, 2	3	5.51	28.68	54.38	131.45	0.28
1, 1	1	4.98	27.61	53.31	130.38	0.48
5, 2	6	4.37	26.49	52.20	129.26	0.36
5, 3	12	3.98	25.55	51.26	128.32	0.91
5, 4	18	0.00[c]	20.29	46.00	123.06	1.40
5, 5[a]	24	--	0.00	25.70	102.77	--
3, 5[a]	22	--	0.00	25.70	102.77	--
3, 4	16	3.70	30.18	55.85	132.92	0.53
3, 3	10	5.08	28.98	54.69	131.75	0.20
3, 2	4	6.27	29.57	55.27	132.33	0.25
1, 1	1	4.98	27.61	53.31	130.38	0.48
6, 2	7	5.44	27.46	53.16	130.23	0.46
6, 3	13	5.03	26.44	52.15	129.21	0.43
6, 4	19	8.08	27.89	53.59	130.66	0.03[c]
6, 5	25	--	25.30	51.00	128.07	--
	D_a (μm) =	4.4	27.1	52.8	129.8	0.4
	$3\sigma_{D_a}$ (μm) =	6.7	7.1	7.1	7.1	1.2
	$3\sigma_{D_a}$ (%) =	152%	26%	13%	5.5%	300%

(a) Spacer location.
(b) Light contact conditions.
(c) Contact spot (assumed).

592 182

TABLE F.6. Local $(D_a)_i$ and Average D_a Gaps Between Asperity Tips for Block 2 DUO_2-Zr4 Sample Pair in Light Contact. Local gaps were calculated from optical height gage measurements.

Coordinate Position θ, r	Index i	$(D_a)_i$ (μm)[a]
1, 5	20	---
1, 4	14	5.96
1, 3	8	2.06
1, 2	2	0.00[b]
1, 1	1	2.31
4, 2	5	0.18
4, 3	11	0.00[b]
4, 4	17	3.10
4, 5	23	---
2, 5	21	---
2, 4	15	4.47
2, 3	9	1.17
2, 2	3	0.05
1, 1	1	2.31
5, 2	6	0.81
5, 3	12	3.58
5, 4	18	5.69
5, 5	24	---
3, 5	22	---
3, 4	16	4.67
3, 3	10	0.00[b]
3, 2	4	2.49
1, 1	1	2.31
6, 2	7	4.55
6, 3	13	3.66
6, 4	19	2.36
6, 5	25	---
	D_a (μm)	= 2.5
	$3\sigma_{D_a}$ (μm)	= 6.0
	$3\sigma_{D_a}$ (%)	= 240%

(a) Light contact conditions.
(b) Contact spot (assumed).

F.2 PROFILOMETER TRACES

Figures F.2 and F.3 show typical profilometer traces obtained from ISM-I, ISM-II, and ISM-III DUO_2 and Zr4 specimen surfaces. Table F.7 summarizes the CLA and γ values for all surfaces. (The determination of γ values is described in Section 4.2.4 of the Experimental Section.)

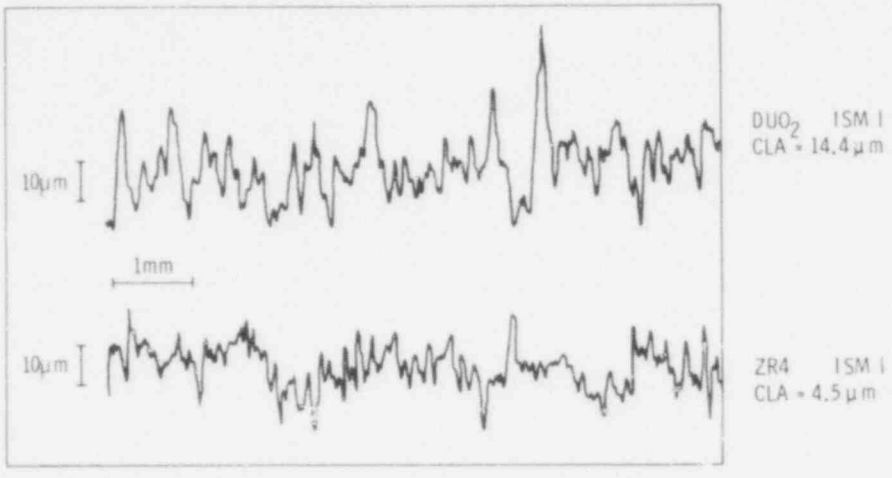

FIGURE F.2. Typical Profilometer Traces of ISM-I DUO_2 and Zr4 Surfaces

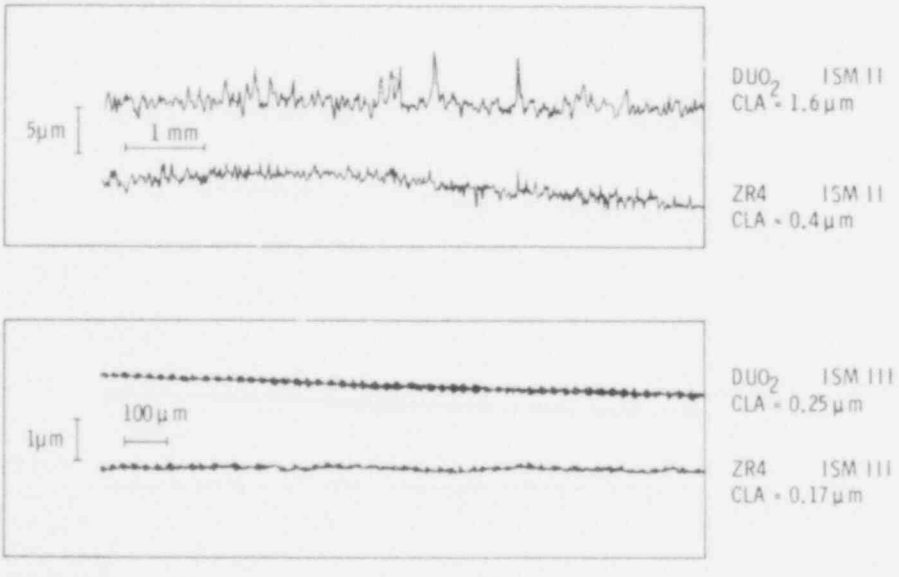

FIGURE F.3. Typical Profilometer Traces of ISM-II and ISM-III DUO_2 and Zr4 Surfaces

TABLE F.7. CLA_1, CLA_2, $\bar{x}$, γ_1, and γ_2 Values for the ISM-I, II, and III Surfaces

	$CLA^{(a)}$ (μm)	3σ (μm)	$\bar{x}^{(a)}$ (μm)	γ (μm)	3σ (μm)
UO_2 ISM-I	14.4	2.8	2	11.3	10.6
UO_2 ISM-II	1.6	0.7	1	1.8	1.1
UO_2 ISM-III	0.25	0.05	0.1	0.15	0.05
Zr ISM-I	4.5	0.4	2	8.0	4.9
Zr ISM-II	0.4	0.2	1	1.4	0.5
Zr ISM-III	0.17	0.05	0.1	0.14	0.03

(a) Cut-off wavelength = 760 μm.
(b) Averaging interval used to determine the position of the mean-plane (line).

F.3 AVERAGE MEAN-PLANE GAP

Tables F.8 and F.9 summarize the values obtained for the average mean-plane gap (D_{mp}) for the MPD and MLD sample pairs.

592 185

TABLE F.8. Determined Values for D_{mp} for all MPD Specimen Pairs

ISM	UO_2 #	UO_2 γ_1 (μm)	Zr #	Zr γ_2 (μm)	Average Gap Between Asperities D_a (μm)(a)	Average Gap Between Asperities $3\sigma_{D_a}$ (μm)	Average Mean-Plane Gap D_{mp} (μm)(c)	Average Mean-Plane Gap $3\sigma_{D_{mp}}$ (μm)	Average Mean-Plane Gap $3\sigma_{D_{mp}}$ %	ψ(d)
I	41	11.3	32	8.0	1.4(b)	3.2	20.7	3.2	15	4.57
I	41	11.3	32	8.0	13.7	2.4	33.0	2.4	7	2.86
II	40	1.8	25	1.4	0.9(b)	1.8	4.1	1.8	44	2.44
II	40	1.8	25	1.4	8.3	2.4	11.5	2.4	21	0.87
II	25	1.8	25	1.4	2.4(b)	3.8	5.6	3.8	68	1.79
II	25	1.8	25	1.4	7.3	6.5	10.5	6.5	62	0.95
II	25	1.8	25	1.4	23.1	6.6	26.3	6.6	25	0.38
III	33	0.15	30	0.14	2.4(b)	3.9	2.7	3.9	144	0.78
III	33	0.15	30	0.14	8.3	2.6	8.6	2.6	30	0.24
III	33	0.15	30	0.14	19.1	2.6	19.4	2.6	13	0.11
III	33	0.15	30	0.14	23.9	4.6	24.2	4.6	19	0.09

(a) $D_a = \left[\sum_{i=1}^{19} (D_a)_i\right] \times 1/19$

(b) Light contact.

(c) $D_{mp} = \frac{1}{19}\left[\sum_{i=1}^{19} (D_a)_i\right] + \gamma_1 + \gamma_2 = D_a + \gamma_1 + \gamma_2$

(d) $\psi = \frac{5(CLA_1 + CLA_2)}{D_{mp}}$

TABLE F.9. Calculation of D_{mp} for all MLD Specimen Pairs

Block	ISM	Sample Pair Sample #	Sample Pair γ_1 (μm)	Sample Pair Sample #	Sample Pair γ_2 (μm)	Average Gap Between Asperities D_a (μm)	Average Gap Between Asperities $3\sigma_{D_a}$ (μm)	Average Mean-Plane Gap D_{mp} (μm)	Average Mean-Plane Gap $3\sigma_{D_{mp}}$ (μm)	Average Mean-Plane Gap $3\sigma_{D_{mp}}$ %	ψ(b)
00	III	Al_2O_3-1	0.15	Zr4-1A	0.14	29.5	3.8	29.8	3.8	13	0.07
00	III	Al_2O_3-1	0.15	Zr4-1A	0.14	134.7	3.8	135.0	3.8	2.8	0.02
0	II	DUO_2-0	1.8	Zr4-0	1.4	4.4(a)	6.7	7.6	6.7	88	1.32
0	II	DUO_2-0	1.8	Zr4-0	1.4	27.1	7.1	30.3	7.1	23	0.33
0	II	DUO_2-0	1.8	Zr4-0	1.4	52.8	7.1	56.0	7.1	13	0.18
0	II	DUO_2-0	1.8	Zr4-0	1.4	129.8	7.1	133.0	7.1	5.3	0.08
1	II	DUO_2-1	1.8	Zr4-1	1.4	0.4(a)	1.2	3.6	1.2	33	2.78
2	I	DUO_2-2	11.3	Zr4-2	8.0	2.5(a)	6.0	21.8	6.0	28	4.33

(a) Light contact.

(b) $\psi = \frac{5(CLA_1 + CLA_2)}{D_{mp}}$

592 186

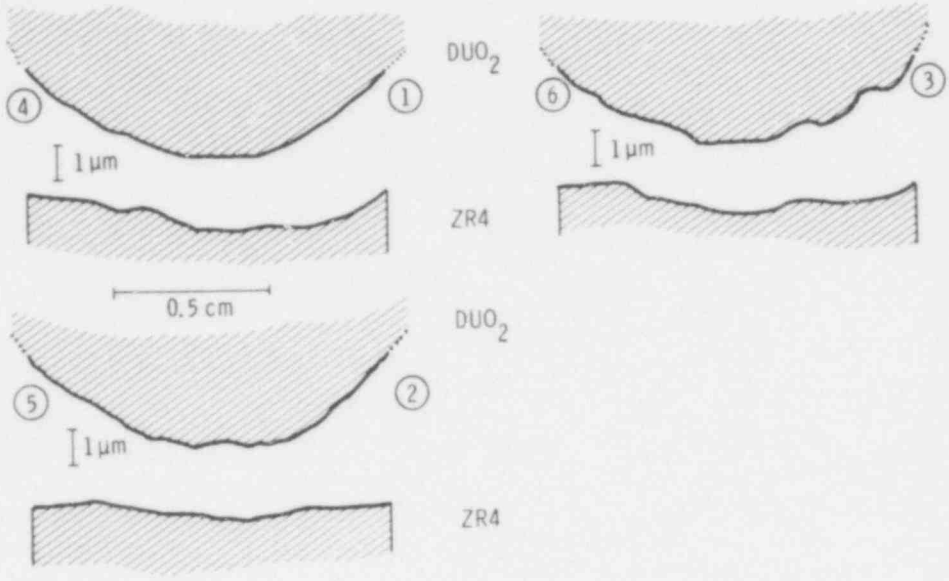

FIGURE F.4. Surface Error of Form for the MPD ISM-III UO_2-33:Zr4-30 Specimen Pair. (Sections correspond to those shown in Figure F.1.)

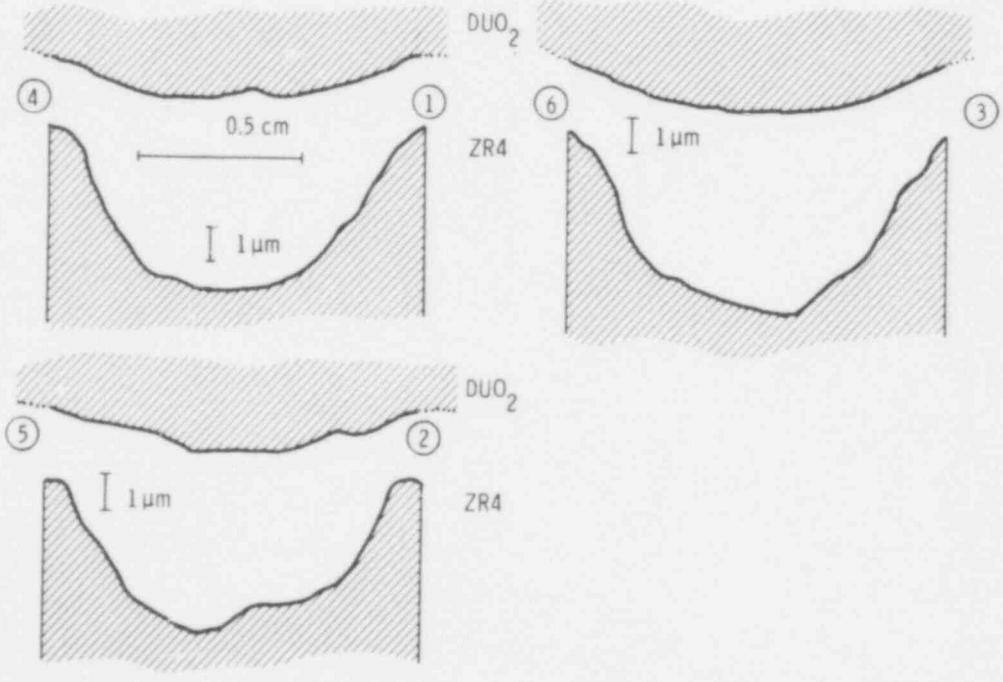

FIGURE F.5. Error of Form for the ISM-II UO_2-40:Zr4-25 MPD Specimen Pair. (Sections correspond to those indicated in Figure F.1.)

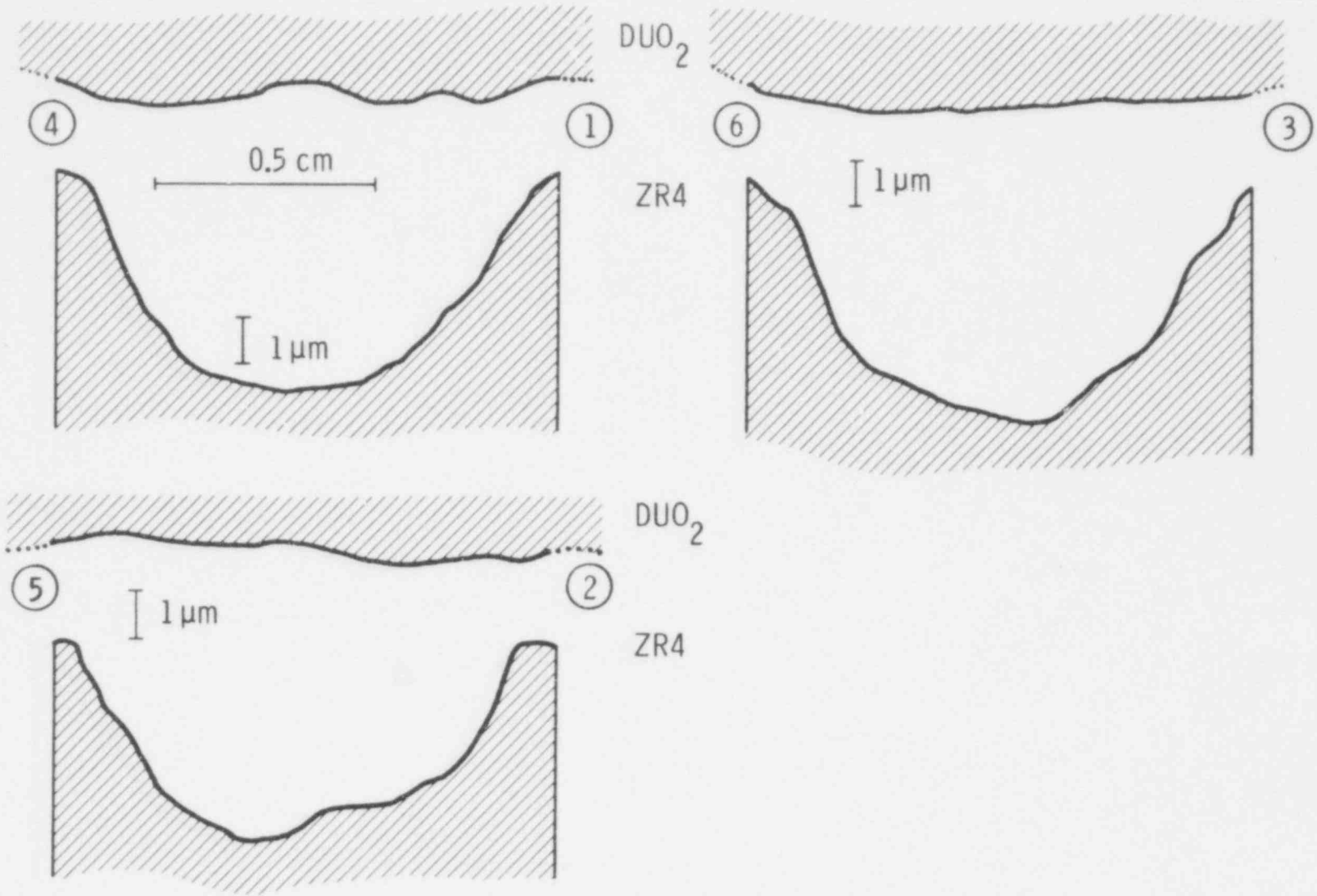

FIGURE F.6. Error of Form for the ISM-II UO_2-25:Zr4-25 MPD Specimen Pair. (Sections correspond to those indicated in Figure F.1.)

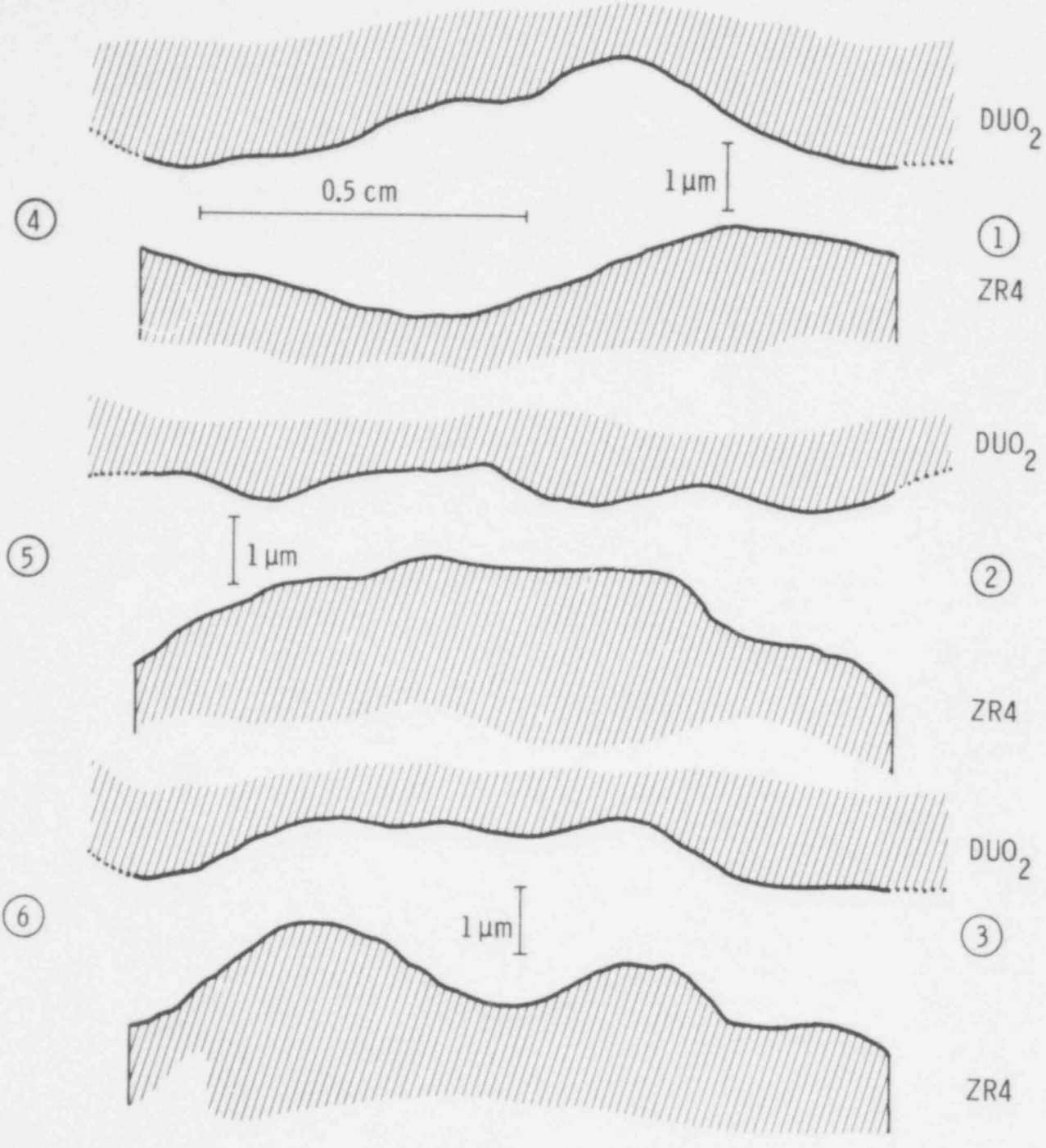

FIGURE F.7. Error of Form for the ISM-I UO_2-41:Zr4-32 MPD Specimen Pair. (Sections correspond to those indicated in Figure F.1.)

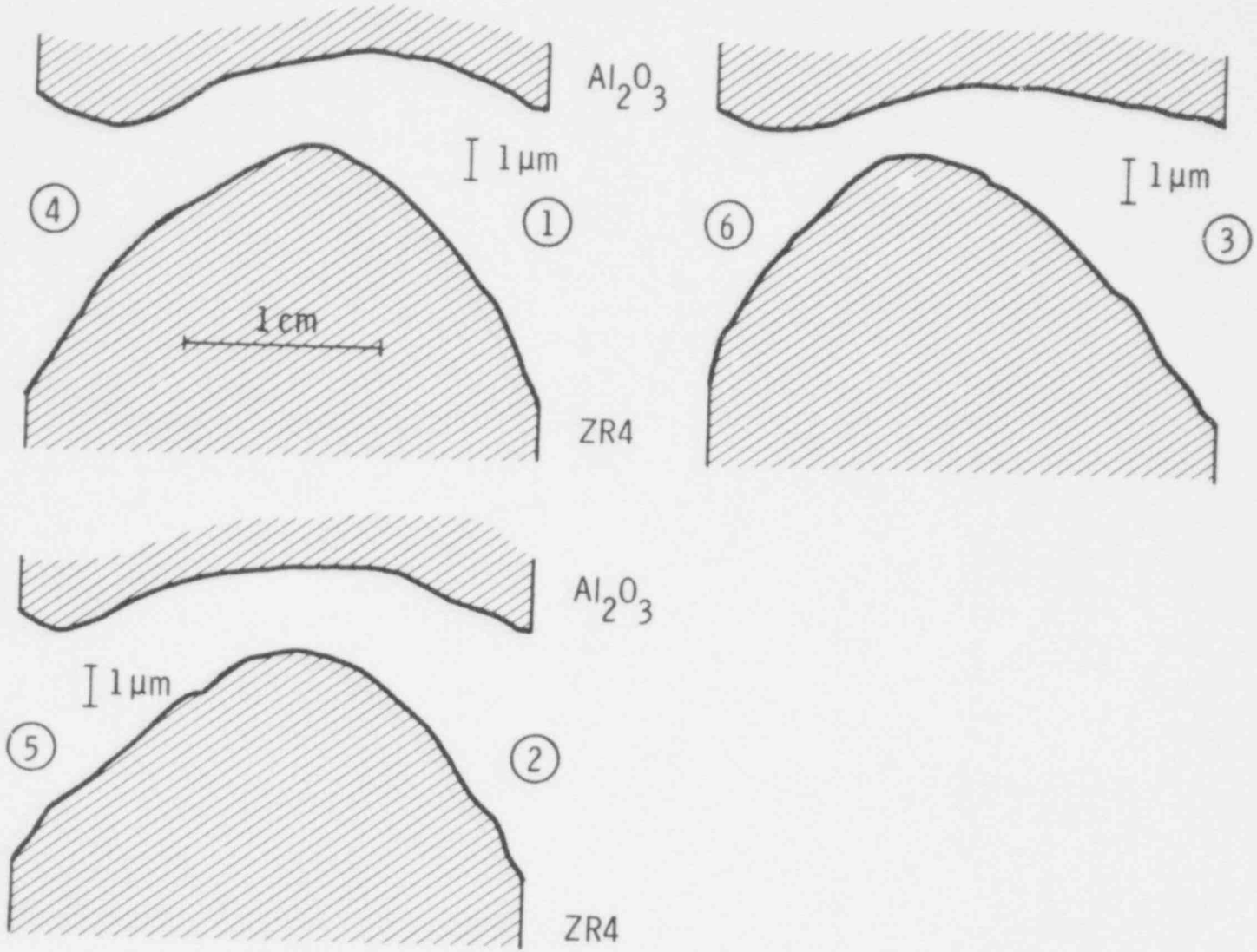

FIGURE F.8. Surface Error of Form Through Three Sections of the Block "00" Al_2O_3:Zr4 Specimen Pair. (Section coordinates are given in Figure F.1.)

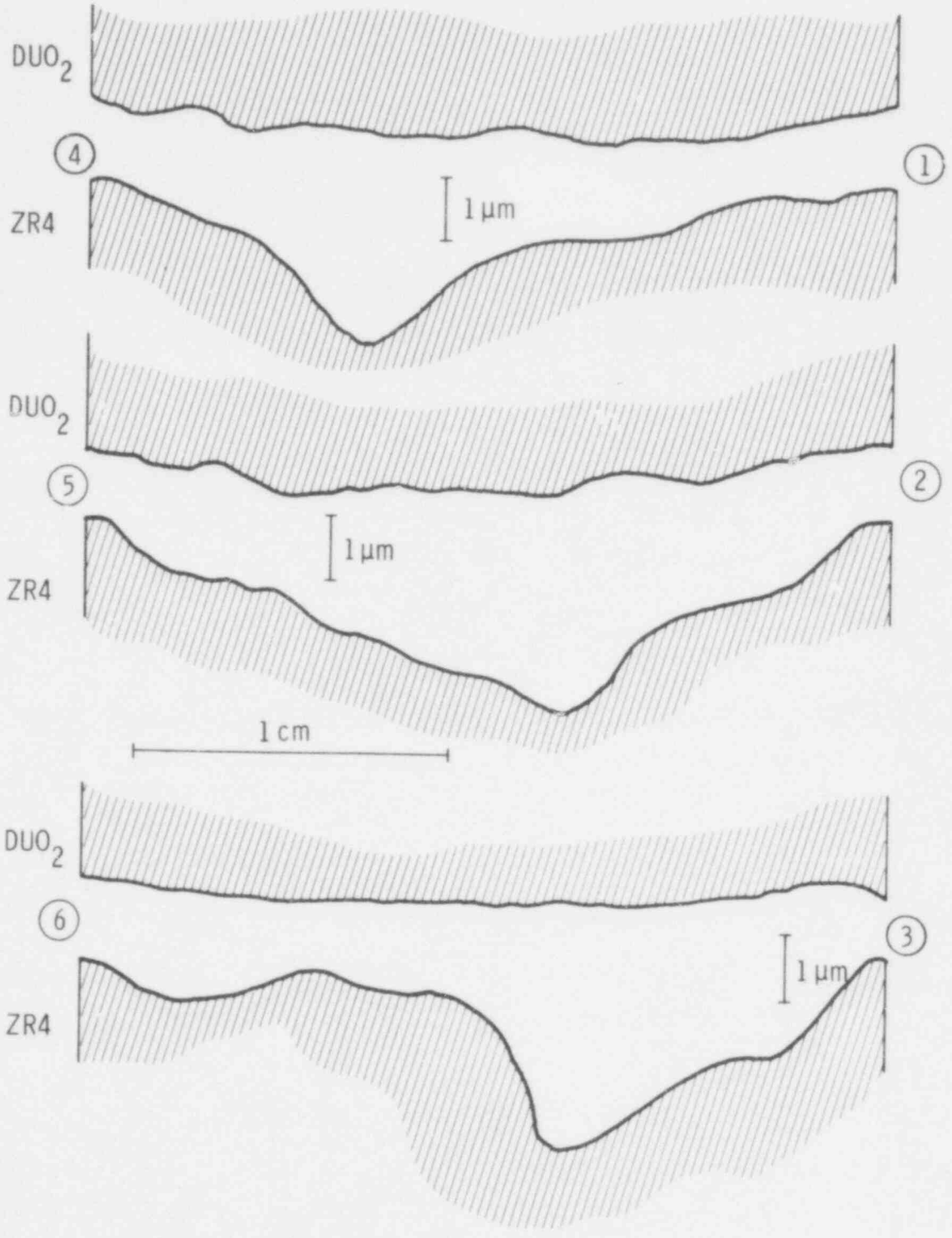

FIGURE F.9. Surface Error of Form Through Three Sections of the ISM-II Block "0" DUO_2:Zr4 Specimen Pair

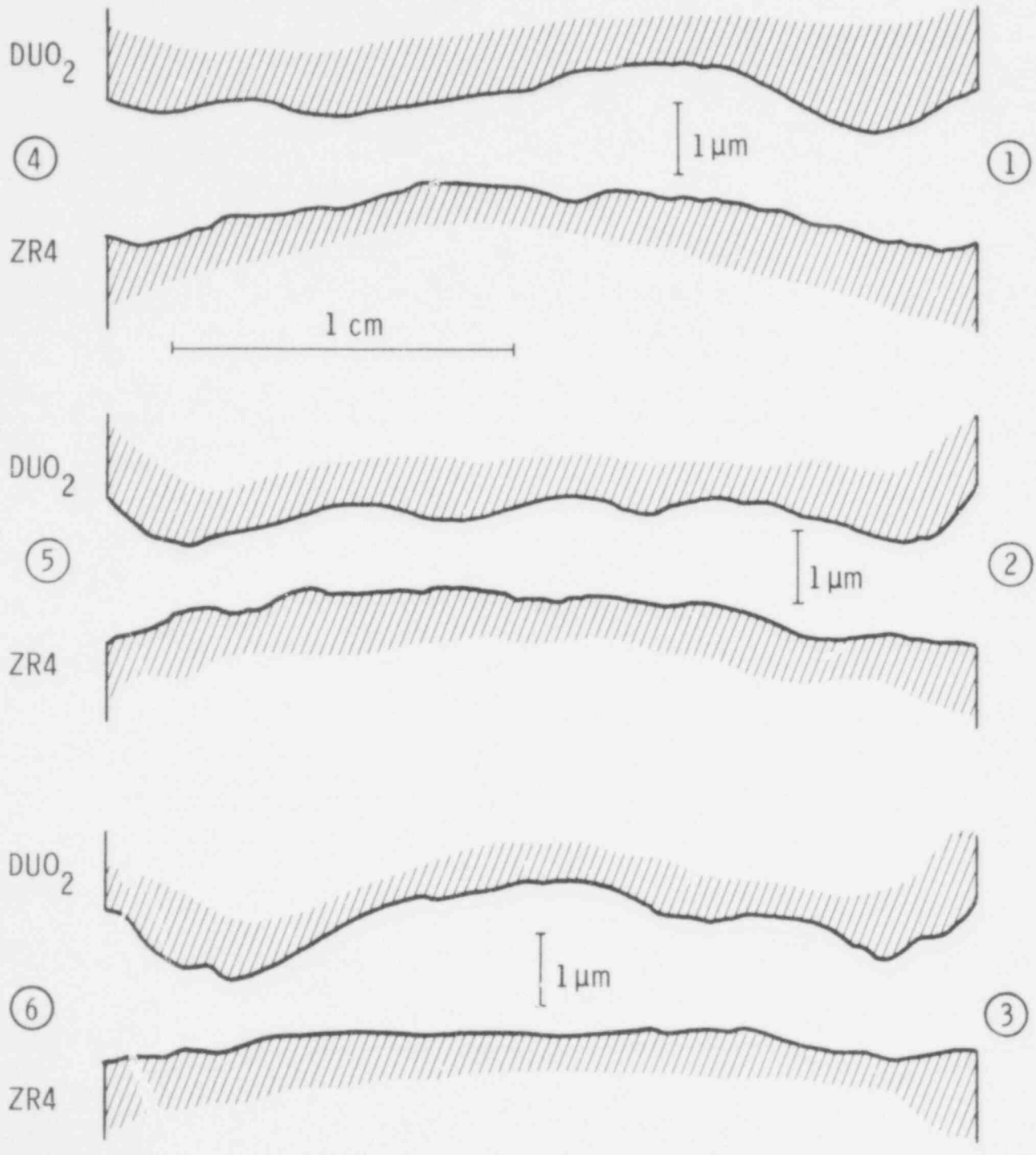

FIGURE F.10. Surface Error of Form for the MLD DUO_2:Zr4 Block 1 Specimens Through Three Sections. (Described previously in Figure F.1.)

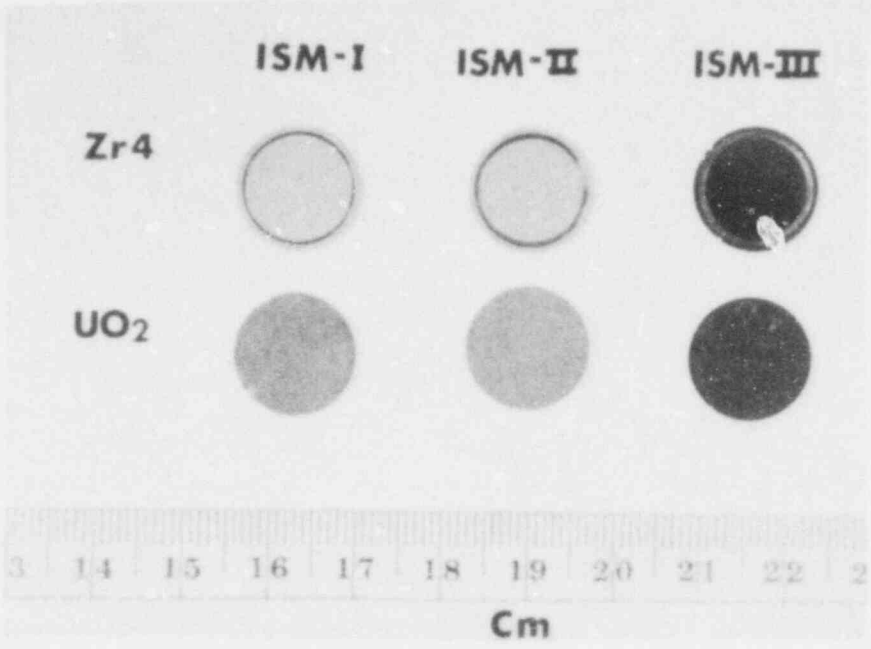

FIGURE F.11. Photograph of MPD UO_2 and Zr4 Specimens (ISM-I, II, and III)[2]

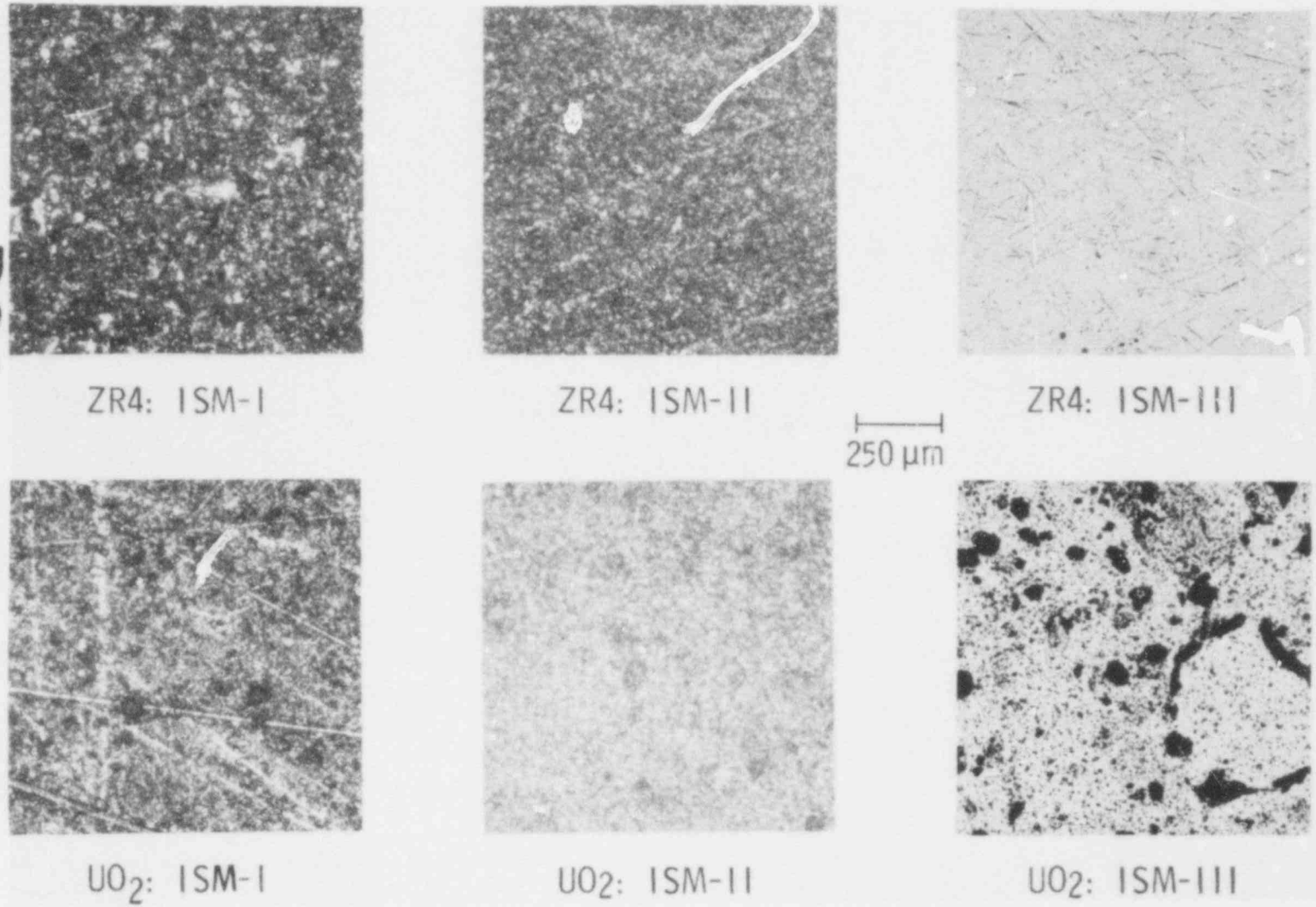

FIGURE F.12. Representative Photographs of ISM-I, II and III UO_2 and Zr4 Specimen Surfaces (50X)

APPENDIX G

NUMERICS FOR CALCULATING THE BEST FITTING MPD H_g VALUES FROM A SET OF DATA

G.0 NUMERICS FOR CALCULATING THE BEST FITTING MPD H_2 VALUES FROM A SET OF DATA

G.1 NUMERICS

The numerics for calculating the best fitting h values for a set of data have been lumped together in one code under the name FLASH. A generalized flow chart is provided in Figure G.1.

The process for determining the unknown parameters is started by reading in the normalized experimental data, the sample thicknesses, conductivities and thermal diffusivities and initial estimates for the h values.

The iterative procedure for finding the optimum h values for a particular set of data begins by generating several random guesses for each of the unknown parameters near some specified initial estimates. For each set of h's (e.g., h_1, h_2, h_3,) an analytic expression for the back face temperature is calculated as described in the Mathematical Model section. The analytic expression is evaluated at $t = t_k$, $k = 1,2...m$ where t_k is the time at which the kth data point was taken. The total error is computed according to Equations 41 and 42.

A new set of h's, based on the total error for each old set of h's, is calculated by the method described by Peckham.[52] The total error for this set of h's is calculated and compared with the total errors resulting from each of the other set of h's. If the total error corresponding to one of the old h sets is larger than the newly calculated error, the new h set replaces the old and the process continues to calculate another, hopefully improved, estimate for the unknown parameters. If a new h set is not an improvement over any of the previous h sets, the new h set is adjusted by using a weighted average of the previous best h set and the new h set. This readjustment may be applied several times if necessary.

By this process either one set of h's will be found which results in a total error less than some acceptable value or all the h sets will be within some small neighborhood and the resulting average h set is taken as the best for the given data.

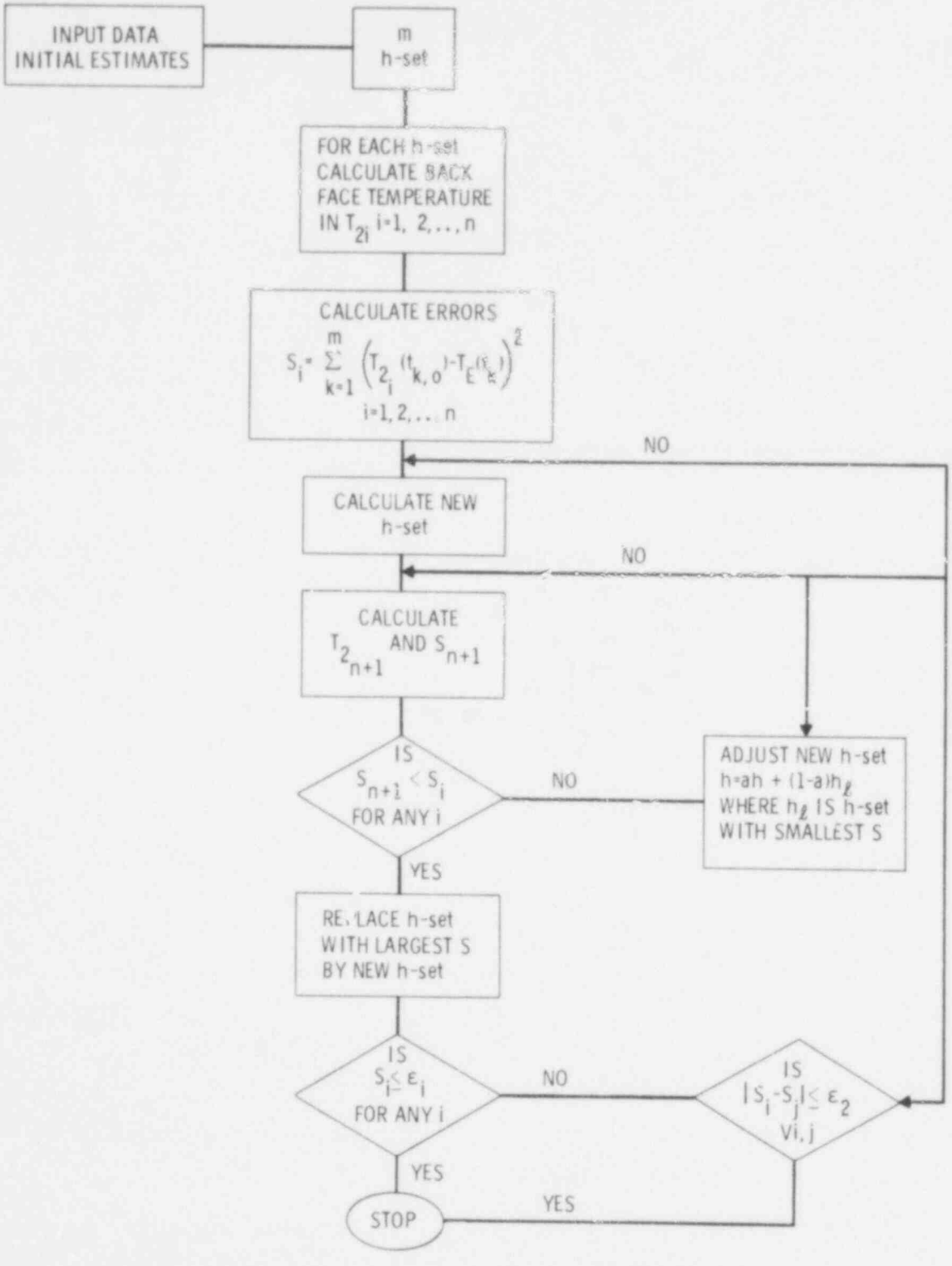

FIGURE G.1. Generalized Flow Chart for FLASH

592 127

- A list of the subroutines and a short description of their function is given below. A FORTRAN listing is supplied in this appendix.

MINSSQ. This is the main calling program. It contains the initialization and iterative process for calculating new h sets as described in the numerics section. It checks on convergence and also handles all the input and output.

LIN2 (A,N,NN,EPS,B,M,MM,LTEMP,IERR,DET,NPIV,PIV,LPR,LPC). This routine solves the matrix equation Ax = B. It is essentially gaussian elimination using a maximum pivot strategy.

A -- coefficient matrix.

N -- order of A.

NN -- number of words of storage provided for each column of A in the calling program.

EPS -- all pivots must exceed this number in magnitude.

B -- right side of the matrix equation.

M -- number of columns of B.

MM -- number of words of storage provided for each column of B.

LTEMP -- temporary storage - at least N words.

IERR -- error indicator 0 if no trouble.
2 if pivot fails to exceed EPS, calaculations stop.

DET -- product of the pivots.

NPIV -- number of the current pivot.

PIV -- current pivot.

LPR, LPC -- integer arrays which hold the pivot locations

ROOTS (HF,HG,HB,TMIN). Given an h set, this finds the poles of the integrand of Equation 38. It also calculates the residues by numerical differentiation according to Equation 40. The poles are found using an interval halving technique and using a first order Taylor Series approximation to find the first step length out from zero.

592 198

HF -- front face film coefficient

HG -- gap conductance

HB -- back face film coefficient

TMIN -- smallest time value for the data. This determines the number of poles required for a given accuracy in the computed temperature.

FUNVAL (KK). This routine fills the array $F_{k,i} = T_{2i}(o,t_k) - TE(T_k)$ where k = 1,2...m, the number of data points and i = k,2 ..n the number of h sets. This routine is the calling subprogram for ROOTS and MAXT.

KK -- number of the h set for which the temperature function and errors is to be computed.

TEMP (TIME). This short routine calculates the back face temperature according to Equation 39.

TIME -- time for which the back face temperature is to be calculated.

MAXT (TMAX,DELT). After a back face temperature function has been calculated, this routine is called to find the maximum for the given temperature function. This is done by finding the root of the derivative of the temperature function. Here again an interval halving technique is used. This routine calls TEMP and DTEMP.

TMAX -- comes into the routine as the largest time value for the data. It is returned as the maximum temperature need to normalize the analytic back face temperature.

DELT -- difference between the largest and smallest time values for the data. It is assumed that TMAX must occur at some time between TMIN and TMAX. If it does not then the temperature at TMAX is taken as the maximum.

DTEMP (TIME). This routine is similar to TEMP but the derivative of the back face temperature is returned.

TIME -- time for which the derivative is to be evaluated.

As the code is listed it requires six data points. These data points should be such that they limit the possible analytic functions which will fit the data within some error bound. That is, they should be well distributed through the time span of the experiment. They should not include

very small times as the model does not accurately describe the transient behavior for small times. It has been found that the best results were obtained when four or five points are taken from data before the maximum temperature is reached and, correspondingly, two or one points after. Also the code uses the five best estimates for the h sets in determining a new estimate. This seems to be an adequate number to give good results without taxing the code as far as the computation time is concerned.

G.2 PROGRAM LISTING/INPUT INSTRUCTIONS

THE FIRST ROUTINE CONCERNS SETTING VARIOUS SYSTEM OPERATION PARAMETERS AND THE DATA INPUT FROM A TEK 4051 GRAPHIC COMPUTER. THE DATA UNITS AND INPUT FORMAT IS GIVEN IN THE 'COMMENTS' ON THE NEXT PAGE.

```
C
C     THIS ROUTINE CREATES A DATA FILE FOR THE FLASH PROGRAM
C     INFORMATION IS RECEIVED FROM THE 4051 TEK GRAPHICS COMPUTER
C     (TRANSMITTED VIA R R 232-C COUPLER).  THE DATA TRANSMITTED
C     IS FROM THE MPD EXPERIMENTS BEING CONDUCTED AT PNL.  THIS
C     WORK IS UNDER THE SPONSORSHIP OF NRC-RSR.  THE PROGRAM IS
C     TITLED: "EX-REACTOR GAP CONDUCTANCE MEASUREMENTS BETWEEN
C     UO2:ZIRCALOY-4 INTERFACES"
C
      IMPLICIT DOUBLE PRECISION (A-H,O-Z)
      DOUBLE PRECISION K1,K2
      COMMON/BLK1/EPSSUM,ITERAT,NADJ,IMAX,KMAX,LMAX,
     1            XCENT(3),XDELTA(3),X(3,6),F(7,6)
      COMMON/POINTS/DATA(7),DATAT(7)
      COMMON/GEN/ROOT(50),RES(50),X1,X2,A1,A2,K1,K2,NROOTS,IROOTS
      COMMON/BLK2/IPRINT,KMAXM1,MAXTRY,IRUN,ANS1,ANS2,ANS3,ANS4
      COMMON/SAMPLE/IGDATA(6),JGDATA(23)
      REAL JGDATA
      READ(2,*) N
      IPRINT=0
      IF(N.LT.0) IPRINT=1
      N=ABS(N)
      KMAXM1=6
      MAXTRY=1
      IEND=99999
      DO 10 I=1,N
      XCENT(1)=0.01
      XDELTA(1)=0
      XDELTA(2)=0
      IRUN=I
      READ(2,*)(IGDATA(J),J=1,4),JGDATA(1),IGDATA(5),(JGDATA(K),K=2,23)
      READ(2,*) IGDATA(6)
C     SCAN DATA FOR INPUT ERRORS PRIOR TO CALL FLASH EXECUTION
      DO 50 II=1,6
      IF (IGDATA(II) .GT. 0) GO TO 50
      PRINT*,' EDT RUN NO. = ',IGDATA(1),'  ERROR VALUE ',IGDATA(II)
      GO TO 54
   50 CONTINUE
      DO 52 II=1,23
      IF (JGDATA(II).GT.0.0) GO TO 52
      PRINT*,' EDT RUN NO. = ',IGDATA(II),' ERROR VALUE ',JGDATA(II)
      GO TO 54
   52 CONTINUE
      IF(IGDATA(6).EQ.9999) GO TO 56
   54 WRITE(6,55) IGDATA(1)
   55 FORMAT(/,3X,'EDT RUN NO.= ',I5,' DATA INPUT ERROR-SKIP RUN')
      GO TO 10
   56 CONTINUE
```

```
C
C
C       IGDATA (I)      INPUT I.D INFORMATION
C
C       1:RUN #           2:UO2 I.D.          3:ZR4 I.D.
C       4:ATM CODE        5:GAP/CONTACT CODE   6:EOF 9999
C
C       JGDATA(K)       I.D. INFORMATION AS INPUTTED
C
C       1:TEMP (DEG C)     2:GW(CM)/LOAD(PA)  3:ATM PRESS (PA)
C       4:GAS COND(W/CM-K)5:X1 CM             6:X2 CM
C       7:K1 W/CM-K        8:K2 W/CM-K        9:DIFF 1 CM↑2/SEC
C      10:DIFF 2 CM↑2/SEC11:H(GUESS) W/CM↑2-K12/13:TIME,Y
C   14/15:TIME,Y       16/17:TIME,Y         18/19:TIME,Y
C   20/21:TIME,Y       22/23:TIME,Y
C

      X1=JGDATA(5)
      X2=JGDATA(6)
      K1=JGDATA(7)
       K2=JGDATA(8)
       A1=JGDATA(9)
       A2=JGDATA(10)
       XCENT(2)=JGDATA(11)
       DATAT(1)=JGDATA(12)
       DATA(1)=JGDATA(13)
       DATAT(2)=JGDATA(14)
       DATA(2)=JGDATA(15)
       DATAT(3)=JGDATA(16)
       DATA(3)=JGDATA(17)
       DATAT(4)=JGDATA(18)
       DATA(4)=JGDATA(19)
       DATAT(5)=JGDATA(20)
       DATA(5)=JGDATA(21)
       DATAT(6)=JGDATA(22)
       DATA(6)=JGDATA(23)
       CALL FLASH
       IDIAG=0
       IF(IDIAG.EQ.0) GO TO 23
       DO 20 II=1,5
       WRITE(3,40)
       WRITE(3,*) IGDATA(II)
       WRITE(3,41)
20     CONTINUE
       DO 21 II=1,23
       WRITE(3,40)
       WRITE(3,*) JGDATA(II)
       WRITE(3,41)
21     CONTINUE
       JGDATA(1)=ANS1
       JGDATA(2)=ANS2
       JGDATA(3)=ANS3
       JGDATA(4)=ANS4
       DO 22 II=1,4
       WRITE(3,40)
       WRITE(3,*) JGDATA(II)
       WRITE(3,41)
22     CONTINUE
```

592 202

```
      WRITE(3,40)
      WRITE(3,*) IEND
      WRITE(3,41)
      WRITE(3,40)
      WRITE(3,42)
      GO TO 10
   23 WRITE(3,*) IGDATA(1)
      WRITE(3,*) IGDATA(2)
      WRITE(3,*)IGDATA(3)
      WRITE(3,*) JGDATA(1)
      WRITE(3,*) JGDATA(2)
      WRITE(3,*) ANS1
      WRITE(3,*) ANS2
      WRITE(3,*) ANS3
      WRITE(3,*) ANS4
      WRITE(3,*) IEND
   10 CONTINUE
      WRITE(3,42)
   40 FORMAT('RO')
   41 FORMAT('RC')
   42 FORMAT('RE')
      RETURN
      END



C
      SUBROUTINE FLASH
      IMPLICIT DOUBLE PRECISION (A-H,O-Z)
      DOUBLE PRECISION K1,K2
C
C     DIMENSION S(LMAX+1),W(LMAX+1),H(KMAX),EP(IMAX,LMAX),
C     F(KMAX,LMAX+1)
C     GTG(IMAX,IMAX),GTH(IMAX),XCENT(IMAX),XDELTA(IMAX),X(IMAX,LMAX+1),
C     EPEPT(IMAX,IMAX),EPFP(IMAX,KMAX),LTEMP(IMAX),LPR(IMAX),LPC(IMAX),
C
      DIMENSION S(6),W(6),H(7),EP(3,5),EPEPT(3,3),EPFP(3,7),
     1 LTEMP(3),LPR(3),LPC(3),GTG(3,3),GTH(3)
      COMMON/BLK1/EPSSUM,ITERAT,NADJ,IMAX,KMAX,LMAX,
     1  XCENT(3),XDELTA(3),X(3,6),F(7,6)
      COMMON /POINTS/  DATA(7),DATAT(7)
      COMMON /DEBUG/JRUN
      COMMON /GEN/  ROOT(50),RES(50),X1,X2,A1,A2,K1,K2,NROOTS,IROOTS
      COMMON /BLK2/IPRINT,KMAXM1,MAXTRY,IRUN,ANS1,ANS2,ANS3,ANS4
      COMMON/SAMPLE/IGDATA(6),JGDATA(23)
      REAL SEED
      REAL LAMBDA
      REAL JGDATA
C     IDIAG=0 DO NOT PRINT DIAGNOSIS INFORMATION
      IDIAG=0
      LAMBDA=0.
      IP=4
      EPSSUM=1.E-8
      EPSX=.01
      NPRINT=1000
      IEND='END '
      IBLANK='  '
      ITERAT=120
      JRUN=IRUN
```

```
      MADJ=20
      NROOTS=10
      IMAX=3
      LMAX=5
      KMAX=KMAXM1+1
      NTRIES=0
      ITEST=0
      N=0
      XCENT(3)=0.
      XDELTA(3)=5.
  752 CONTINUE
      N=0
      NTRIES=NTRIES+1
      HSURF=XCENT(1)
      HGAP=XCENT(2)
      LMAXP1=LMAX+1
  814 CONTINUE
      XDELM=.3
      IF(NTRIES.GT.1)XDELM=.1
      DO982 I=1,2
      XDELTA(I)=XCENT(I)*XDELM
  982 CONTINUE
      SEED=0.
      DO 10 I=1,IMAX
      DO 20 L=1,LMAX
      IF(IDIAG.EQ.0)GO TO 19
      PRINT*,'I= ',I,' L= ',L,' SEED = ',SEED,' XCENT =',XCENT(I)
   19 CONTINUE
      X(I,L)=XCENT(I)+XDELTA(I)*(1.-2.*RANF(SEED))
      IF(IDIAG.EQ.0)GO TO 20
      PRINT*,'XDELTA = ',XDELTA(I),' SEED = ',SEED,' X= ',X(I,L)
   20 CONTINUE
   10 CONTINUE
      DO 15 I=1,LMAX
   15 CALL FUNVAL(I)
      DO 30 L=1,LMAX
      RECO1=0.0
      DO 40 K=1,KMAX
C     RECO1=RECO1+ABS(F(K,L))
      RECO1=RECO1+F(K,L)**2
40    CONTINUE
      S(L)=RECO1
      W(L)=1./SQRT(RECO1)
30    CONTINUE
45    N=N+1
      RECO1=0.0
      DO 50 L=1,LMAX
      RECO1=RECO1+1./S(L)
50    CONTINUE
      DO 60 I=1,IMAX
      RECO2=0.0
      DO 70 L=1,LMAX
      RECO2=RECO2+X(I,L)/S(L)
70    CONTINUE
      XCENT(I)=RECO2/RECO1
60    CONTINUE
```

592 204

```
      DO 80 K=1,KMAX
      RECO2=0.0
      DO 90 L=1,LMAX
      RECO2=RECO2+F(K,L)/S(L)
90    CONTINUE
      H(K)=RECO2/RECO1
80    CONTINUE
      INCO=0
      DO 100 I=1,IMAX
      RECO1=EPSX*ABS(XCENT(I))
      DO 110 L=1,LMAX
      RECO2=X(I,L)-XCENT(I)
      IF(ABS(RECO2).GT.RECO1) INCO=1
      EP(I,L)=W(L)*RECO2
110   CONTINUE
100   CONTINUE
      IF(INCO.NE.0) GO TO 105
      PRINT 6001
      PRINT*,'   CONVERGED SOLUTION'
      GO TO 450
  105 CONTINUE
      DO 120 J=1,IMAX
      DO 130 I=J,IMAX
      RECO1=0.0
      DO 140 L=1,LMAX
      RECO1=RECO1+EP(J,L)*EP(I,L)
140   CONTINUE
      EPEPT(I,J)=RECO1
      EPEPT(J,I)=RECO1
130   CONTINUE
      DO 150 K=1,KMAX
      RECO1=0.0
      DO 160 L=1,LMAX
      RECO1=RECO1+EP(J,L)*W(L)*F(K,L)
160   CONTINUE
      EPFP(J,K)=-RECO1
150   CONTINUE
120   CONTINUE
      IF(MOD(N-1,NPRINT).NE.0) GO TO 213
       IF(IDIAG .EQ. 0) GO TO 213
 5002 FORMAT(1H0,3X,'RUN NO.',I5/)
      PRINT 1000,N
      WRITE(6,5002)IRUN
      PRINT*,' SET\     HF        HF-BAR        HG        HG-BAR        HB
     $    HB-BAR'
      PRINT 1010,(L,(X(I,L),XCENT(I),I=1,IMAX),L=1,LMAX)
      PRINT 1005
      PRINT 1006
      DO 700 L=1,LMAX
      PRINT 1020,L,(F(K,L),K=1,KMAX),S(L)
  700 CONTINUE
 1006 FORMAT(//41X,'TCALC-TDATA'//'  SET\    TIME1       TIME2       TIME3
     $    TIME4       TIME5       TIME6                    S')
  213 CONTINUE
      CALL LIN2(EPEPT,IMAX,IMAX,0.0,EPFP,KMAX,IMAX,
     1 LTEMP,IERR,DET,NPIV,PIV,LPR,LPC)
      IF(IERR.NE.2) GO TO 217
      IF(ITEST.NE.1)GO TO 521
      PRINT 6001
```

```
      PRINT*,'   ILL-CONDITIONED MATRIX FOUND   RECOVERY FAILED'
      WRITE(6,5001)IGDATA(1),NTRIES
      PRINT*,'  PROGRAM TO CONTINUE ON NEXT RUN'
      GO TO 745
  521 CONTINUE
      ITEST=1
      GO TO 814
  217 CONTINUE
      DO 200 J=1,IMAX
      DO 210 I=J,IMAX
      RECO1=0.0
      DO 220 K=1,KMAX
      RECO1=RECO1+EPFP(J,K)*EPFP(I,K)
  220 CONTINUE
      GTG(I,J)=RECO1
      GTG(J,I)=RECO1
  210 CONTINUE
      RECO1=0.0
      DO 230 K=1,KMAX
      RECO1=RECO1+EPFP(J,K)*H(K)
  230 CONTINUE
      GTH(J)=RECO1
  200 CONTINUE
      DO 305 I=1,IMAX
  305 GTG(I,I)=GTG(I,I)*(1.+LAMBDA)
      CALL LIN2(GTG,IMAX,IMAX,0.0,GTH,1,IMAX,
     1 LTEMP,IERR,DET,NPIV,PIV,LPR,LPC)
      IF(IERR.NE.2) GO TO 218
      IF(ITEST.NE.1)GO TO 522
      PRINT 6001
      PRINT*,'   ILL-CONDITIONED MATRIX FOUND   RECOVERY FAILED'
      WRITE(6,5001)IGDATA(1),NTRIES
      PRINT*,'  PROGRAM TO 8CONTINUE ON NEXT RUN'
      GO TO 745
  522 CONTINUE
      ITEST=1
      GO TO 814
  218 CONTINUE
      DO 250 I=1,IMAX
      X(I,LMAXP1)=XCENT(I)+GTH(I)
      IF(I.EQ.IMAX) GO TO 252
      IF(X(I,LMAXP1).GT. 1.5*XCENT(I)) X(I,LMAXP1)=1.5*XCENT(I)
      IF(X(I,LMAXP1).LT.  .5*XCENT(I)) X(I,LMAXP1)= .5*XCENT(I)
      GO TO 250
  252 IF(X(I,LMAXP1).GT.1.E6) X(I,LMAXP1)=1.E6
      IF(X(I,LMAXP1).LT.-1.E6) X(I,LMAXP1)=-1.E6
  250 CONTINUE
      LOOP=0
  255 CONTINUE
      IF(MOD(N,NPRINT).NE.0) GO TO 214
       IF(IDIAG .EQ. 0) GO TO 214
      PRINT 1005
      PRINT*,' SET\     HF        HF-BAR        HG        HG-BAR        HB
     $     HB-BAR'
      PRINT 1010,LMAXP1,(X(I,LMAXP1),XCENT(I),I=1,IMAX)
  214 CONTINUE
      CALL FUNVAL(LMAXP1)
      RECO1=0.0
      DO 260 K=1,KMAX
C     RECO1=RECO1+ABS(F(K,LMAXP1))
      RECO1=RECO1+F(K,LMAXP1)**2
  260 CONTINUE
```

592 206

```
      S(LMAXP1)=RECO1
      W(LMAXP1)=1./SQRT(RECO1)
      IF(MOD(N-1,NPRINT).NE.0) GO TO 215
       IF(IDIAG .EQ. 0)GO TO 215
      PRINT 1005
      PRINT 1006
      PRINT 1020,LMAXP1,(F(K,LMAXP1),K=1,KMAX),S(LMAXP1)
  215 CONTINUE
      IF(S(LMAXP1).GT.EPSSUM) GO TO 216
      PRINT 6001
  219 PRINT*,'   CONVERGED SOLUTION'
      GO TO 450
  216 CONTINUE
      IF(LOOP.NE.0) GO TO 308
      LSMALL=1
      LLARGE=1
      SMIN=S(1)
      SMAX=S(1)
      DO 300 L=2,LMAX
      IF(S(L).GE.SMIN)GO TO 304
302   SMIN=S(L)
      LSMALL=L
      GO TO 300
  304 IF(S(L).LE.SMAX)GO TO 300
306   SMAX=S(L)
      LLARGE=L
300   CONTINUE
      IF(SMIN.LE.EPSSUM) GO TO 219
308   IF(S(LMAXP1).LT.SMAX) GO TO 315
      IF(LOOP.NE.NADJ) GO TO 309
      PRINT 6001
      PRINT*,'   MAXIMUM NUMBER OF READJUSTMENTS  -  CHECK CONVERGENCE'
      GO TO 450
  309 CONTINUE
      LOOP=LOOP+1
      DO 310 I=1,IMAX
      X(I,LMAXP1)=(W(LMAXP1)*X(I,LMAXP1)+W(LSMALL)*X(I,LSMALL))/
     1 (W(LMAXP1)+W(LSMALL))
310   CONTINUE
      GO TO 255
  315 IF(N.LT.ITERAT) GO TO 316
      PRINT 6001
      PRINT*,'MAXIMUM NUMBER OF ITERATIONS  -  NO CONVERGENCE'
      GO TO 450
  316 CONTINUE
      DO 320 I=1,IMAX
      X(I,LLARGE)=X(I,LMAXP1)
320   CONTINUE
      DO 330 K=1,KMAX
      F(K,LLARGE)=F(K,LMAXP1)
330   CONTINUE
      S(LLARGE)=S(LMAXP1)
      W(LLARGE)=W(LMAXP1)
      GO TO 45
  450 CONTINUE
      WRITE(6,5001)IGDATA(1),NTRIES

 5001 FORMAT(/,3X,'EDT RUN NO. = ',I4,'  # ITERATIONS = ',I4)
       PRINT*,'  EDT TAPE: B C D E F G H I J K L M N O P Q R S T U V W
     $X Y Z (CIRCLE)'
       WRITE(6 3121)
       WRITE(6,3111) IGDATA(2),IGDATA(4)
```


592 207

```
      WRITE(6,3112) IGDATA(3),IGDATA(5)
      WRITE(6,3113)JGDATA(1),JGDATA(2)
      WRITE(6,3118)JGDATA(3),JGDATA(4)
      WRITE(6,3115) JGDATA(11)
     IF(IPRINT.EQ.0) GO TO 852
      WRITE(6,3121)
852 WRITE(6,2188)X1,X2
      WRITE(6,2189)K1,K2
      WRITE(6,2190)A1,A2
     IF(IPRINT.EQ.0) GO TO 854
     WRITE(6,3121)
    PRINT*,'   INITIAL ESTIMATES'
      WRITE(6,3116)HSURF,XDELTA(1)
      WRITE(6,3117)HGAP,XDELTA(2)
     WRITE(6,3121)
    PRINT*,'   EXPERIMENTAL DATA'
    IP=KMAX-1
    DO 14 I=1,IP
      WRITE(6,2187) DATA(I),DATAT(I)
 14 CONTINUE
     WRITE(6,3121)
      PRINT 2191
854 WRITE(6,3121)
    WRITE(6,3123) N
      PRINT 2191
    PRINT*,' SET\     HF        HF-BAR       H(GAP)     HG-BAR        HB
   $    HB-BAR'
    XCENT(3)=10.*XCENT(1)*(1.01+XCENT(3)/(1.+ABS(XCENT(3))))
    DO 460 L=1,LMAX
    X(3,L)=X(1,L)*(1.01+X(3,L)/(1.+ABS(X(3,L))))*10.
     IF(IPRINT.EQ.0) GO TO 460
    PRINT 1010,L,(X(I,L),XCENT(I),I=1,IMAX)
460 CONTINUE
    PRINT 2191
    SMAX=100.
     LLARGE=1
    DO 744 L=1,LMAX
    IF(S(L).GT.SMAX) GO TO 744
    SMAX=S(L)
    LLARGE=L
744  CONTINUE
     L=LLARGE
     ANS1=X(1,L)
     ANS2=X(2,L)
     ANS3=X(3,L)
     ANS4=S(L)
     PRINT3122,ANS1,ANS2,ANS3,ANS4
      WRITE(6,3121)
     IF(IPRINT.EQ.0) GO TO 856
      PRINT 705
705  FORMAT(30X,'TCALC-TDATA'/' SET     TIME1',6X,'TIME2',6X
   $,'TIME3',6X,'TIME4',6X,'TIME5',6X,'TIME6')
      DO 706 L=1,LMAX
      PRINT 1010,L,(F(K,L),K=1,KMAX-1)
706   CONTINUE
      PRINT 2191
      PRINT*,'     SET #       STATS: (S) SUM SQUARE OF RESIDUALS'
      DO 710 L=1,LMAX
      PRINT 2192,L,S(L)
710   CONTINUE
856 WRITE(6,3121)
     WRITE(6,3121)
     WRITE(6,3121)
```

```
      WRITE(6,3121)
       WRITE(6,3121)
       WRITE(6,3121)
  743 CONTINUE
      ERROR=ABS(XCENT(2)-HGAP)/HGAP
      IF(ERROR.GT..01.AND.NTRIES.LT.MAXTRY) GO TO  752
  745 CONTINUE
      RETURN
 1000 FORMAT(1H1,I65,/)
 1005 FORMAT(1H0)
 1010 FORMAT(I5,6E11.4)
 1020 FORMAT(I5,11E11.4)
 6001  FORMAT(1H1,/)
 2187  FORMAT('   NORMALIZED TEMP = ',F10.4,'  AT TIME(SEC) = ',F10.5)
 2188 FORMAT('   THICKNESS 1 (CM): ',F10.6,'  THICKNESS 2 (CM): ',F10.6)
 2189 FORMAT('   COND 1  (W/CM-K): ',F10.6,'  COND 2  (W/CM-K): ',F10.6)
 2190 FORMAT('  DIFF 1 (CM**2/SEC): ',F10.6,' DIFF 2 (CM**2/SEC): ',F10.6)
 2191  FORMAT(3X,' ')
 2192   FORMAT(3X,I5,10X,E11.4)
 3111   FORMAT('           UO2 I.D.: ',I4,'            ATM CODE: ',I4)
 3112   FORMAT('           ZR4 I.D.: ',I4,'   GAP/CONTACT CODE: ',I4)
 3113   FORMAT(4X,' TEMP (DEG C) : ',F6.1,'   GW(CM)/LOAD(PA) : ',E11.4)
 3118 FORMAT('  ATM PRESS  (PA) :',E11.4,' GAS COND(W/CM**2-K) = ',E11.4)
 3115   FORMAT('    H(GAP) GUESS  =  ',F10.4)
 3116   FORMAT('    HSURF = ',F10.6,'    DELTA SURF = ',F10.6)
 3117   FORMAT('    HGAP =  ',F10.6,'    DELTA HGAP = ',F10.6)
 3121 FORMAT('-------------------------------------------------------------
     $-------------',2X)
 3122  FORMAT(' BEST:',E11.4,10X,E11.4,11X,E11.4,' S =',E11.4)
 3123  FORMAT('      ANALYTICAL RESULTS  # LOOP ITERATIONS = ',I5)
       END



      SUBROUTINE FUNVAL(KK)
      IMPLICIT DOUBLE PRECISION (A-H,O-Z)
      COMMON/BLK1/EPSSUM,ITERAT,NADJ,IMAX,KMAX,LMAX,HCENT(3),HDELTA(3)
     $   ,H(3,6),FUNC(7,6)
      COMMON /POINTS/  DATA(7),DATAT(7)
      KMAY=KMAX-1
      EPSHFB=2.
      DATA1H=DATA(1)/2.
      CALL ROOTS(H(1,KK),H(2,KK),H(3,KK),DATA1H)
      DELT=DATAT(KMAY)-DATAT(1)
      TMAX=DATAT(KMAY)
      CALL MAXT(TMAX,DELT)
      DO 20 J=1,KMAY
      T=TEMP(DATAT(J))/TMAX
      FUNC(J,KK)=T-DATA(J)
   20 CONTINUE
      FUNC(KMAX,KK)=0.
      RETURN
      END
      FUNCTION TEMP(TIME)
      IMPLICIT DOUBLE PRECISION (A-H,O-Z)
      DOUBLE PRECISION K1,K2
      COMMON /GEN/  ROOT(50),RES(50),X1,X2,A1,A2,K1,K2,NROOTS,IROOTS
      TEMP=0.
      DO 10 I=1,IROOTS
   10 TEMP=TEMP+RES(I)*EXP(-ROOT(I)*TIME)
      RETURN
      END
```

592 209

```
      FUNCTION DTEMP(TIME)
      IMPLICIT DOUBLE PRECISION (A-H,O-Z)
      DOUBLE PRECISION K1,K2
      COMMON /GEN/  ROOT(50),RES(50),X1,X2,A1,A2,K1,K2,NROOTS,IROOTS
      DTEMP=0.
      DO 10 I=1,IROOTS
   10 DTEMP=DTEMP-RES(I)*ROOT(I)*EXP(-ROOT(I)*TIME)
      RETURN
      END



      SUBROUTINE ROOTS(HF,HG,HR,TMIN)
      IMPLICIT DOUBLE PRECISION (A-H,O-Z)
      DOUBLE PRECISION K1,K2
      COMMON /DEBUG/JRUN
      COMMON /GEN/  ROOT(50),RES(50),X1,X2,A1,A2,K1,K2,NROOTS,IROOTS
      F(S)=(HF*((G1*CV1+HG*SV1)*(-G2*G2/HB*SV2+G2*CV2)+G1*CV1*(G2/HB*HG*
     $  CV2+HG*SV2))+G1*((-G1*SV1+HG*CV1)*(-G2*G2/HB*SV2+G2*CV2)-
     $  G1*SV1*(G2/HB*HG*CV2+HG*SV2)))*HB/(HG*G1*G2)
      HB=HF*(1.01+HR/(1.+ABS(HR)))*10.
      TEMTOT=0.
      IROOTS=NROOTS
C     IDIAG=0 THEN DO NOT PRINT DIAGNOSIS INFORMATION
      IDIAG=0
      J=0
      W=1
      ISTART=1
      E=1.E-5
      NN=1000
      D=0.
      S=0.
      DS=1.E-8
      DO 200 NI=1,2
      S=S+DS
      SQ1=SQRT(S/A1)
      SQ2=SQRT(S/A2)
      G1=K1*SQ1
      G2=K2*SQ2
      V1=SQ1*X1
      V2=SQ2*X2
      SV1=SIN(V1)
      SV2=SIN(V2)
      CV1=COS(V1)
      CV2=COS(V2)
      D=F(S)
      IF(NI.EQ.1) D1=D
      IF(NI.EQ. 2) D2=D
  200 CONTINUE
      IF(IDIAG.EQ.0) GO TO 199
      IF(JRUN.GT.3)PRINT*,'DS= ',DS,' D1= ',D1,' D2= ',D2,' HG= ',
     $HG,' HB= ',HB,' HF= ',HF,' HR= ',HR
  199 CONTINUE
      DS=-D1*DS/(D2-D1)*.5
      S=0.
  100 CONTINUE
```


592 210

```
      DO 10 I=ISTART,NN
      ITEST=0.
      IF(J.GE.1)DS=AMAX1(DS,.1)
      IF(J .GE. 2) DS=.2*(ROOT(J)-ROOT(J-1))
      E=DS*1.E-5
      E=AMIN1(E,1.E-4)
      S=S+DS
   50 CONTINUE
      SQ1=SQRT(S/A1)
      SQ2=SQRT(S/A2)
      G1=K1*SQ1
      G2=K2*SQ2
      V1=SQ1*X1
      V2=SQ2*X2
      SV1=SIN(V1)
      SV2=SIN(V2)
      CV1=COS(V1)
      CV2=COS(V2)
      D=F(S)
      IF(I.EQ.1) DOLD=D
      IF(ITEST .EQ. 1) GO TO 20
      IF(D*DOLD .GT. 0.) GO TO 30
      SSAVE=S
      DSAVE=D
      DOLDL=DOLD
      SOLDL=SOLD
      DOLDR=D
      SOLDR=S
      S=.5*(S+SOLD)
      ITEST =1
      GO TO 50
   20 CONTINUE
      IF((SOLDR-SOLDL).LT.E) GO TO 40
      IF(DOLDL*D .LT. 0.) GO TO 60
      SOLDL=S
      DOLDL=D
      GO TO 70
   60 DOLDR=D
      SOLDR=S
   70 CONTINUE
      S=.5*(SOLDL+SOLDR)
      GO TO 50
   40 CONTINUE
      J=J+1
      IF(J .GT. NROOTS) GO TO 90
      ROOT(J)=S
      RES(J)=-W*(SOLDR-SOLDL)/(DOLDR-DOLDL)
      IF (J .LT. 2) GO TO 80
      TPLUS=RES(J)*EXP(-TMIN*ROOT(J))
      TEMTOT=TEMTOT+TPLUS
      IF(ABS(TPLUS/TEMTOT) .GT. .000001) GO TO 80
      IROOTS=J
      GO TO 90
   80 CONTINUE
      S=SSAVE
      D=DSAVE
   30 CONTINUE
      SOLD=S
      DOLD=D
   10 CONTINUE
```

```
      IF(J .GE. NROOTS) GO TO 90
      ISTART=NN+1
      NN= NN+1000
      IF(NN.LT.10000) GO TO 100
      PRINT*,'    EXCESSIVE STEPS TAKEN IN ROOTS CALCULATIONS STOPPED'
      PRINT*,'NEED TO DELETE THIS RUN FROM THE STREAM'
      STOP
   90 CONTINUE
      RETURN
      END



      SUBROUTINE MAXT(TMAX,DELT)
      IMPLICIT DOUBLE PRECISION (A-H,O-Z)
      DOUBLE PRECISION K1,K2
      COMMON /GEN/  ROOT(50),RES(50),X1,X2,A1,A2,K1,K2,NROOTS,IROOTS
      TMAX=2.*TMAX                                                    T
EST
      DT=.05*DELT
      TIME=.01-DT
      DO 10 I=1,400
      TIME=TIME+DT
      D=DTEMP(TIME)
      IF(I .EQ. 1) DOLD=D
      IF(DOLD .LT.0.) GO TO 15
      IF(DOLD*D .LT. 0.) GO TO 20
   15 CONTINUE
      DOLD=D
      TOLD=TIME
   10 CONTINUE
      TMAX=TEMP(TMAX)
      PRINT*,'   MAXIMUM TEMPERATURE NOT FOUND,   TMAX SET TO LAST DATA
     $VALUE.'
      RETURN
   20 CONTINUE
      TOLDL=TOLD
      DOLDL=DOLD
      TOLDR=TIME
      DOLDR=D
      N=ALOG(DT/.001)/ALOG(2.)+1.
      DO 30 I=1,N
      TIME=.5*(TOLDL+TOLDR)
      D=DTEMP(TIME)
      IF(DOLDL*D .LT. 0.) GO TO 60
      TOLDL=TIME
      DOLDL=D
      GO TO 30
   60 DOLDR=D
      TOLDR=TIME
   30 CONTINUE
      TMAX=TEMP(TIME)
      RETURN
      END
```

592 212

```
      SUBROUTINE LIN2(A,N,NN,EPS,B,M,MM,LTEMP,IERR,DET,NPIV,PIV,LPR,
     1           LPC)
      IMPLICIT DOUBLE PRECISION (A-H,O-Z)
      DIMENSION A(NN,N),B(MM,M)
      DIMENSION LTEMP(1),LPC(1),LPR(1)
C
C SUBROUTINE LIN2
C DECK 8046A
C
C SUBROUTINES CALLED - NONE
C
C THIS ROUTINE SOLVES THE MATRIX EQUATION AX+B=0 OVERWRITING B WITH THE
C SOLUTION MATRIX X. A MUST BE SQUARE AND NON-SINGULAR. B MUST
C HAVE THE SAME NUMBER OF ROWS AS A. THE DETERMINANT OF A IS
C COMPUTED. BOTH A AND B ARE DESTROYED.
C
C THIS ROUTINE IS RECOMMENDED FOR THE SOLUTION OF SIMULTANEOUS LINEAR
C EQUATIONS.
C
C THE METHOD CONSISTS OF GAUSSIAN ELIMINATION FOLLOWED BY BACK
C SUBSTITUTIONS. THIS IS MORE EFFICIENT THAN SOLUTION BY MATRIX
C INVERSION REGARDLESS OF THE NUMBER OF COLUMNS IN B. BOTH ROWS AND
C COLUMNS ARE SEARCHED FOR MAXIMAL PIVOTS. INTERCHANGING OF ROWS OR
C COLUMNS OF A IS AVOIDED. CHAPTER 1 OF E.L. STIEFLE,INTRODUCTION TO
C NUMERICAL MATHEMATICS,ACADEMIC PRESS,N.Y.,1963,SHOULD BE HELPFUL IN
C FOLLOWING THE CODE.
C
C THE CALLING PROGRAM MUST SET A,N,NN,EPS,B,M,MM,LTEMP TO-
C
C     A-THE COEFFICIENT MATRIX
C
C     N-THE ORDER OF A
C
C     NN-THE NUMBER OF WORDS OF STORAGE PROVIDED FOR EACH COLUMN OF
C        A IN THE CALLING PROGRAM
C
C     EPS-A NON-NEGATIVE NUMBER WHICH EACH PIVOT IN THE ELIMINATION
C         PROCESS IS REQUIRED TO EXCEED IN ABSOLUTE VALUE (CUSTOMARILY
C         ZERO)
C
C     B-THE CONSTANT TERM MATRIX
C
C     M-THE NUMBER OF COLUMNS OF B
C
C        B IN THE CALLING PROGRAM
C     MM-THE NUMBER OF WORDS OF STORAGE PROVIDED FOR EACH COLUMN OF
C
C     LTEMP-A BLOCK OF AT LEAST N WORDS OF TEMPORARY INTEGER STORAGE
C
C IN ADDITION TO OVERWRITING B WITH THE SOLUTION MATRIX X,THE ROUTINE
C SETS IERR,DET,NPIV,PIV,LPR,AND LPC TO
C
C     IERR-  2 IF NO COLUMNS OF X ARE FOUND, THE ELIMINATION PROCESS
C              BEING HALTED BECAUSE THE CURRENT PIVOT FAILS TO EXCEED
C              EPS IN MAGNITUDE
C
C            0 IF ALL COLUMNS OF X ARE FOUND, NO TROUBLE BEING DETECTED
C
```

```
C      DET-PLUS OR MINUS THE PRODUCT OF THE CURRENT AND ALL PRECEDING
C          PIVOTS
C
C      NPIV-THE NUMBER OF THE CURRENT PIVOT (FIRST,SECOND,ETC.)
C
C      PIV-THE CURRENT PIVOT
C
C      LPR-THE FIRST NPIV POSITIONS LIST THE PIVOT ROW INDICES IN ORDER
C          OF USE,A VECTOR OF LENGTH N
C
C      LPC-THE FIRST NPIV POSITIONS LIST THE PIVOT COLUMN INDICES IN
C          ORDER OF USE,A VECTOR OF LENGTH N
C
C IF THE ELIMINATION PROCESS IS HALTED PREMATURELY (IERR NEGATIVE),THEN
C THE DATA NPIV,PIV,LPR,LPC,MAY BE HELPFUL IN DIAGNOSING THE UNDERLYING
C CAUSE OF THE TROUBLE. IF THE PROCESS GOES TO COMPLETION THEN NPIV=N,
C DET SHOULD BE THE DETERMINANT OF A,PIV WILL BE THE NTH PIVOT,AND LPR
C AND LPC LIST ALL PIVOT POSITIONS.
C
C DO INITIALIZATIONS
C
    1 IERR=0
      DET=1.
      DO 2 I=1,N
      LPR(I)=I
    2 LPC(I)=I
C
C BEGIN ELIMINATION PROCESS
C
      DO 18 NP=1,N
      NPIV=NP
C
C SELECT PIVOT
C
      PIV=0.
      DO 4 K=NP,N
      I=LPR(K)
      DO 4 L=NP,N
      J=LPC(L)
      IF (ABS(A(I,J))-ABS(PIV)) 4,3,3
    3 KPIV=K
      LPIV=L
      IPIV=I
      JPIV=J
      PIV=A(I,J)
    4 CONTINUE
C
C UPDATE DETERMINANT AND PIVOT ROW AND COLUMN LISTS
C
      DET=DET*PIV
      ITEMP=LPR(NP)
      LPR(NP)=LPR(KPIV)
      LPR(KPIV)=ITEMP
      ITEMP=LPC(NP)
      LPC(NP)=LPC(LPIV)
      LPC(LPIV)=ITEMP
C
C EXIT IF PIVOT TOO SMALL
C
```

592 214

```
      IF (EPS-ABS(PIV)) 8,7,7
    7 IERR= 2
      RETURN
C
C MODIFY PIVOT ROW OF A AND B (ELEMENTS IN PRESENT OR PREVIOUS PIVOT
C    COLUMNS OF A ARE SKIPPED)
C
    8 IF(NP-N)9,11,9
    9 NNP=NP+1
      DO 10 L=NNP,N
      J=LPC(L)
   10 A(IPIV,J)=-A(IPIV,J)/PIV
   11 DO 12 J=1,M
   12 B(IPIV,J)=-B(IPIV,J)/PIV
C
C MODIFY NON-PIVOT ROWS OF A AND B (ELEMENTS IN PRESENT OR PREVIOUS
C    PIVOT ROWS OR COLUMNS ARE SKIPPED)
C
      IF(NP-N)13,18,13
   13 DO 17 K=NNP,N
      I=LPR(K)
      TEMP=A(I,JPIV)
      IF(TEMP)14,17,14
   14 DO 15 L=NNP,N
      J=LPC(L)
   15 A(I,J)=A(I,J)+A(IPIV,J)*TEMP
      DO 16 J=1,M
   16 B(I,J)=B(I,J)+B(IPIV,J)*TEMP
   17 CONTINUE
   18 CONTINUE
C
C END  ELIMINATION PROCESS
C
C DO BACK SUBSTITUTIONS
C
      DO 23 J=1,M
      DO 21 K=2,N
      KK=N-K+1
      I=LPR(KK)
      DO 21 L=2,K
      LL=N-L+2
      II=LPR(LL)
      JJ=LPC(LL)
   21 B(I,J)=B(I,J)+B(II,J)*A(I,JJ)
   23 CONTINUE
C
C UNSCRAMBLE ROWS OF SOLUTION MATRIX AND ADJUST SIGN OF DETERMINANT
C
      DO 24 I=1,N
      L=LPR(I)
   24 LTEMP(L)=LPC(I)
      DO 28 I=1,N
   25 K=LTEMP(I)
      IF(I-K)26,28,26
   26 DET=-DET
      DO 27 J=1,M
      TEMP=B(I,J)
```

```
      B(I,J)=B(K,J)
   27 B(K,J)=TEMP
      LTEMP(I)=LTEMP(K)
      LTEMP(K)=K
      GO TO 25
   28 CONTINUE
      RETURN
      END
```

```
      FUNCTION RANF(SEED)
      DOUBLE PRECISION RANF
      DATA CHANCE/.314159265/,PRIME/997./
      IF(SEED.GT.0.)CHANCE=SEED
      CHANCE=PRIME*CHANCE**2
      CHANCE=CHANCE-AINT(CHANCE)
      RANF=CHANCE
      RETURN
      END
```

592 216

```
  EXAMPLE RUN NUMBER ONE.....


  EDT RUN NO. =   41  # ITERATIONS =    1
  EDT TAPE: B C D E F G H I J K L M N O P Q R S T U V W  X Y Z (CIRCLE)
-------------------------------------------------------------------------
        UO2 I.D.:   40            ATM CODE:     4
        ZR4 I.D.:   25   GAP/CONTACT CODE:     1
   TEMP (DEG C) :  600.5   GW(CM)/LOAD(PA) :   .7510-003
ATM PRESS  (PA) :  .1027+006 GAS COND(W/CM*2-K) =   .2346-002
  H(GAP) GUESS  =      1.4537
-------------------------------------------------------------------------
  THICKNESS 1 (CM):    .103163  THICKNESS 2 (CM):    .096804
  COND 1  (W/CM-K):    .039088  COND 2  (W/CM-K):    .195905
 DIFF 1 (CM*2/SEC):    .012324 DIFF 2 (CM*2/SEC):    .080550
-------------------------------------------------------------------------
   INITIAL ESTIMATES
   HSURF =     .010000    DELTA SURF =     .003000
   HGAP =    1.453734     DELTA HGAP =     .436120
-------------------------------------------------------------------------
   EXPERIMENTAL DATA
  NORMALIZED TEMP =       .5000  AT TIME(SEC) =      .30402
  NORMALIZED TEMP =       .7000  AT TIME(SEC) =      .42117
  NORMALIZED TEMP =       .8500  AT TIME(SEC) =      .55721
  NORMALIZED TEMP =       .9800  AT TIME(SEC) =      .84338
  NORMALIZED TEMP =       .9900  AT TIME(SEC) =      .90166
  NORMALIZED TEMP =       .9880  AT TIME(SEC) =     1.28683
-------------------------------------------------------------------------

    ANALYTICAL RESULTS  # LOOP ITERATIONS =    58

 SET\     HF         HF-BAR       H(GAP)     HG-BAR       HB         HB-BAR
    1  .4926-002  .4925-002  .9589+000  .9589+000  .9714-001  .9713-001
    2  .4925-002  .4925-002  .9589+000  .9589+000  .9714-001  .9713-001
    3  .4926-002  .4925-002  .9589+000  .9589+000  .9712-001  .9713-001
    4  .4925-002  .4925-002  .9589+000  .9589+000  .9712-001  .9713-001
    5  .4925-002  .4925-002  .9589+000  .9589+000  .9712-001  .9713-001

BEST:  .4925-002             .9589+000              .9712-001 S =  .6685-005
-------------------------------------------------------------------------
                                TCALC-TDATA
SET     TIME1        TIME2        TIME3        TIME4        TIME5        TIME6
   1 -.1325-002  .1595-002 -.2907-003  .7289-003  .2091-003  .1314-002
   2 -.1329-002  .1591-002 -.2938-003  .7277-003  .2082-003  .1315-002
   3 -.1342-002  .1575-002 -.3092-003  .7198-003  .2023-003  .1323-002
   4 -.1341-002  .1577-002 -.3077-003  .7208-003  .2031-003  .1321-002
   5 -.1345-002  .1572-002 -.3121-003  .7186-003  .2015-003  .1323-002

    SET #      STATS: (S) SUM SQUARE OF RESIDUALS
      1              .6686-005
      2              .6685-005
      3              .6686-005
      4              .6685-005
      5              .6685-005
-------------------------------------------------------------------------
```

592 217

EXAMPLE RUN NUMBER TWO.....

```
 EDT RUN NO. =   42  # ITERATIONS =    1
 EDT TAPE: B C D E F G H I J K L M N O P Q R S T U V W  X Y Z (CIRCLE)
-------------------------------------------------------------------
        UO2 I.D.:   40            ATM CODE:     4
        ZR4 I.D.:   25   GAP/CONTACT CODE:     1
   TEMP (DEG C) :  400.4   GW(CM)/LOAD(PA) :   .7510-003
ATM PRESS  (PA) :  .1034+006 GAS COND(W/CM*2-K) =   .1966-002
  H(GAP) GUESS  =      1.5356
-------------------------------------------------------------------
 THICKNESS 1 (CM):    .102952  THICKNESS 2 (CM):    .096665
 COND 1  (W/CM-K):    .048200  COND 2  (W/CM-K):    .182286
DIFF 1 (CM*2/SEC):    .015631 DIFF 2 (CM*2/SEC):    .074925
-------------------------------------------------------------------
  INITIAL ESTIMATES
  HSURF =    .010000    DELTA SURF =    .003000
  HGAP =    1.535612    DELTA HGAP =    .460684
-------------------------------------------------------------------
  EXPERIMENTAL DATA
 NORMALIZED TEMP =       .5000  AT TIME(SEC) =      .26746
 NORMALIZED TEMP =       .7000  AT TIME(SEC) =      .37374
 NORMALIZED TEMP =       .8500  AT TIME(SEC) =      .49738
 NORMALIZED TEMP =       .9800  AT TIME(SEC) =      .76374
 NORMALIZED TEMP =       .9900  AT TIME(SEC) =      .81963
 NORMALIZED TEMP =       .9880  AT TIME(SEC) =     1.22737
-------------------------------------------------------------------


-------------------------------------------------------------------
   ANALYTICAL RESULTS  # LOOP ITERATIONS =    40

SET\     HF         HF-BAR       H(GAP)      HG-BAR        HB         HB-BAR
  1  .4560-002  .4560-002  .1020+001  .1020+001  .8496-001  .8495-001
  2  .4560-002  .4560-002  .1020+001  .1020+001  .8496-001  .8495-001
  3  .4560-002  .4560-002  .1020+001  .1020+001  .8495-001  .8495-001
  4  .4560-002  .4560-002  .1020+001  .1020+001  .8496-001  .8495-001
  5  .4560-002  .4560-002  .1020+001  .1020+001  .8491-001  .8495-001

BEST:  .4560-002            .1020+001            .8495-001 S =  .7454-005
-------------------------------------------------------------------
                                TCALC-TDATA
SET     TIME1       TIME2       TIME3       TIME4       TIME5       TIME6
  1 -.3238-003  .1971-002 -.1667-002 -.3221-003 -.5053-003 -.5726-003
  2 -.3189-003  .1977-002 -.1661-002 -.3192-003 -.5031-003 -.5756-003
  3 -.3291-003  .1965-002 -.1673-002 -.3250-003 -.5075-003 -.5696-003
  4 -.3187-003  .1977-002 -.1661-002 -.3191-003 -.5031-003 -.5757-003
  5 -.3530-003  .1937-002 -.1700-002 -.3389-003 -.5180-093 -.5550-003

   SET #      STATS: (S) SUM SQUARE OF RESIDUALS
     1              .7455-005
     2              .7456-005
     3              .7454-005
     4              .7456-005
     5              .7455-005
-------------------------------------------------------------------
```

592 218

DISTRIBUTION

No. of Copies

OFFSITE

A. A. Churm
DOE Patent Division
9800 S. Cass Avenue
Argonne, IL 60439

287 U.S. Nuclear Regulatory Commission
Division of Technical Information and Document Control
7920 Norfolk Avenue
Bethesda, MD 20014

25 NTIS

2 DOE Technical Information Center

2 Nuclear Regulatory Commission
Division of Reactor Safety Research
Fuel Behavior Research Branch
Washington, DC 20545

Attn. W. V. Johnston, Chief

2 Nuclear Regulatory Commission
Division of Reactor Safety Research
Fuel Behavior Research Branch
Washington, DC 20545

Attn. H. H. Scott

No. of Copies

ONSITE

50 PACIFIC NORTHWEST LABORATORY

J. L. Bates
S. Begej (4)
T. D. Chikalla (4)
M. E. Cunningham
M. D. Freshley
J. E. Garnier (24)
C. R. Hann (4)
D. D. Lanning
R. P. Marshall
C. L. Mohr
R. E. Williford

Technical Information Files (5)
Publishing Coordination (2)

592 219